Study of Sensitivity to Search for a Charged Lepton Flavor Violating Process

Kou Oishi

Kyushu University

March 3, 2021

Abstract

The search for charged lepton flavor violation (CLFV) plays a vital role in probing a profound nature that even the standard model (SM) of high-energy particle physics cannot explain. The muon-to-electron (μ-e) conversion process, in which a muon captured by an atom decays to only a single electron with constant energy of 105 MeV, violating the muon and electron flavor conservation, is one of the most investigated CLFV channels. The COMET (COherent Muon-to-Electron Transition) experiment will search for μ-e conversion in aluminum at J-PARC in Japan in a staging approach. The second-phase (Phase-II) experiment aims for an excellent sensitivity of 10^{-17}, which improves the latest record 10000 times and reaches the conversion rate suggested by several theories beyond the SM.

The Kyushu University group has contributed to the development of the StrECAL detector system, consisting of the straw tube tracker and electromagnetic calorimeter (ECAL), which measure the momentum and energy of the 105 MeV electrons with a great resolution. The straw tube tracker tracks spiral particle trajectories in a magnetic field with layers of straw-shaped extremely-thin gaseous chambers that can even work in a vacuum to minimize energy loss. The ECAL has adopted the LYSO inorganic scintillating crystal, which has desirable properties in energy measurement.

This thesis is to present a simulation-based study result to check the feasibility of the Phase-II sensitivity based on realistic StrECAL performance. In order to evaluate the performance, a StrECAL detector prototype was constructed and examined with electron beams at ELPH in Tohoku University, Japan. The straw tube showed a spatial resolution of around 100 μm, and the ECAL showed an energy resolution of $3.91 \pm 0.07\%$, a time resolution of 0.54 ± 0.12 nsec, and a position resolution of 7.65 ± 0.07 mm at 105 MeV/c; they meet all the requirements.

With the COMET-official suite for simulation and analysis, the observed StrECAL performance was successfully reproduced, and full-simulated Phase-II events from the primary proton beam to the detector response were produced. The reconstruction algorithms were also developed and implemented by utilizing machine learning techniques, as well as several quality cuts. They give a momentum resolution of 190 keV/c for the signal electrons with an overall efficiency of 72.5% while securing a good signal-event purity of 97.6% in the reconstructed events.

Based on the evaluated analysis performance, the total experimental acceptance of Phase-II is estimated at 0.034 with the default measurement timing window from 600 to 1200 nsec, which means a single event sensitivity of 1.4×10^{-17} can be accomplished in one-year data taking. Although the systematic uncertainty is evaluated at 11.6% in total, the reconstruction and analysis parts have only 1.2%. They also show a stable performance for different timing-window configurations.

Acknowlegements

I owe a huge debt of gratitude to Professor Kiyotomo Kawagoe, Professor Junji Tojo, and Professor Tamaki Yoshioka, who were my supervisors for a long period and provided me with several opportunities to learn the necessary knowledge and skills required to become a scientist. Professor Kawagoe and Professor Yoshioka established the laboratory, taught me (one of the first students of the lab without any senior students) everything directly, and helped me organize my work on the international linear collider project. For a long time after the foundation of the COMET group, I have been indebted to Professor Tojo. He strongly led the group and the development of ECAL (electromagnetic calorimeter) for COMET, and I am happy that I could complete that work with him; I not only learned the skillsets required for research but also gained an understanding of the lifestyle as a scientist.

I would like to appreciate the support provided by several COMET collaborators for my studies. Professor Yoshitaka Kuno at Osaka University and Professor Satoshi Mihara at KEK extended the collaboration into a large and well-known group, which enabled me to work and communicate with international scientists. Dr. Youichi Igarashi, Dr. Hajime Nishiguchi, and Dr. Kazuki Ueno always provided fruitful advice, worked hard with me in the experiments for my studies, and cared for me when I was staying at KEK and J-PARC. Dr. Yuki Fujii, Dr. Manabu Moritsu, Dr. Hiroshi Yamaguchi, and Dr. Hisataka Yoshida were postdoctoral researchers in the COMET Japan group who helped me considerably. Although I reserve their names here, I am grateful for the excellent inspiration I received from all student collaborators I worked with for COMET. Further, I would like to thank Professor Yoshi Uchida, my current supervisor at Imperial College London, who understood the trouble I suffered during this PhD assessment and patiently supported me.

I would like to mention that my research was partly assisted by the KAKENHI Grant 16J00188.

The staff and colleagues at Kyushu University helped me experience a meaningful time in both my research and in my daily life in Fukuoka. Dr. Dai Kobayashi, Dr. Susumu Oda, Dr. Hidetoshi Otono, Dr. Taikan Suehara, and Dr. Takashi Yamanaka provided suggestions for my study and suggested exciting topics from their research and collaboration. Ms. Saori Shigematsu helped me several times in my business. I considerably appreciate the contribution of my colleagues in the COMET group to this study; in particular, Dr. Yuki Nakai and Mr. Kyohei Noguchi cooperated with me for years.

In addition, I am grateful to Mr. Satoru Matsumoto, Mr. Yohei Miyazaki, and Mr. Hiraku Ueno, with whom I enjoyed the same period in the master's program, and Mr. Jun Koga, Mr. Yuta Miyazaki, Mr. Shusuke Takada, Dr. Tatsuhiko Tomita, Dr. Shohei Shirabe, Dr. Naoyuki Sumi, and Mr. Naoki Yamaguchi, who encouraged me to spend the doctoral program together.

Finally, I thank my family for their enduring support.

Contents

List of Figures

List of Tables

Introduction

The SM (standard model) is the most fundamental theory in high-energy particle physics. Several experimental results have shown good agreement with the SM, including the historical discovery of the Higgs boson. Nevertheless, several observations indicate there are phenomena that cannot be explained by the SM. In the Super Kamiokande experiment at Kamioka, Japan, neutrino oscillation were observed [1]. Transitions among three generations of neutrinos can occur while moving through a long path, which implies neutrinos have finite masses, and neutral-lepton flavor violation exists. Since the SM assumes that the neutral-lepton flavor would be conserved.

Charged-lepton flavor violating processes have been explored since the early beginning of high-energy physics, and one such process is the muon-to-electron conversion process (μ-e conversion). Muons trapped in an atomic orbit undergo either muon capture, or they decay to one electron and two neutrinos like in free muon decay. In μ-e conversion, the muon decays to only one electron, whose energy becomes $\sim$ 105 MeV because of the two-body decay with the atom. Since this violates the muon and electron flavor conservation, its branching ratio is suppressed in the SM to practically zero. However, some BSM (beyond the standard model) theories can increase it to the level that can be reached by modern experimental techniques. Owing to the difference between the SM and BSM, searching for μ-e conversion has now become a nearly background-free experiment, and its observation will directly indicate the existence of new BSM physics.

COMET (coherent muon-to-electron transition) is the international collaboration to search for the μ-e conversion at J-PARC (Japan Proton Accelerator Research Complex), Ibaraki, Japan by utilizing the high-intensity proton beam [2–4]. The experiment will be conducted in two stages: Phase-I and Phase-II. In Phase-II, the final goal of the sensitivity is $O(10^{-17})$, which is an approximately 10,000 times improvement over the current upper limit set by the SINDRUM-II experiment in 2000 [5]. The primary particle-detector system for Phase-II, StrECAL, comprises the straw tube tracker and ECAL (electromagnetic calorimeter).

The straw tube tracker measures the particle trajectories to reconstruct their momentum; it comprises multiple layers of long gaseous chambers fabricated from very low materials, and it works in a vacuum to minimize distorting the trajectory and gain a high momentum resolution.

The ECAL is composed of segmented crystal scintillators that measure the the energy lost by the particle in them. We adopted LYSO (lutetium-yttrium oxyorthosilicate), which is an inorganic compound that possesses excellent properties to meet the energy, time, and position resolutions required for the ECAL.

The Kyushu University Group has participated in the development of StrECAL and has been leading the activities for the ECAL part since the initial design stage. Starting with the development

of individual items such as straw tubes and crystals, we constructed several prototypes and evaluated their performance via experiments. In 2017, we eventually constructed the final StrECAL prototype based on the practical detector design for COMET, evaluated its performance using the electron beam facility at ELPH (Research Center for Electron Photon Science) in Tohoku University, Japan, and successfully obtained the required performance.

This study aims to estimate the Phase-II sensitivity for the electron of μ-e conversion from the detector point of view via a simulation. The first simulation study successfully showed that the desired sensitivity is achievable and that the background contamination into the signal region becomes sufficiently small [6]. However, because the first study focused on optimizing the geometrical design of the beamline components, it excluded the simulation and analysis related to the realistic detector performance and only assumed a tentative analysis efficiency. In the Phase-II experiment, the beam power will be considerably high and definitely introduce a tremendous number of hits into the detectors, which may disturb the momentum and energy reconstruction from the StrECAL hits and deteriorate measurement performance. This study aims to consider this concern in the simulation, develop and optimize practical reconstruction algorithms and analysis schemes, and evaluate the overall sensitivity.

The remainder of this thesis is organized as follows: Chapter 1 briefly reviews the historical and theoretical backgrounds of the lepton flavor violation and μ-e conversion. Chapter 2 introduces the COMET experiment and its novel techniques to search for μ-e conversion. In Chapters 3 and 4, for each detector of StrECAL, the required performance, design, and underlying study results are discussed. Chapter 5 shows the performance of the final StrECAL prototype evaluated in 2017 at ELPH, including the detail of the experiment and analysis. Switching to simulation topics, Chapter 6 explains the mechanism to reproduce the obtained detector performance and details of the simulation data production. Chapter 7 presents the developed reconstruction algorithms and their performance. Finally, Chapter 8 estimates the Phase-II sensitivity from the results above, and Chapter 9 summarizes the study.

1

Lepton Flavor Violation and Muon-to-Electron Conversion

The history of LFV (lepton flavor violation) can be traced back to the discovery of the muon in cosmic rays. A muon is the second-lightest lepton next to the electron in the SM (standard model) of high-energy physics, and has the same properties as the electron except for its approximately 200 times heavier mass.

Initially, researchers believed that it was a specific excited state of the electron. Under this supposition, E. P. Hincks and B. Pontecorvo attempted to observe its deexcitation in 1947, $\mu^+ \to e^+\gamma$; however, they were not successful [7]. Further, even today, no experiment has successful observed the deexcitation. This is now understood in the context of the conservation of lepton flavor.

1.1 Lepton Flavor Conservation

Leptons comprise electron (e), muon (μ), tau (τ), and each uncharged partner neutrinos (ν_e, ν_μ, and ν_τ); antiparticles associated with every particle. The lepton flavor is a particular quantum number assigned to each type of lepton. The electron and electron neutrino have an electron number of $L_e = +1$, and the positron and electron antineutrino have $L_e = -1$. Similarly, the muon and tau numbers are L_μ and L_τ, respectively. In the SM, any physics process must conserve individual numbers in total between its initial and final states.

The following muon decays are the most leading examples to demonstrate the conservation of electron and muon numbers.

$$\mu^- \to e^- + \bar{\nu}_e + \nu_\mu \quad \text{or} \quad \mu^+ \to e^+ + \nu_e + \bar{\nu}_\mu. \tag{1.1}$$

In the initial states, both electron and muon numbers are $L_e = 0$ and $L_\mu = \pm 1$ ($\mu^\mp$), respectively. In the final states, $L_e = \pm 1$ ($e^\mp$) ∓ 1 ($\bar{\nu}_e$ or ν_e) $= 0$ and $L_\mu = \pm 1$ (ν_μ or $\bar{\nu}_\mu$) in total, which are the same.

Since the existence of the muon was confirmed in 1937 [8–10], many experiments have been conducted to view any process that violate it; however, they failed for charged leptons. Here, we emphasize "charged" because NLFV (neutral lepton flavor violation) has already been observed.

1.2 Neutral-Lepton Flavor Violation: Neutrino Oscillation

In the late 1960s, R. Davis led the Homestake experiment at Brookhaven in the US, which was the first to measure electron neutrinos originating from the Sun (i.e., solar neutrinos) and find a contradiction in the observed flux to the expectation [11]. Currently, we are aware that it is attributed to the transition of electron neutrinos into other flavors, which is called neutrino oscillation. Further, if the experiment had a sensitivity to them, we may not have needed to wait for the experimental solution obtained by the Super Kamiokande in Japan and SNO (Sudbury Neutrino Observatory) in Canada in the year 2000.

Prior to this solar neutrino problem, B. Pontecorvo proposed neutrino-antineutrino oscillation in 1957 [12,13] based on the idea of neutral kaon mixing reported by Gell-Mann and Pais [14]. Although such a matter–antimatter oscillation has not been confirmed, this idea was followed by Z. Maki, M. Nakagawa, and S. Sakata [15], and then by Pontecorvo [16]. Finally, their works were summarized as the PMNS (Pontecorvo–Maki–Nakagawa–Sakata) matrix, which successfully describes neutrino oscillation and provides us a key factor related to the problem of why matters dominate the present universe (matter–antimatter asymmetry). In the context of the LFV, we focus on its impact on the neutrino mass in terms of the nondiagonal matrix linking the flavor eigenstates (ν_e, ν_μ, ν_τ) and the mass eigenstates of the three neutrinos (ν_1, ν_2, ν_3). For the sake of simplicity, the probability that a neutrino changes its flavor state a to b after flying a distance L in a vacuum under a two-neutrinos oscillation hypothesis is given as

$$P_{a\to b} = \sin^2 2\theta \sin^2\left(\frac{1.27\ \Delta m^2\,(\mathrm{eV}^2)\,L\,(\mathrm{km})}{E_\nu\,(\mathrm{GeV})}\right), \tag{1.2}$$

where E_ν, θ, and Δm^2 denote neutrino energy, mixing angle between flavor and mass eigenstates, and mass squared difference of the mass eigenstates, respectively. It indicates that the transition never occurs if the neutrinos have no mass as defined by the SM.

The Super Kamiokande experiment investigated atmospheric neutrinos arising from cosmic rays and demonstrated that the oscillation to tau neutrinos could explain the decreases in the muon neutrino flux [1]. The SNO experiment was the first experiment to observe all neutrino flavors[1] [17] and achieve the direct measurement of the transition of solar electron neutrinos to either mu or tau neutrinos in 2001; this finally resolved the solar neutrino problem [18]. Further, the K2K experiment in Japan confirmed the oscillation with the long-baseline neutrino beam from KEK (High Energy Accelerator Research Organization) in Ibaraki to Kamioka in Gifu [19]. Moreover, the K2K experiment was the first neutrino oscillation experiment that placed the neutrino source under control.

In conclusion, neutrino oscillation itself proved that NLFV exists and that it is caused by the nonzero neutrino mass. These facts helped introduce modifications to the SM. Today, neutrino oscillation is counted among the so-called physics BSM (beyond the standard model)—or customarily BSM physics—similar to the matter–antimatter asymmetry problem.

[1] It could not distinguish muon and tau neutrinos.

1.3 Charged-Lepton Flavor Violating Muon Decays

The discovery of NLFV stimulated searches for CLFV (charged lepton flavor violation) using muons. The SM allow its existence by adding a finite mass into the neutrinos. There are three muon CLFV processes that have been extensively studied via many experiments since the discovery of the muon: $\mu^{\pm} \to e^{\pm}\gamma$, $\mu^{\pm} \to e^{\pm}e^{\mp}e^{\pm}$[2], and $\mu^{-}N \to e^{-}N$ (μ-e conversion). Figure 1.1 illustrates the improvements made in the experiments to search for them chronologically. These experiments have employed different muon sources (from cosmic rays to accelerators) to improve the statistics and resulting sensitivity. To this day, the upper limits set for the processes have significantly been reduced by more than ten orders of magnitude. Indeed, scientists have not yet given up on improving sensitivity, and several experimental collaborations are being conducted globally to search for these muon rare decays with more improved sensitivity; for example, the MEG II experiment for $\mu^{+} \to e^{+}\gamma$ [20] and the Mu3e experiment for $\mu^{+} \to e^{+}e^{-}e^{+}$. In particular, the COMET experiment has two competitors: the DeeMe [21] and Mu2e [22] experiments.

This section starts with $\mu^{\pm} \to e^{\pm}\gamma$, which is the simplest decay mode that is included by the other two processes as well. For each process, we briefly introduce the experiments mentioned above.

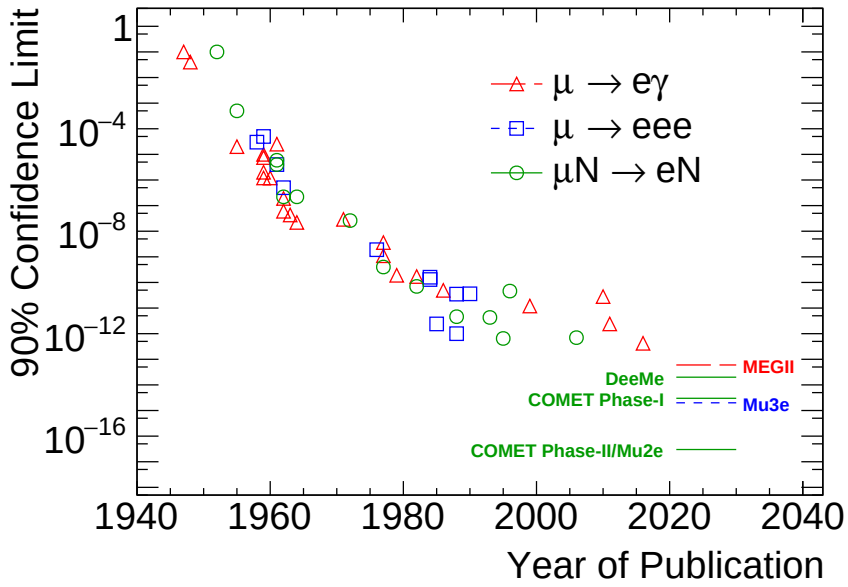

Figure 1.1: History and prospects of experimental searches for three muon CLFV processes: $\mu^{+} \to e^{+}\gamma$, $\mu^{+} \to e^{+}e^{-}e^{+}$, and $\mu^{-}N \to e^{-}N$ (μ-e conversion). The vertical axis indicates the upper limit on the branching ratio or conversion rate (see the definition in Section 1.3.3) of each objective process at 90% CL (confidence level), and the horizontal axis represents the year of the result publication. Data are compiled by [23], except for the point of $\mu^{+} \to e^{+}\gamma$ in 2016 [24]. The lines represent new limits expected to be set in the next decade by experiments under the construction or operation as of 2020.

[2]Unfortunately, there do not seem to be a common name for $\mu \to e\gamma$ and $\mu \to eee$; they are often shortened to "mu-e-gamma" and "mu-three-e."

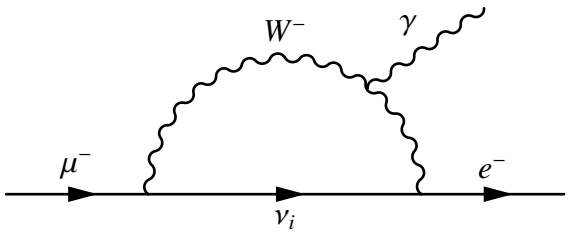

Figure 1.2: Feynman diagram for $\mu^- \to e^-\gamma$ in the SM

1.3.1 $\mu^\pm \to e^\pm\gamma$

The challenge to CLFV started with

$$\mu^\pm \to e^\pm\gamma, \tag{1.3}$$

and its Feynman diagram is shown in Figure 1.2. The neutrino ν_i with a mass eigenstate i includes all flavor states, and it can couple both the muon and the electron in the initial and final states. The photon emitted from the W boson is required to conserve the energy and momentum. Kinematically, the electron and photon from this two-body decay at rest originate in opposite directions with fixed energies, which is the signature of the process.

The branching ratio is reported in [25–28] and calculated as

$$\mathrm{BR}\,(\mu \to e\gamma) \propto \left| \sum_{i=1}^{3} U^*_{\mu i} U_{ei} \frac{m^2_{\nu_i}}{M^2_W} \right|^2 < O(10^{-54}), \tag{1.4}$$

where M_W and m_{ν_i} represent the neutrino and W-boson masses, respectively. Further, $U_{\alpha i}$ denotes the PMNS matrix between the neutrino flavor eigenstates α and the mass eigenstates i. The calculated value is attributed to the small mass ratio of m_{ν_i}/M_W and the leptonic version of the GIM (Glashow–Iliopoulos–Maiani)-mechanism suppression [29].

Indeed, the present technology is not equipped to observe this rare decay and any other CLFV processes even if the SM admits the neutrino mass. However, if new physics hides in nature and can enhance the probability by about 40 orders so that we can observe it, this feature offers us a clean laboratory, wherein CLFV processes occur because of only BSM physics and not the SM. In that scenario, an observation of CLFV directly represents the discovery of new BSM physics. In other words, searching for muon CLFV is one of the most excellent probes for BSM physics.

It is obvious that present technology cannot allow us to observe this rare decay, and of course, any other CLFV processes even if the SM admits the neutrino mass. However, if new physics hides in nature and can enhance the probability by about 40 orders so that we can observe it, this feature rather offers us a clean laboratory, in which CLFV processes happen due to only BSM physics, not the SM. In that situation, an observation of CLFV directly stands for the discovery of new BSM physics. In other words, searching for muon CLFV is one of the most excellent probes for BSM physics. We shall review several BSM models in the next section.

The latest upper limit on the branching ratio $\mathrm{BR}\,(\mu^+ \to e^+\gamma) = 4.2 \times 10^{-13}$ was provided by the MEG experiment at PSI (Paul Scherrer Institut) in Switzerland [24]. Currently, the MEG II experiment—the MEG's successor—will soon be commissioned and operated with an order of magnitude improvement in sensitivity [20].

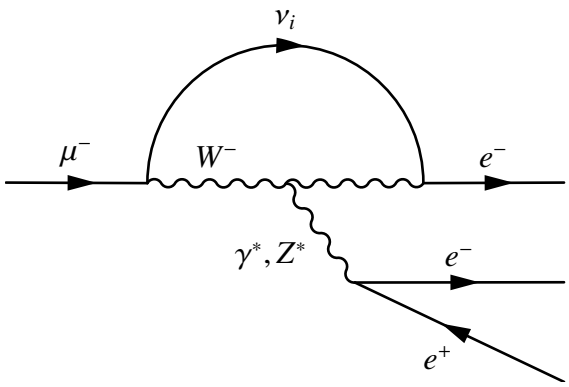

Figure 1.3: Feynman diagram for $\mu^- \to e^- e^+ e^-$ in the SM

1.3.2 $\mu^\pm \to e^\pm e^\mp e^\pm$

A three-body decay process is realized under the SM as shown by Figure 1.3. Since it partially contains $\mu \to e\gamma$ (Figure 1.2), the branching ratio is also too low to detect. However, this is the advantage of this process and of μ-e conversion in that the intermediate boson from the W boson can be off-shell. Hence, the process has a sensitivity to nonphotonic channels; for instance, those mediated by the Z boson [30].

The current limit of $\mathrm{BR}(\mu^+ \to e^+e^-e^+) = 1.0 \times 10^{-12}$ was reported in 1988 by [31]. As well as the MEG II experiment, the Mu3e experiment is also now being prepared at PSI to begin its commissioning in 2021 [20, 32]. It is expected to reduce the limit down to $\mathcal{O}(10^{-15})$ at once.

1.3.3 Muon-to-Electron (μ-e) Conversion: $\mu^- N \to e^- N$

When a negative muon is trapped by an atom and falls to the ground state by emitting an X-ray, the consequent muonic atom—under the SM frame—proceeds either towards muon capture or muon DIO (decay in orbit),

$$\mu^- + N(A,\, Z) \to \nu_\mu + N'(A,\, Z-1), \tag{1.5}$$

$$\mu^- + N(A,\, Z) \to e^- + \bar{\nu}_e + \nu_\mu + N(A,\, Z), \tag{1.6}$$

where $N(A,\, Z)$ denotes a nucleus of the muonic atom with mass and atomic numbers of A and Z. The muonic-atom lifetime varies based on the type of nucleus.

For DIO, the lifetime is almost the same as that of the free muon decay of 2.2 μsec[3]. The capture process changes it more effectively because a heavier nucleus has more protons that can contribute to the capture and broader wavefunction that can interfere with the muon. In total, a lifetime shortens with an atomic number; for example, it is 864 nsec in the case of aluminum—the target material of the COMET experiment—whose capture rate is 61% [33].

A CLFV process arising from muonic atoms is neutrinoless muon decay, literally μ-e conversion:

$$\mu^- + N(A,\, Z) \to e^- + N(A,\, Z), \tag{1.7}$$

[3]The lifetime slightly increases because of the limited phase-space that the final state can employ compared to the free muon and time dilation effect of the muon moving along the orbit.

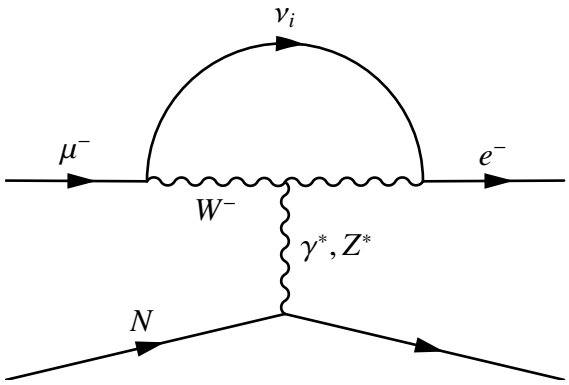

Figure 1.4: Feynman diagram for μ-e conversion, $\mu^- + N \to e^- + N$, in the SM

as shown by Figure 1.4. Different from $\mu^\pm \to e^\pm e^\mp e^\pm$, the virtual particle interacts with either a u or d quark in the nucleus. Again, this process can hardly occur under the SM but is sensitive to nonphotonic channels. The nucleus after the decay can be either in the ground state or an excited state.

The former, called the "coherent" transition, dominates the total decay width [34]. This gives us an experimental advantage in that, as a two-body decay, the electron can have a monochromatic energy specific to the nucleus of

$$E_e = m_\mu - E_{\text{bind}} - \frac{(m_\mu - E_{\text{bind}})^2}{2m_N}, \tag{1.8}$$

where $m_\mu = 105.66\ \text{MeV}/c^2$ and m_N represent the muon and nucleus mass, respectively, and E_{bind} denotes the binding energy of the ground-state muonic atom. The last term represents the kinetic energy of the recoiling nucleus and is negligibly small. In the case of aluminum, $E_e = 104.97$ MeV. Owing to this constant energy, we do not need to measure any other coincident particles for identifying the conversion ("signal") electron. That is, it is not easy to measure this for "incoherent" signal electrons, whose energy drifts and goes below the end-point energy of the DIO electron. This is why all μ-e conversion experiments concentrate on the coherent process[4].

We refer to the following "conversion ratio" to the total muon capture rate instead of the branching ratio to the total decay width,

$$\text{BR}\,(\mu^- N \to e^- N) = \frac{\Gamma(\mu^- N \to e^- N)}{\Gamma(\mu^- N \to \text{capture})}, \tag{1.9}$$

where Γ represents the corresponding decay width. Besides the nucleus difference, the SINDRUM-II experiment at PSI set the lowest constraint on μ-e conversion in gold as $\text{BR}\,(\mu\text{Au} \to e\text{Au}) = 7.0 \times 10^{-13}$ in 2006 [5]. Currently, not only COMET but also two experiments plan to search for μ-e conversion. First, the DeeMe experiment will use carbon or silicon carbide, thereby targeting sensitivities of $O(10^{-14})$ [21] with a simple setup compared to COMET. The construction of the beamline is built at the MLF (Materials and Life Science Experimental Facility) of the J-PARC (Japan Proton Accelerator Research Complex)[5] in Japan. In 2019, they performed a series of measurements of momentum distribution of the DIO electron from a carbon target; the analysis is ongoing [35]. Second,

[4]This is emphasized in the name of COMET: *coherent* muon-to-electron transition.

[5]A different facility from the NP hall where the COMET experiment will be performed.

the Mu2e experiment will be performed for aluminum at FNAL (Fermi National Accelerator Laboratory) in the US. They aim to obtain a sensitivity of $O(10^{-17})$, the same as the COMET final goal, and to adopt a similar experimental configuration conceptually. The experimental facility has been constructed. It is expected that the detector construction and installation will finish in 2021, and the commissioning will start with the beam at the end of 2022, followed by data collection [36].

1.4 Physics beyond the Standard Model (BSM)

There are various BSMs enhancing the rate of the muon CLFV processes to a level that the present-day experimental techniques can reach. Two typical cases are introduced below, in addition to the method on how to distinguish such different models with the three muon CLFV processes.

1.4.1 Supersymmetry (SUSY) model

The SUSY (supersymmetry) model was proposed to resolve problems in the SM, such as the hierarchy problem between the electroweak breaking scale ($O(10^2)$ GeV) and the Plank scale ($O(10^{19})$ GeV). In MSSM (minimal supersymmetric standard model)—the minimal extension model—each SM particle has an associated "superpartner," whose spin differs by 1/2. The superpartners for a fermion, quark, lepton, gauge boson, and Higgs boson are named "sfermion" ($\tilde{f}$), "squark" ($\tilde{q}$) and "slepton" ($\tilde{l}$), "gaugino," and "higgsino," respectively. For example, "selectron" ($\tilde{e}$) and "smuon" ($\tilde{\mu}$) are scalar bosons. Further, "bino" ($\tilde{B}$) and "wino" ($\tilde{W}^0$, $\tilde{W}^{\pm}$) correspond to the electroweak gauge bosons. Moreover, two Higgs doublets are required in contrast to the SM, and each contains a neutral and charged Higgs, and the same applies to the higgsinos. The neutral gauginos (bino and wino) and two neutral higgsinos have the same quantum numbers, and they thus mix to form four mass eigenstates named "neutralinos," $\tilde{\chi}_i^0$ (i = 1, ..., 4). Every SUSY pair belongs to a single superfield, and their mass is degenerate if the supersymmetry is satisfied. However, since such new particles have never been discovered, the symmetry should be broken. That also introduces the potential for flavor mixing.

Figure 1.5 shows a possible Feynman diagram for $\mu \to e\gamma$. The smuon would change to the selectron if the off-diagonal element of the slepton mass matrix between $\tilde{\mu}$ and $\tilde{e}$, $m^2_{\tilde{\mu}\tilde{e}}$, is nonzero. In general, diagonalizing the lepton mass matrix does not necessarily imply that the slepton mass matrix can be diagonalized simultaneously. The branching ratio of $\mu \to e\gamma$ is given approximately as [37]

$$\mathrm{BR}\,(\mu \to e\gamma) \sim \left(\frac{\left|m^2_{\tilde{\mu}\tilde{e}}\right|}{m^2_{\tilde{l}}}\right)^2 \left(\frac{100\ \mathrm{GeV}}{m_{\tilde{l}}}\right)^4 10^{-16}, \tag{1.10}$$

where $m_{\tilde{l}}$ denotes the slepton mass that is supposed to be degenerate. However, according to the latest upper limit [24], $m^2_{\tilde{\mu}\tilde{e}}$ should be considerably suppressed as

$$\frac{\left|m^2_{\tilde{\mu}\tilde{e}}\right|}{m^2_{\tilde{l}}} \lesssim 10^{-4}\left(\frac{100\ \mathrm{GeV}}{m_{\tilde{l}}}\right)^2. \tag{1.11}$$

Any SUSY scenario must satisfy this constraint. The mSUGRA (minimal supergravity) or CMSSM (constrained MSSM) model [38–41] is the most famous SUSY model that reduces the number of

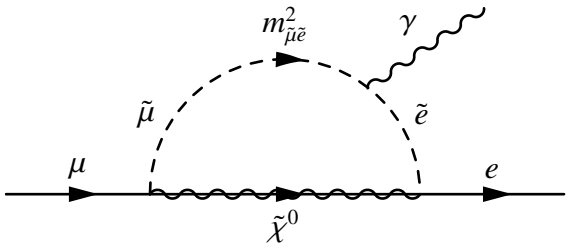

Figure 1.5: Feynman diagram for $\mu \to e\gamma$ in the MSSM

parameters, that is more than 100 in the MSSM, with a hypothesis to m_0, $m_{1/2}$, A_0, $\tan\beta$, and sign(μ). m_0 and $m_{1/2}$ represent the universal scalar and gaugino masses, A_0 denotes a universal trilinear coupling, $\tan\beta$ represents the ratio of vacuum expectation values of the two neutral Higgs bosons[6], and μ corresponds to a mass term that mixes the two Higgs doublets. All scalar particles are required the m_0 universality at the Plank scale, and the slepton mass matrix does not have any off-diagonal element. This meets (1.11); however, it allows a finite value of $m^2_{\tilde{\mu}\tilde{e}}$ through quantum corrections if some interactions exist between the Plank and electroweak scales [42]. The SUSY GUT (grand unified theory) and SUSY seesaw models are major scenarios that include such interactions.

The SUSY GUT assumes the unification of the three SM gauge groups into an upper group at a high-energy scale [43, 44]. Then, their coupling constants are unified at 2×10^{16} GeV [45–47], which are consistent with the precise measurements of the coupling constants by LEP (Large Electron–Positron Collider) at CERN (European Organization for Nuclear Research) in Switzerland and SLC (Stanford Linear Collider) at SLAC in the US. At that scale, we cannot distinguish quarks and leptons, and hence, an LFV interaction occurs and provides finite off-diagonal elements to the matrix [48, 49]. Based on these parameters, BR ($\mu^- N \to e^- N$) can increase up to $O(10^{-14})$ [50].

The SUSY model including the seesaw mechanism predicts a detectable branching ratio. The seesaw mechanism clarifies why the neutrino mass of $O(10^{-1})$ eV/c^2 that is considerably small compared to other particles by introducing two or more heavy right-handed neutrinos [51, 52]. The SM does not contain right-handed neutrinos and left-handed antineutrinos because the weak interaction applies only to left-handed (right-handed) particles (antiparticles). Therefore, introducing such neutrinos does not contradict the fact that we have never detected them experimentally. The neutrino could be a Majorana particle[7] because of its neutral charge. When two Majorana fields N_1 and N_2 are introduced, their generic mass term contains[8]

$$\begin{pmatrix} \bar{N}_1 & \bar{N}_2 \end{pmatrix} \begin{pmatrix} m_L & m_D \\ m_D & m_R \end{pmatrix} \begin{pmatrix} N_1 \\ N_2 \end{pmatrix}. \tag{1.12}$$

The matrix has two mass eigenvalues, which are approximately m_D^2/m_R and m_R when $m_L = 0$ and $m_D \ll m_R$. We can interpret that the latter's eigenstate corresponds to the right-handed neutrino, and the other is the normal neutrino, the mass of which is considerably suppressed by the heavy mass of m_R.

[6] In SUSY, there are two Higgs doublets, each of which contain a neutral Higgs.

[7] A Majorana particle is a fermion that is the same as its own antiparticle; however, only neutral fermions can be this particle.

[8] In the case of the type-I seesaw model.

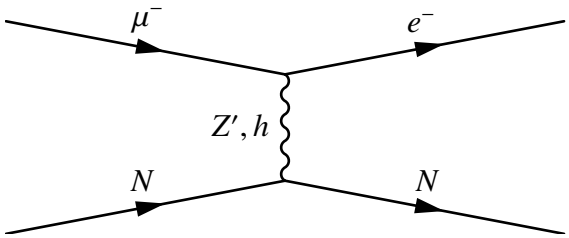

Figure 1.6: Tree-level Feynman diagram for μ-e conversion by Z' boson or LFV Higgs decay

In the SUSY frame, the Yukawa interaction of a left-handed slepton with a higgsino and a right-handed neutrino provides quantum corrections to $m^2_{\tilde{\mu}}\tilde{e}$ that breaks the flavor conservation [53, 54]. Without the SUSY model, it is still difficult for the seesaw mechanism to pull up the branching ratio [55][9].

The ATLAS and CMS experiments using the LHC (Large Hadron Collider) at CERN have been searching for indications of the SUSY particles and placing strong constraints on the parameters based on their null results. However, the CLFV experiments have higher sensitivities to the electroweak sector mediated the bino, wino, and higgsinos of the SUSY than the LHC experiments using the strong force in the collision. In the CMSSM case, low $m_{1/2}$ (roughly $< 0.5--1$ TeV) has been already scanned [56]; however, the latest value of BR $(\mu \to e\gamma)$ yields a considerably stronger constraint of a few TeV depending on the other parameters [57]. Beyond the CMSSM, more extensions of the SUSY that are different and have broader ranges of the parameters are still allowed [58].

1.4.2 Exotic Z and Higgs Bosons

μ-e conversion (and $\mu \to eee$ also) has other BSM possibilities wherein massive exotic bosons contribute at the tree level. The Z' boson is associated with extra gauge symmetry. There are several sources [59]; for example, a considerably larger symmetry as suggested by GUT breaks with the SM gauge group. If the Z' boson causes a flavor changing neutral current, it allows μ-e conversion [60]. Moreover, non-SM Higgs that decays into different flavor lepton pairs can also introduce a tree-level μ-e conversion [61], as shown in Figure 1.6. These Yukawa interactions are characterized by each coupling: Q^l_{12} for the Z' boson decay, and $Y_{\mu e}$ for the Higgs decay. It is assumed that Q^l_{ii} is the same as the SM Z couplings, and $Q^l_{ij} = 1$ for all off-diagonal elements $(i \neq j)$. In the direct search at CERN, lower limits on the Z' boson mass were set at 4.5 and 4.4 TeV/c^2 for the ATLAS and CMS experiments [62, 63]. However, the limit would increase up to $O(10^3)$ TeV/c^2 with the COMET Phase-II sensitivity. Further, $\sqrt{|Y_{\mu e}|^2 + |Y_{e\mu}|^2} < 3.6\times10^{-6}$ (4.6×10^{-5}) was set by the current limit on the $\mu \to e\gamma$ (μ-e conversion) branching ratio[10]. They are already better than $\sim 2 \times 10^{-4}$, which was obtained by the LHC experiments [64, 65]. In addition to the SUSY channels, the CLFV experiments can improve those limits further than the direct searches.

[9] In this case, BR $(\mu^+ \to e^+\gamma)$ is calculated by replacing $\frac{m^2_{\nu_i}}{M^2_W}$ in (1.4) with $\frac{m_{\nu_i}}{m_R}$.

[10] Precisely, the upper limits as of 2014 are used in the calculation.

1.4.3 Model Discrimination with the Muon CLFV Processes

The three CLFV decay modes that we reviewed have complementarity in terms of discriminating the model that is more favored. For example, when $\mu \to e\gamma$ is found, the available channel would be photonic. In this case, the rate of $\mu^+ \to e^+e^-e^+$ would be expected to become smaller because of the additional vertex between γ^* and e^+e^- in Figure 1.3 by a factor of α, which is the fine structure constant of about $1/137$.

The vertex of μ-e conversion has a different coupling because of the participation of all nucleons. If the CLFV is more friendly with a nonphotonic channel such as the Z' boson exchange, $\mu \to e\gamma$ cannot realize at tree level, and the rate of μ-e conversion (and $\mu \to eee$ also) could be higher.

Further, it should be emphasized that the μ-e conversion rate itself varies depending on both the model and nucleus that forms the muonic atoms [66]. This leads us to examining different materials for the muon target even if the COMET experiment succeeds in observing μ-e conversion from aluminum. In summary, all three CLFV processes have equal worth to be searched for, and it is quite interesting that they can be explored in a close period.

2

The COMET Experiment

2.1 Principle of the μ-e Conversion Search

Figure 2.1 illustrates the essential components required to observe μ-e conversion. We use the sequence of $p \to \pi^- \to \mu^-$ to produce abundant negative muons; this approach will be followed until a good muon source and its accelerating method are established in the future.

The proton beam is injected into the fixed pion-production target. Of the produced secondary particles, negative pions decay to muons, which are transported and form muonic atoms in the muon stopping target. If μ-e conversion occurs, a signal electron is emitted with a constant energy and is measured by the detector at the end. However, muonic atoms introduce some intrinsic BG (background) electrons, and the remaining beam particles hit the detector. Although they have relatively low momenta, a spectroscopic means needs to be adopted to reject such BG particles. All current μ-e conversion experiments—Mu2e, DeeMe, and COMET—are based on this idea.

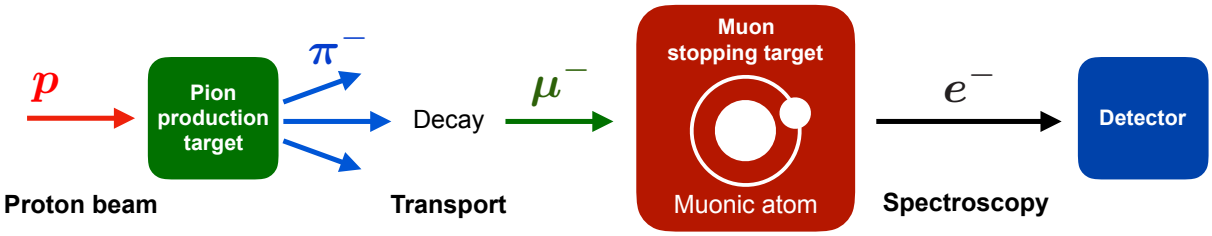

Figure 2.1: Principle procedure of μ-e conversion experiments. A proton beam is injected into the pion production target; the produced negative pions decay to negative muons before stopping at the muon stopping target. Electrons arise from the formed muonic atoms, and they include both the signal of μ-e conversion and the intrinsic BG. Some spectroscopic means are employed to select the high-momentum part effectively.

2.1.1 Backgrounds

BG processes are classified into three categories: intrinsic, beam, and cosmic BGs.

Intrinsic BGs are electrons that arise from muonic atoms, radiative muon capture (γ is added to the final state of (1.5)), and muon DIO (1.6). The photon emitted from the radiative nuclear capture and the electron converted from it have a sufficiently high energy to contaminate the signal region of

μ-e conversion although the DIO electron is a more frequent BG object. Two neutrinos from DIO can move back-to-back with small energies; the nucleus is more massive than the electron and it does not require high kinetic energy. Consequently, the DIO electron has a considerably high energy compared to that of free muon decay. Further, its energy spectrum is calculated in [67] and shown for aluminum in Figure 2.2. Although the largest fraction concentrates immediately before 52.8 MeV—the maximum energy in the case of free muon decay—the spectrum can last up to $\sim$ 105 MeV. Therefore, we need a detector system with a high resolution to distinguish signal electrons from DIO electrons.

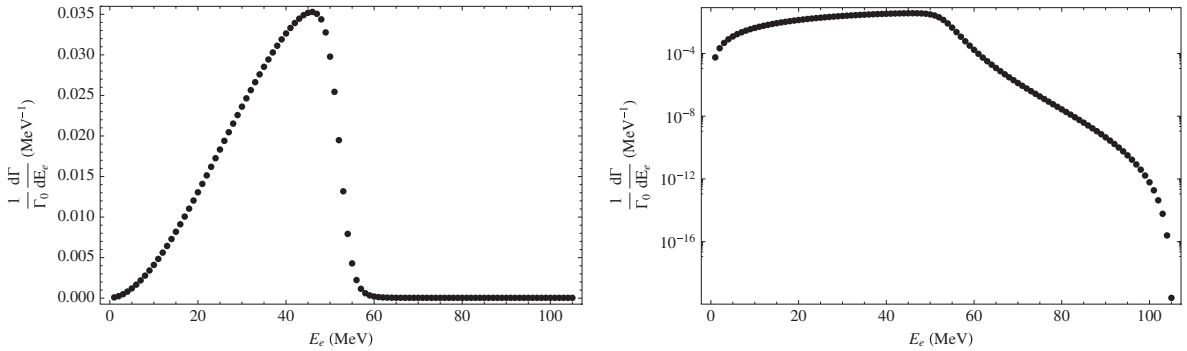

Figure 2.2: Energy spectrum of DIO electrons that arise from aluminum nuclei in linear (left) and logarithmic (right) scales; image adopted from [67]. The peak falls before 52.8 MeV, which is the endpoint energy of the free-muon-decay electrons. However, because of some kinematical arrangements allowed for DIO secondaries, the spectrum can continue to be near the interested energy of μ-e conversion.

For beam BGs, electrons with energies similar to those of the signal electron are present in beam particles, e.g., high-momentum muons and electrons, pions, and antiprotons. We classify them into prompt and delayed BGs based on their different time structure related to proton-beam injection. For example, the former includes muon and pion decays during their flight and radiative pion capture. They produce many signal-like electrons, and their hit rate in the detector is considerably high for a stable operation from a technical point of view. We need to use a pulsed beam and a timing window to mask most of the prompt BGs, as discussed in Section 2.2.2. The delayed BG originates from low-energy neutrons via neutron capture. Since they are slow and can repeat reflection on facility walls, they can reach the detector. Further, antiprotons would be slow until reaching the detector region. Moreover, the mirroring effect of the magnetic field would make it possible for electrons that gone upstream once to return. Besides signal-like electrons, the pile-up of any beam particles introduces difficulties in event reconstruction; some nonelectron particles can also be incorrectly identified as signal electrons, which then become BG.

The cosmic-ray BG is temporally independent of any experimental configuration. When a cosmic-ray muon hits any material around the muon stopping target, it can decay to a high-momentum electron that cannot be distinguished from a signal electron. Recent studies indicated that this is a relatively major contamination, and therefore, a cosmic-ray vetoing detector system needs to cover the beamline and detector.

2.2 COMET (Phase-II) Experiment

The COMET experiment will be conducted in two phases (Phase-I and -II) at J-PARC in Japan. The final Phase-II experiment aims to improve the sensitivity to $O(10^{-17})$ or better; a simplified schematic of the experiment is shown in Figure 2.3. The proton beam from the J-PARC accelerator first enters the pion capture solenoid and collides with a fixed target. The solenoid collects the pions generated in the backward direction and passes them to the first 180°-bent solenoid called the muon transport solenoid. The part with the lower momentum in muons to which the pions decay is selected with the solenoid magnetic field and trapped by the muon stopping target. The muon stopping target section links to the second-bent solenoid, i.e., the electron spectrometer, which selects high momentum signal electrons and rejects others such as most DIO electrons. The final section is the detector solenoid, wherein the detector system (StrECAL)—the combination of the straw tube tracker and the ECAL (electromagnetic calorimeter)—measures the momentum and energy of the incoming particles. The CRV (cosmic-ray veto) system surrounds the detector solenoid to recognize cosmic-induced BGs.

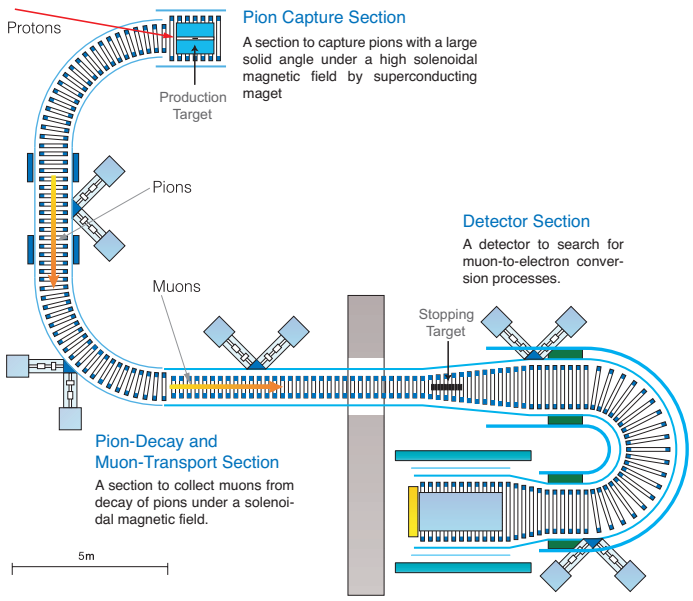

Figure 2.3: Schematic of the COMET Phase-II experiment. Protons accelerated by the J-PARC main ring are injected into the pion production target. The pions decay to muons, which are transported to the muon stopping target section by the transport solenoid. The magnetic field in the bent solenoid is utilized to select the momentum of the particles for decreasing the beam BG. Electrons arising from the muon stopping target are then separated again by the 180°-bent solenoid (called electron spectrometer) to suppress low-momentum particles. The straw tube tracker and electromagnetic calorimeter, which are installed in the detector solenoid, measure the particles. The cosmic-ray veto surrounds the detector solenoid.

2.2.1 Facility and Proton Beam

The COMET experiment is hosted by J-PARC[1] in Tokai, Ibaraki, Japan (Figure 2.4), which offers several particle beamlines based on its high-intensity proton beam. The proton-beam creation begins from the LINAC, where hydrogen ions generated from hydrogen gas are accelerated up to 400 MeV. The electrons are removed with a thin carbon film at the entrance of RCS (Rapid-Cycling Synchrotron) to form protons, and the RCS accelerates them to 3 GeV. Finally, the MR (Main Ring) synchrotron accelerator speed them up to 50 GeV.

However, we limit the speed to 8 GeV to suppress antiproton-induced BGs, as explained in Section 2.2.3. The neutrino-oscillation experiment (T2K) uses all protons at once (fast extraction), whereas our proton beam is extracted partially with kicker magnets (slow extraction) into the NP Hall (Nuclear and Particle Physics Experimental Hall).

The beam power will be 3.2 kW and 56 kW in Phase-I and Phase-II, respectively.

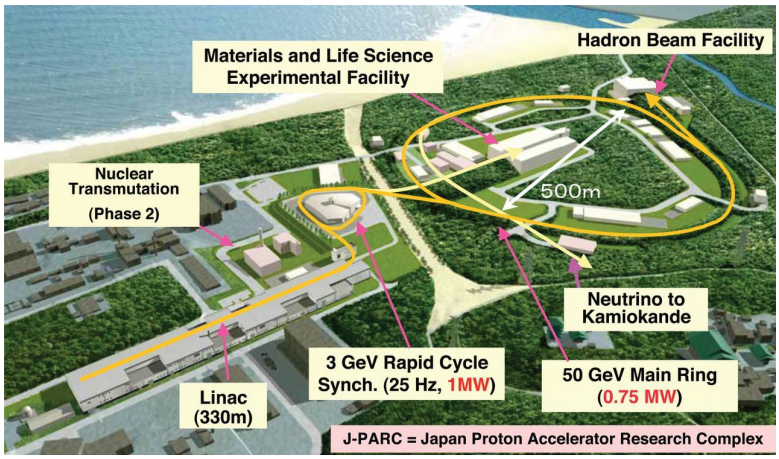

Figure 2.4: Bird's-eye view of the entire facilities in the Japan Proton Accelerator Research Complex (J-PARC), Ibaraki, Japan. Protons are accelerated by three accelerators: LINAC, RCS, and MR. The COMET facility is located next to the NP Hall (Hadron Beam Facility), into which slow-extracted (partially kicked) protons are injected.

The proton beam must be formed in pulses to differentiate the signal electrons from multiple beam BGs. Further, the distance between the pulses is crucial and correlated with the selection of the muon stopping target. To this end, we adopt the time structure illustrated in Figure 2.5. The RCS and MR have two and nine buckets, respectively, and we fill only one and four of them, respectively, with a bunch of protons with a width of 100 nsec. The buckets in MR are 585 nsec apart, and hence, proton bunches have distances of 1170 nsec but 1755 nsec partly.

The COMET facility was constructed adjacent to the NP Hall. Figure 2.6 shows the layout of the NP Hall and COMET facility, including their beamlines. The A-line has been used for experiments in the NP Hall; however, it will branch off to the B-line for the COMET experiment. Beam switching is performed by a Lambertson magnet and septum magnets.

[1] Although J-PARC is the name of the accelerator complex in the Nuclear Science Research Institute, it is also used to refer to all facilities that are part of it.

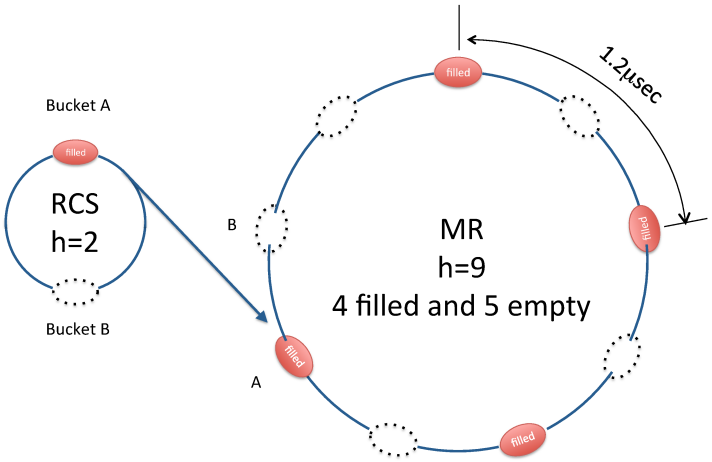

Figure 2.5: Time structure of the pulsed proton beam for COMET in the J-PARC RCS and MR. The protons fill one out of two buckets in the RCS and four out of nine buckets in the MR. The COMET proton-beam bunches are at the shortest distance of 1170 nsec.

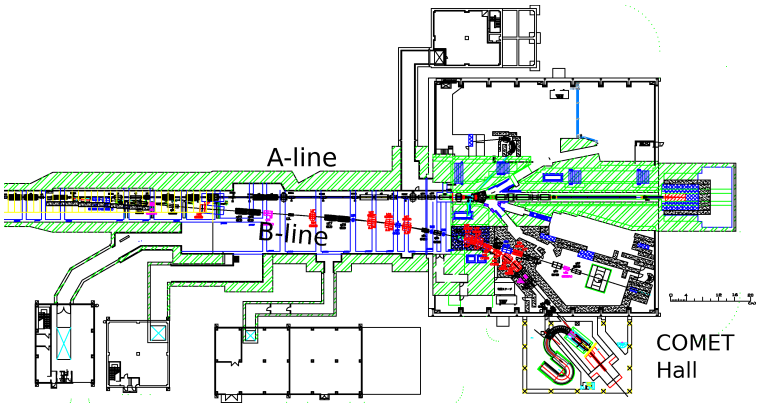

Figure 2.6: Layout of the NP Hall and COMET facility hall, and their beamlines in J-PARC. The proton beam from the MR is split into A- and B-lines; the latter is dedicated to the COMET experiment.

2.2.2 Beam Bunching and Timing Window

The μ-e conversion experiments need to use a pulsed beam and a timing window to separate the measurement from the term wherein many prompt BGs arrive at the detector; this is illustrated by Figure 2.7. Although it is necessary to use an intense proton beam to collect extensive statistics of muonic atoms, it results in a higher detector hit rate because of the prompt BG and multiple pile-ups, which makes it technically very challenging to distinguish the signal electrons. As discussed previously, the prompt BG correlates more temporally with original protons compared to the delayed BG. Therefore, protons need to be compiled into pulses to gather many prompt particles.

The timing window is used to enable the detectors system to measure the incoming particles that arrive during the window, and therefore, the window is set to not include the prompt BG. When the muonic-atom decay constant is sufficiently long compared to the proton-bunch width, part of the signal electrons enter the window.

If beam protons come between bunches, they can introduce prompt BGs containing signal-like

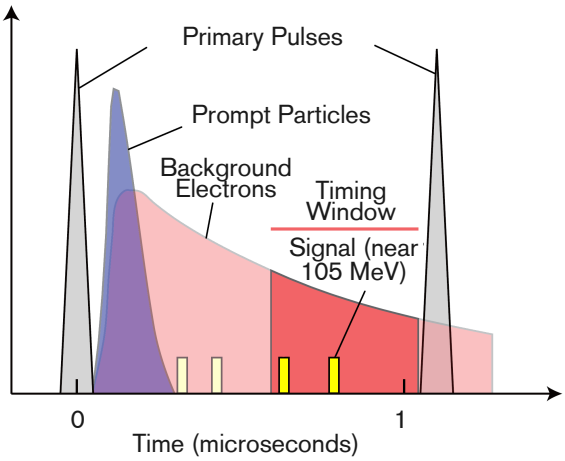

Figure 2.7: Time structure of events generated by bunched proton beams and the associated timing window. The vertical axis indicates the detector hit rate. The bunch distance in the case of COMET is 1.17 μsec. After each primary pulse, the direct secondaries (prompt particles) come first, and this corresponds to the delayed BG mentioned in Section 2.1.1. The timing window is set after their arrival until the next injection. From the muonic atoms, the electrons appear as per the decay constant, part of which enter the timing window.

electrons into the timing window. We defined the extinction factor as the ratio of the number of protons between bunches to that in a bunch, and it needs to be as small as possible or at least better than 10^{-10}. We conducted measurements as a function of the RF (radio frequency) voltage applied to the accelerator at the MR abort line in 2014, and we found it to decrease exponentially as per the voltage. Although below 100 kV, beam protons tend to be scattered when accelerated in the MR, and the extinction factor is poorer than that for the minimal requirement; it can achieve 10^{-12} with an RF voltage of 255 kV. We plan to optimize the voltage because the RF cavity and its cooling system can maintain a stable temperature during the experiment.

2.2.3 Proton Energy and Pion Production

In principle, higher energy protons and heavier atoms can help produce more pions when used as the pion production target; however, several points limit this approach. We need to suppress antiproton production because their cross-section increases with higher energy protons. The minimum kinetic energy of a proton beam required to produce antiprotons in $pp \to ppp\bar{p}$ is 6.56 GeV, and it is known that the cross-section steeply increases above that threshold. The COMET experiment adopts 8 GeV kinetic energy. The selection of the target material depends on mechanical stability, including thermal resistance with a realistic cooling system. The Phase-II experiment uses tungsten, whereas Phase-I adopts graphite that is lighter. This is because activation by the proton beam of the target and the support materials are minimized, and this makes it easier to transit to the Phase-II experiment.

The pion capture solenoid collects pions generated in the direction opposite to the proton beam using a magnetic field whose strength ranges from 5 T at the target to 3 T at the transport-solenoid entrance. This not only removes a large number of secondary particles that are boosted in the beam direction from the muon beamline but also helps obtain low-momentum pions that tend to decay to muons.

Figure 2.8 shows the different momentum spectra generated by the pions in the forward and backward directions. Most backward-appearing pions have low momenta for both graphite and tungsten targets. This eases the pions to decay to low-momentum muons that stop in the muon stopping target. Forward pions containing more high-momentum pions are less desirable because they are more likely not to lead to stopped muons.

The solenoid magnetic field in the capture solenoid decreases from 5 T at the target to 3 T at the transport-solenoid entrance. When a charged particle flies helically in a solenoid magnetic field, the transverse momentum p_T and the field strength B have the following relationship.

$$p_T \times R \propto \frac{p_T^2}{B} = \text{constant}, \tag{2.1}$$

where R denotes the radius of the trajectory. This adiabatic transition suppresses the lateral component with the gradient field and carries the particles forward.

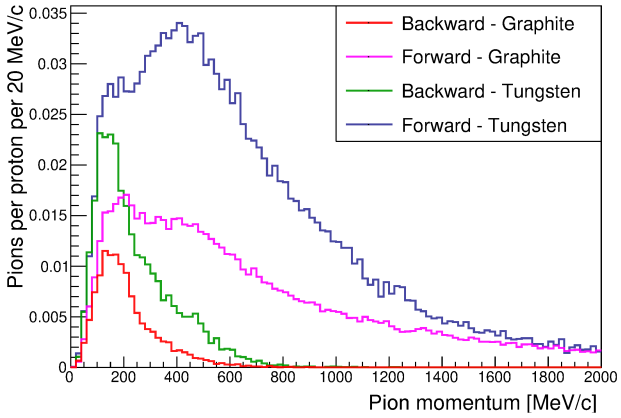

Figure 2.8: Pion production rate of graphite and tungsten targets in the forward and backward directions against the proton beam as a function of the pion momentum; image adopted from [4]. The data are generated by the `Geant4` simulation with the `QGSP-BERT` hadronization model [68]. Owing to the larger atomic number, tungsten wholly provides more pions. Backward-generated pions do not have high momentum compared to the forward-generated ones.

2.2.4 Spectroscopy Using Solenoid Magnetic Field

The muon transport solenoid and electron spectrometer utilize solenoid magnetic fields in their curved paths to transport the target particles and eliminate others effectively. The negative muons in the beam need to have a sufficiently low momentum to stop the target. In the muon transport solenoid, other particles such as positive particles or high-momentum muons need to be rejected as far as possible. Similarly, since most BG electrons (i.e., DIO electrons) that enter the electron spectrometer have momenta lower than that of the signal (i.e., $\sim$ 105 MeV), the magnetic field should be designed to pass high-momentum particles.

Figure 2.9 demonstrates how we realize it. In a curved solenoid magnetic field, the center of the

helix drifts perpendicularly to the plane on which the beamline lies. The drift distance is given as

$$\begin{aligned} D &= \frac{1}{qB}\frac{s}{R}\frac{p_L^2 + \frac{1}{2}p_T^2}{p_L} \\ &= \frac{1}{qB}\frac{s}{R}\frac{p}{2}\left(\cos\theta + \frac{1}{\cos\theta}\right), \end{aligned} \tag{2.2}$$

where q represents the electric charge including the sign, and B denotes the strength of the magnetic field along the beam axis. s and R denote the path length and curvature radius of the bent solenoid, respectively. Further, p_L and p_T represent the longitudinal and transverse momenta ($p^2 = p_L^2 + p_T^2$), respectively, and θ denotes the pitch angle. In addition, D is proportional to s/R, which denotes the total bending angle of the solenoid; the drift direction becomes opposite because of the different signs of the charges. These features cause the beam particles to separate according to their charge and momentum.

We use dipole magnets and collimators to transmit particles with a specific charge and range of momentum. The vertical magnetic field can compensate for the drift of the target momentum and keep its helical center unchanged. The collimator is useful to block other unwanted momenta. In the muon transport solenoid, several collimator disks are located at the exit. In the electron spectrometer, DIO electrons drift downwards, and therefore, the area underneath is filled with a heavy material, which we call the DIO blocker; currently, we plan to use tungsten.

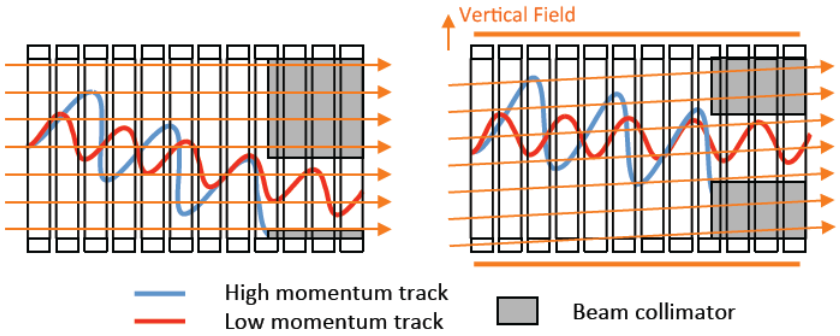

Figure 2.9: Spectroscopy using a curved solenoid magnetic field. The figures indicate cross-sectional views of the curved solenoid sliced along the curvature. Orange arrows indicate the direction of the magnetic field. The center of helical trajectories flying in the solenoid drifts according to (2.2). By installing the dipole magnets and collimators, only a certain range of momentum is allowed to pass through.

2.2.5 Muon Stopping Target Section

The muon stopping targets are thin disks—more accurately, films—made of aluminum, and they are located in the muon stopping target section between the two curved solenoids. The latest design calls for a series of 17 200-μm-thick disks set at intervals of 5 cm along the beamline to prevent outgoing electrons from losing energy. Muon stopping efficiency is a critical factor that determines experimental sensitivity. Therefore, their geometrical parameters (thickness, number of disks, and alignment) are still being optimized by collaborators to ensure higher efficiency. We prefer electrons

emitted laterally from the target to avoid a massive energy loss in the series of disks. These electrons are then boosted forward by the adiabatic transition (2.1). To this end, the magnetic field is kept constant at 3 T in the muon transport solenoid, and it declines to 1 T in this straight section.

The nucleus of the muon stopping target determines the number of signal electrons that can be captured by the timing window. Generically, the heavier the atoms of the material, the higher is the conversion rate. However, the muonic-atom decay constant shortens because of an increase in the muon capture rate. Therefore, we cannot use too high-Z atoms wherein most signal electrons hide in the prompt BG. For COMET, because the prompt BGs take about 200 nsec after proton injection to arrive at the detector region, signal electrons need to appear after it. Therefore, materials lighter than the element whose lifetime becomes longer than 200 nsec; i.e., iron ($Z = 26$), is used

Further, considering industrial aspects such as mechanical stability, purity, and cost, aluminum and titanium are candidates whose lifetimes are 864 and 330 nsec, respectively. COMET adopted aluminum because its lifetime is more appropriate for the bunch structure of the COMET beam[2]. However, titanium remains an attractive second objective after performing the experiment with aluminum.

Meanwhile, an X-ray detector is placed outside the solenoid to monitor the formation of muonic atoms. Characteristic X-rays are emitted when the bound muon drops to the $1s$ state. This enables us to count the number of muonic atoms formed in the aluminum disks and normalize the measured statistics for calculating sensitivity.

2.2.6 Detector Section

The electron spectrometer connects the detector solenoid at the end of the beamline, where the magnetic field has a continuous strength of 1 T until the end. The whole detector solenoid is surrounded by the CRV, which comprises layers of scintillating plastic bars readouts obtained using SiPM (silicon photon multiplier)[3]. When the CRV detects that a cosmic ray passes through the detector solenoid, we mask the measurement in the period where any BG arising from it may hit the detector. However, in accordance with the fact mentioned in Section 2.1.1, i.e., cosmic-ray BG is a major BG component, discussions are ongoing to expand the region covered by the CRV to the further upstream side.

Finally, in the detector solenoid, we will install the straw tube tracker (or simply, straw tracker) and the ECAL to measure the momentum and energy of the incoming particles, respectively. We call those combined detectors StrECAL collectively. Figure 2.10 shows the StrECAL built in the COMET-official simulation software, wherein the straw tracker is located in front of the ECAL. The straw tracker measures the two-dimensional positions at each plane through which the particles pass to reconstruct the momentum, which helps minimize the energy loss with its low materials. The ECAL absorbs the particle energies by stopping them with massive segmented crystals and generates the trigger signals for the readout electronics to start recording the induced signals.

StrECAL is required to satisfy the following concerns.

Pile-up separation: All COMET detectors suffer from pile-up hits. Most DIO electrons have ener-

[2] In fact, the bunch structure was determined based on material selection.

[3] See Section 4.2.2 for the general description of the SiPM.

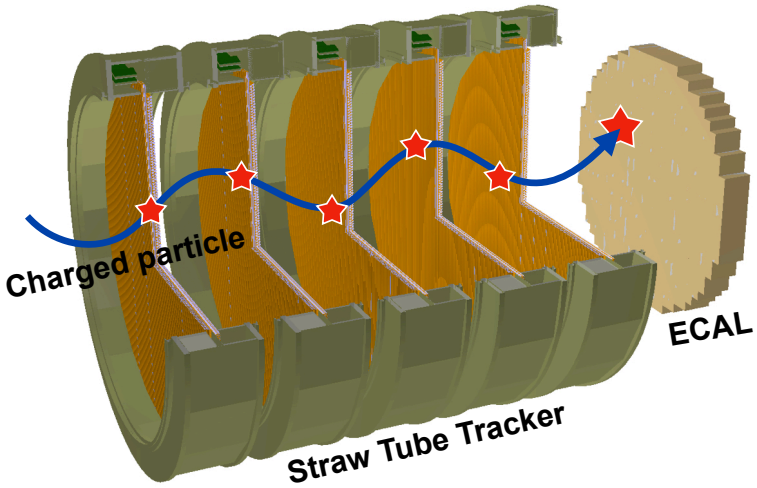

Figure 2.10: Schematic of the StrECAL in the COMET Phase-II experiment. The incoming charged particle hits the straw tube tracker at each plane where the hit position is measured to reconstruct the trajectory and its momentum. The ECAL measures the total energy deposited by the induced electromagnetic shower.

gies smaller than that of the signal electrons. However, when a couple of two independent DIO electrons are piled-up in nearby crystals in the ECAL, they appear as hits of a single signal electron. Therefore, StrECAL detectors need a response time[4] that is as short as possible. The short response time of the waveform helps us separate multiple signals that are little farther apart in time.

PID (particle identification): StrECAL is required to measure not only electrons of μ-e conversion exclusively in Phase-II but also a wide range of momentum for each particle type for investigating the beam before the Phase-I experiment discussed in Section 2.3. Since different types of particles can give different features to hits in the StrECAL detector, an analysis combining all these parameters would help identify the particle type.

Radiation tolerance: The high-intensity proton beam introduces a considerable number of secondary-charged particles and neutrons that cause severe damages to all electric devices. From a simulation study, they must withstand the radiation damage of 1 kGy and 10^{12} n_{1MeV}/cm^2 in total[5], considering a safety factor of 10.

2.3 Phase-I Experiment

Before Phase-II, we will perform the Phase-I experiment with a sensitivity of $O(10^{-15})$ by constructing half of the muon transport solenoid. The beam power will be 3.2 kW, and the pion production target will be graphite as explained in Section 2.2.3.

Figure 2.11 shows the schematic of the layout and the dedicated detector system. The detector solenoid is connected to the 90°-bent muon transport solenoid. Compared to Phase-II wherein the

[4] In this thesis, we defined the response time as the time length occupied by an electronic waveform.

[5] n_{1MeV}/cm^2 is the total neutron flux per 1 cm^2, where neutrons are weighted with their energy to normalize them to 1 MeV, based on the neutron-induced damage in silicon [69]

four-times-longer curved solenoid can suppress BGs efficiently, more beam particles flow into the detector solenoid. Then, it is difficult for StrECAL to work stably even in the timing window, and StrECAL may be damaged by the vast amount of prompt particles. Therefore, it is necessary to use a cylindrical detector (CyDet) system to avoid the beam that passes through the central region. The CyDet comprises CDC (cylindrical drift chamber) and CTH (cylindrical trigger hodoscope), and it holds the aluminum muon stopping target disks at the center.

A charged particle with a helix trajectory ionizes atoms of the gas in the CDC, and the wires read the induced electric signals to measure the path. As of 2020, we have completed the CDC construction and are performing a long-term cosmic-ray measurement to test it and develop its analysis schemes. The CTH has two layers of plastic scintillators and acrylic Cherenkov radiators. The scintillator provides the timing information, which is an important input to reconstruct the trajectory in the CDC and its momentum. Since Cherenkov radiators with a refractive index of ~ 1 emit Cherenkov photons only when very fast ($\beta \sim 1$) charged particles penetrate it, and therefore, the electrons can be identified. The CTH issues trigger signals and the ECAL in Phase-II. Inside the CTH, lead absorbers protect the CTH from particles that enter through the CDC region.

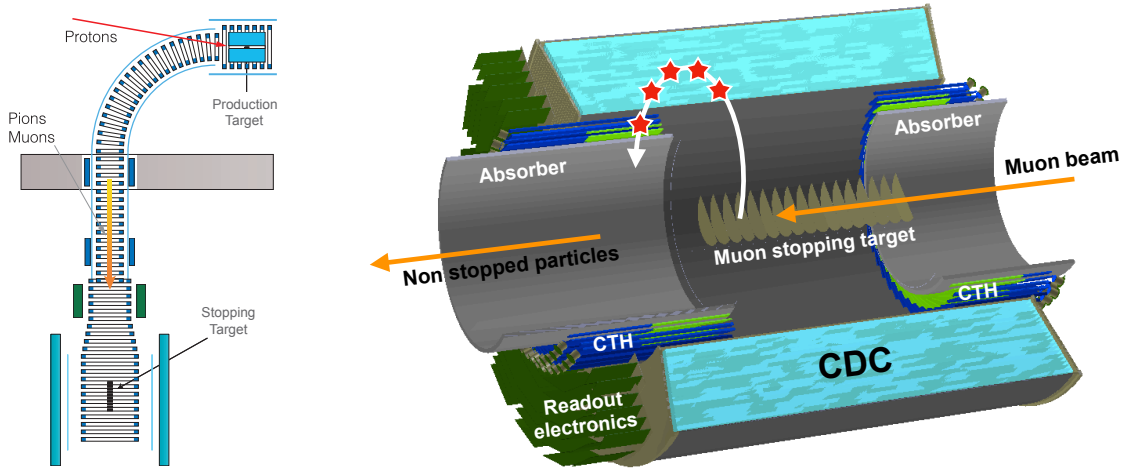

(a) Beamline **(b)** CyDet

Figure 2.11: Schematic of the COMET Phase-I experiment and CyDet detector system. (a) The muon transport solenoid is constructed until 90°. The muon stopping target disks are located at the center of the CyDet detector system, and they comprise CDC and CTH. (b) Muons originate from the right side and stop in the stopping target disks; however, most other beam particles go out. The emitted charged particle draws a spiral trajectory in CDC and hits CTH.

2.3.1 Beam Measurement Program

We will also perform a beam measurement program before the Phase-I experiment to measure the momentum and timing spectra for each particle in the beam with the real beamline to investigate all related BGs that may appear in Phase-I and -II in the future. Because the beamline is newly built for COMET, we have no experimental data yet. Not only relying on the simulation, we have to obtain experimental data to validate simulation studies achieved by the collaboration. Further, it

allows estimating systematic uncertainties reasonably. Unlike the μ-e conversion search to focus on electrons only, we must measure all particle types even if they come outside the timing window; thus, we plan to employ different approaches.

First, we will use StrECAL instead of CyDet because StrECAL has a better PID ability than CyDet for both the momentum and energy information. Therefore, the program is the first opportunity to demonstrate the StrECAL performance for Phase-II. Second, we will separate the measurement for the momentum and timing. The momentum reconstruction requires a detector hit occupancy that is sufficiently low to classify hits into each associated particle. When the pile-up considerably confuses the momentum and energy reconstruction of individual particles, it results in considerable uncertainty in terms of the momentum and PID.

Therefore, we reduce the beam power in the momentum measurement by a factor of 10^2–10^3 so that the hit rate becomes safe even outside of the timing window. In the timing measurement, we switch off the magnetic field in the detector solenoid that makes the particle trajectories straight. Instead of the straw tracker that will be switched off, we will use a hodoscope counter to measure not only the timing but also the TOF (time of flight) until ECAL and energy deposition ($\mathrm{d}E/\mathrm{d}x$); this will enhance the PID performance. The measurement of those two parameters is more tolerant of many pile-ups. Nevertheless, the hit rate immediately after the proton injection may still be considerably high, and hence, we will presumably install a beam blocker at the entrance to limit the flux further.

2.4 Back-End Systems

Individual detectors have their own readout electronics, which help digitize their electric pulses and transmit it to the back-end data disk. The trigger system is used to determine when to perform those actions and to propagate the decisions to all electronics; the trigger management electronics named FC7 work on this. The ECAL front-end trigger electronics monitor electric signals from the ECAL continuously [6]. When a significant energy deposition is recognized, they pass it to FC7. The FC7 collects and examines all information, and it evaluates whether to issue the trigger signal and distribute it to all readout electronics.

Further, FC7 communicates with the DAQ (data acquisition) system. Once a trigger signal is distributed, the DAQ system collects digitized data associated with it from all readout electronics, and it writes out the data disk with trigger information. The DAQ software is being developed based on MIDAS (Maximum Integrated Data Acquisition System) [70], which can manage any readout subsystem via its online web system. Further, MIDAS can manipulate slow control systems. They include the configuration of the electronics and the monitoring of the environments such as the internal state of the electronics and the temperature and vacuum pressure around StrECAL.

[6] Section 4.2 describes the procedure for the ECAL in more detail.

3

Straw Tube Tracker

The straw tube tracker or straw tracker is used to sample the trajectory of particles that enter the detector solenoid at several planes before reaching the ECAL. The momentum of the particles can be measured by attaching a trajectory to the hit points considering a realistic magnetic field. A high momentum resolution is necessary to separate the signal electron from many DIO electrons whose energy irreducibly contaminates the signal region. Thus, materials in the straw tracker need to be as light as possible, and therefore, the particles scatter significantly or lose their energy considerably, which fluctuates the quality of the track fitting and energy measurement using the ECAL.

The straw tracker comprises arrays of long drift chambers called "straw tubes" that are made of low-density materials. The KEK group is leading the design and development of the straw tracker, and the Kyushu group has made contributions through collaborations.

3.1 Requirements

The straw tracker should have a momentum resolution less than 200 keV/c for signal electrons with a momentum of $\sim$ 105 MeV/c to ensure target sensitivity. This requirement is split into the spatial resolution of the straw tube and the vacuum pressure in the detector solenoid. First, every straw tube can measure the distance from its center to the trajectory that penetrates it. Because fluctuations in the measurement can distort the track-fitting result, measurement precision affects momentum resolution. Second, the air is massive and it causes multiple scattering of particles with momentums up to a few hundred MeV/c. The effect of the material needs to be smaller than that of the straw tubes. Figure 3.1 illustrates the dependence of momentum resolution on both parameters estimated by the simulation. Thus, we need the spatial resolution to be less than 200 μm and the vacuum pressure to be less than 100 Pa.

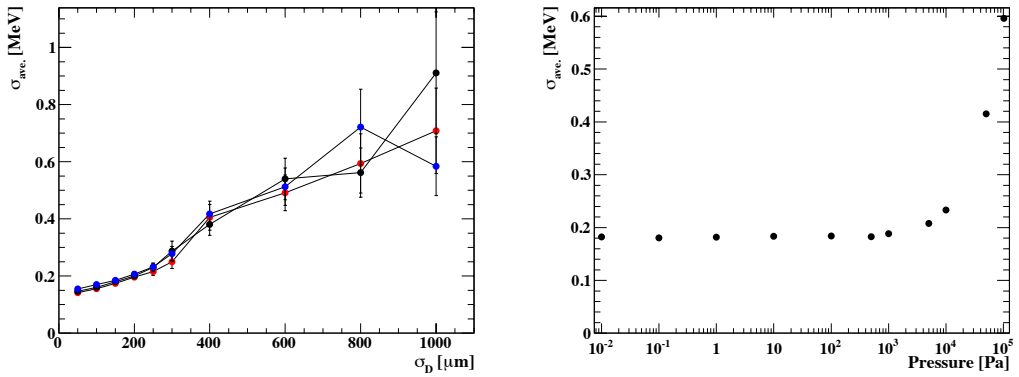

Figure 3.1: Momentum resolution of the straw tube tracker as functions of (left) the spatial resolution of the straw tube and (right) vacuum pressure in the detector solenoid, as estimated by the `Geant4` simulation. The spatial resolution and vacuum pressure must be less than 200 μm and 100 Pa, respectively, to achieve a momentum resolution less than 200 keV/c.

3.2 Design

Figure 3.2 shows the straw tube tracker schematically in the side and sectional views. In the side view, the beam particles from the left side. The largest component is the "straw station," which is repeatedly installed along the beamline. Every straw station comprises two ring-shaped aluminum supporters and each of them contain two layers of straw tubes, gas manifolds, and electronics. A particle is presumed to pass through one of the aligned straw tubes per layer, and hence, the layer can determine the hit position along the alignment direction. Further, one can infer the direction of the penetrating particle from the two-layer hits. Both supporters are coupled in a straw station to face the horizontal and vertical directions to measure the two-dimensional hit position and orientation, respectively. The gas mixture is supplied from the outside of the detector solenoid in 1 atm via the gas manifold, and it is taken out again. Similarly, the lines are distributed to carry the electrical signals that control the electronics and the HV (high voltage) that drives the straw tubes.

The sectional schematic depicts the interior of the support ring. It is divided into two gas manifolds that stream the gas continuously via the straw tubes. The HV is applied to generate a high potential in the straw tube. The front-end electronics are connected to the straw tubes to digitize the induced charge.

3.2.1 Straw Tube

Figure 3.3 illustrates how the straw tube detects particle hits. When a charged particle penetrates the straw tube, it ionizes the filled gas, and electron–ion pairs are generated along this path. The HV applied between the sense wire (anode) and inner surface (cathode) of the straw tube results in a high electric field gradient, which drifts electrons towards the wire and ions towards the other. The gradient becomes steeper near the wire and further accelerates the drift velocity. Electrons start to displace other electrons, which in turn displace more electrons; this amplification procedure is called

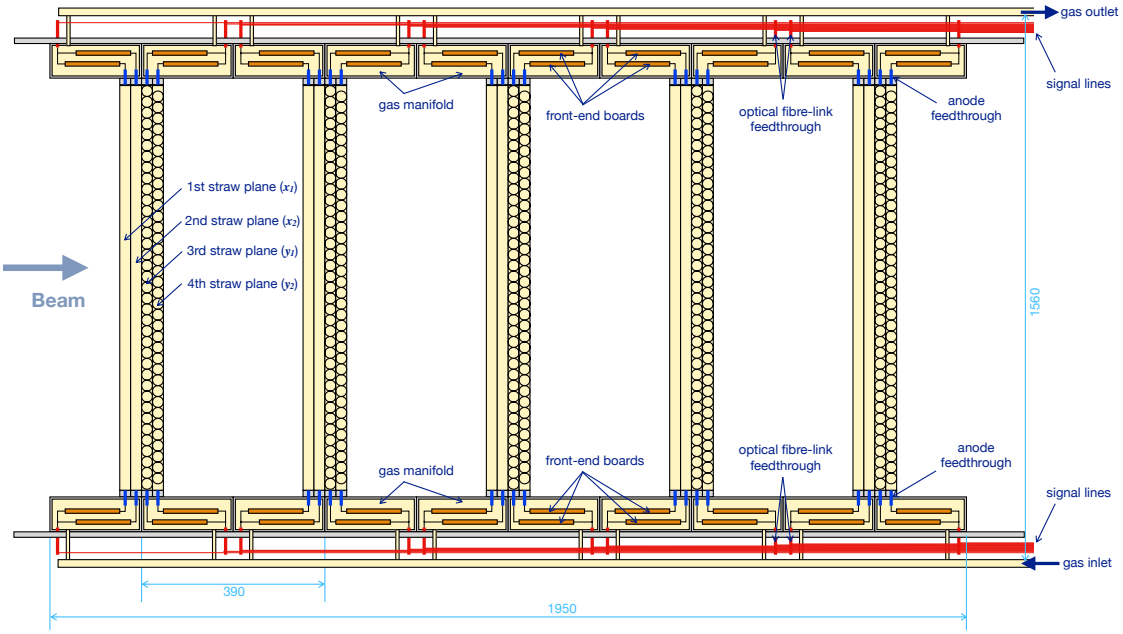

(a) Side view

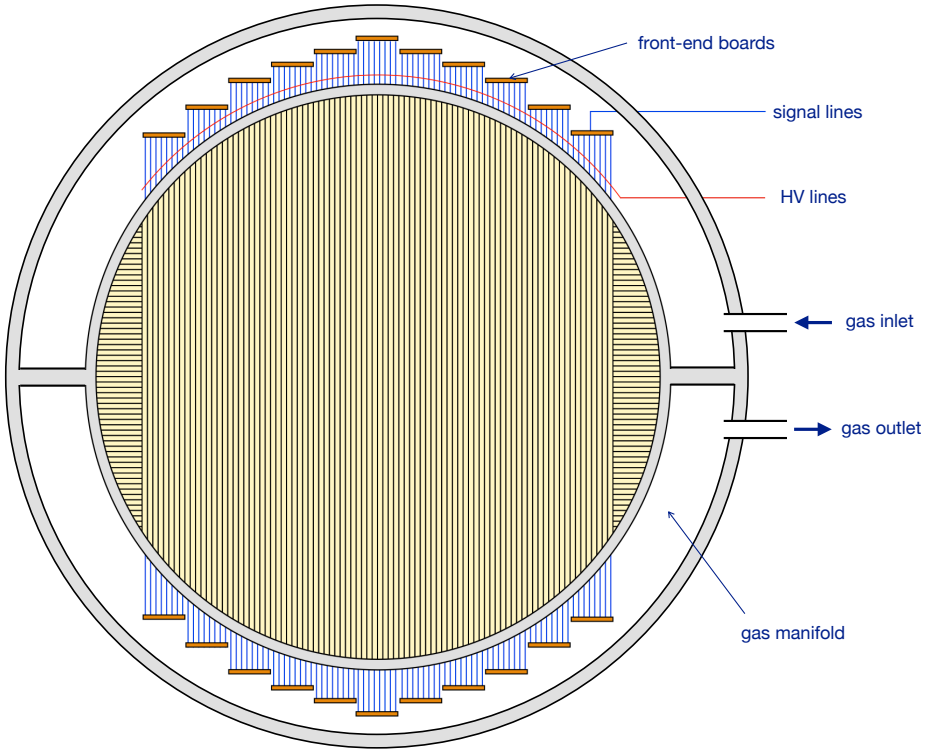

(b) Sectional view

Figure 3.2: Schematic of the straw tube tracker in the (a) side and (b) sectional views. (a) The straw tube dimension is magnified three times for clarity. The beam particles penetrate a series of straw stations, and each of them comprise two support rings that are directed horizontally and vertically to detect the hit points on the plane. Each support ring contains the straw tubes aligned in two layers, gas manifolds, and electronics. The gas manifolds and signal lines are supplied from the outside of the detector solenoid via feedthroughs. (b) The support ring is internally separated into the input and output gas manifolds. The HV line and front-end electronics are connected to the straw tubes.

an avalanche process[1]. Then, the cluster of generated electrons forms an electric pulse, which is read by the front-end electronics.

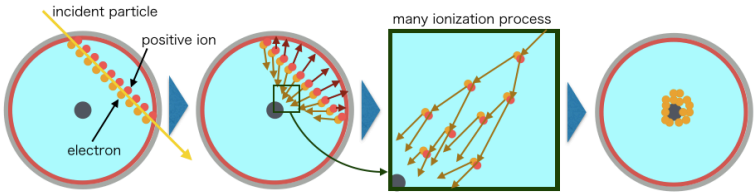

Figure 3.3: Mechanism of signal generation in the straw tube. A charged particle ionizes the gas in the straw tube and creates electron–positive ion pairs. The electrons drift because of the electric field between the wire and the surface, thereby causing avalanche amplification near the wire because of the steep gradient, which finally induces a charge current on the wire.

Straw tubes have lengths varying between 692 and 1300 mm as the installation position becomes closer to the center of the straw station. The diameter of the tubes is 9.75 mm in Phase-I (beam measurement program) while it will be 5 mm in Phase-II to minimize the hit occupancy per straw tube as the beam intensity increases. The production technology was developed by the JINR (Joint Institute for Nuclear Research) and CERN group for the NA62 experiment at CERN [71]; however, they have been developing it further to make it even lighter for the COMET experiment [72]. There are two approaches to use the tube part as the cathode plane: "doubly wound" and "straight adhesion," as shown in Figure 3.4. In the former, a double layer of metalized polyimide film is glued into a spiral shape. In the latter, the film is rolled and attached at both ends. The JINR group successfully fabricated a tube by ultrasonic welding; this tube can operate in a vacuum of a single-layer aluminized PET (polyethylene terephthalate) film. Thus, the wall thickness became thinner than that in the doubly wound approach, which was 20 μm in the Phase-I experiment. However, the R&D is still ongoing, and a thickness of 12 μm is expected for the Phase-II experiment. Owing to this thin wall straw tube, the material effect induced on a particle when flying in the straw tracker is considerably less than $0.01X_0$, where X_0 represents the radiation length.

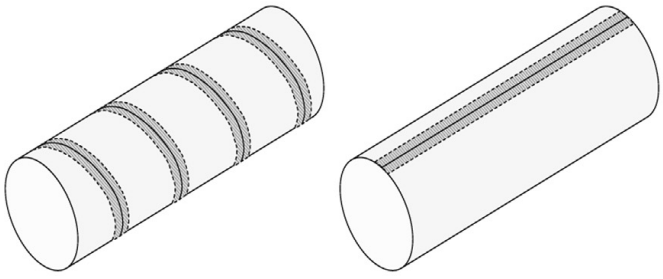

Figure 3.4: Two adhesion approaches to construct the tube. The doubly wound approach (left) requires the welding seam more than the straight adhesion approach (right) adopted for the COMET experiment.

The tube is installed under tension with a metallic end plug to prevent it from deforming in vacuum. Figure 3.5 shows the effect of tensioning on the sag and elongation of a 1 m straw tube, where

[1]The amplification process is discussed in more detail in Section 4.2.2.

the sag is defined as the deformation caused by gravity. After subtracting the measurement offsets of 1.5 mm and 2.0 mm, the sag can be sufficiently minimized with a tension of 1 kg_F. Consequently, the elongation becomes about 2 mm, and therefore, we concluded to stretch the straw tubes by 2 mm in the installation to avoid deformation.

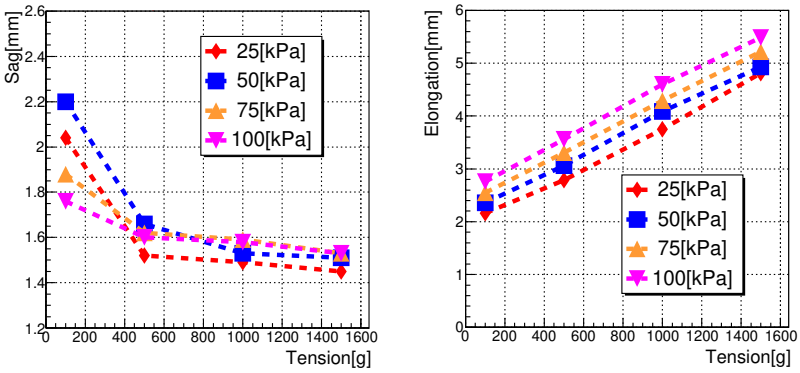

Figure 3.5: Sag (left) and elongation (right) of the straw tube as a function of the installing tension of a 1 m straw tube. The colors indicate the gas pressure in the straw tube. The sag and elongation values have measurement offsets of 1.5 mm and 2.0 mm, respectively. A tension of 1 kg_F can minimize the sag sufficiently, and the straw tube stretches by about 2 mm.

The anode wire is fabricated using gold-coated tungsten containing 3% rhenium; it has a radius of 12.5 μm. The stability can be estimated using

$$L_c = \frac{\pi R}{CV}\sqrt{2\pi\epsilon_0 T}, \tag{3.1}$$

where T, V, C, L_c, R, and ϵ_0 denote the wire tension, applied HV, capacitance per unit length, critical length for a given tension, straw-tube radius, and electric constant, respectively [73]. Assuming $C = 10.5$ pF/m, $V = 2.2$ kV, and $L_c = 2$ m, the tension should be $T \sim 70$ g.

3.2.2 Gas Mixture

The default gas supplied to the straw tubes is a 50:50 mixture of argon and ethane (C_2H_6). The drift velocity of the electrons in this gas mixture is roughly 5 cm/μsec and it does not vary considerably, which results in a linear relationship between the drift distance and time[2]. The Lorentz angle and diffusion coefficient[3] are also relatively small in a magnetic field of 1 T. These characteristics can help realize the required spatial resolution with a reasonable time resolution. Further, we have a 70:30 mixture of argon and carbon dioxide (CO_2) as a gas candidate. Although it has a lower multiplication gain compared to that of C_2H_6, it is easier to handle because of its incombustibility. We compared these two gas mixtures experimentally to select the gas.

[2]This relationship is discussed in detail in Section 5.3.3.2.

[3]The Lorentz angle is defined as the angle between the directions of the drifting electrons and electric field; it is caused by a finite magnetic field and the Lorentz force. The diffusion coefficient indicates how the drifted electrons are diffused via collision with the gas atoms. Both distort the relationship between the drift distance and time, which result in a worse spatial resolution.

3.2.3 Straw Tube Assembly

The end-plugs made of aluminum shown in Figure 3.6 are used to attach the straw tube to the support ring and ensure that the gas moves effectively. First, the female end-plug is attached to the inner wall at the straw-tube end with a conductive glue. Second, the male end-plug is hooked to the hole in the gas manifold. Third, combining both plugs with the screw, (the male one is already fixed to the support) the female one and the attached straw tube are be pulled until the elongation reaches 2 mm, which corresponds to 1 kg_F. Both plugs are kept hollow to transmit the gas, and they each contain a feedthrough pin.

We thread a dummy wire through the straw tube and the end plugs in advance. After securing the tension of the straw tube, we replace it with the anode wire by tying it to one end. The feedthrough pins are finally inserted at both ends, wherein the anode wire is soldered while maintaining a tension of 70 g. In the last picture, the installation is demonstrated with a prototype system for a single straw tube of the Phase-I type (20 μm thickness and 9.75 mm diameter).

We measured the gas leakage from the straw tube, too. The leak rate estimated from the single-straw prototype was 0.0035 $cm^3/min/m$, and this implies that the entire straw-tracker system can continue operation, which helps maintain the vacuum pressure. In addition, we evaluated it with a full-scale prototype (introduced in Section 5.1.2) that suggested the leakage is even less than the expectation from the result of the single-straw prototype.

(a) Female end-plug **(b)** Male end-plug **(c)** Combined end-plugs **(d)** Pulling the straw tube

Figure 3.6: End plugs to attach the straw tube to the gas manifold while maintaining proper tension. (a) The inner wall of the straw tube is glued to the left side (round part). (b) The middle part with the largest diameter is hooked to the stay in the gas manifold. (c) Both end plugs are hollow to allow transmission of the gas from and to the gas manifolds. (d) The straw tube can be pulled by screwing the male end plug whose one end is fixed at the support (demonstrated with a prototype support structure in this picture).

3.3 Front-End Electronics

Front-end electronics are installed in the gas manifold as close as possible to the sensing wires to read the signal pulses with minimal electrical noise. They need to digitize the waveform shape so that a waveform analysis technique can be used to distinguish the piled-up pulses after the experiment. In addition, the digitizing sampling speed of the front-end electronics should be sufficiently high to ensure a time resolution of less than 1 nsec for the goal spatial resolution. Because these two conditions

incur considerable cost when commercial products are used, the KEK electronics group and OpenIt (Open Source Consortium of Instrumentation) have been developing a dedicated electronics board called ROESTI (read-out electronics for straw tracker instrument) [74]. As of 2020, the development is almost finalized, and the latest version (ver.4) has been produced; however, the previous prototype (ver.3) was used in this study.

The radiation hardness of all electronic parts used in ROESTI has been investigated with neutron and gamma-ray sources. Most parts have been confirmed to be tolerant of the criterion radiation damage, and the examination for the remaining parts is ongoing. We measured the performance of ROESTI by feeding it test pulses; we obtained an overall gain of ~ 1 V/pC and an S/N (signal-to-noise) ratio of > 5 at the minimum input charge.

ROESTI possesses all functions of signal amplification and shaping, discrimination, digitization, and data transmission, which can be controlled by the back-end DAQ system. Figure 3.7 shows how ROESTI processes signals with several specific parts and a picture of the prototype ver.3. First, signal lines are combined per 16 straw tubes into a flat cable that is mounted on the input connector; the signal pulses enter ASD (Amplifier-Shaper-Discriminator) chips[4] every eight channels. The ASD amplifies the input charges—the strength of which is too low to read—and outputs them in a more readable waveform shape. It can also distinguish pulses with a significant magnitude using a simple threshold; the nondiscriminated channels are not processed anymore to reduce the data transmission.

The DRS4 (domino-ring sampler ver.4) chip[5] has a series of 1024 capacitors per channel. Each capacitor can preserve the voltage of the input waveform at each moment with a fast sampling rate of several gigahertz. Since capacitors are connected in a ring, the voltage values are overwritten at each cycle. ROESTI uses a 1 GHz sampling rate, and hence, each capacitor maintains its voltage for 1024 nsec. However, when a trigger signal is introduced, the previously held 1024 voltages are sequentially passed to the later ADC (analog-to-digital converter) chip and digitized. The advantage of DRS4 is that its transmission speed to the ADC can be slowed to match ADC specifications. Therefore, we can realize a multichannel waveform sampler with a high sampling rate by combining an inexpensive ADC with the DRS4[6].

Other than the two ADC chips that each deal with eight channels, another small ADC chip is used. A DRS4 chip can sample the input trigger-signal waveform in addition to the eight channels, and the small ADC chip is used to digitize it for the timing synchronization among different DRS4 chips. Every DRS4 chip has a large timing jitter to start sampling. Further, it is coherent only for all waveforms sampled by the same chip simultaneously. When the time difference between two waveforms across different chips is compared, the time resolution becomes tremendously worse. The same trigger signal is distributed to all chips without any significant time fluctuation, and hence, we exploit its characteristic timing such as at the rising edge of its pulse, as indicated by the standard timing. By subtracting it from the waveform timing, the jitter effect can be almost eliminated.

[4]This ASD chip was originally developed for the ATLAS experiment at CERN, and it was modified for the CDC of the Belle II experiment [75], which is also used in ROESTI.

[5]The DRS4 chip and the DRS series have been developed by the MEG experiment.

[6]There are some commercial products called flash ADC that can perform high-speed sampling; however, it incurs a considerable costs to accommodate many channels.

The FPGA (field programmable gate array)[7] is used to control all chips and the functions of ROESTI. The firmware is downloaded with the JTAG connection. When a trigger signal is introduced, the chip distributes it to the DRS4 chips to stop their sampling and start transmitting the sampled voltages to the ADCs. After collecting their digitized values, the chip adds some header information such as trigger information provided by trigger electronics and board-specific identification tags. The SiTCP technology [76] is implemented in the firmware. This enables an FPGA chip to emulate TCP/IP (transmission control protocol/internet protocol) data processing and 1 Gbps transmission at the hardware level, and it can be configured interactively with the UDP (user datagram protocol) protocol. Data are packed into TCP/IP packets and sent to the DAQ system via the SFP (small form-factor pluggable) transceiver, which supports optical communication by converting electric signals into optical signals and vice versa.

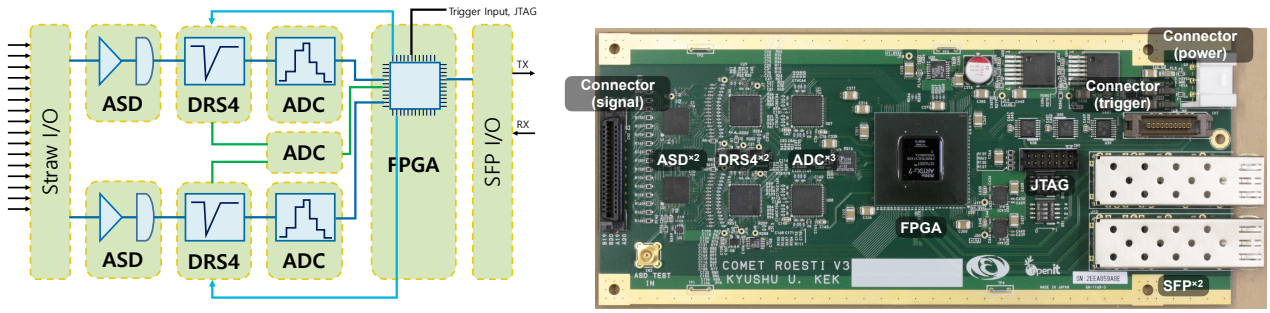

(a) Diagram **(b)** Prototype ver.3

Figure 3.7: Front-end electronics for straw tracker, ROESTI: (a) Diagram of signal-processing flow and (b) Picture of prototype ver.3. The ASD chips perform input signal current amplification, pulse shaping, and discrimination. The DRS4 chips sample the waveform and transmit it slowly to the ADC chips to digitize them. The trigger waveform to the DRS4 is digitized by the central ADC chip for timing synchronization. The FPGA chip controls all chips, and it transmits data to the back-end DAQ system via the SFP connectors.

We developed the firmware so that it supports a daisy-chain connection [77] among multiple ROESTI boards, which is schematically explained in Figure 3.8. In the TCP/IP standard, it is assumed that every terminal device, i.e., a ROESTI board, is linked with a single cable to another device. Since multiple boards are installed in the gas manifold, there is an optical fiber cable per board that connects the board and the network switch hub outside of the vacuum; further, there are other cables for the HV, triggering, and slow controls. However, they are too many cables for the available feedthrough to handle, and therefore, we need to reduce the number. It is realized using a daisy chain wherein every board is related to the next board with a cable serially, and this is the reason why a ROESTI board has two SFP transceivers. When the DAQ system calls a particular board, the FPGA in every board checks the data packet; if the board is not the destination, the data packet is transferred to the next board. Thus, a one-to-one communication of the TCP/IP protocol is secured.

[7] An FPGA chip contains an array of logic gates, and their connection and functionality can be programmed by developers as required. ROESTI has adopted the Xilinx's Artix-7 series product.

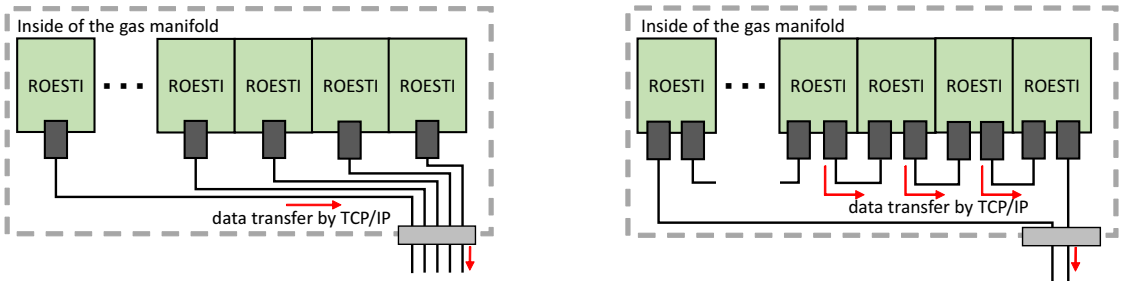

(a) Without the daisy-chain

(b) With the daisy-chain

Figure 3.8: Daisy chain connection of the ROESTI boards in the gas manifold. With (a) the conventional connection, there are too many optical cables extracted via the feedthrough. (b) The daisy chain links multiple boards serially but continues to support one-to-one communication.

3.3.1 Time Resolution

ROESTI has a good time resolution that can meet the requirement for the straw tracker; however, it has a characteristic variation. We measured the time resolution of prototype ver.3 by inputting the same pulses into two different DRS4 channels and evaluating the fluctuation in their time difference. We also delayed the arrival time of one input and checked the dependence on the delay time. Figure 3.9 shows the result as a function of the delay time between the input pulses. When the examined channels belong to different DRS4 chips, the time resolution is roughly 0.4 nsec, which is sufficiently smaller than the requirement of 1 nsec; however, it arises from the fluctuation in the synchronization when using the trigger signals.

It is no longer in the same chip, and the resolution can be greater than 0.1 nsec. However, the resolution deteriorates as the delay expands. We found that this feature was caused by a defect in the ROESTI design. This has been modified in ROESTI ver.4; the time resolution is approximately 0.2 nsec even for a long delay.

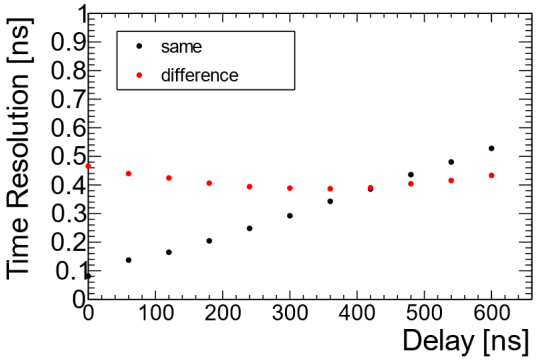

Figure 3.9: Time resolution of the ROESTI prototype ver.3. The same test pulse is divided into two channels of DRS4, and the resolution is evaluated from the fluctuation in the measured time difference between them. The arrival time of one channel is varied as indicated by the horizontal axis. When the examined channels belong to different DRS4 chips, the resolution is roughly 0.4 nsec. However, it has a characteristic dependence in the case of the same chip.

3.4 Slow Control

To operate the straw tracker in a stable manner, the slow control system needs to handle the gas gain monitor, HV, LV (low voltage) distribution, and most importantly, gas flow and vacuum pumping in the detector solenoid. The HV system should have the ability to be controlled remotely and to monitor the current precisely. When the HV is applied to the straw tubes, it is slowly ramped up as a large current does not flow through the wire. Since the current fluctuates finely, a quick and precise measurement performance is required. Further, the system needs a safety interlock function to stop the HV supply in the case of any accidental scenarios and to protect the sensing wires from damage. The straw tube performance can vary during the experiment because of a change in the environmental temperature and humidity or the aging of the wires. The gain monitor system will need to use some controllable light source such as a laser or ultra-violet lamps, which can generate a constant number of seed electrons in every straw tube. The gas gain can be monitored by measuring the response to it. The development of the two abovementioned systems, including the use of commercial products, is underway.

The LV distributor controls and monitors the individual power supply voltages of the electronics. Each electronics board requires several different voltages. If an electronics board is broken, its current value becomes strange, and therefore, the distributor should be able to monitor each current value separately and switch off only the broken channels. Owing to the large number of electronics that we will handle, it would be very expensive to use commercial products. Furthermore, for the same reason that the daisy chain is used for the ROESTI connection, the power cable passing through the feedthrough also needs to be reduced. Figure 3.10 shows the prototype distributor developed in this study. This distributor can arbitrarily generate an output voltage per channel from a single input voltage higher than all outputs, it can be manipulated remotely, and it can monitor its current. Further, it withstood prolonged use in the experiment, as discussed in Chapter 5. However, some electric parts on the board have problems in terms of their radiation tolerance; the selection of these parts is ongoing.

3.5 Gas, Cooling, and Vacuum Systems

The gas system mixes two gases and supplies the blended gas to the gas manifolds, which circulates it in the system. Further, the gas is required to cool the ROESTI boards, which overheat quickly and break. The vacuum system keeps the detector solenoid in vacuum, and monitors it to drive the vacuum pump safely. Figure 3.11 illustrates the system design.

The mass-flow controllers control the flow of both gases from the cylinders to mix them in the blender in the desired ratio. The blended gas flows in the gas manifolds of the straw tracker. The gauges at the entrance and exit monitor the pressure; the relief valve releases the gas for safety if its pressure exceeds a certain threshold.

The green gas line in the figure indicates the cooling system through which the gas emitted from the manifolds is circulated. A heat sink is attached to every board and the compressor enhances the gas flow rate to 50 l/min to exhaust the heat out of the ROESTI boards efficiently. In addition, the

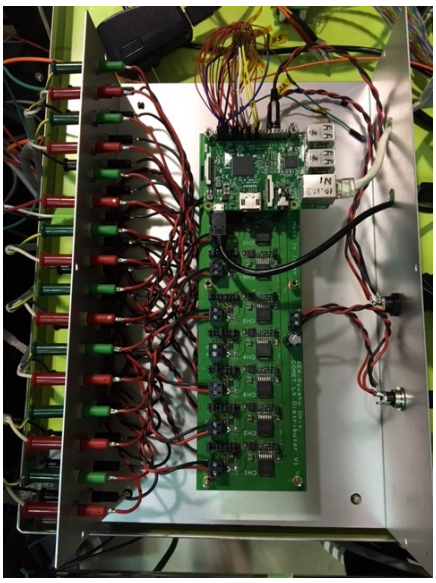

Figure 3.10: Prototype LV divider. The input voltage supplied from the bottom right plug is regulated for each output channel on the left panel, whose voltage and current are monitored.

heat exchanger and tiller are used to make the gas even colder. The first pilot system was built to examine the design that uses a diaphragm pump and refrigerator instead of the compressor and the tiller, and the required flow rate was achieved.

The air in the detector solenoid was exhausted by a rotary pump and turbomolecular pump through the purple line in the figure. However, if the vacuum is broken, such as when a straw tube breaks, the pressure rises rapidly and can destroy the turbomolecular pump. Therefore, the vacuum pressure needs to be monitored constantly so that gate valve can be closed instantly and the vacuum system can be disconnected in such a situation.

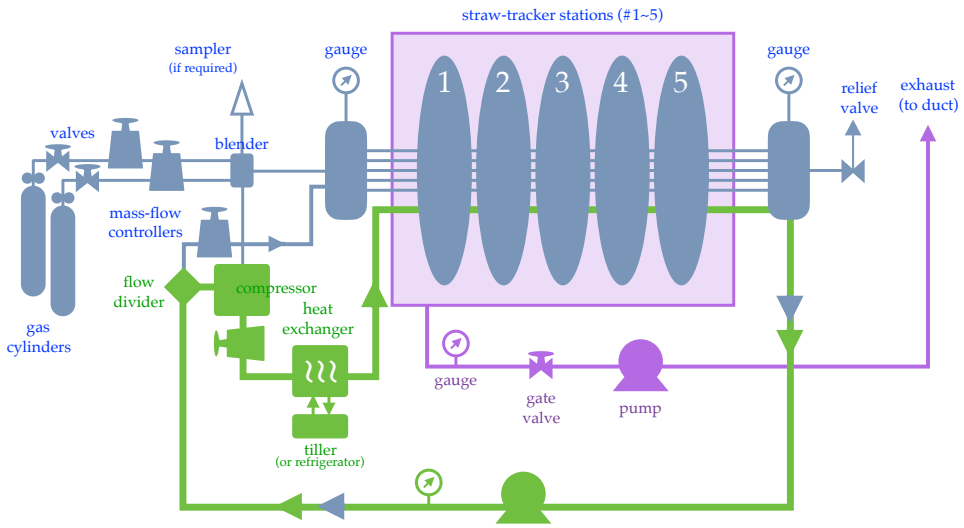

Figure 3.11: Diagram of the gas, cooling, and vacuum systems for the straw tracker. The two gases are blended and flown into the gas manifolds. The cooling system (green line) compresses and cools down the gas to exhaust the heat out of the ROESTI boards. The air is expelled through the vacuum system (purple line), and it is decoupled from the detector solenoid by the gate valve when the vacuum breaks.

We constructed a prototype of the gas and vacuum systems as shown in Figure 3.12 for the experiment to evaluate a prototype of StrECAL, as discussed in Chapter 5. The mass-flow controllers mounted on the right panel control the flow rate of argon, C_2H_6, and CO_2. Either C_2H_6 or CO_2 is shut out by the valve, and the other is mixed with argon via the blender behind the panel. The gas mixture enters the gas manifold through the controllable valve. In this prototype, the return gas is not circulated but released into the air through the bubbler and the pressure gauge. Both mass-flow meters and the bubbler are used to confirm the gas flow visually. The vacuum pressure gauge monitors the pressure in the container of the straw tracker prototype. The digitizer and controller devices communicate with the mass-flow controllers and vacuum pressure gauge, configure the flow rate, read the actual flow rates and vacuum pressure, and send the data to the DAQ computer. Further, they can open and close gas-line valves and close the gate valve (not shown in the picture). We can control and monitor the environmental status with these systems.

Figure 3.12: Prototype of gas and vacuum systems. The right panel contains all items used for controlling, mixing, and monitoring the gas flows. The digitizer and controller devices digitize the values monitored by the mass-flow controllers and vacuum pressure gauge, send them to the DAQ computer, and control the valves to open and close the gas-flow line.

4

Electromagnetic Calorimeter (ECAL)

An ECAL is installed at the end of the beamline, and it measures the total energy deposition, position, and timing of the incoming particles. The role of the ECAL is divided into the following considering the beam measurement program before the Phase-I experiment.

Trigger: The ECAL is the only trigger detector used in Phase-II. Its trigger electronics monitor the energy depositions in real time, generate trigger candidates, and transmit them to a trigger system that makes the trigger decision.

Determination of time origins Some COMET detectors require the time origin (T_0) of events. For example, any tracking algorithm needs to first reconstruct a drift time or distance in each straw tube. Thus, the exact timing required for the track to pass through the straw tubes—calculated from T_0 considering the track path—is required.

Support of Tracking by the Straw Tracker The ECAL can measure the two-dimensional position on its surface where particles arrive. Further, this role can tend to track fitting. Alternatively, it is a good criterion for track reconstruction to verify its consistency with the track reconstructed from the straw tracker hits.

To accomplish these, the ECAL must exhibit high energy, position, and time resolutions; a detailed investigation into its response against each particle type is also required. Since 2012, the Kyushu University group has been developing an ECAL by constructing prototypes and conducting experiments to evaluate their performance. Considering all roles of the ECAL, we designed it to comprise segmented inorganic scintillating crystals.

This chapter describes the detail of the requirements for the ECAL and the design created to meet these requirements; further, it includes several experimental results that support the philosophy of the design.

4.1 Requirements

The ECAL needs to have an energy resolution of 5%, time resolution of 1 nsec, and position resolution of 10 mm at the μ-e conversion signal energy of 105 MeV. However, we set these values as minimum requirements and aim to realize resolutions as high as possible.

The energy resolution is critical for both triggering and analysis. Since the energy of the DIO electrons can reach the signal region, a high energy threshold with a precise resolution is required to suppress the trigger rate caused by the DIO electrons as strongly as possible.

The time origin obtained by the ECAL is an important parameter for the straw tracker, as described above. Its accuracy affects the performance of the tracking and momentum resolution. The effect on the experimental sensitivity is more direct than that of the energy resolution.

The hit-position information assists momentum reconstruction performed by the straw tracker. The tracking performance partially depends on the precision. The straw tracker has a fear of ghost hits [1]. The ECAL does not have this problem and can thus help correct it.

4.2 Design

Figure 4.1 schematically illustrates the upstream part from the scintillating crystal to the front-end electronics. The crystal module is a minimal module that comprises the LYSO (lutetium-yttrium oxyorthosilicate) crystal wrapped by optical reflector materials—PTFE (polytetrafluoroethylene) and ESR (enhanced specular reflector)—with the APD (avalanche photodiode) photodetector. An APD is mounted on a small PCB (printed circuit board), and it is called an APD holder board that holds a temperature sensor and an LED (light emitting diode) chip to calibrate and monitor the APD gain. A set of 2×2 crystal modules form the upper module, which is called the block module, and it is combined using an an aluminized mylar bag. Further, another PCB (intermediate board) groups 2×2 block modules (4×4 crystal modules), and it distributes slow control signals from the back-end system for each crystal module. Because block modules are in the vacuum of the detector solenoid, the feedthroughs made with PCB at the endcap of the solenoid mediate the electric signals to the outside. The slow control signals also go outside via the feedthrough. The preamplifier boards mounted on the feedthrough amplify the APD signals. All slow-control signals travel into the vacuum through the slow-control transmission boards mounted on the feedthrough.

Figure 4.2 shows the remaining downstream part and illustrates how the signals are processed. The preamplifiers send the amplified signals to the readout electronics named EROS (ECAL read-out system). The DAQ machines record all waveforms digitized by EROS.

Meanwhile, the preamplifier follows another route for triggering, which his different from that for EROS. Hereafter, we use the terms “trigger line” and “signal line” to indicate the former and the latter, respectively. Because the trigger electronics incur a cost to observe all channels of the signal line, the preamplifier sums up the four waveforms from each block module, and they send it through the trigger line. The trigger electronics make trigger decisions by processing the summed signals.

[1] When two particles hit both horizontal and vertical straw tubes simultaneously, up to four candidates are considered for their two hit positions; this ambiguity is called a ghost hit.

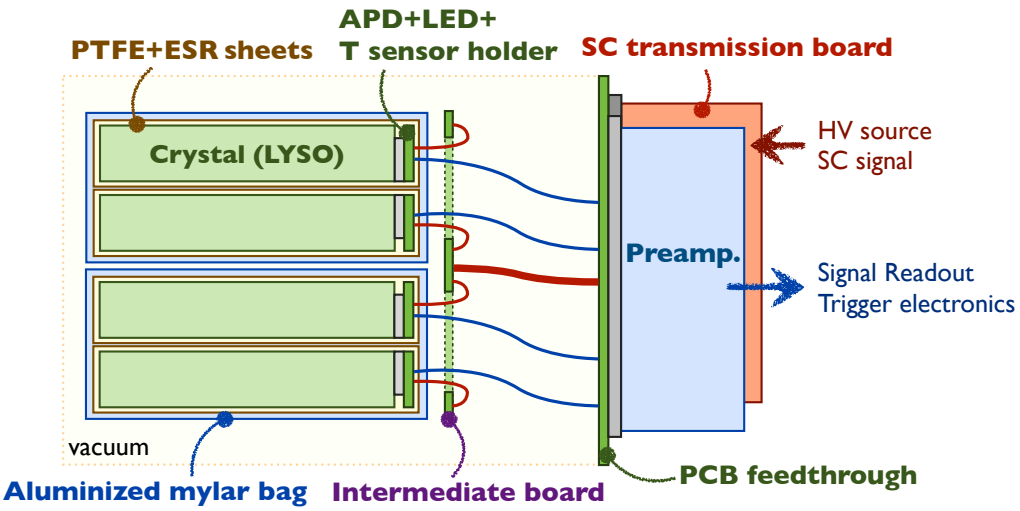

Figure 4.1: Schematics of the front-end modules of the ECAL

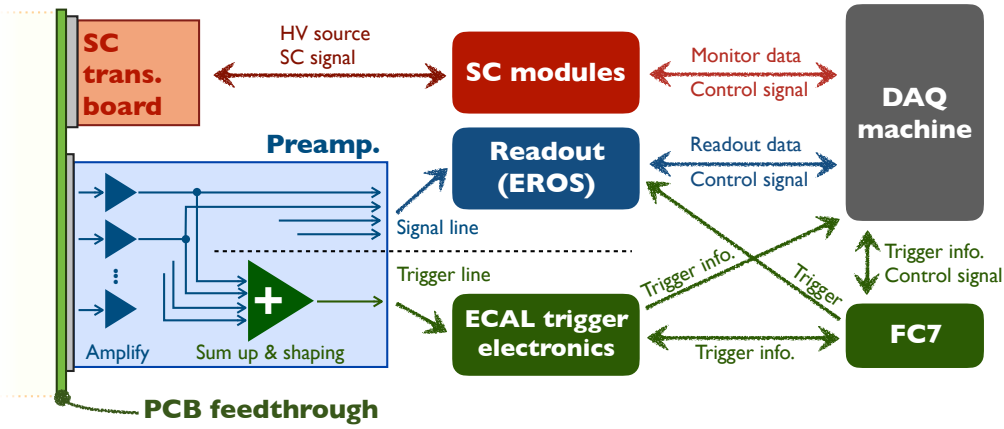

Figure 4.2: Schematics of the back-end modules of the ECAL

4.2.1 Scintillating Crystal

The selection of the scintillating crystal determines the intrinsic performance. To meet the requirements for the energy and position resolutions, inorganic crystals are presumably the only candidates. They are relatively dense and heavy, which limits the size of the electromagnetic shower growing in the ECAL and reduces the pile-up. It is characterized by the Molière radius, which is defined as the transverse radius containing 90% of the total energy of the shower. However, inorganic scintillators generically have the worse time resolution compared to the organic crystals caused by their relatively long decay constants; this also troubles the pile-up separation[2]. Considering these two conflicting conditions, we initially found two candidates: cerium[3]-doped GSO (Gadolinium oxyorthosilicate), Gd_2SiO_5, and LYSO, $Lu_{2(1-x)}Y_{2x}SiO_5$, produced by Hitachi Chemical Co., Ltd., Japan, and Saint-Gobain Co., Ltd., France, respectively. Modern crystal manufacturing techniques have successfully

[2]The scintillation time structure is often expressed by $e^{-t/\tau}$, where τ denotes the decay constant. We need τ to be considerably shorter than 1 μsec to accommodate the entire waveform into the sampling length of EROS.

[3]Cerium doping shortens the decay constant but decreases the light yield.

increased their sizes. The GSO and LYSO crystals have dimensions of 2×2×15 cm^3 and 2×2×12 cm^3, respectively. Table 4.1 lists their properties together with several other inorganic scintillating crystals that have relatively short decay constants. The features of GSO and LYSO are their high light yields. The others crystals, i.e., PWO (Lead Tungstate) and pure CsI (caesium iodide), have short decay constants but insufficient light yields.

Table 4.1: Properties of inorganic scintillating crystals with relatively short decay constants. Some properties are separated into fast(^{f}) and slow(^{s}) decay components. The wavelength and light yield also differ for each; however, they are usually dominated by the fast components. The light yield is normalized using that of the NaI(Tl) crystal.

Name	GSO(Ce)	LYSO	NaI(Tl)	PWO	CsI(Pure)
Density (g/cm^3)	6.71	7.4	3.67	8.3	4.51
Radiation length (cm)	1.38	1.14	2.6	0.89	1.86
Molière radius (cm)	2.23	2.07	15.1	2	3.57
Decay constant (nsec)	600^s, 56^f	40	250	30^s, 10^f	35^s, 6^f
Wavelength (mm)	430	420	415	425^s, 420^f	420^s, 310^f
Reflection index	1.85	1.82	1.85	2.2	1.95
Light yield (NaI(Tl)=100)	3^s, 30^f	83	100	0.083^s, 0.29^f	3.6^s, 1.1^f

LYSO has a considerably better performance; however, it incurs a cost that is few tens of percentages more than GSO. We constructed an ECAL prototype to compare their energy resolutions; in this prototype, the examined GSO and LYSO crystals were replaced with each other, and then, the prototype was assessed using electron beams at ELPH (Research Center for Electron Photon Science) in Tohoku University, Japan in 2014 [78]. The result is shown in Figure 4.3, and it indicates that LYSO has a better energy resolution than GSO, and the difference is significant. GSO could not satisfy the requirement, and therefore, we concluded to use LYSO.

4.2.2 Photodetector

The photodetector is used to detect scintillation photons and output electric signals accordingly. We imposed some conditions for the selection. First, the cross-section of the photodetector must not exceed that of the crystal. Second, it must tolerate or be nonsensitive against magnetic field around 1 T to ensure that that the gain remains stable. Third, it should work in vacuum. The first two criteria inevitably refused PMT (photomultiplier tube) because of its typically large size and sensitivity to the magnetic field. Semiconductor sensors were found to be appropriate candidates; nowadays, there are several variations and products to choose from. Semiconductor photosensors employ the following steps for detecting photons:

1. Photons that enter the depletion layer[4] generate electron–hole pairs. The ratio of the number of electrons to that of incident photons is referred to as quantum efficiency.

[4]Outside the depletion layer, the separation of the electron–hole pairs does not work.

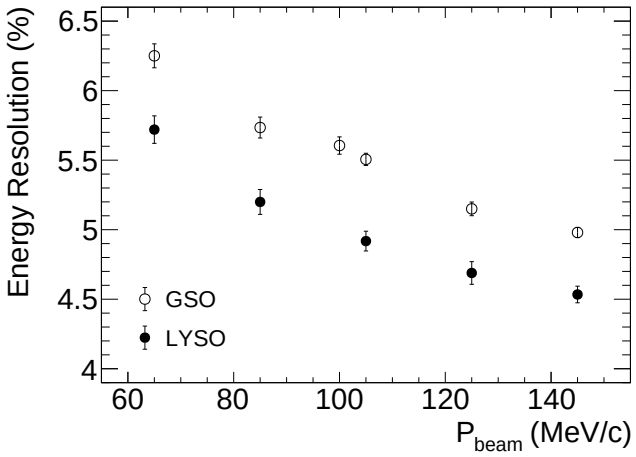

Figure 4.3: Energy resolutions of an old ECAL prototype using GSO and LYSO as a function of the electron momentum [78]. The error bars contain both static and systematic uncertainties.

2. The HV applied to the sensor results in a strong electric field whose high gradient protects them from the recombination, accelerates the electrons, and moves them to the electrode.

3. The drifted electrons further ionize atoms and generate new pairs. Repeating this process leads to the amplification of the incident photons. The number of electrons arising from a single photon indicates the gain.

4. The amplification forms an electric pulse on the electrode that is read by the readout electronics.

There are three categories in the amplification process for a given electric field strength: ionization, proportional, and Geiger modes. Each of these categories is associated with different products.

The PD (photodiode) works in the ionization mode, wherein the gain is almost unity; the outputs are too weak to use for the ECAL. In the Geiger mode, the amplification process saturates immediately, and the number of output electrons is no longer proportional to the initial electrons. This feature is not appropriate for energy measurement, whereas the SiPM overcomes it by combining many pixels of very tiny Geiger-mode silicon sensors[5]. Although many experiments have adopted SiPM for modern detectors, it is too weak for neutrons, which causes lattice defects and new excitation bands that considerably increase dark-current noise. Consequently, the ECAL adopted the APD that operates in the proportional mode.

To this end, there were two candidate products of Hamamatsu Photonics: S8664-55 and S8664-1010. Both have a rectangular shape but they differ in terms of their sensitive area, i.e., 5×5 and $10 \times 10 \text{mm}^2$, respectively. Their nominal bias is around 400 V, and the gain is about 50, which requires amplifier electronics. Finally, we select S8664-1010 as follows.

Table 4.2 lists the experiments conducted to examine their radiation hardness. The first assessment used the tandem electrostatic accelerator at Kyushu University in Japan, which accelerates deuterons

[5]The magnitude of an output charge from SiPM is proportional to the number of pixels that the photons hit unless multiple photons enter the same pixel simultaneously. It can maintain the countability of the incoming photons.

Table 4.2: Radiation-tolerance tests for the APDs. (*) S8664-1010 was exposed by this flux; however, its tolerance was evaluated for up to 2.4×10^{11} n_{1MeV}/cm^2 for a technical reason as explained in the text.

Date	Facility	Examined item	Irradiated flux
Oct. 2014	Tandem facility at Kyushu Univ.	S8664-55	2.2×10^{12} n_{1MeV}/cm^2
Jul. 2015	Tandem facility at Kobe Univ.	S8664-55	2.5×10^{12} n_{1MeV}/cm^2
		S8664-1010	2.5×10^{12} n_{1MeV}/cm^2 (*)
Oct. 2015	^{60}Co facility at Kyushu Univ.	S8664-55	12 kGy

to 9 MeV and generates neutron beams with a $^{12}C(d, n)^{13}N$ reaction in a carbon fixed target. We prepared three samples of S8664-55 and exposed them to neutrons up to 2.2×10^{12} n_{1MeV}/cm^2. To evaluate the performance, we created a test bench wherein an LED provided a constant light input to the tested APD, and a PMT monitored its magnitude and stability. The APD signals were amplified by amplifier electronics and measured by a waveform-sampling digitizer. We calculated their maximum wave height G_h and integrated charge G_c by fitting them with the averaged waveform template; we evaluated their fluctuations σ_h and σ_c. Figure 4.4 shows changes in the S/N ratio G_h/σ_h and the resolution σ_c/G_c as a function of the input light strength. The waveform became 1.3 times noisier, and the S/N ratio deteriorated. However, it is not fatal because the waveform fitting compensates it and preserve the resolution.

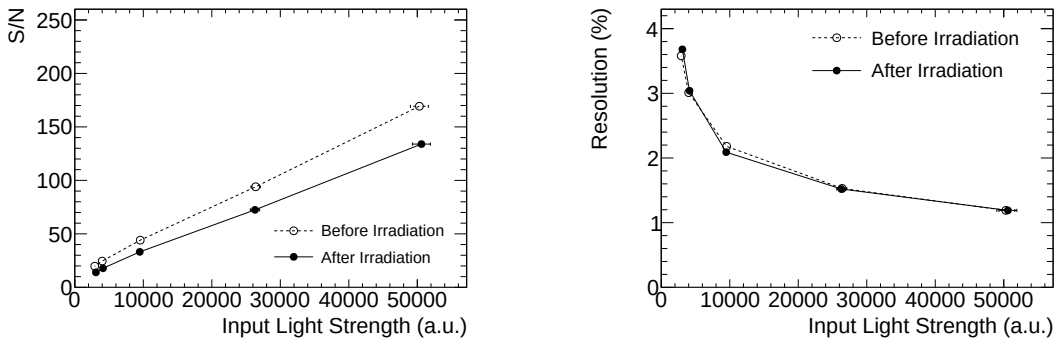

(a) S/N ratio **(b)** Resolution

Figure 4.4: Changes in (a) the S/N ratio and (b) resolution of S8664-55 after neutron irradiation of 2.2×10^{12} n_{1MeV}/cm^2. The horizontal axis represents the strength of the input LED light.

The neutron tolerance of S8664-1010 was evaluated with the tandem accelerator facility at Kobe University in 2015, where neutrons were produced with the $^{9}Be(d, n)^{10}$ reaction from its 3 MeV deuteron beam. S8664-1010 showed a good tolerance against neutrons up to 2.4×10^{11} n_{1MeV}/cm^2. Although the APD was exposed to 2.5×10^{12} n_{1MeV}/cm^2 at most, the dark current increased considerably and the prepared electronics could not work safely to evaluate the performance. However, since S8664-1010 also hardly changed its resolution at 2.4×10^{11} n_{1MeV}/cm^2 as well as S8664-55, it was assumed to possess the required tolerance.

Gamma-ray tolerance was studied using the ^{60}Co facility at Kyushu University in 2015. S8664-55

was exposed to gamma rays of 12 kGy in total with energies of 1173 and 1332 keV from the ^{60}Co beta decay. The resolution did not change considerably, and the dark-current was only 340 nA. We found that the neutron damage was more significant for the APD in COMET.

Finally, we performed the same evaluation procedure mentioned above to compare the nominal performance of S8664-55 and S8664-1010. Figure 4.5 shows the S/N ratio and resolution of both products. As expected, S8664-1010 has a distinct difference from S8664-55. The noise rises only by 30%, and the S/N ratio improves nearly four times, which is better than the cost that is 2.2 times as expensive as that of S8664-55.

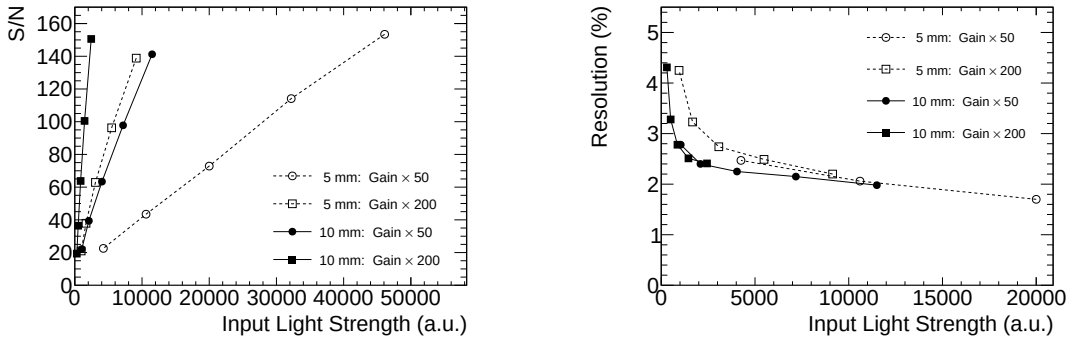

(a) S/N ratio

(b) Resolution

Figure 4.5: Comparison of the (a) S/N ratio and (b) resolution between S8664-55 (5×5 mm^2) and S8664-1010 (10×10 mm^2) at gains of 50 and 200. The horizontal axis represents the strength of the input LED light.

4.2.3 APD Holder Board, Temperature Sensor, and LED

The APD holder board attached to the back of the crystal contains a temperature sensor and LED with an APD. The temperature sensor monitors a variation of the temperature around the APD because the APD gain has an inescapable temperature dependence of 2–3%/°C. Only one of the four boards in a block module holds the sensor to reduce the number of cables. Further, there may be other sources to introduce a change in the gain. The LED in every crystal module monitors the gain directly with its light. Because crystal transparency degradation would be a source of the gain drop, the LED is placed such that its light passes and reflects in the crystal before entering the APD.

Figure 4.6 shows the PCB layouts, whose size are the same as the crystal, i.e., 2×2cm^2. The APD is placed in the corner with the temperature sensor. The distance between the LED and APD electrodes is maximized to minimize the optical and electrical interferences. A black spacer sheet with a thickness of 0.3 mm is used to protect the APD from the lights passing through the PCB.

Figure 4.7 shows the complete APD holder board. The L-shaped white frame is originally black but it is painted using a reflecting material (EJ-510, ELJEN Technology). The frame includes a black window made of an ND (neutral density) filter (ND3.0 of FUJIFILM Corporation) that is used to pass the LED light toward the crystal partly. The HV and APD signals propagate in the brown coaxial cable that is soldered to the board. The other cables are used for slow control, and they contain five

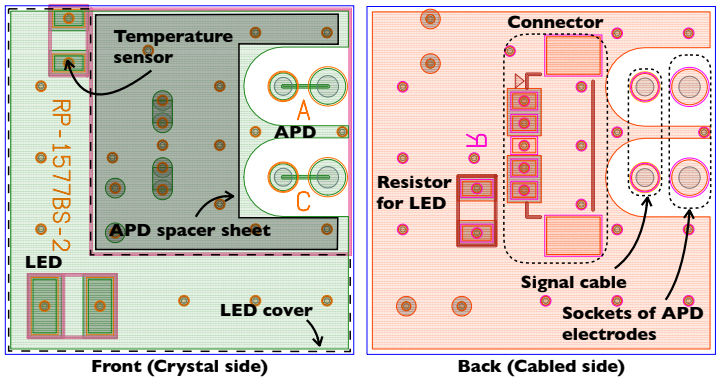

Figure 4.6: PCB layout of the (left) front and (right) back sides of the APD holder board. The APD is mounted on a corner, and the temperature sensor is attached next to it. The LED is installed on the opposite side of the APD.

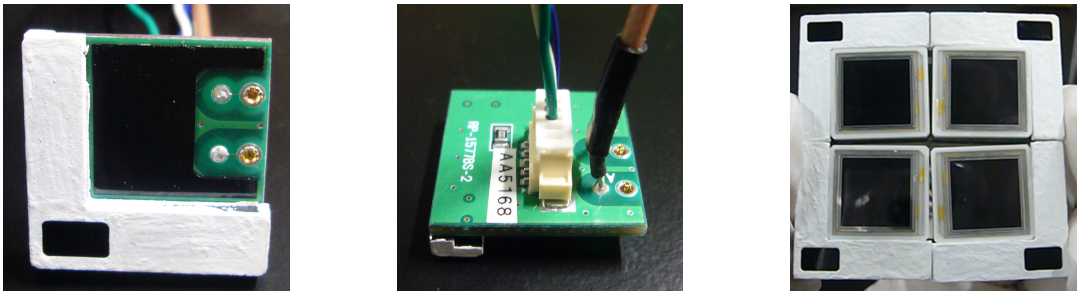

(a) Front side without APD **(b)** Back side **(c)** 2 × 2 APD holder boards

Figure 4.7: APD holder boards. (a) The white frame covers the temperature sensor and the LED with the ND filter. The APD is mounted on the black sheet. (b) Slow control cables are attached with a connector. The coaxial cable is divided and soldered to the holes close to the APD pin sockets. (c) The four boards of a block module are aligned such that all APDs gather at the center.

wires: one for grounding, two for the LED, and two for the temperature sensor. Since only one board contains the temperature sensor; the board in the picture does not have its cables. The board has another symmetric layout to concentrate all APDs to the center of the block module. Finally, an optical connector (EJ-560 of Eljen Technology) is used to connect the APD and the crystal. The total thickness is optimized to be 0.5 mm thicker than the white frame so that it does not touch the crystal.

The temperature sensor is a platinum resistance temperature detector of the SMD0805V series of Heraeus Holding GmbH. It has a large temperature coefficient of 3850 ppm/K, which enables it to measure its temperature. Although this type of sensor requires four-wire sensing[6], we use two-wire sensing to reduce the wires across the feedthrough. The sensor has the maximum resistance in the series (10 kΩ), which is considerably higher than the total unknown resistance in the wires and electrode contacts that would be a few tens Ω at most. Such a high resistance does not heat up. The sensor was examined in the irradiation tests at Kobe University and Kyushu University, and it

[6]Four-wire sensing uses two pairs of wires separately for supplying the current and for voltage sensing to eliminate finite resistance in the wires and their contacts from the measurement

showed a neutron tolerance of 10^{11} n_{1MeV}/cm^2 and gamma ray tolerance of 4 kGy. The linearity of the resistance did not change by more than 0.1%, and it proved that the radiation damage would never affect the measurement.

An essential condition for selecting the LED is determining if it can realistically imitate the real LYSO signals. The wavelength must be similar to that of the scintillation lights from LYSO. A faster response to the driving pulse helps control the time structure of the LED light. Seven candidate products from different manufacturers were prepared and examined in the neutron tolerance test at Kobe University. Any defects in the energy-band structure of LEDs are detrimental to the luminance. Finally, the ECAL adopted KA-3528QBS-D of Kingbright Electronic Co, Ltd., which was the most tolerant but sensitive to radiation damage. Another firm technique must be used to trace the LED deterioration. Once possible approach would be to compare the difference in responses to the LED light and cosmic rays.

4.2.4 Reflector

Optical reflectors enhance photon-collection efficiency, and they comprise PTFE with a thickness of 65 μm and ESR. The former is a popular diffusing reflector used for various scintillating crystals, and the latter is a specular reflector, a product of 3M. The initial design used only two layers of PTFE to minimize the insensitive region in the ECAL, but it showed a light leakage; hence, we adopted ESR. We compared variations of the number of layers of each reflector and approaches to cut the ESR and wrap the crystal. The best approach is to use one layer of ESR, followed by one layer of PTFE, which successfully magnifies light yields by 30% from the initial design. Figure 4.8 shows the selected approach to cut and bend an ESR film covering an LYSO crystal.

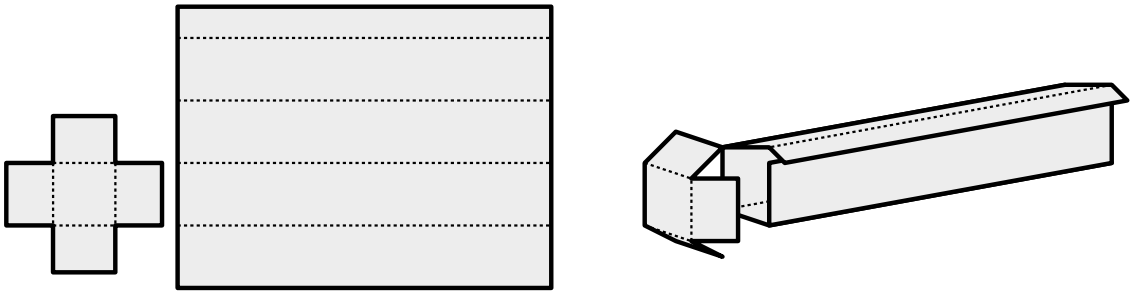

Figure 4.8: Method to cut and bend the ESR film surrounding the LYSO crystal

4.2.5 Module and Cabling

The crystal module comprises an LYSO crystal and an APD holder board wrapped by reflectors. Each 2×2 combination constitutes a block module.

A bag made of an aluminized polyester (mylar) film is used to fix the crystal modules, and it shrinks tightly after heating. In addition, an aluminum frame and a cover are mounted on the back of the block module. The cover is fixed with screws on the frame, and it involves the bag between the frame and the cover. The brown coaxial cable for the APD is RG178 of RADIALL, and it protects

weak signals from the external noise and crosstalk from the pulses driving the LED. The temperature sensor and LED use normal metallic wire cables. Figure 4.9 shows the gathered APD holders with the cables and a complete block module.

The next upper module holds 2×2 block modules with the intermediate board. This is the basic unit for slow control because the intermediate board distributes the slow control signals from the back-end system to each crystal module. Figure 4.10 shows the module with all cables.

(a) APD holder boards and frame with cabling. **(b)** Complete block module

Figure 4.9: Block module. The brown cables are for the APDs, the blue and white cables are for the LEDs, the red and white cables are for the temperature sensor, and the green cables are for grounding each board.

4.2.6 Feedthrough

The feedthrough mediates the electric signals from the vacuum in the detector solenoid to the outside. The APD signals are so weak that a preamplifier is necessary; however, it is not preferred to place electronics that generate heat in the vacuum. We carefully designed the feedthrough to minimize external noise and crosstalk contamination.

We attempted to make the feedthrough with the PCB to deal with multiple signal lines. The feedthroughs are made of sturdy metal to maintain the high vacuum pressure; however, it is not trivial to pass many cables. The feedthroughs are also a noise source because of the increase in the number of electrical contacts. Using PCBs as the feedthrough can enable dense wirings and help mount any electronics on the board. Although the PCB cannot shut a high-pressure difference and tolerate its stress, we require only a vacuum pressure of $O(1)$ Pa at the lowest. Figure 4.11 shows a feedthrough prototype attached to the latest ECAL prototype.

4.3 Electronics

4.3.1 Signal Line

The preamplifier shown in Figure 4.12 is designed for the ECAL to enhance the weak charge currents from 16 APDs to magnitudes that can be read by the readout electronics. Further, the preamplifier comprises two types of components: charge sensitive and transimpedance components. The charge sensitive component is used to amplify an input charge from an APD with a gain of 0.15 V/pC. The

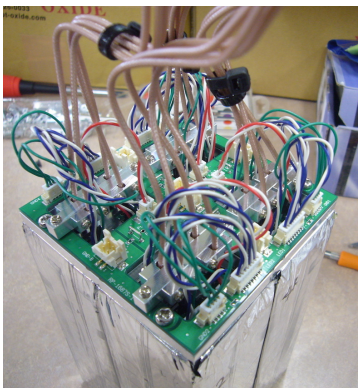

Figure 4.10: 2×2 block modules with the intermediate board, to which the slow-control cables from the crystal modules are connected.

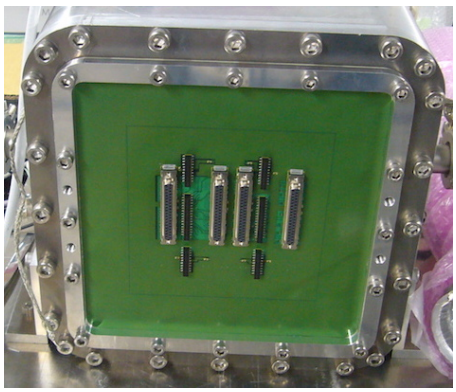

Figure 4.11: Feedthrough board made of PCB installed in the ECAL prototype. The preamplifiers and slow-control transmission boards are mounted.

transimpedance part converts it into a couple of differential waveforms. These differential waveforms can prevent themselves from external noises[7]. The entire circuit does not include an explicit shaping circuit to maintain the original time structure of the LYSO light emission for the pile-up separation.

The trigger line includes an adder circuits that sum the waveforms every four channels of the signal line. Further, it includes a shaping circuit with a time constant of about 100 nsec at present, whereas it may change depending on the studies in the future.

EROS is the ECAL version of ROESTI, and it was introduced in Section 3.3. Figure 4.13 shows a picture of the entire EROS. Although it has the same components as that in ROESTI, the only difference is the mezzanine board; instead of ASD, it is connected to the main board. It converts the differential waveform from the preamplifier into a single-end waveform.

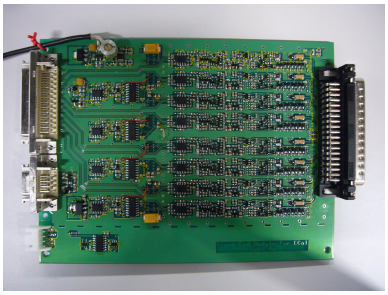

Figure 4.12: Preamplifier board handling 16 APD channels from the right connector

Figure 4.13: Waveform digitizer board for the ECAL, EROS. The mezzanine board on the left side converts the input differential waveforms into single-end waveforms.

[7] A pair of differential waveforms has the same shape $v(t)$ with opposite polarity as $v_{\pm}(t) = \pm v(t)$. Any noise $n(t)$ can contaminate both waveforms simultaneously with the same phase: $v_{\pm}(t) \to v'_{\pm}(t) = v_{\pm} + n(t)$. This noise can be eliminated by considering the difference $v'_{+}(t) - v'_{-}(t) \propto v(t)$.

4.3.2 Trigger Line

Currently, the Phase-II trigger system has two candidate electronics: Pre-trigger and COTTRI (COMET trigger). The former is specific to the ECAL; however, the latter is shared with the Phase-I trigger system. Each systems comprises front-end or mezzanine boards and motherboards. The front-end board processes the trigger line waveforms and compiles them for the motherboard. The motherboard holds several mezzanine boards, collects their data, and generates trigger signals for FC7 if they exceed some trigger criteria. If FC7 makes trigger decisions after receiving the trigger signals, they are distributed to every EROS to digitize and record waveforms. Figure 4.14 displays the pictures of the Pre-trigger and COTTRI electronics. The Pre-trigger and COTTRI electronics contain 8 bit flash ADC chips operating at a 100 MHz sampling frequency. These ADC chips can monitor the input waveforms continuously, separately from EROS, and therefore, they can generate trigger signals instantly.

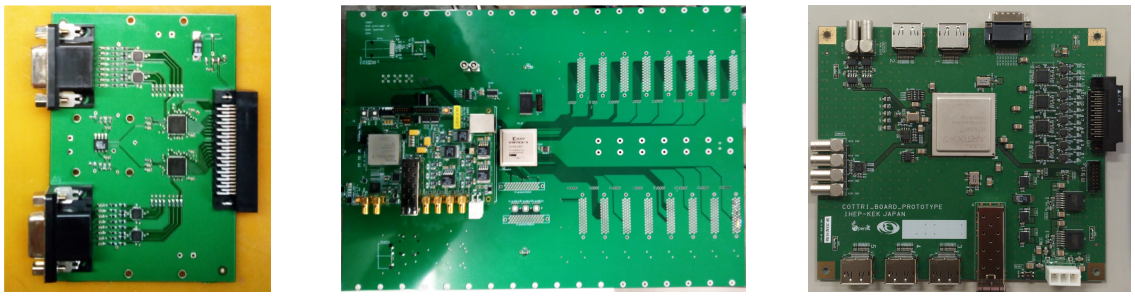

(a) Pre-trigger mezzanine board **(b)** Pre-trigger motherboard **(c)** COTTRI front-end board

Figure 4.14: Phase-II trigger electronics.

4.3.3 Slow Control

The ECAL system employs several slow-control modules to maintain the performance. First, the HV for the APDs must be controlled and recorded. Their optimum values vary depending on, for example, temperature and radiation damage. Hence, APD gains should be maintained by adjusting the HV. We developed the prototypes of the controller and monitor separately. However, the controller prototype remains under development and is not remotely controllable. Second, an electronics board is dedicated to monitoring the temperature and driving the LED. Third, slow-control transmission boards are installed on the feedthrough to carry all slow control signals.

The prototypes of the HV controller device and monitor board are displayed in Figure 4.15. Both handle 32 channels. The controller contains a series of capacitors and resistances to stabilize the HV. The individual channel values are adjustable. Furthermore, the controller supplies other voltages reduced by a constant factor to a few volts for the monitor board. The monitor board contains ADC chips to read them, and it communicates with the DAQ machine to transmit them.

Figure 4.16 shows the prototype board that measures the temperature and operates the LEDs. For LED operation, a NIM (nuclear instrumentation module)-standard input from outside generates the LED driving pulse. The board uses adjusters to change the shape of the driving pulse so that the LED

light-emission time structure becomes similar to that of the LYSO scintillation. The driving-pulse amplitude is set considerably higher than that of the usual LED activation threshold of about 0.7 V because the threshold is sensitive to temperature. The ND filter moderates the consequent light that is too bright for the APD. However, such a robust driving signal introduces a considerable amount of crosstalk into the nearby APD. Therefore, we use differential signaling for the LED driving pulse. A differential pulse pair looks ±0 V in total from the APD, and hence, it can reduce crosstalk.

Finally, the slow-control transmission board was designed for HVs and slow-control signals to access the vacuum region. It also has a simple HV filtering circuit.

(a) Controller device **(b)** Monitor board

Figure 4.15: Prototype of the (a) controller and (b) monitor devices for the APD HV. Output HVs are adjusted individually with volumes.

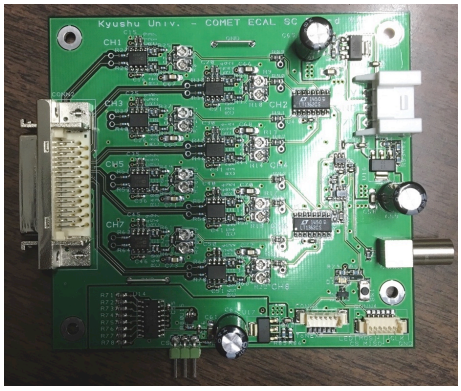

Figure 4.16: Prototype of the LED controller and temperature monitor board. The left connector links to the slow-control transmission board.

5

Performance Evaluation of the StrECAL Prototype

Understanding the response and performance of StrECAL for the signal electrons is the most fundamental milestone to study the Phase-II sensitivity. At the beginning of 2017, we completed a StrECAL prototype and performed a test-beam experiment to evaluate its performance on March 2017 at ELPH in Tohoku University, Japan. All estimated performances successfully satisfied all requirements.

5.1 Experimental Setup

5.1.1 Facility: Research Center for Electron Photon Science

Figure 5.1 shows the entire facility of ELPH [79]. We took part in the experiment at the gamma-ray irradiation room or GeV-γ Experimental Hall.

ELPH owns three beamlines (Beamlines I, II, and III), and we used Beamline III. Beamline I starts from the 70 MeV Electron LINAC (Linear accelerator) and is injected into experimental room number 1 for radioactive isotope experiments. The beamline starting from the 90 MeV injector, which is also an electron LINAC, caters to Beamlines II and III for nuclear experiments. The 1.3 GeV BST (booster-storage) ring is a synchrotron accelerator that accelerates electrons up to 1.3 GeV with a coherent radio frequency of 500 MHz. Beamline III continues until GeV-γ Experimental Hall. On the electron-beam orbit in the BST ring, two very fine carbon wires with a diameter of 11 μm are inserted to generate high-energy gamma rays via bremsstrahlung radiation.

In GeV-γ Experimental Hall, the $\mathcal{R}$TAGX dipole magnet whose layout and performance are shown in Figure 5.2, is installed. A 20 μm thick gold foil located again converts the gamma rays into electrons and positrons. $\mathcal{R}$TAGX produces an electron or positron beam with the required momentum by changing its current polarity and magnitude and by utilizing lead collimators. A vacuum chamber and the pipes cover the beamline from the first collimator to the beam exit 5 m away from the last collimator. A Mylar film with a thickness of 50 μm was used for the vacuum window; further, momenta ranging from 65 MeV/c to 185 MeV/c was used. The beam-energy resolution is considered in the analysis to extract the ECAL energy resolution from the observation. The given resolution assumes an old beamline configuration where the vacuum pipe finishes at the last collimator; however,

it was extended to the detector site in the experiment. Thus, it is expected that the actual resolution is better, and we refer to it conservatively.

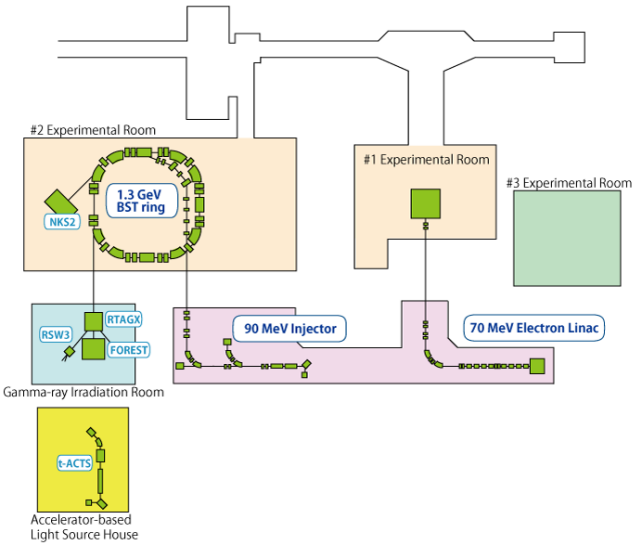

Figure 5.1: Schematic of Research Center for Electron Photon Science (ELPH) [79]. Gamma-ray irradiation room or GeV-γ Experimental Hall used for the experiment.

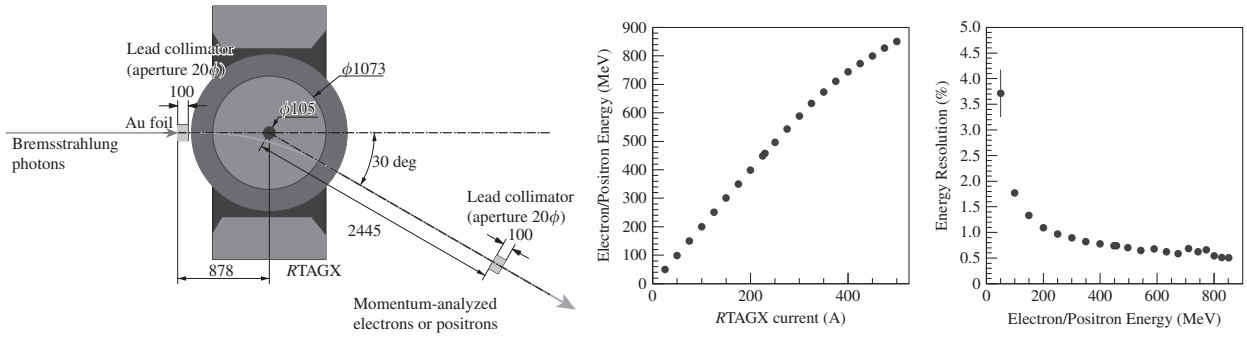

(a) Layout **(b)** Beam energy and resolution

Figure 5.2: Layout of the $\mathcal{R}$TAGX dipole magnet in GeV-γ Experimental Hall and its beam profiles [80]. (a) Gold foil converts the Bremsstrahlung photons into electrons and positrons. The magnet was configured for the electron beam. (b) Energy and resolution of the produced electron beam at the beam exit as a function of the $\mathcal{R}$TAGX current, which his estimated with `GEANT3` [81].

5.1.2 Detectors Including StrECAL Prototype

Figure 5.3 shows a schematic layout of all the detectors in the experiment and their pictures. We combined vacuum chambers to install them in a continuum vacuum region and achieved a vacuum pressure under 1 Pa, which meets the requirement. The straw tracker prototype detects the beam electrons in two horizontal (X) and vertical (Y) axes, where the beam axis is the Z axis. The ECAL prototype chamber contains 64 LYSO crystals to form an 8×8 matrix.

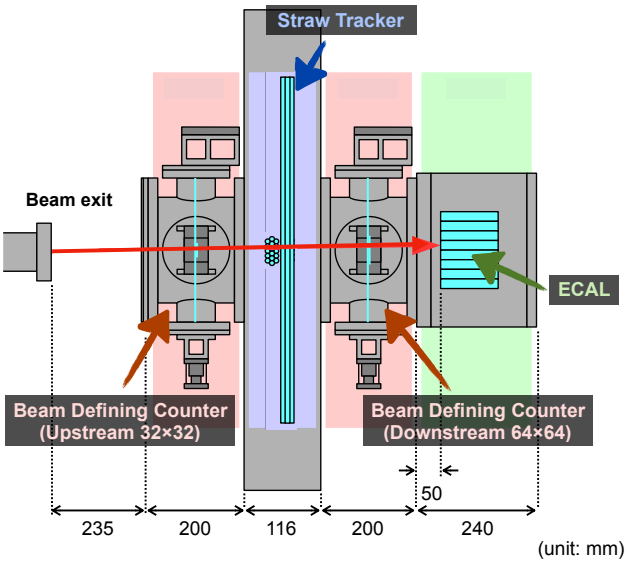

(a) Layout

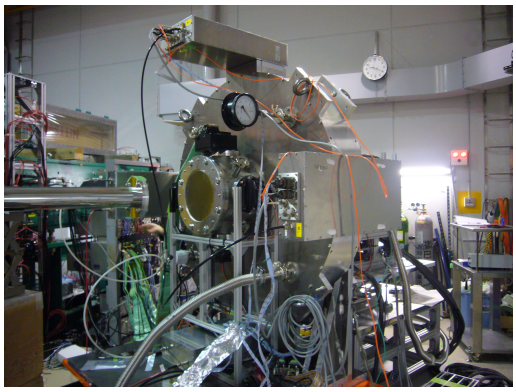

(b) Upstream view

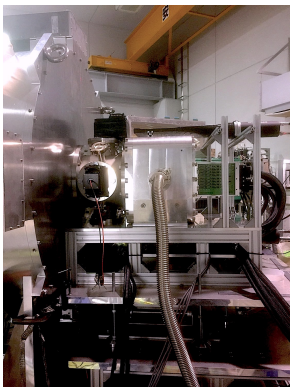

(c) Downstream view

Figure 5.3: Full detector system. (a) Beam electrons come from the beam exit. There are upstream BDC, straw tracker, downstream BDC, and ECAL. (b) The upstream BDC and straw-tracker prototype are displayed. (c) The downstream BDC and ECAL prototype are behind the straw tracker, and the two cosmic ray counters are installed on the top and bottom of the ECAL.

We placed two cosmic-ray counters on the top and bottom of the ECAL chamber for the energy calibration of each crystal with the energy deposit of a cosmic muon. The counters comprise a plastic scintillator, light guide, and PMT wrapped in an aluminized-mylar reflector sheet, and they are tightly shielded with black tape. The plastic scintillator is EJ-230 (Eljen Technology), and it has a dimension of $200 \times 160 \times 10$ mm^2. The PMT assembly is H11284 MOD (Hamamatsu Photonics), whose photocathode has an acceptance of 2 inches. The operation HV was adjusted so that their response to the cosmic rays became similar and sufficiently high. The centers of the top and bottom counters are 185 mm above and 234 mm below the center of the ECAL, respectively.

There is also a couple of tubes that sandwich the straw tracker and unite both the StrECAL chambers. Each tube accommodates a hodoscope counter, which is named BDC (beam-defining counter), to measure each path of the electron.

The straw tracker prototype holds 16 straw tubes of the Phase-I type for each axis. Figure 5.4

shows the layout, straw-tube alignment, channel assignment, and inside view of the completed instrument. Each axis contains three layers of five, six, and five straw tubes. The chamber has four gas manifolds in the outer ring, two gas inlets and two gas outlets. In each gas-inlet manifold, a ROESTI board connects to the straw tubes on each axis via a filtering circuit to cut the applied HV.

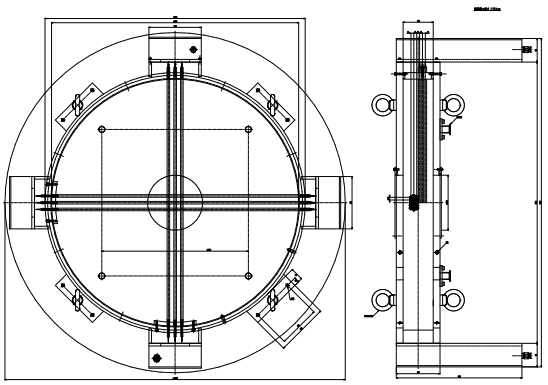

(a) Blueprints

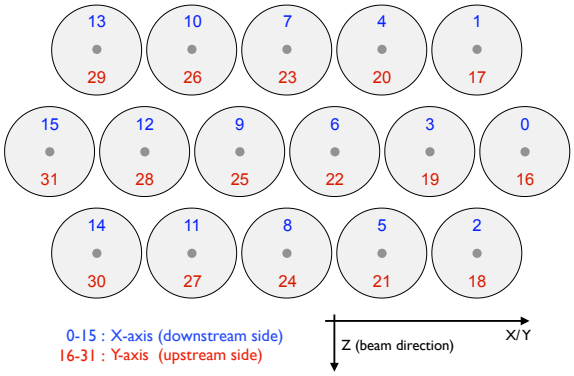

(b) Straw-tube alignment and channel assignment

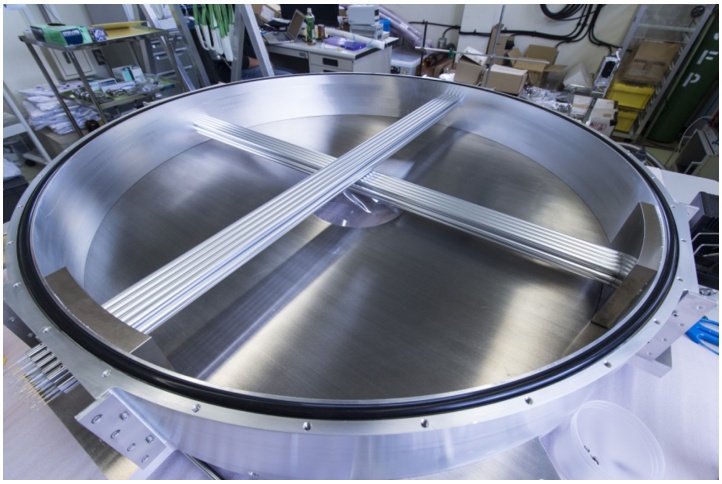

(c) Inside of the chamber

Figure 5.4: Straw-tracker prototype. (a) The chamber accommodates 32 straw tubes, and the four gas manifolds in the outer ring supply the gas. (b) The alignment and channel maps on each axis are shown; Channels 0 to 15 and 16 to 31 belong to the X- and Y- axes, respectively. (c) There are three layers of straw tubes in each axis.

The ECAL prototype contains 4×4 block modules that correspond to 64 crystals, as shown in Figure 5.5. The fixtures in the chamber tightly push all modules to minimize the insensitive space. Cables from the intermediate boards are connected to the PCB feedthrough board. After the feedthrough board closes the chamber, four preamplifier and two slow-control transmission boards are mounted with a supporting frame. We found that the EROS mezzanine board had a defect in their chips after the experiment. However, this introduces a significant challenge to the waveform-fitting algorithm for the ECAL analysis, and it is discussed in Section 5.3.1.

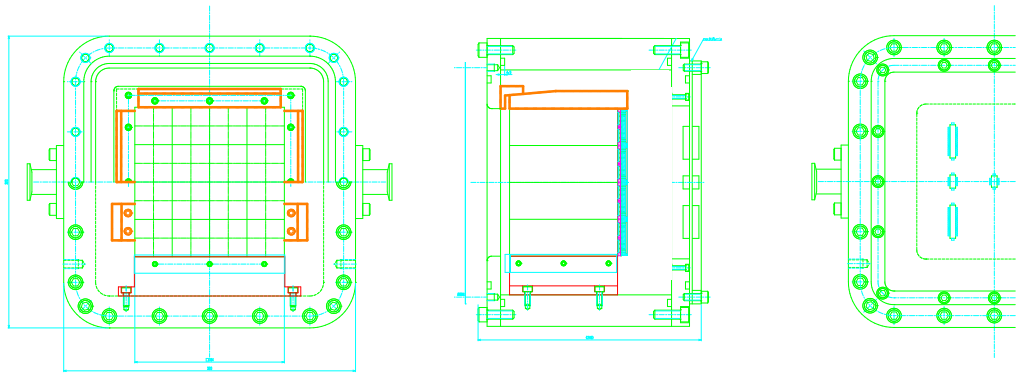

(a) Blue prints

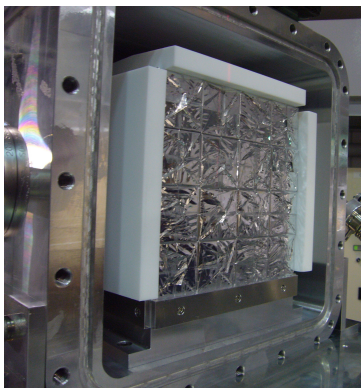

(b) Upstream view

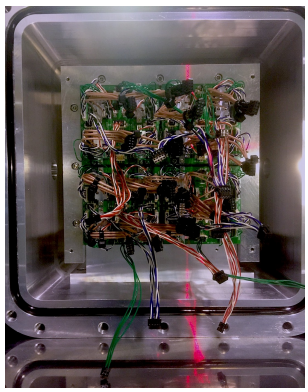

(c) Downstream view

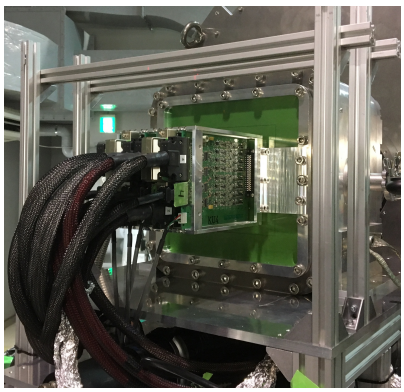

(d) Electronics on the feedthrough

Figure 5.5: ECAL prototype. (a) A matrix of 8×8 crystals stays on the bottom basement, and it is fixed by the orange-colored arms. The outlets on both sides connect to a vacuum gauge and pump. (b) The arms fix the matrix of the block modules. (c) The four intermediate boards combine each of the 2×2 block modules, and all cables are connected to the modules. (d) The preamplifier and slow-control transmission boards are mounted on the feedthrough with a fixture frame.

5.1.3 Beam-Defining Counter (BDC)

The BDC is a two-dimensional hodoscope detector using scintillating plastic fibers. Figure 5.6 displays a schematic view of the upstream BDC and its pictures, whereas the downstream BDC looks similar. Collecting the two-dimensional hit positions from both BDCs enables us to reconstruct a trajectory of the track. However, we used only the upstream BDC during the runs evaluating the ECAL performance to minimize the amount of material before the ECAL and replaced the downstream vacuum tube with a plain tube. In that case, the straw tracker is substituted for the downstream BDC.

The upstream and downstream BDCs are composed of 32×32 and 64×64 fibers, respectively; this difference allows covering the possible beam spread. The fiber is SCSF-78J (Kuraray Co., Ltd) and it has a cross-section of 1×1 mm^2. The end of every fiber is read out by an MPPC (multipixel photon counter) photosensor (S13360-1350PE, Hamamatsu Photonics), which is equivalent to SiPM. Further, the BDC played the role of a reliable trigger detector. The other end of the fibers is clustered and read out by a metal-packaged PMT (R11265U-100, Hamamatsu Photonics). Several NIM-standard modules process the PMT signals to generate the trigger signals immediately. The feedthrough plate

on each flange has holes to thread the fibers, and the fibers are attached with epoxy-resin glue (EP331, CEMEDINE) to shield the vacuum. Next to the feedthrough plate, there are containers for the MPPC and PMT to fix their connection with the fibers. A 125 μm-thick Mylar sheet shields the front end of the upstream BDC, followed by a 25 μm-thick aluminum-deposited Mylar sheet to prevent light leakage.

We used a generic MPPC-readout NIM device developed by KEK OpenIt in Japan [82]. Since it works using the embedded ASIC (application specific integrated circuit) chip EASIROC (extended analogue silicon PM integrated read-out chip) invented by Omega [83] in France, it is referred to as EASIROC for short in this thesis. An EASIROC module handles 32 MPPCs individually and communicates with the DAQ system with SiTCP technology. We adjusted the power voltages—as every MPPC has the same gain—to a single photon using a ^{90}Sr radioactive source. In the experiment, we could not establish a suitable optical coupling for the PMT on the Y-axis side in the downstream BDC (Channel 4). Its apparent gain dropped, and hence, some corresponding properties such as time resolution also deteriorated, as discussed in Section 5.3.2.

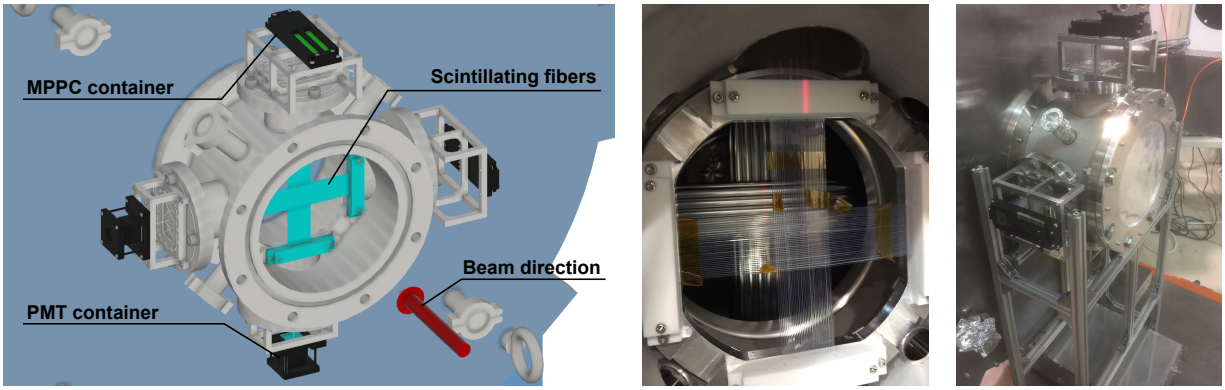

(a) Outline **(b)** Inside **(c)** Outside

Figure 5.6: (a) Schematic view and (b, c) pictures of the upstream BDC. In the vacuum tube, 32 scintillating fibers are aligned on each axis and fixed with feedthrough plates at each end. The MPPCs and PMTs are attached to them in the containers at the flanges. Aluminum-deposited Mylar sheets shut the front side.

5.1.4 Data Acquisition (DAQ) System

The development of the DAQ and its demonstration are important topics of the experiment. Since we successfully prepared most COMET-specific electronics for the experiment, we also developed a MIDAS-based DAQ prototype for the first time. Figure 5.7 shows a diagram of the DAQ system.

There are three types of trigger setups for the (a) beam, (b) cosmic ray, and (c) LED calibration purposes. The COTTRI front-end trigger board—referred to as COTTRI—works as the trigger manager, and it was customized so that it can solely play the minimum roles of FC7. It continuously distributes 40 MHz clocks to synchronize the readout electronics except for EASIROC, which is the only third-party readout electronics used. The NIM coincidence module at the center of the diagram requests COTTRI to trigger if certain signals are received simultaneously from the trigger devices in

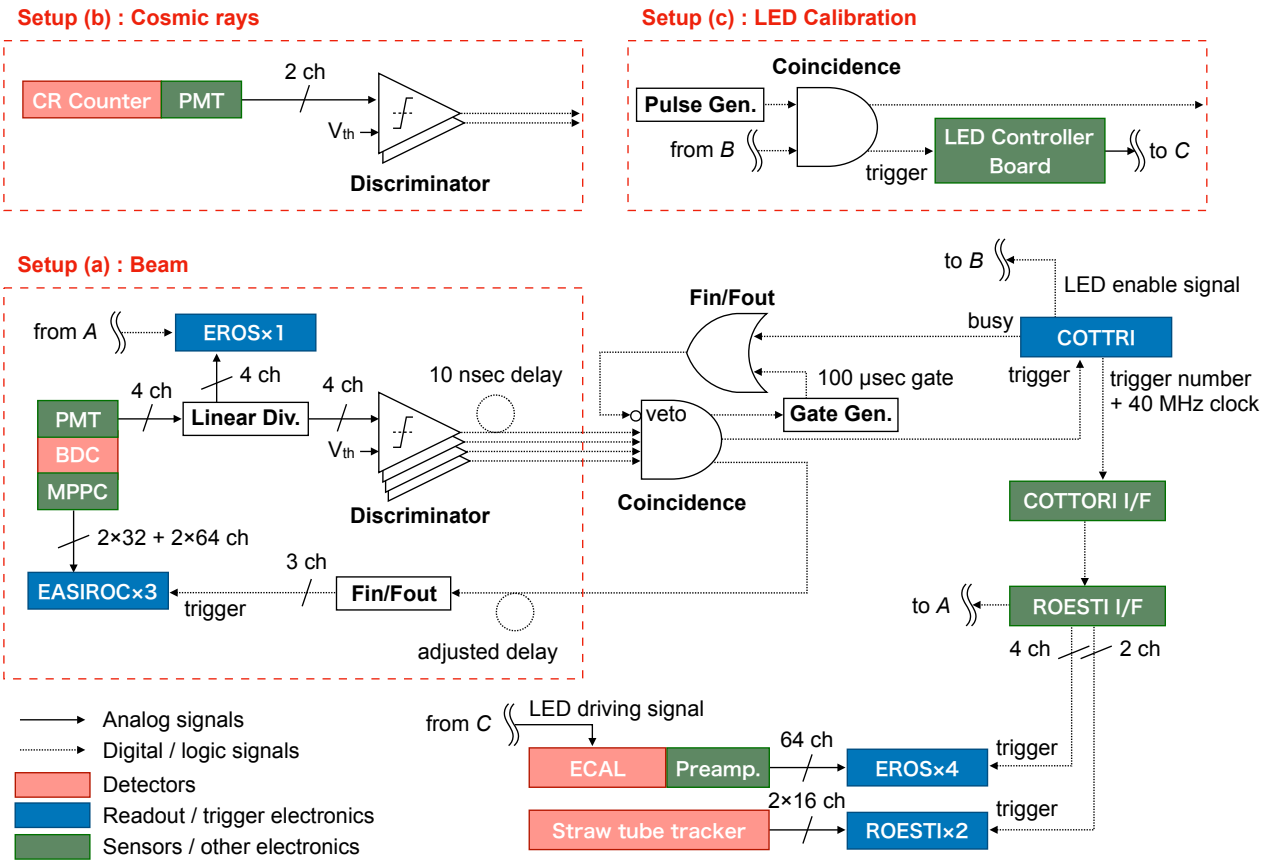

Figure 5.7: Diagram of the DAQ system. The white components represent NIM modules. The three red boxes represent different trigger setups for (a) beam, (b) cosmic ray, and (c) LED calibration.

each setup. Thus, COTTRI distributes a trigger signal with a unique identification number to the readout electronics, which append the provided trigger number to the data to be submitted. If COTTRI is busy processing former triggers, neither the number assignment nor the readout is performed. In case the COTTRI busy signal and gate signal with a length of 100 μsec (generated by the coincidence signal) enter the veto input, they stop the next trigger signal that arises in a short time. Both COTTRI and ROESTI interface (I/F) boards mediate between COTTRI and the multiple ROESTI and EROS boards because they use different cables to communicate. All electronics are manipulated by a single desktop computer, i.e., the main DAQ machine; it is not shown in the diagram. Once a trigger occurs, it collects data from the electronics, packs a bunch associated with the same trigger number, and saves it on the disk.

For the trigger system, first, the BDCs are used the trigger detectors in the (a) beam setup. Each BDC-PMT signal is separated by the linear-divider module into an EROS board to read and the discriminator modules to trigger. We delayed only one channel by 10 μsec to ensure that channel causes coincidence signals every time, which prevents time fluctuation among the channels. Furthermore, we excluded Channel 4 from the coincidence because it had a low gain as mentioned above. The coincidence output travels to EASIROC to trigger it directly because its readout is sensitive to the trigger timing.

Second, the (b) cosmic-ray setup is used to collect the events induced by cosmic rays for the indi-

vidual crystal energy calibration. Similar the beam setup, the discriminated signal from the cosmic-ray-counter signal arrives at the central coincidence module. The signals from their PMTs make the trigger requests.

Third, we used the (c) LED-calibration setup to regulate the APD gains. A periodic pulse from the pulse generator drives the LED controller boards that are remotely controlled by the enabling gate signals from COTTRI.

Slow control is independent and does not synchronize with the trigger system. We used the StrECAL slow-control prototype modules introduced in Sections 3.4 and 4.3.3[1]. Further, the readout electronics have slow-control functionalities. The SiTCP offers slow-control meanings based on UDP independently. The DAQ software fully utilizes them and realizes controlling and monitoring of EASIROC, ROESTI, and EROS. We employed Raspberry Pi 3 Model B [84] as the sub-DAQ machine to manipulate other devices. The developed slow-control electronics require serial communication that needs many wires and specific signaling functionality, whereas the main machine cannot directly cater to it. It supports multiple protocols of serial communication for the developed slow-control devices, and it can run MIDAS-based software. We prepared several Raspberry Pis to operate each module independently and to outsource the slow-control tasks to these modules.

5.1.5 Adjustment of the APD High Voltages

To secure an identical gain among the APDs, the individual HVs were adjusted using two datasets captured using the LED-calibration and cosmic ray setups. Figure 5.8(a) displays the typical response waveforms to a single LED flush and cosmic ray[2]. Although both shapes look different, the shape of the LED driving signals was tuned so that they look as similar as possible. We obtained a relative gain curve of every APD by scanning the average amplitude of the response with different HV around the nominal voltage provided by the manufacturer. Figure 5.8(b) shows an example gain curve for an APD. The gain curve is fitted well by an exponential function to extrapolate the gain curve. With the fitted gain curves, all HVs were set so that the response to cosmic rays becomes 80 mV at MPV (most-probable value) in the digitized data. It is sufficient to ensure that the response waveform up to 185 MeV electrons is within the DRS4 dynamic range. Figure 5.8(c) shows the variation in the observed MPV on all channels before and after HV tuning, and it shows APD gains were successfully regulated.

[1] Since we had not developed the APD HV monitor board of Figure 4.15(b) at that time, we used a handmade PCB with the same design

[2] The response to the beam electrons is the same as the latter.

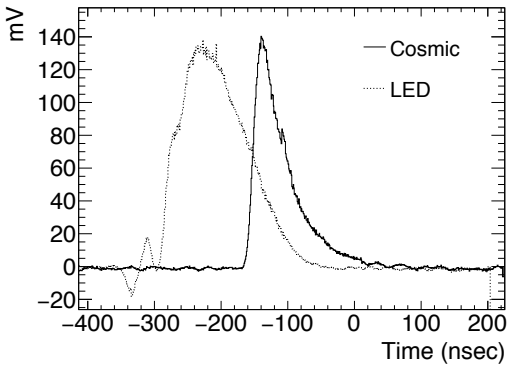

(a) Typical response waveforms

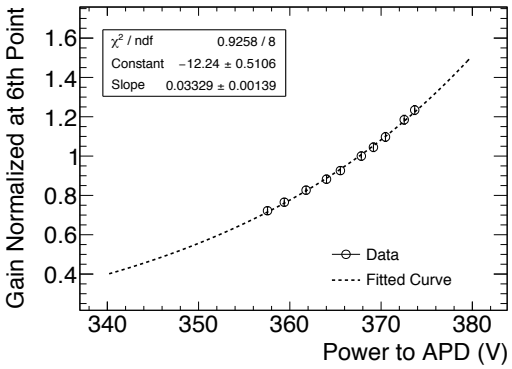

(b) Gain curve

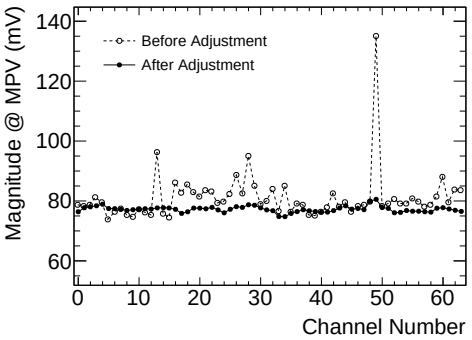

(c) Variation of all the APD gains

Figure 5.8: APD gain calibration. (a) The response to LED (broken line) is similar to that of cosmic rays (solid line). (b) Exponential function is fitted to an APD gain curve as a function of the applied HV. (c) APD gains measured with cosmic rays are well regulated after HV adjustment.

5.2 Obtained Data

We carried out the experiment from the 6th to 11th March in 2017, wherein the terms from 7th to 8th and from 9th to 11th were dedicated to the StrECAL performance evaluation. Tables 5.1 and 5.2 list all congregated data. There are certain names that will be referred to in the analysis stage later.

For assessing the straw-tracker prototype, we examined two types of gas mixtures, i.e., Ar:CO_2 and Ar:C_2H_6 with ratios of 70:30 and 50:50. The beam momentum was fixed at 105 MeV/c, and brass was used for the beam converter in front of $\mathcal{R}$TAGX to spread the beam. We compared the following two characteristics between both gas mixtures. First, the detection efficiency study investigated how significantly the combination of the straw tubes and ROESTI can recognize hit signals by varying the applied HV. Second, to evaluate the spatial resolutions of the straw tubes for several HVs, we recorded an abundant quantity of events to collect a sufficient amount of statistics on each drift distance. In both cases, we changed only the HV to the Y-axis straw tubes, which is the front layer in the chamber; however, we fixed the HVs to the others at 1900 V.

In the ECAL case, the data collection repeated a sequence every two days to investigate its energy, timing, and position resolutions as a function of the electron-beam momentum, which ranges from

Table 5.1: Data for the straw tracker performance evaluation. There are two study purposes for each gas mixture. Different HVs were applied to Y-axis straw tubes, while a constant HV was applied to the X-axis straw tubes. The names in the last column are referred to in text, where `XXXX` = HV.

Date	Gas mixture	Purpose	HV (V)	#Events (10^3)	Referred name
7th Mar.	Ar:CO_2	Detection efficiency	1600	100	`ar70co30.effXXXXv`
			1650	50	
			1700 to 1950 every 50	30	
		Spatial resolution	1800	797	`ar70co30.XXXXv`
			1900	796	
8th Mar.	Ar:C_2H_6	Detection efficiency	1600 to 2100 every 50	30	`ar50et50.effXXXXv`
		Spatial resolution	1850	200	`ar50et50.XXXXv`
			1950	799	
			2050	799	

Table 5.2: Data for the ECAL performance evaluation. P_e denotes the beam-electron momentum ranging from 65–185 MeV/c for studying the resolutions. Cosmic-ray data collection was performed twice for energy calibration. Names in the last column are referred to in text, where `XX` = P_e.

Date	Purpose	P_e (MeV/c)	#Events (10^3)	Referred name
9th Mar.	Energy calibration	cosmic rays	11	`cosmic1`
10th Mar.	Resolutions	65	60	`mscan1.XX`
		75	60	
		85	60	
		95	100	
		105	100	
		125	107	
		145	101	
		165	100	
		185	120	
	Energy calibration	cosmic rays	13	`cosmic2`
11th Mar.	Resolutions	65	179	`mscan2.XX`
		75	199	
		85	200	
		95	160	
		105	161	
		125	160	
		145	160	
		165	160	
		185	150	

65–185 MeV/c. We used gold for the beam converter because the beam energy resolution had already been reported by [80]. We operated the straw tracker with the Ar:C_2H_6 mixture and applied 2050 V to all straw tubes. In this thesis, we refer to the `mscan1` and `mscan2` datasets together as `mscan`. A plain vacuum tube substituted the downstream BDC tube. During the night hours, we accumulated cosmic-ray events for energy calibration.

Figure 5.9 shows examples of the obtained waveforms from the straw tracker, ECAL, and BDC-PMT line. The straw tracker waveform changes its shape every time depending on when the drifted electrons first reach the wire. The scintillating process in the ECAL and BDC is so immediate that it always has the same shape.

We monitored environmental variables related to the system with the slow control modules. Figure 5.10 shows the temporal variation in some of these variables. Although the vacuum pressure was stable around 10 and 0.5 Pa in both the straw tracker and ECAL datasets, it worse at the following

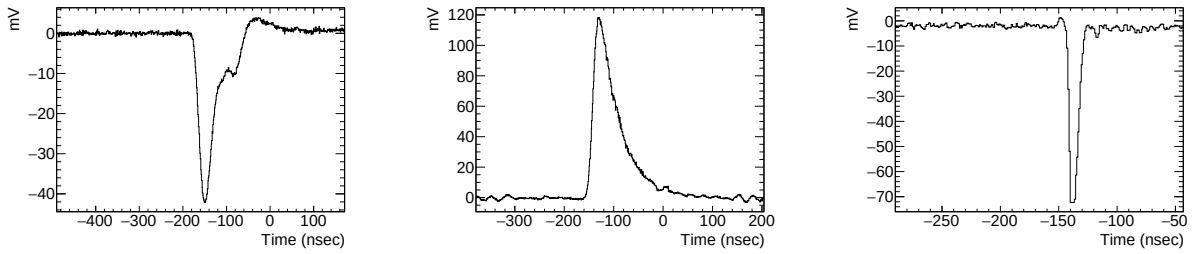

(a) Straw tracker **(b)** ECAL **(c)** BDC PMT

Figure 5.9: Examples of the obtained waveforms from the straw tracker, ECAL, and BDC-PMT line.

points. First, at the end of `ar50et50`, the vacuum pump accidentally stopped, and the pressure consequently started increasing; therefore, this part was excluded from the dataset. Second, the pressure was still decreasing initially for `cosmic1` because of the pumping has just started; however, it was not critical for the cosmic-ray measurement. Third, the gate valve worked incorrectly when detaching the vacuum line at the beginning of `ar50et50`; however, we noticed it soon and corrected it. The argon, CO_2, and C_2H_6 mass flows were stable over the entire period of the data collection. Although we did not explicitly control the temperature around the ECAL, the fluctuation in `mscan1` and `mscan2` is less than 0.1 °C in standard deviation, which indicates that it hardly affects the gain fluctuation or the energy resolution compared to other components.

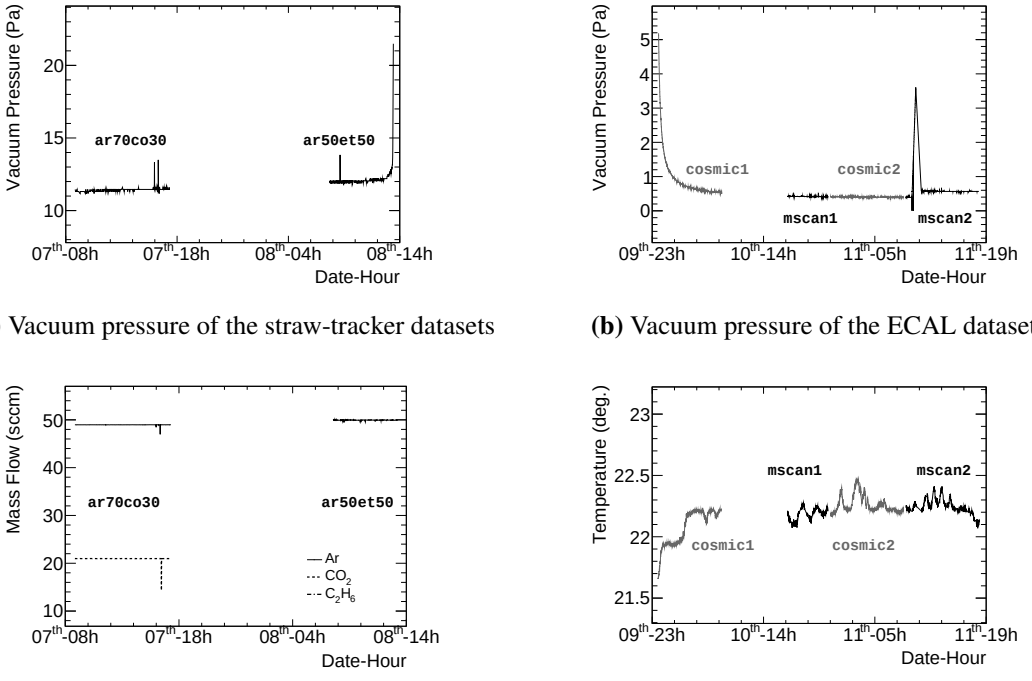

(a) Vacuum pressure of the straw-tracker datasets **(b)** Vacuum pressure of the ECAL datasets

(c) Mass flows of the straw-tracker datasets **(d)** Temperature of the ECAL datasets

Figure 5.10: Temporal variations in environmental parameters monitored by slow-control modules. Dataset names are placed near the corresponding parts.

5.3 Data Analysis and Physics Object Reconstruction

This section describes the essential details of the data analysis and physics object reconstruction algorithm. The algorithm first uses a waveform analysis scheme on the waveforms to obtain several quantities. Next, a physics object reconstruction scheme is applied to obtain physically meaningful variables such as time origin, track, and energy. BDC-PMT signals define the time origin of events T_0 that is also used by the straw tracker and the ECAL analyses. Track reconstruction infers the trajectory of the beam electrons from the BDC and straw tracker hits. Clustering reconstruction combines the ECAL hits into a "(energy) cluster" and calculates its total energy, average position, and timing.

5.3.1 Waveform Analysis

The idea of waveform analysis is shared among all detectors. The algorithm aims at extracting the height (maximum height), timing, and charge from signal-induced pulses in every waveform as

1. The waveform baseline w_{base} is obtained by averaging the waveform from 120 nsec to 20 nsec before the rising edge of the pulse and subtracting it from the waveform.
2. The wave height h_{max} is the maximum pulse amplitude after baseline subtraction.
3. The signal timing $t_{\text{th.}}$ is calculated by interpolating the two points closest to where the amplitude exceeds a fixed threshold $w_{\text{th.}}$. This is essential to obtain a time resolution of < 1 nsec from the waveform recorded at a 1 GHz sampling rate.
4. The charge $q_{\text{int.}}$ is the integral from the 20 nsec prior to $t_{\text{th.}}$ when the pulse disappears.

We use only h_{max} for the ECAL analysis, and only $q_{\text{int.}}$ for the straw tracker and T_0 (PMT) analyses. The charge information is more tolerant of the baseline random noise that results in zero in total. However, the ECAL front-end electronics have a bandwidth narrower than the assumed value. It introduces bad linearity to $q_{\text{int.}}$; however, it was found that it does not considerably affect h_{max}.

We found two particular types of noise in straw tracker waveforms: coherent and crosstalk. Coherent noise spreads over all channels, whereas crosstalk is induced by a signal pulse in neighbor channels. Appendix A explains them in detail with the schemes to remove them. However, crosstalk cannot be fully eliminated, and it distorts the spatial-resolution curve shown in Section 5.4.2.

5.3.1.1 Time-Slewing Correction

Since signal pulses require a finite amount of time to reach h_{max}, $t_{\text{th.}}$ shifts based on both $w_{\text{th.}}$ and h_{max}. $w_{\text{th.}}$ is fixed throughout the analysis, and this time-slewing effect correlates with h_{max}. Figure 5.11(a) shows it in the ECAL case. This correlation curve is fitted by

$$p_0 + u(h_{\text{max}} - p_1)\frac{p_2}{\sqrt{h_{\text{max}} - p_1}} + u(h_{\text{max}} - p_3)\frac{p_4}{h_{\text{max}} - p_3}, \tag{5.1}$$

where $u(x)$ denotes the step function of 1 when $x > 0$ or 0 otherwise, and p_{i} $(i = 0, ..., 4)$ denote the fitting parameters. By subtracting the second and third terms and an offset from $t_{\text{th.}}$, time slewing is corrected in Figure 5.11(b).

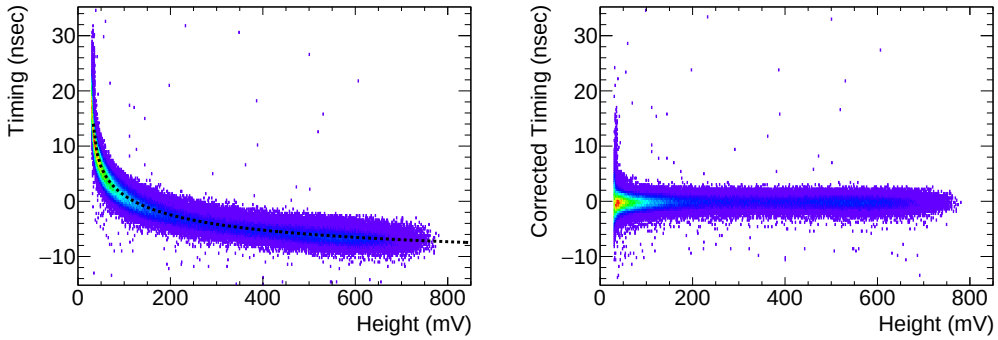

(a) Uncorrected **(b)** Corrected

Figure 5.11: Time-slewing correction for ECAL waveforms. The horizontal and vertical axes correspond to $h_{\max}$ and $t_{\text{th.}}$ in text, respectively. The correlation caused by time slewing in (a) is fitted by (5.1), and it is corrected in (b).

Time-slewing correction is applied to both the ECAL and the BDC-PMT; however, it cannot be applied to the straw tracker because $t_{\text{th.}}$ shifts owing to the drift time in the straw tube that is greater than the time slewing.

5.3.2 Time-Origin Reconstruction

T_0 is a charge-weighted average of $t_{\text{th.}}$ among all PMT channels. Figure 5.12 shows the charge distributions in all straw tracker datasets. Channels 1 and 2 (3 and 4) belong to the upstream (downstream) BDC. Only Channel 4 is different because of its low gain, as mentioned in Section 5.1. The $q_{\text{int.}}$ of each channel is normalized to its MPV.

The time difference between two channels yields σ_t^{PMT}, which is the average time resolution per single PMT channel. Figure 5.13 shows the distribution between the two channels of the upstream BDC. σ_t^{PMT} is calculated from its FWHM (full width at half maximum) as

$$\sqrt{2}\sigma_t^{\text{PMT}} = \frac{\text{FWHM}}{2\sqrt{2\ln 2}} = \frac{\text{FWHM}}{2.35}. \tag{5.2}$$

where 2.35 is the conversion factor for Gaussian σ (deviation). Because of Channel 4, the σ_t^{PMT} of the upstream and downstream BDCs, i.e., σ_t^{UsPMT} and σ_t^{DsPMT}, become different. Figure 5.14 shows them as a function of Q_{PMT}. The error bar convolutes all statistical uncertainties from the number of events.

The data points are fitted by

$$\sigma_t^{\text{PMT}}(Q_{\text{PMT}}) = \frac{p_{\text{stat.}}}{\sqrt{Q_{\text{PMT}} - p_{\text{offset}}}} \oplus p_{\text{const.}}, \tag{5.3}$$

where $a \oplus b = \sqrt{a^2 + b^2}$, and $p_{\text{stat.}}$, p_{offset}, and $p_{\text{const.}}$ represent the fitting parameters whose values are displayed in the figure. Finally, σ_t^0 at $Q_{\text{PMT}} = 1$ is obtained for each dataset as

$$\sigma_t^0 = \begin{cases} \frac{1}{4}\sqrt{2\left(\sigma_t^{\text{UsPMT}}\right)^2 + 2\left(\sigma_t^{\text{DsPMT}}\right)^2} & = 0.481 \pm 0.004 \text{ nsec} \quad \text{(the straw-tracker datasets)} \\ \frac{1}{\sqrt{2}}\sigma_t^{\text{UsPMT}} & = 0.590 \pm 0.007 \text{ nsec} \quad \text{(the ECAL datasets)} \end{cases}. \tag{5.4}$$

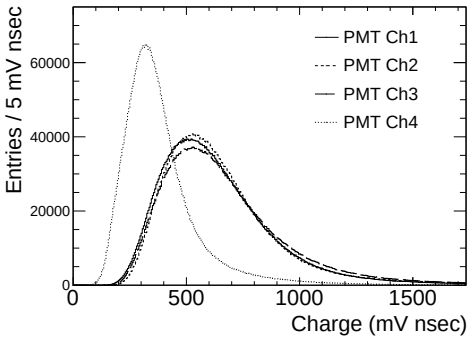

Figure 5.12: Charge distributions of all BDC-PMT channels. The gain of Channel 4 was lower because of a weak optical connection.

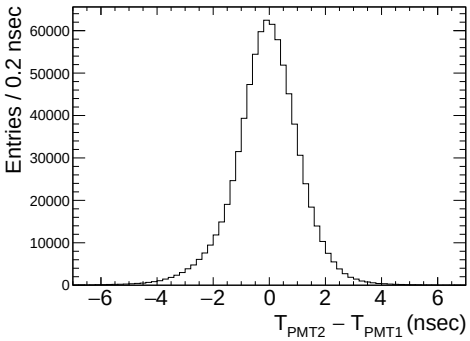

Figure 5.13: Time-difference distribution between the two channels of the upstream BDC. The width convolutes the time resolution of both channels.

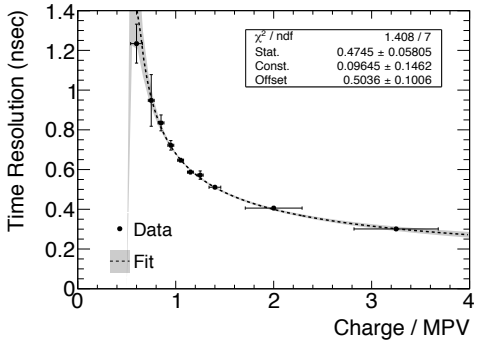

(a) Upstream channels

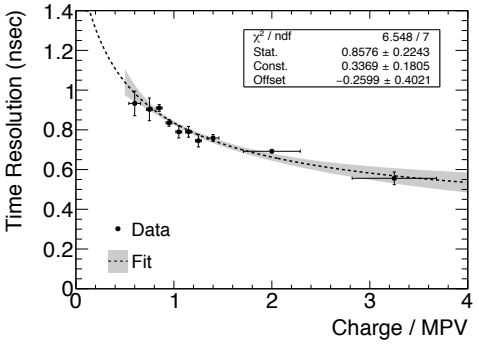

(b) Downstream channels

Figure 5.14: Time resolutions of the PMT channels for (a) upstream and (b) downstream BDCs as a function of the signal charge normalized to MPV. The points are fit using a function, and the grey regions represent its uncertainty.

5.3.3 Track Reconstruction

5.3.3.1 BDC-Level Track Reconstruction

The combination of MPPC hits in both the upstream and downstream BDCs yields an electron track. This track becomes the seed information for global-level track reconstruction.

Figure 5.15 shows the signal amplitude distribution of an MPPC channel, read using EASIROC. The separated peaks represents the number of photons that hit the MPPC simultaneously. Therefore, the horizontal axis is normalized to the width between the peaks. The left-side tail is attributed to heat noise, while the middle peak indicates the MPV of the energy deposit in a fiber of about 0.2 MeV. For individual channels, the number of detected photons is normalized to the MPV, and a different threshold is set considering the noise width. If there are hits above the threshold on both axes, then the hit position on each axis is reconstructed by averaging the fiber positions by the signal strength around the fiber with the most significant hit.

Figure 5.16 shows the reconstructed hit-position map on each BDC plane `ar50et50.2050v`. Both BDCs have some dead channels wherein the optical coupling between the fiber and MPPC

appears to be worse than that in the others. This is why there are some hollow lines that are relatively inefficient against the incoming beam electrons. The mean position and standard deviation [3] are $(\bar{x}, \bar{y}) = (0.4, -3.4)$ mm and $(\sigma_x, \sigma_y) = (8.6, 6.8)$ mm in the upstream BDC, respectively, and $(-4.6, -4.5)$ mm and $(10.7, 9.9)$ mm in the downstream BDC, respectively. The beam spreads slightly when flying along the beamline.

The track is reconstructed by connecting both hit positions in the upstream and downstream BDCs with a straight line. Figure 5.17 shows the angular distribution of the reconstructed tracks to the beam axis on each axis. The fluctuations are only a few degrees in all straw tracker datasets.

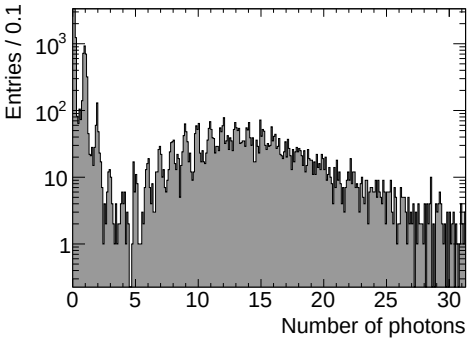

Figure 5.15: Signal-strength distribution of an MPPC normalized by the signal gain per photon. Separated peaks are attributed to the photon-counting ability.

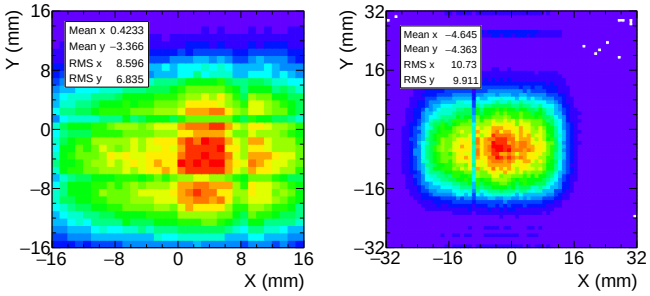

(a) Upstream BDC **(b)** Downstream BDC

Figure 5.16: Hit-position map on the upstream and downstream BDCs in `ar50et50.2050v`. Some hollow lines are caused by dead channels.

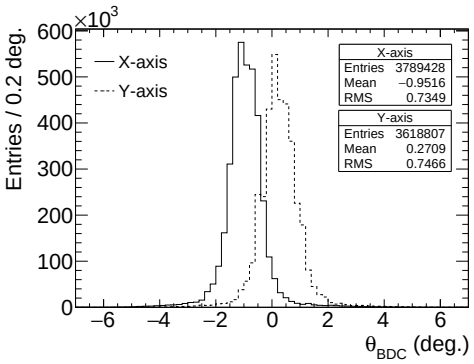

Figure 5.17: Angular distributions of reconstructed tracks on each axis in all straw tracker datasets. The mean and standard deviations are displayed in the figure.

5.3.3.2 Garfield++ Simulation

We need to know the correlation curve between the drift time and distance, which is called the X-T curve, that is $t = f_{\mathrm{XT}}(x)$, to extract a drift distance from every straw tube hit. Its shape varies by different gas mixtures, HV, and the straw tube shape. Although it is necessary to produce the gain experimentally, the initial assumption needs to be provided by the simulation; to this end, we used the Garfield++ toolkit [85]. The Garfield++ toolkit can simulate all processes in gaseous detectors[4] [85]:

[3] Not the RMS (root mean square) values shown in the figure.

[4] In particular, the Garfield++ can deal with semiconductor detectors.

Generation of seed electron–ion pairs along a passage of a charged particle, drifting of the pairs in an electromagnetic field, and electron avalanche using a high gradient electric force.

We employed the following preparation process to simulate the gaseous processes in the straw tube. The straw tube geometry is modeled in a mesh network with Gmsh [86]. Elmer [87] calculates the electric field between the straw tube and the wire for each HV. Magboltz [88] solves the Boltzmann equation for each combination of the field and gas mixture.

The simulation ran a 105 MeV electron track passing through the straw tube. The DCA (distance of closest approach) from the track to the central wire is denoted by X, which corresponds to the drift distance. The drift time T is evaluated from the time required for the drifted seed electrons to arrive at the wire first. Repeating this single process provides the average relationship between X and T, i.e., the X-T curve.

Figure 5.18 shows the obtained X-T curves for both gas mixtures and the used HV. The Ar:CO_2 mixture shows a clear difference with a 100 V gap, while Ar:C_2H_6 has an identical linear response.

Both the X-T curves and other intrinsic parameters were also obtained for decomposing the spatial resolution. We revise it in Section 5.4.2.

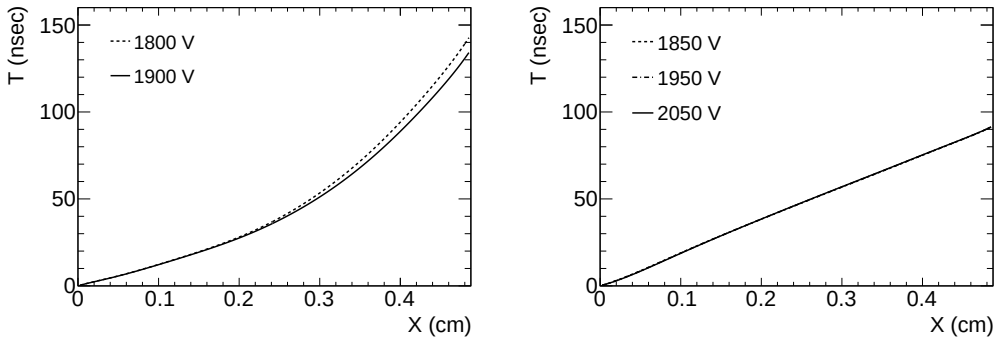

(a) Ar:CO_2 (70:30) **(b)** Ar:C_2H_6 (50:50)

Figure 5.18: Simulated X-T relationship curves for the Ar:CO_2 (70:30) and Ar:C_2H_6 (50:50) gas mixtures with all applied HV. The horizontal and vertical axes represent the drift distance and time, respectively.

5.3.3.3 Hit Finding

Before reconstructing a track from the straw tracker hits, we need to find hits from each layer. First, a straw tube hit is defined as the pulse that has a $q_{\text{int.}}$ larger than the threshold. When no pulse exists in the waveform, the fluctuation width of $q_{\text{int.}}$ is $\sigma_{\text{noise}} = 43.6 \pm 0.6$ mV nsec on average among all channels. Second, the hit-detection efficiency ϵ_{hit} and the single-hit ratio R_{single} are defined as

$$\epsilon_{\text{hit}}(q_{\text{th.}}) = \frac{N_{\text{detect}}(q_{\text{th.}})}{N_{\text{pass}}}, \tag{5.5}$$

$$R_{\text{single}}(q_{\text{th.}}) = \frac{N_{\text{single}}(q_{\text{th.}})}{N_{\text{detect}}(q_{\text{th.}})}, \tag{5.6}$$

where q_{th} represents the threshold for $q_{\text{int.}}$, and N_{pass}, N_{detect}, and N_{single} denote the numbers of events that satisfy

N_{pass}: A track must be reconstructed from the BDC hits in advance. This suggests a straw tubes in each layer that presumably has a hit. Then, it is checked if the two outer-layer straw tubes have $q_{\text{int.}}$ and $t_{\text{th.}}$ of $q_{\text{int.}} > 2\sigma_{\text{noise}}$ and $\Delta t_{1\text{ mm}} < t_{\text{th.}} - T_0 < \Delta t_{4\text{ mm}}$, where $\Delta t_{1\text{ mm}} = f_{\text{XT}}(x = 1\text{ mm})$ and $\Delta t_{4\text{ mm}} = f_{\text{XT}}(x = 4\text{ mm})$. This implies the track penetrates the middle-layer straw tube and it has an induced charge.

N_{hit}: In addition, the $q_{\text{int.}}$ of the middle-layer straw tube exceeds q_{th}.

N_{single}: Further, the other middle-layer straw tubes do not contain the $q_{\text{int.}}$ of $> q_{\text{th}}$.

Figure 5.19 shows ϵ_{hit} as a function of q_{th} in σ_{noise} for `ar70co30.eff1950v` and `ar50et50.eff1950v`. At lower q_{th}, the ϵ_{hit} is 100%, while the R_{single} is low.

Figure 5.20 shows the minimum q_{th} in the σ_{noise} to realize $R_{\text{single}} > 0.99$ as a function of the applied HV evaluated from all `ar70co30.eff` and `ar50et50.eff` datasets. These minimum q_{th} are used to recognize hits in the following analysis.

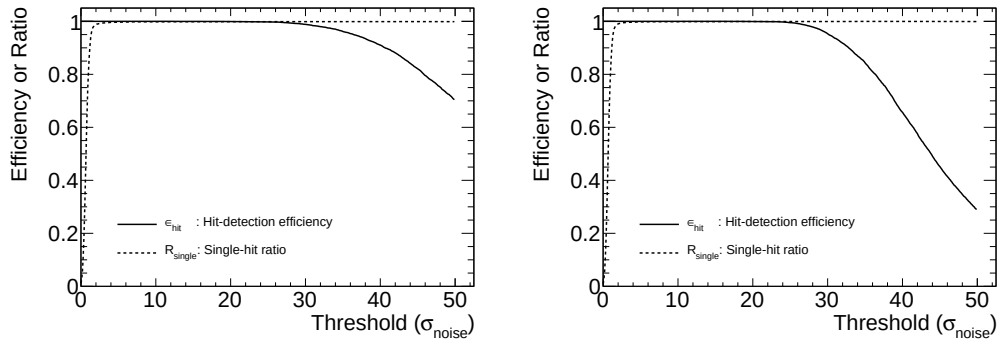

(a) `ar70co30.eff1950v` **(b)** `ar50et50.eff1950v`

Figure 5.19: ϵ_{hit} and R_{single} as a function of q_{th} for `ar70co30.eff1950v` and `ar50et50.eff1950v`. q_{th} is expressed in the unit of the nominal noise width σ_{noise}. ϵ_{hit} and R_{single} decrease and increase, respectively, as q_{th} increases.

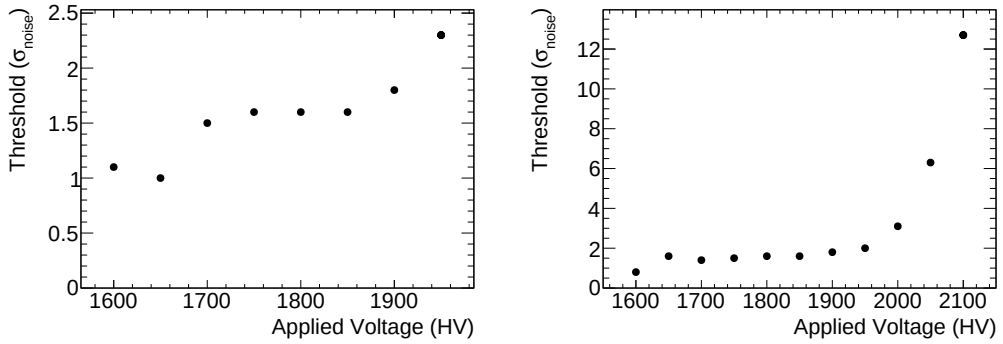

(a) `ar70co30.eff` datasets **(b)** `ar50et50.eff` datasets

Figure 5.20: Minimum thresholds to realize the single-hit ratio of 99% as a function of the applied HV. The threshold is expressed in the unit of the nominal noise width, σ_{noise}. The threshold needs to be increased because the noise is enhanced by a higher HV.

5.3.3.4 Track Finding

Track finding is employed to collect the most significant hit exceeding the charge threshold from each layer for identifying the most likely track path. It also aims to resolve the "left–right ambiguity," which is the side of the wire the electrons have passed through that cannot be reconstructed from a single straw hit. For each axis, both the geometrical hit pattern and the track reconstructed from the BDC hits are considered, and a presumable trajectory is obtained. Next, the left–right ambiguity is resolved, for example, as shown in Figure 5.21. Because the electrons enter straw tubes almost in parallel to the beam axis, there are not many presumable hit patterns and they are categorized into vertical and diagonal patterns. In `ar50et50.2050v`, the vertical hit pattern occupies more than 98% of the events on both axes.

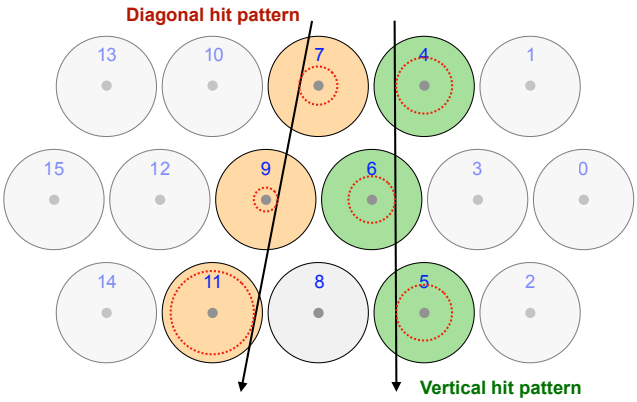

Figure 5.21: Examples of tracks passing through the three layers. The red circles represent the drift circles of the hits. The geometrical hit patterns are classified into vertical and diagonal patterns. The left–right ambiguity can be resolved in most cases based on the illustrated pattern.

5.3.3.5 Drift-Distance Reconstruction

Reconstructing the drift distance starts with drift-time reconstruction. The drift time is given by

$$\Delta t_{\text{drift}} = t_{\text{th.}} + t_{\text{offset}} - T_0, \tag{5.7}$$

where t_{offset} denotes an offset value that arises from experimental conditions such as a delay caused by the cable, and it is tuned for each channel as discussed in Section 5.3.3.7. Next, the Δt_{drift} is converted into the drift distance or DCA r with the X-T curve[5], as $r = f_{\text{XT}}^{-1}(\Delta t_{\text{drift}})$.

5.3.3.6 Track Fitting

In this step, we fit a straight line to the reconstructed drift circles and BDC hit positions. Given a Y-axis wire located at $(z,\ x) = (z_{\text{str.}},\ x_{\text{str.}})$, its DCA to the line, i.e., $x = f_{\text{trk.}}(z) = az + b$ where a and b are the fitting parameters, is given as

$$r_{\text{DCA}}\left(z_{\text{str.}}, x_{\text{str.}}\right) = \frac{az_{\text{str.}} + b - x_{\text{str.}}}{\sqrt{a^2 + 1}}, \tag{5.8}$$

[5]The drift distance is denoted by "r" in this thesis to distinguish it from the X-axis

where $r_{\mathrm{DCA}} < 0\ (> 0)$ indicates the line runs on the left (right) side of the wire. When the reconstructed drift distance from the wire is r_{drift}, its residual from r_{DCA} below is minimized by fitting.

$$\Delta r = r_{\mathrm{drift}} - \left| r_{\mathrm{DCA}} \right| . \tag{5.9}$$

The χ^2 to be minimized is defined as

$$\chi^2 = \sum_{i=1}^{N_{\mathrm{str.}}} \left\{ \frac{\Delta r^i}{\sigma_r^{\mathrm{str.}}(r^i_{\mathrm{DCA}})} \right\}^2 + \sum_{i=1}^{N_{\mathrm{BDC}}} \left\{ \frac{x^i_{\mathrm{BDC}} - f_{\mathrm{trk.}}(z^i_{\mathrm{BDC}})}{\sigma_x^{\mathrm{BDC}}} \right\}^2 , \tag{5.10}$$

where $N_{\mathrm{str.}}$ and N_{BDC} are the number of straw tube and BDC hits, and x_{BDC} is the hit position in the BDC located at z_{BDC}. $\sigma_r^{\mathrm{str.}}$ denotes the spatial resolution as a function of r_{drift}, and σ_x^{BDC} denotes the BDC position resolution.

In the spatial resolution study, the second term related to the BDC hits is not used to interpret the result with a simple model involving only the straw tubes. The ECAL analysis includes all hits to extrapolate the fitted track onto the ECAL surface with less uncertainty.

5.3.3.7 Spatial-Resolution Evaluation

The outer-layer straw tubes join the track fitting to evaluate the straw spatial resolution, and Δr of the remaining straw tube in the middle layer is evaluated. For example, for Channel 25 in `ar70co30.1900v` and `ar50et50.2050v`, Figures 5.22 shows the scatter plots between Δr and r_{DCA}, and the Δr distributions fitted by a Gaussian function. There are seldom data points around the wire and edge because of a finite gap between the straw tubes and the nearly vertical beam trajectories. From Gaussian fitting, an overall spatial resolution of 200 μm and 140 μm is obtained for each dataset. The spatial resolution as a function of r_{DCA} is obtained by fitting slices of the plots at each r_{DCA}, and it is shown in Section 5.3.3.9. However, these data still involve other components besides the intrinsic spatial resolution of a straw tube, which will be separated in Section 5.4.2.

The mean of the residual distribution needs to be zero, as shown in the figures; however, it deviates when t_{offset} in (5.7) is not appropriate. Thus, it was adjusted for individual channels.

5.3.3.8 X-T-Curve Update

The X-T curve is reconstructed along with the spatial resolution. Figure 5.23 shows the scatter plots between $\Delta t_{\mathrm{drift}}$ and r_{DCA} for Channel 25 in `ar70co30.1900v` and `ar50et50.2050v` and when fitting them with polynomial functions. In the scatter plots, there is a lack around zero because of the geometrical reason explained above. To perform polynomial fitting, the scatter plots are folded at $r_{\mathrm{DCA}} = 0$ and sliced to calculate the mean and fluctuation at several points on r_{DCA}. The fitted polynomial functions shown in the figure are defined as

$$f_{\mathrm{XT}}(x) = \sum_{n=1}^{N_{\mathrm{par}}} p_{\mathrm{i}-1} \left| x \right|^n , \tag{5.11}$$

where $N_{\mathrm{par}} = 7$ and 5 for the Ar:CO_2 and Ar:C_2H_6 datasets, respectively.

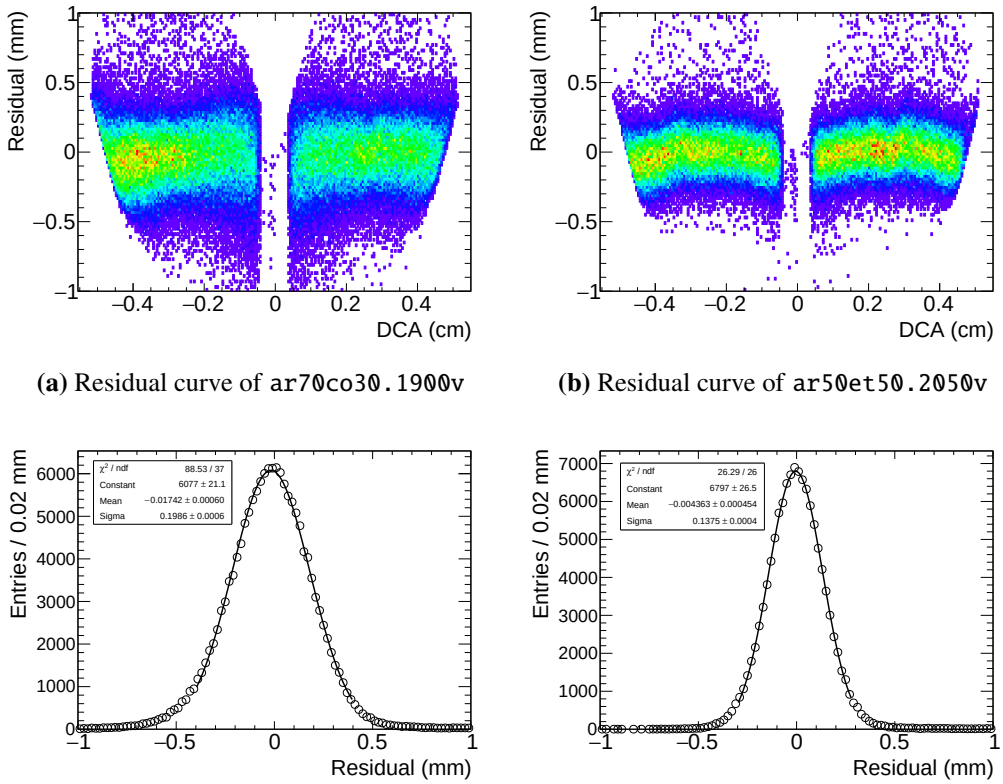

(a) Residual curve of `ar70co30.1900v`

(b) Residual curve of `ar50et50.2050v`

(c) Overall residual of `ar70co30.1900v`

(d) Overall residual of `ar50et50.2050v`

Figure 5.22: Distributions of the residual from the fitted track of Channel 25 in `ar50et50.2050v` and `ar70co30.1900v`. (a, b) Scatter plots between Δr and r_{DCA}. (c, d) Projections on the residual axis fitted by a Gaussian function.

5.3.3.9 Iterative Analysis

We repeat the procedure explained above a few times because we relied on some assumptions at the initial iteration. For example, we used the simulated X-T curves in Section 5.3.3.5 and a constant value as the spatial resolution $\sigma_r^{\mathrm{str.}}(r_{\mathrm{DCA}})$ in Section 5.3.3.5. At the end of the first iteration, we eventually have a realistic X-T curve and a spatial resolution from the data, and we can input them into the second and subsequent iterations.

The obtained results should converge to stop the iterative analysis. However, our trials did not converge as expected. Figure 5.24 shows how the reconstructed X-T and spatial-resolution curves of Channel 25 in `ar70co30.1900v` and `ar50et50.2050v` change during the five iterations. Although the X-T curves do not appear to change considerably in the form of the drift-velocity curves of the drifted electrons as calculated by $\left(\frac{\mathrm{d}f_{\mathrm{XT}}}{\mathrm{d}x}\right)^{-1}$, they obviously deviate from the initial simulated shape and do not seem to be able to converge. The spatial resolutions also change slightly with a small bias. The deviation can be attributed to the lack of data points near the straw tube wire and wall. In conclusion, we decided to stop the analysis at the fifth turn to consider all obtained fluctuations in the spatial resolution as a systematic uncertainty.

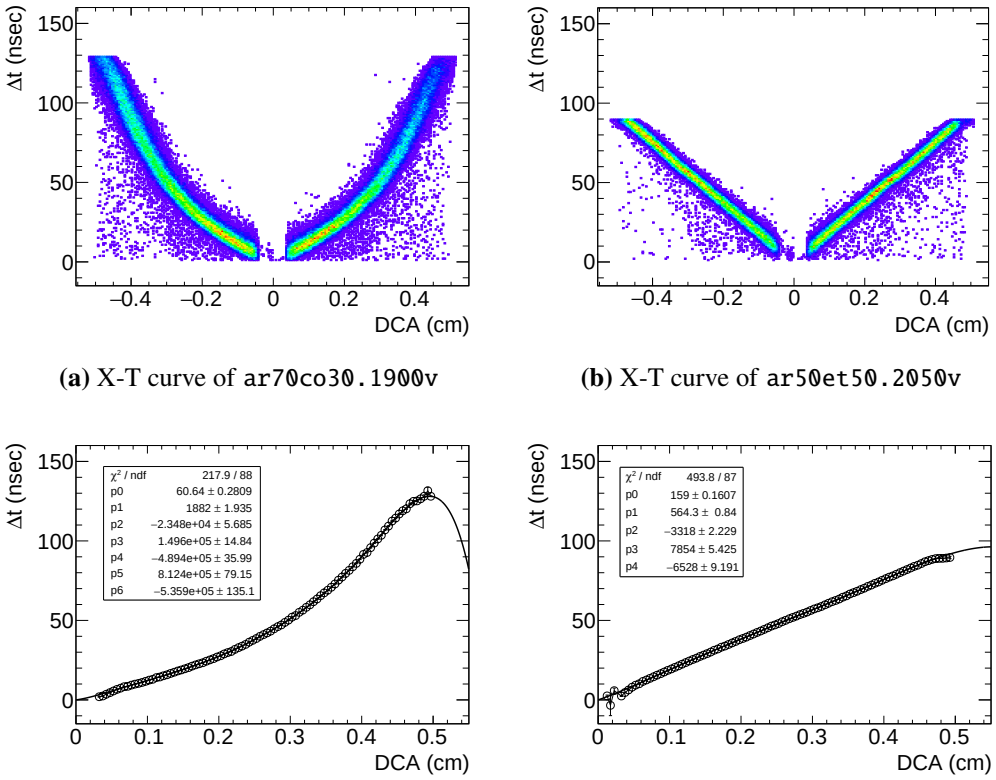

(a) X-T curve of `ar70co30.1900v`

(b) X-T curve of `ar50et50.2050v`

(c) Fitted profile of `ar70co30.1900v`

(d) Fitted profile of `ar50et50.2050v`

Figure 5.23: Reconstructed X-T curves of Channel 25 in `ar70co30.1900v` and `ar50et50.2050v`. (a, b) Scatter plots between $\Delta t_{\mathrm{drift}}$ and r_{DCA}. (c, d) Profiles calculated from (a, c) folded at $r_{\mathrm{DCA}} = 0$. Polynomial functions fit them.

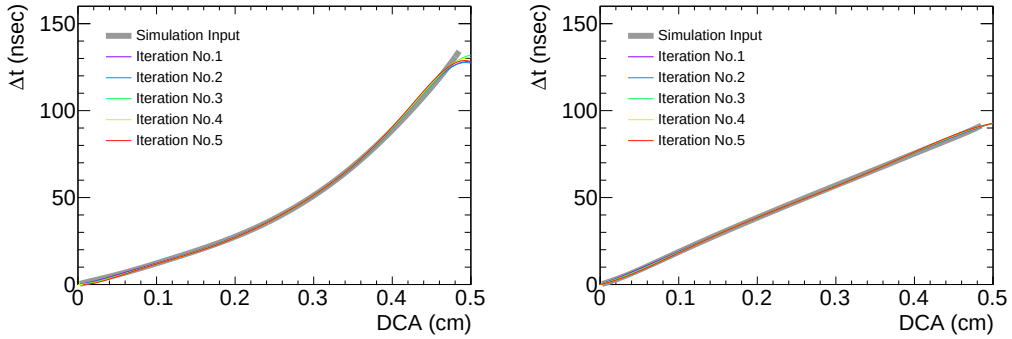

(a) X-T curve of `ar70co30.1900v`

(b) X-T curve of `ar50et50.2050v`

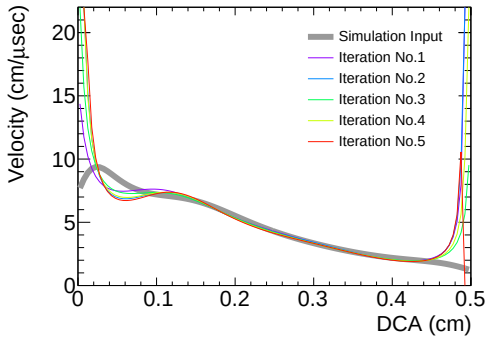

(c) Drift velocity of `ar70co30.1900v`

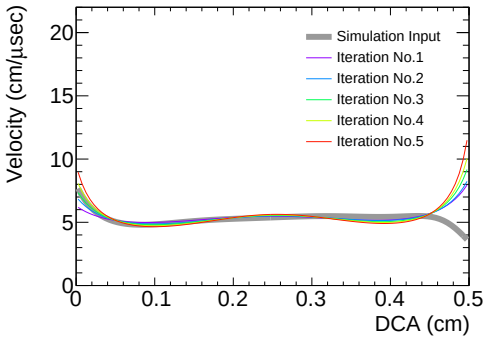

(d) Drift velocity of `ar50et50.2050v`

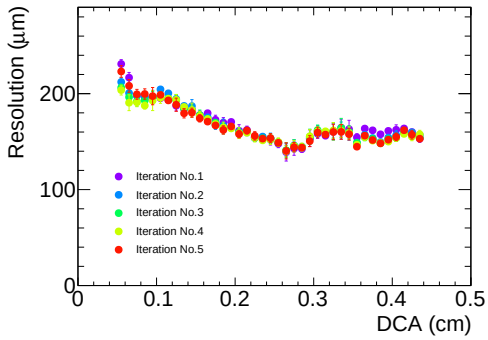

(e) Spatial resolution of `ar50et50.2050v`

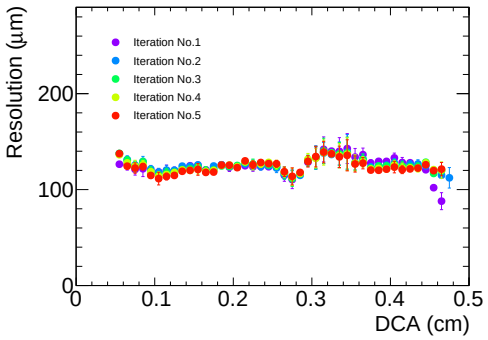

(f) Spatial resolution of `ar50et50.2050v`

Figure 5.24: Change in the reconstructed (a, b) X-T, (c, d) drift-velocity, and (e, f) spatial-resolution curves of Channel 25 in `ar70co30.1900v` and `ar50et50.2050v` during five iterations. The color of the lines and points indicates the number of iterations. The X-T curves do not change drastically during the iteration; however, the drift-velocity and spatial-resolution curves do not converge.

5.3.4 Cluster Reconstruction

The algorithm to reconstruct energy clusters from the ECAL hits starts with two energy calibrations: the channel-level energy calibration applied to individual crystals with the cosmic ray measurement and global-level energy calibration applied to the total energy deposit. The energy clustering collects the calibrated energies, expels noises effectively, and reconstructs the total energy deposit and incident position and timing. Finally, the resolutions are evaluated from the distributions.

For the reconstruction and analysis, we produced several bunches of simulation data with the `Geant4` toolkit [68] that is described below.

5.3.4.1 Geant4 Simulation

`Geant4` simulates all physical processes such as interactions between particles and matters and particle decays. We utilize the simulated energy deposit in the ECAL using cosmic muons and beam electrons to understand the experimental data and analytical effects thoroughly.

Figure 5.25 shows the geometry constructed in the simulation frame. We place all instruments that should interact with the beam, i.e., the BDCs, straw tracker, ECAL, and their chambers, together. The cosmic ray counters are installed above and below the ECAL for the energy calibration. Figure 5.25(b) displays an event starting from an electron. The electron penetrates the equipment and generates an electromagnetic shower that spreads and deposits its energy over the crystals.

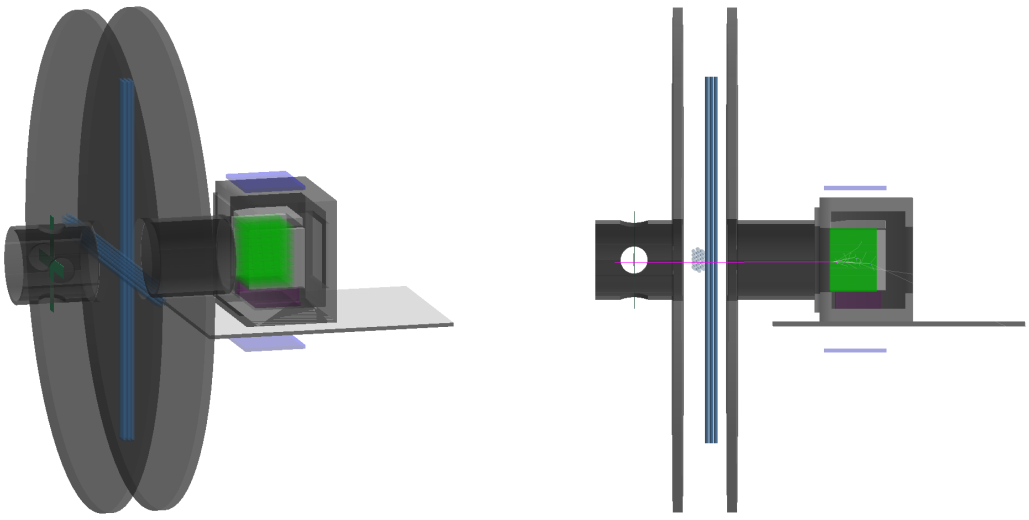

(a) Bird's-eye view **(b)** Side view with an electron beam

Figure 5.25: Geometry in the simulation frame based on `Geant4`. (a) From the left side: the upstream BDC, straw tracker, downstream BDC, and ECAL, including their chambers. The cosmic-ray counters are located above and below the ECAL chamber. (b) An electron beam (purple line) is injected from upstream. It changes into an electromagnetic shower in the ECAL; the disappearing blue and white lines indicate positrons and gamma rays.

We adopted track parameters reconstructed from the `mscan` datasets for the initial state of the simulated beam electrons. Figure 5.26 compares those realistic data-driven tracks and ideal pencil tracks in terms of the total energy deposit in the ECAL by 105 MeV electrons. Owing to the limited size of the ECAL on the beam direction, oblique injections can deposit more energy. Therefore, the distribution for the pencil beam shows a slightly larger leakage.

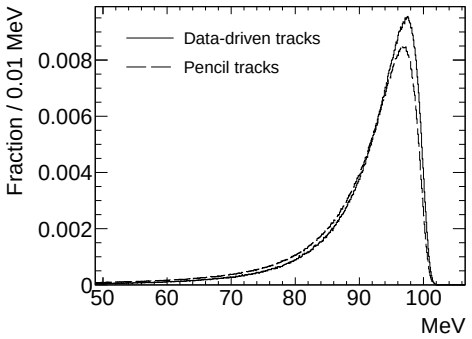

Figure 5.26: Distributions of simulated total energy deposits by the data-driven and ideal pencil tracks of 105 MeV/c electrons. The latter case has more shower leakage than that of the former case.

5.3.4.2 Energy Calibration

Since the gains of the crystal modules are different from each other, the pulse strength observed in Channel i, $h^i_{\max}$, must be converted into energy e^i by

$$e^i = c^i_{\text{ch.}}\, h^i_{\max}, \tag{5.12}$$

where $c^i_{\text{ch.}}$ represents the channel energy-calibration factor. We compared the energy deposit by cosmic rays between the data and the simulation to calculate $c^i_{\text{ch.}}$. Figure 5.27 shows the distributions of $h_{\max}$ from the `cosmic` dataset and the simulated e^i in Channel 24. The component on the low energy side refers to particles passing through the edge of the crystal. By fitting a Landau function convoluting a Gaussian function, their MPVs are obtained as w^i_{MPV} and e^i_{MPV}. $c^i_{\text{ch.}}$ is then given as

$$c^i_{\text{ch.}} = \frac{e^i_{\text{MPV}}}{w^i_{\text{MPV}}}. \tag{5.13}$$

Different from the statistic uncertainty provided by the fitting, we estimated systematic uncertainties that come from the fitting and geometrical errors of the cosmic ray counters. For the first item, we varied the bin width of the $h_{\max}$ histogram and shifted the fitting range to evaluate the fluctuation in the fitted MPV. The second term is associated only with the simulation case. Since the cosmic ray counters were not firmly fixed and did not have sufficient geometrical acceptance to detect all cosmic rays penetrating the ECAL, their alignment could have some unknown errors that lead to an uncertainty of e_{MPV} The position of the cosmic-ray counters was shifted by ±2 cm and ±1 cm in the horizontal and vertical directions in the simulation to check the effect. However, this term was considerably smaller than the first item. As the result, the mean values of the fitted MPVs among all channels are $w_{\text{MPV}} = 80.7 \pm 0.5\,(\text{stat}) \pm 0.4\,(\text{syst})$ mV and $e_{\text{MPV}} = 18.78 \pm 0.04\,(\text{stat}) \pm 0.26\,(\text{syst})$ MeV, and the resulting $c_{\text{ch.}}$ has a total uncertainty of 1.7% on average.

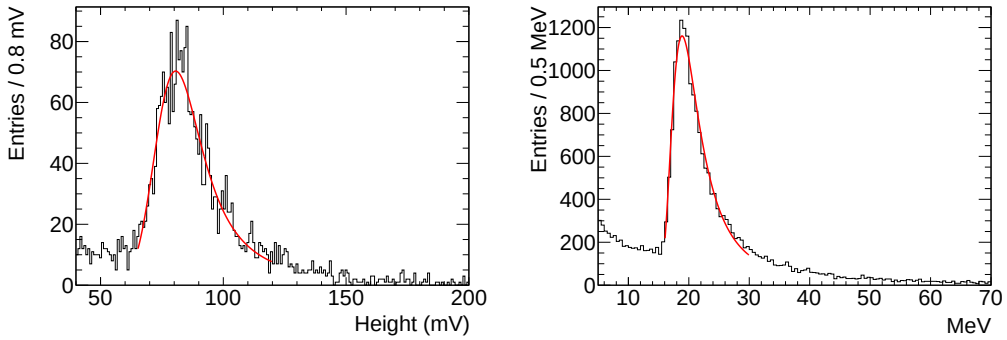

(a) Data **(b)** Simulation

Figure 5.27: Energy-deposit distribution in Channel 24 by cosmic rays in the case of (a) `mscan` and (b) simulation. The horizontal axes represent the reconstructed wave height and the simulated energy deposit. A Landau function convoluting a Gaussian function (red line) is fitted to obtain their MPVs.

After channel-level energy calibration, the global-level energy calibration occurs because of

$$E_{\mathrm{ECAL}} = C_{\mathrm{glob.}} \sum_{i}^{N_{\mathrm{clst.}}} e^{i} = C_{\mathrm{glob.}} \sum_{i}^{N_{\mathrm{clst.}}} c^{i}_{\mathrm{ch.}} h^{i}_{\mathrm{max}}, \tag{5.14}$$

where E_{ECAL} represents the total energy deposit in the ECAL, $C_{\mathrm{glob.}}$ denotes the global energy-calibration factor, and $N_{\mathrm{clst.}}$ represents the number of channels that belong to the clustering. We adjust $C_{\mathrm{glob.}}$ in Section 5.3.4.6 so that the reconstructed energy distribution is consistent with the simulated distribution. $C_{\mathrm{glob.}}$ is used to compensate the following aspects. First, the MPV of the cosmic energy distribution shifts because of a finite energy resolution and creates a bias in the calibration factor. Second, even the MPV evaluated from the simulation can differ from the real values because of our limited knowledge of the materials. Third, the clustering process applies a noise cut on channels with a little energy deposit, and it also changes the energy scale.

5.3.4.3 Energy Clustering

This process combines all calibrated energies to reconstruct the total energy deposit and incident position and timing.

First, similar to Section 5.3.3.3, we evaluated the fluctuation of h_{max} of each channel from the data where no signal pulse appeared. The result shows $\sigma_{\mathrm{noise}} = 0.60 \pm 0.07$ mV among all channels, and it corresponds to 0.14 ± 0.02 MeV. For the experimental data, channels with $h_{\mathrm{max}} < f_{\mathrm{noise}}\sigma_{\mathrm{noise}}$ are cut, wherein f_{noise} is the noise cut factor identical for all channels. For the simulation data, those with $e < C_{\mathrm{glob.}} c_{\mathrm{ch.}} f_{\mathrm{noise}}\sigma_{\mathrm{noise}}$ are cut.

Second, all channels that have passed the noise cut are simply summed by (5.14). The incident position and timing, $\boldsymbol{R}_{\mathrm{ECAL}}$ and T_{ECAL}, are reconstructed by

$$\boldsymbol{R}_{\mathrm{ECAL}} = \frac{\sum_{i}^{N_{\mathrm{clst.}}} e^{i}\boldsymbol{r}^{i}}{\sum_{i}^{N_{\mathrm{clst.}}} e^{i}}, \tag{5.15}$$

$$T_{\mathrm{ECAL}} = \frac{\sum_{i}^{N_{\mathrm{clst.}}} e^{i}(t^{i}_{\mathrm{th.}} - t^{i}_{\mathrm{sync.}})}{\sum_{i}^{N_{\mathrm{clst.}}} e^{i}}, \tag{5.16}$$

where $\boldsymbol{r}^i$ is the crystal central position of Channel i on the ECAL surface. $t^i_{\text{sync.}}$ is $t_{\text{th.}}$ obtained from the trigger signal to the DRS4 chip to which Channel i belongs, and it is crucial for the timing synchronization among all channels, as explained in Section 3.3.

5.3.4.4 Hit-Region Based Event Separation

From a previous study [78], it is known that the performance varies based on the incident position on the crystal surface. Therefore, we separated the cross-section of every crystal into three regions—`center`, `border`, and `corner`—as illustrated in Figure 5.28. The further from the center the beam electrons hit, the more equally the resulting electromagnetic showers deposit their energy into several crystals. This makes the performance susceptible to subtle individual differences between crystals.

We distributed all events into each region based on the position extrapolated to the ECAL surface from tracks reconstructed from the BDC and straw tracker hits. Then, all events are again mixed with weights based on the following equation to estimate the average performance.

$$w_i = \frac{s_i/N_i}{\sum_j s_j/N_j}, \tag{5.17}$$

where i denotes the index for the hit regions, w_i and N_i denote the weight and number of events in each hit region, respectively, and s_i represents the area ratio, $s_{\texttt{center}} : s_{\texttt{border}} : s_{\texttt{corner}} = 1 : 2 : 1$. In the following, these events are recognized as the `mix`-region events, and the results are shown based on them unless otherwise specified.

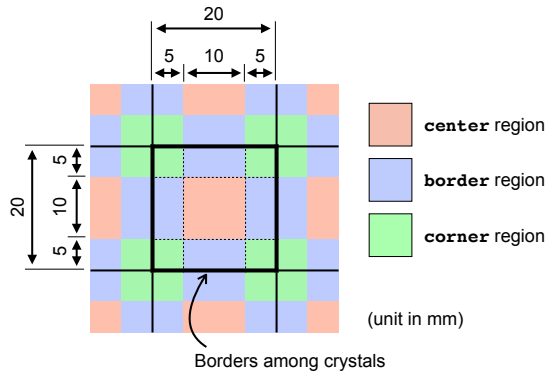

Figure 5.28: Definition of the hit regions on the ECAL surface. The black solid lines represent the borders between the crystals. The central red region of 10×10 mm^2 is `center`. The blue regions with an area of 5×10 mm^2 belong to `border`, and the remaining yellow regions with an area of 5×5 mm^2 belong to `corner`.

5.3.4.5 Energy-Resolution Evaluation

The approach to evaluate the energy resolution is slightly complicated compared to the other two resolutions because the total energy distribution shows an asymmetric shape as shown in Figure 5.26. Other experiments have each defined their own approach for similar cases, and we concluded to focus on the tail on the higher side. Although the lower-side tail is attributed to the shower leakage that is unavoidable when using any experimental technique unless we can use longer LYSO crystals, the higher-side tail is more optimal to investigate our measurement accuracy.

The energy resolution is defined as $\sigma_E^{\text{tot.}}/E_{\text{peak}}$, where E_{peak} is the energy at which the distribution has the peak. The width, $\sigma_E^{\text{tot.}}$, is calculated from the HWHM (half width at half maximum) of the higher-side tail by converting into the Gaussian standard deviation as

$$\sigma_E^{\text{tot.}} = \frac{\text{HWHM}}{\sqrt{2\ln 2}} = \frac{\text{HWHM}}{1.175}. \tag{5.18}$$

We fit the simulated spectrum F_{MC} to the experimental one $F_{\text{obs.}}$ to calculate the HWHM precisely, based on the following model.

$$\begin{aligned} F_{\text{obs.}}(E;\sigma_E^{\text{tot.}}) &= F_{\text{MC}}(E/A_{\text{scale}};\sigma_E^{\text{asym.}}) * N(E;\sigma_E^{\text{sym.}}) \\ &= \int \mathrm{d}E'\ F_{\text{MC}}(E'/A_{\text{scale}};\sigma_E^{\text{asym.}})\ \frac{1}{\sqrt{2\pi}\sigma_E^{\text{sym.}}} e^{-\frac{1}{2}\left(\frac{E-E'}{\sigma_E^{\text{sym.}}}\right)^2}, \end{aligned} \tag{5.19}$$

where A_{scale} represents a scaling parameter of F_{MC} that has to be 1.0 when the energy calibration is complete. $N(E,\sigma_E^{\text{asym.}})$ represents a Gaussian function with a width of $\sigma_E^{\text{sym.}}$ that denotes a symmetric part of $\sigma_E^{\text{tot.}}$. In contrast, $\sigma_E^{\text{asym.}}$ represents an asymmetric part that is evaluated from F_{MC} with (5.18). The noise cut changes the shape of F_{MC} and subsequently $\sigma_E^{\text{asym.}}$, as demonstrated in Figure 5.29. After the reconstruction procedure with the noise cut by $f_{\text{noise}} = 0, ..., 7$, the resulting energy spectra change their shapes, which are not similar to each other. For instance, F_{MC} cut by $f_{\text{noise}} = 0$ cannot fit that by $f_{\text{noise}} = 4$, where A_{scale} is fixed at 1.0. Therefore, $\sigma_E^{\text{sym.}}$ does not represent the noise-cut effect, and $\sigma_E^{\text{asym.}}$ should be selected appropriately because F_{MC} matches $F_{\text{obs.}}$ with a finite $\sigma_E^{\text{sym.}}$.

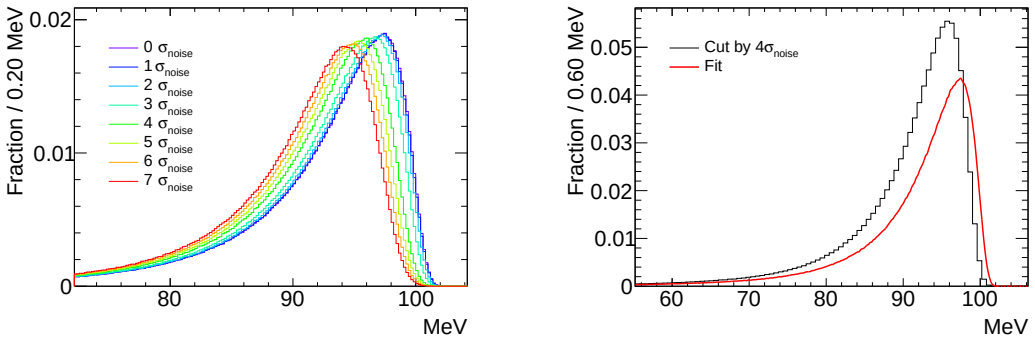

(a) Energy spectra with several noise-cut factors **(b)** Fit of the non-cut spectrum to the $4\sigma_{\text{noise}}$-cut one.

Figure 5.29: Effect of noise cut on energy spectra simulated with the 105 MeV/c electron. (a) As the noise-cut factor f_{noise} increases, the spectrum shape becomes broader, and its peak shifts to the lower side. (b) The spectrum cut by $f_{\text{noise}} = 1$ cannot fit that by $f_{\text{noise}} = 4$ with $A_{\text{scale}} = 1$, which indicates that the Gaussian convolution does not reproduce the noise-cut effect.

Figure 5.30 shows $\sigma_E^{\text{asym.}}/E_{\text{peak}}$ for each beam momentum as a function of f_{noise}. We evaluated uncertainties by varying the binning of the histograms. The noise cut degrades $\sigma_E^{\text{asym.}}$ as f_{noise} increases, and it is more potent for the lower momenta because the total eliminated energy occupies a higher fraction of the total energy.

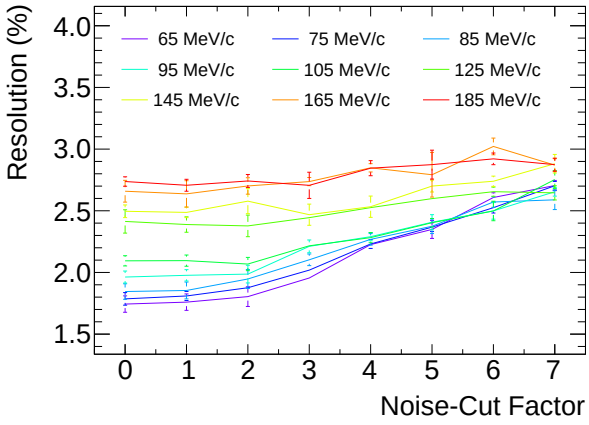

Figure 5.30: Asymmetric term of the energy resolution for each beam momentum as a function of the noise-cut factor, f_{noise}. As f_{noise} increases, the resolution deteriorates entirely.

5.3.4.6 Determination of the Global Calibration and Noise-Cut Factors

The value of $C_{\text{glob.}}$ is determined to realize $A_{\text{scale}} = 1$ in the spectrum fitting, and a reasonable f_{noise} is also selected.

First, we prepared a set of pairs of $F_{\text{obs.}}$ and F_{MC} reconstructed with the same $C_{\text{glob.}}$ and f_{noise}, and we fit F_{MC} to $F_{\text{obs.}}$ with A_{scale} as a free fitting parameter. Figure 5.31 shows the case of `mscan.105` created by $C_{\text{glob.}} = 0.85, 0.90, 0.95, 1.00, 1.05$ and $f_{\text{noise}} = 4.0$. The fitted A_{scale} are displayed in the legend and vary with $C_{\text{glob.}}$. It appears that a $C_{\text{glob.}}$ in between 0.90 and 0.95 would cause the fitted A_{scale} to be nearly 1.0. Figure 5.32 summarizes the fitted A_{scale} for several f_{noise} as a function of $C_{\text{glob.}}$. The error bars include the variation among all `mscan` datasets; however, they are not significant. Based on these correlations, $C_{\text{glob.}} = 0.93$ is adopted.

Next, f_{noise} should be fixed to maintain the performance based on $C_{\text{glob.}} = 0.93$. We checked the validity of the noise cut in terms of $N_{\text{clst.}}$. When using a low f_{noise}, both numbers cannot be consistent between the experimental and simulated data because tiny energy deposits with noises in the former contribute to the cluster. The difference becomes smaller with a high f_{noise}. Figure 5.33 compares the distributions of $N_{\text{clst.}}$ in `mscan.105` with the simulation for $f_{\text{noise}} = 2, 4, 7$. The distribution of the simulation is normalized to the area of each data.

The case using $f_{\text{noise}} = 2$ shows a large discrepancy; however, the others are well consistent. A too large f_{noise} essentially deteriorates the energy resolution, as shown by Figure 5.30. We calculated a total χ^2 residual between the data and the simulation for all `mscan` datasets; Figure 5.34 shows the results as a function of f_{noise}. It decreases rapidly until $f_{\text{noise}} = 4$ and then settles. In conclusion, we use $C_{\text{glob.}} = 0.93$ and $f_{\text{noise}} = 4$ as the basic reconstruction parameters.

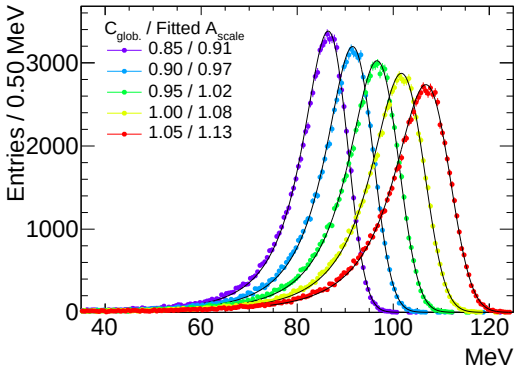

Figure 5.31: Energy spectra of `mscan.105` reconstructed using various global calibration factors $C_{\text{glob.}}$ from 0.85 to 1.05 with a fixed noise-cut factor $f_{\text{noise}} = 4.0$. The black lines represent the simulated spectrum reconstructed in the same manner, and it is fitted to each spectrum. The fitted scale parameter A_{scale} is shown in the legend for each $C_{\text{glob.}}$.

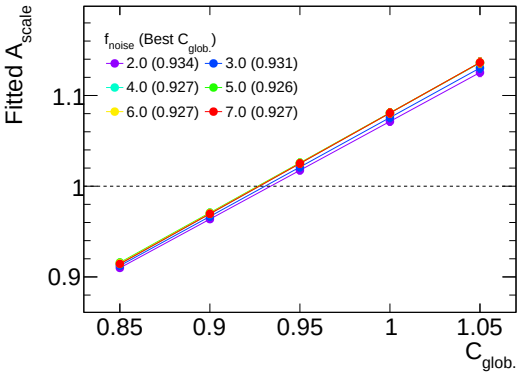

Figure 5.32: Correlation between the global calibration factor $C_{\text{glob.}}$ and the fitted scale parameter A_{scale} for several noise-cut factors f_{noise} in all `mscan` datasets. The variations of the fitted A_{scale} among all datasets contribute to the error bars. The desired $C_{\text{glob.}}$ to realize $A_{\text{scale}} = 1.0$ is shown in the legend for each f_{noise}.

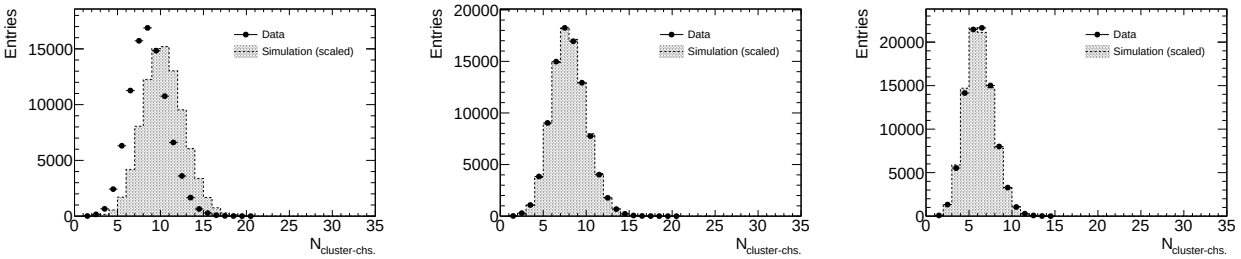

(a) $f_{\text{noise}} = 2.0$ **(b)** $f_{\text{noise}} = 4.0$ **(c)** $f_{\text{noise}} = 7.0$

Figure 5.33: Distributions of the number of hits after the noise cut in `mscan.105` and the simulation for several noise-cut factors, f_{noise}. The distribution of the simulation (filled) is normalized to the area of each data (markers). There is a large discrepancy with $f_{\text{noise}} = 2$; however, they become consistent with $f_{\text{noise}} \geq 4$.

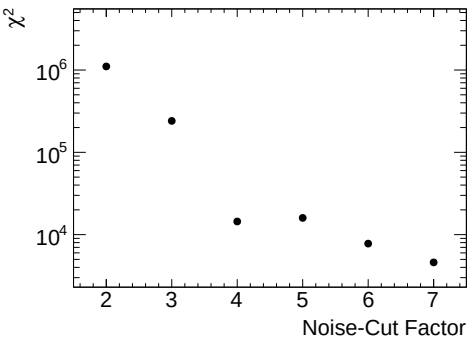

Figure 5.34: Total χ^2 residual between the distributions of the number of hits after the noise cut between all `mscan` datasets and the simulation as a function of the noise-cut factor. $f_{\text{noise}} \geq 4$ minimizes χ^2 sufficiently.

5.4 Performance of the Straw Tracker

5.4.1 Hit-Detection Efficiency

The hit-detection efficiency is the probability of distinguishing pulses from the baseline noise. As explained in Section 5.3.3.3, the thresholds for $q_{\text{int.}}$ are determined to perform 99% of the single-hit ratio, R_{single} (5.6). Figure 5.35 presents the results as a function of the applied HV. Both curves imply that an HV higher than 1800 V realizes an efficiency of 100%.

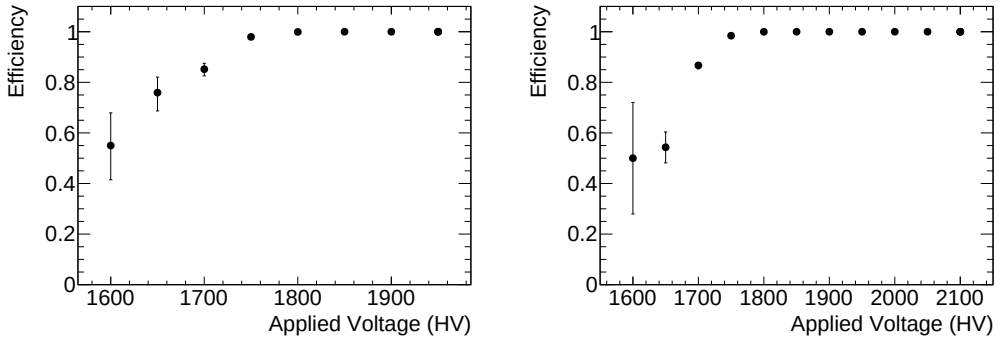

(a) Ar:CO_2 (70:30) **(b)** Ar:C_2H_6 (50:50)

Figure 5.35: Hit-detection efficiency as a function of the applied HV of the (a) Ar:CO_2 (70:30) and (b) Ar:C_2H_6 (50:50) gas mixtures. The uncertainties are calculated based on the Clopper–Pearson interval as a binomial-probability confidence interval. Both begin to reach 100% fully from 1800 V.

5.4.2 Spatial Resolution

A mathematical model is introduced to decompose spatial resolutions into several terms to understand the intrinsic resolution of a single straw tube.

Figure 5.36 shows the spatial resolutions of all datasets, where $w_{\text{th.}} = 1$ mV is used for reconstructing $t_{\text{th.}}$. The horizontal axes represent the DCA to the wire from the reconstructed tracks. The resolution diverged after the iterative reconstruction (see Section 5.3.3.9), and hence, its fluctuation until the fifth iteration was considered as part of the error. The kinks around 0.3 cm are attributed to the crosstalk in the waveforms, as explained in Section 5.3.1 and Appendix A.

The resolutions of Ar:CO_2 strongly depend on the DCA, and they do not satisfy the requirement of 200 μm at 1800 V. Those of Ar:C_2H_6 have a flat trend and meets the requirement. However, all these curves include external components and do not represent the resolution of a single straw tube.

5.4.2.1 Decomposition Model

The following analytical model is suggested to extract the pure spatial resolutions from observed data.

$$\sigma_{\text{obs.}}(r) = \sigma_{\text{single}}(r) \oplus \sigma_{\text{trk.}}(r), \tag{5.20}$$

where $\sigma_{\text{obs.}}$ and σ_{single} are the observed and wanted resolutions as a function of r and DCA, respectively, and $\sigma_{\text{trk.}}$ denotes the tracking uncertainty.

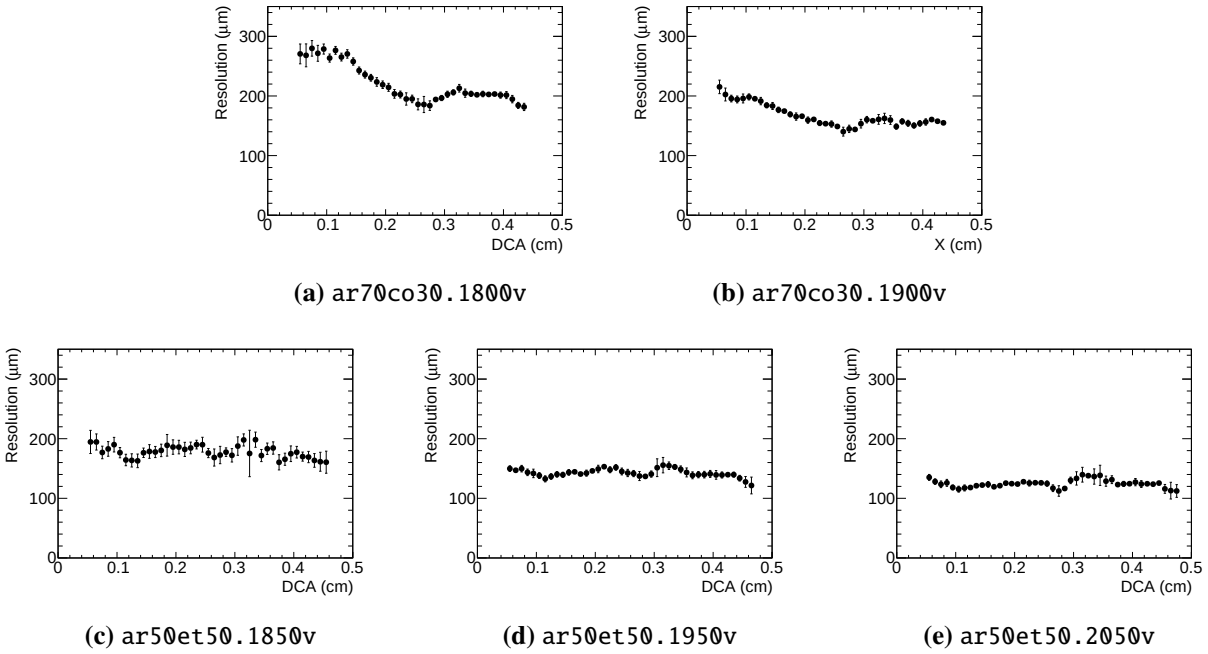

(a) ar70co30.1800v **(b)** ar70co30.1900v

(c) ar50et50.1850v **(d)** ar50et50.1950v **(e)** ar50et50.2050v

Figure 5.36: Observed spatial resolutions of the straw tubes of all datasets with a threshold of 1 mV. The horizontal axes are DCA from the reconstructed track to the wire. The errors contain the fluctuation during the five iterations of the reconstruction procedure.

Figure 5.37 illustrates the idea to calculate $\sigma_{\text{trk.}}$. This model assumes that all trajectories are parallel to the beamline, as observed from the data. Then, the examined straw tube on the middle layer has a hit with a DCA of r, and the others have an identical DCA of $d_{\text{straw}} - r$, where $d_{\text{straw}} = 5.15$ mm is the distance along the straw-alignment direction between the straw tubes on the middle and outer layers. The resolution at the outer-layer hits $\sigma_{\text{single}}(d_{\text{straw}} - r)$ contributes to $\sigma_{\text{trk.}}$. Under this model, the track fitting of (5.10) becomes a standard least-square fitting on the $z - x$ plane, wherein r and σ_{single} are along the X-axis. In this case, the fitted track $f_{\text{trk.}}$ has a fitting uncertainty at z of

$$\delta f_{\text{trk.}}(z) = \frac{\delta f_{\text{trk.}}(z_{\text{layer}})}{\sqrt{2}} \sqrt{1 + \left(\frac{z}{z_{\text{layer}}}\right)^2}, \tag{5.21}$$

where z_{layer} represents the distance from the middle layer to the outer layers. $\sigma_{\text{trk.}}$ is evaluated at $z = 0$ as

$$\sigma_{\text{trk.}}(r) = \frac{\sigma_{\text{single}}(d_{\text{straw}} - r)}{\sqrt{2}}, \tag{5.22}$$

where $\delta f_{\text{trk.}}(z_{\text{straw}}) = \sigma_{\text{single}}(d_{\text{straw}} - r)$.

σ_{single} is further decomposed to

$$\sigma_{\text{single}}(r) = v\,\sigma_t(r) = \left(\frac{\mathrm{d}f_{\text{XT}}(r)}{\mathrm{d}r}\right)^{-1} \sigma_t(r), \tag{5.23}$$

where v represents the drift velocity of the electrons that is the reciprocal of the X-T curve, and σ_t denotes the net time resolution. σ_t is split into four terms as discussed below.

$$\sigma_t(r) = \delta t_{\text{int.}}(r) \oplus \delta t_{\text{const.}} \oplus \delta t_{\text{ROESTI}}\left(\Delta t_{\text{sync.}}(r)\right) \oplus \delta t_{\text{wf}}(r; w_{\text{th.}}). \tag{5.24}$$

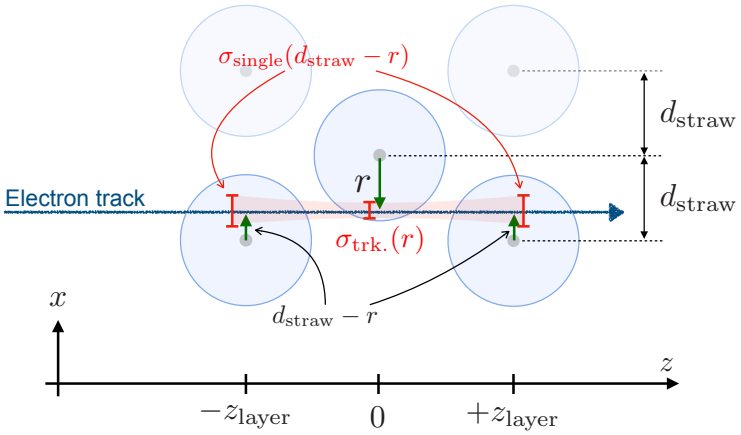

Figure 5.37: Model to calculate the tracking resolution, $\sigma_{\mathrm{trk.}}$. The electron track is parallel to the horizontal axis and equivalent to the beamline axis, and therefore, the DCA and its uncertainty lie on the vertical axis. When it passes through a DCA of r in the middle-layer straw tube, the DCAs in both outer-layer straw tubes are d_{straw}–r. Both hits have the spatial resolution of a single straw tube $\sigma_{\mathrm{single}}(d_{\mathrm{straw}} - r)$, and they contribute to $\sigma_{\mathrm{trk.}}(r)$.

$\delta t_{\mathrm{int.}}$ denotes the time fluctuation of the first drifted electron that reaches the wire and induces a pulse. That is, it is the most fundamental fluctuation of the X-T curves, and it is determined by the gas mixture and applied HV. Figure 5.38 shows $\delta t_{\mathrm{int.}}$ for each dataset, as obtained from the Garfield++ simulation. They are fitted by the ninth-order polynomial functions. There are two different effects to enhance them at lower and higher DCAs: statistical fluctuation of seed electrons and diffusion, as illustrated by Figure 5.39. When an electron runs in a gas medium, seed electrons arise discretely besides it. The seed electron nearest to the wire has a gap of δ to the point where the DCA is defined. Therefore, the drift time along the actual drift path extends because of $r' = \sqrt{r^2 + \delta^2}$; this statistical effect increases at a shorter DCA. Further, the electrons diffuse during drifting by interacting with the gas, and it influences the drift time. A longer DCA introduces a greater diffusion.

$\delta t_{\mathrm{const.}}$ denotes external effects that are independent of the gas mixture and applied HV. Although it is difficult to determine all of them accurately, $\delta t_{\mathrm{const.}}$ includes the fluctuation in T_0 caused by the BDC time resolution.

$\delta t_{\mathrm{ROESTI}}$ is a fixed component that is part of $\delta t_{\mathrm{const.}}$ conceptually. However, as discussed in Section 3.3.1, ROESTI has a feature in its time resolution that varies depending on the time distance between a pair of waveforms in the same DRS4 chip. This feature is also applicable in $\Delta t_{\mathrm{sync.}}$, which is the time distance between the signal pulse and the synchronization signal. Figure 5.40 demonstrates the calculation, which is given as

$$\Delta t_{\mathrm{sync.}}(r) = \Delta t_{\mathrm{sync-max}} - \Delta t_{\mathrm{drift}} = 200 - f_{\mathrm{XT}}(r)\ (\mathrm{nsec}), \tag{5.25}$$

where $\Delta t_{\mathrm{sync-max}} = 200$ nsec represents a parameter depending on the experimental setup and the maximum value of $\Delta t_{\mathrm{sync.}}$ when $\Delta t_{\mathrm{drift}} = 0$. The following function is defined from Figure 3.9 to express $\delta t_{\mathrm{ROESTI}}$.

$$\delta t_{\mathrm{ROESTI}}(\Delta t_{\mathrm{sync.}}) = 0.0707 + 0.0007\,\Delta t_{\mathrm{sync.}}\ (\mathrm{nsec}). \tag{5.26}$$

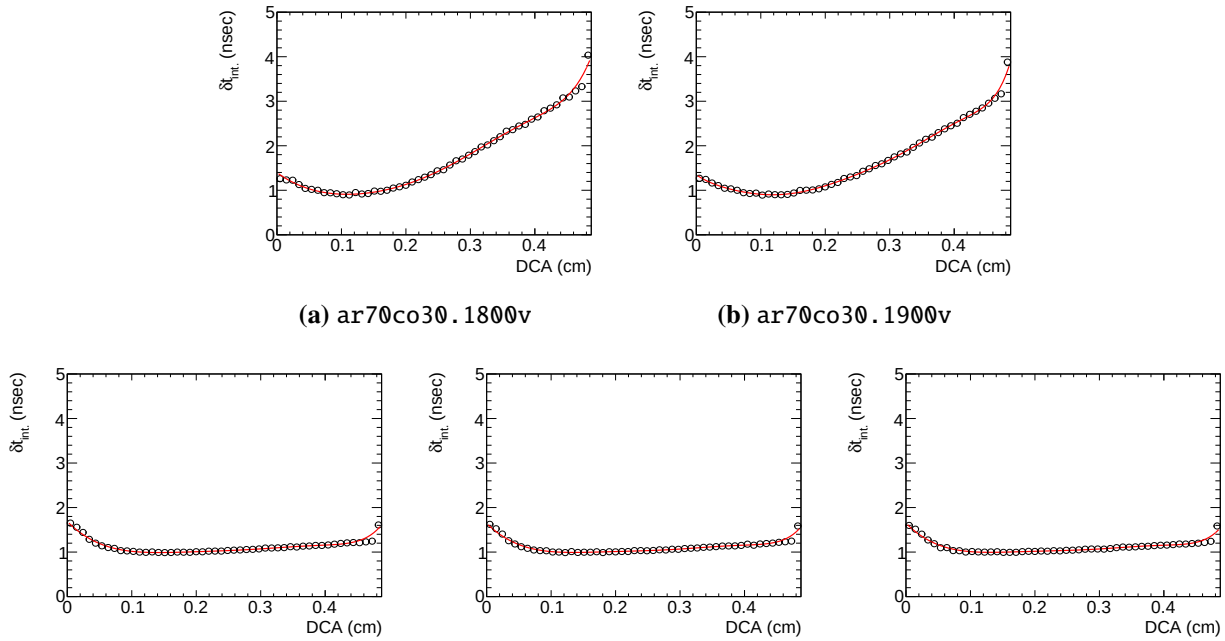

(a) `ar70co30.1800v` **(b)** `ar70co30.1900v`

(c) `ar50et50.1850v` **(d)** `ar50et50.1950v` **(e)** `ar50et50.2050v`

Figure 5.38: Drift-time fluctuations of the first drifted electron that reaches the wire, as simulated by Garfield++. The increasing fluctuations at lower and higher DCAs are attributed to the statistical effect and diffusion. The data are fitted using polynomial functions.

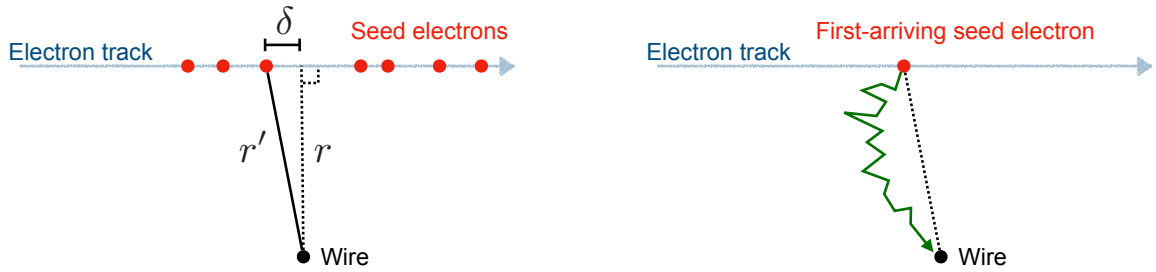

(a) Statistical effect **(b)** Diffusion effect

Figure 5.39: Two intrinsic effects of fluctuating the timing of the first-arriving seed electron. (a) Since seed electrons are generated discretely on the electron track, even the one closest to the wire has a longer distance r to the wire than the DCA because of δ. (b) The gas medium diffuses the passage of the drifted electrons.

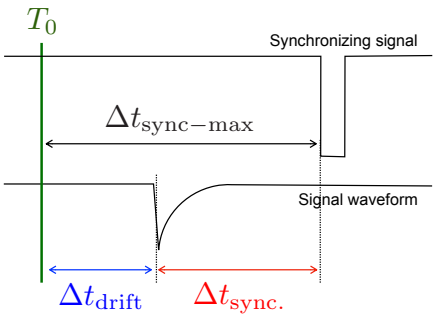

Figure 5.40: Calculation of the time distance between the signal pulse and synchronizing signal. The horizontal axis represents the timeline of ROESTI waveforms. $\delta t_{\mathrm{ROESTI}}$ depends on $\Delta t_{\mathrm{sync.}} = T_{\mathrm{sync-max}} - \Delta t_{\mathrm{drift.}}$, which is the difference between the signal pulse and synchronizing signal.

The final term δt_{wf} is the most important part and originates from the waveform analysis; further, it inevitably depends on $w_{\mathrm{th.}}$, which is the threshold to reconstruct $t_{\mathrm{th.}}$. Since we cannot apply the time-slewing correction to straw tracker waveforms, $t_{\mathrm{th.}}$ shifts as $w_{\mathrm{th.}}$ changes, and we need to consider its effect.

The following $w_{\mathrm{lead.}}(t)$ models the leading edge part of a signal pulse.

$$w_{\mathrm{lead.}}(t) = A(t - t_0)^2 \quad (t_0 \leq t), \tag{5.27}$$

where A represents a scale parameter, and t_0 denotes the true timing when the signal pulse starts rising. Then, $t_{\mathrm{th.}}$ is given by $w_{\mathrm{lead.}} = w_{\mathrm{th.}}$ as

$$t_{\mathrm{th.}} = t_0 + \sqrt{\frac{w_{\mathrm{th.}}}{A}}, \tag{5.28}$$

This yields the following three uncertainties.

$$\begin{aligned}
\delta t_{\mathrm{wf}}^{w_{\mathrm{th.}}} &= \left|\frac{\partial t_{\mathrm{th.}}}{\partial w_{\mathrm{th.}}}\right| \delta w_{\mathrm{th.}} = \frac{1}{2}\sqrt{\frac{1}{A\, w_{\mathrm{th.}}}}\delta w_{\mathrm{th.}} = \frac{C_{\mathrm{noise}}}{\sqrt{w_{\mathrm{th.}}}}, \\
\delta t_{\mathrm{wf}}^{A} &= \left|\frac{\partial t_{\mathrm{th.}}}{\partial A}\right| \delta A = \frac{1}{2}\sqrt{\frac{w_{\mathrm{th.}}}{A^3}}\delta A = C_{\mathrm{gain}}\sqrt{w_{\mathrm{th.}}}, \\
\delta t_{\mathrm{wf}}^{t_0} &= \left|\frac{\partial t_{\mathrm{th.}}}{\partial t_0}\right| \delta t_0 = \delta t_0 = C_{\mathrm{2nd}}\delta t_{\mathrm{2nd}}.
\end{aligned} \tag{5.29}$$

These three uncertainties have different dependencies on $w_{\mathrm{th.}}$, and the coefficients C_{noise}, C_{gain}, and C_{2nd} have different physical meanings. C_{noise} is proportional to $\delta w_{\mathrm{th.}}$, which is the waveform instability caused waveform baseline noise. C_{gain} is proportional to $\delta A\, A^{-3/2}$, and it stands for the relative amplification-gain fluctuation of the gas mixture and applied HV.

The third component is more complicated.C_{2nd} represents a scale parameter of δt_{2nd}, which is another intrinsic component that originates from the gas mixture and applied HV.

We assume that only the first-arriving seed electron forms $w_{\mathrm{lead.}}$. However, if the gas-amplification gain is insufficient, the contribution of the second electron becomes significant. δt_{2nd} indicates the fluctuation of the time difference between the first- and second-arriving drifted electrons. We evaluated it for each dataset via the simulation (Figure 5.41), and we fit a ninth-order polynomial function to each curve.

All expressions introduced in this model are listed below.

$$\begin{aligned}
\sigma_{\mathrm{obs.}}(r; w_{\mathrm{th.}}) &= \sigma_{\mathrm{single}}(r; w_{\mathrm{th.}}) \oplus \sigma_{\mathrm{trk.}}(r; w_{\mathrm{th.}}) = \sigma_{\mathrm{single}}(r; w_{\mathrm{th.}}) \oplus \frac{\sigma_{\mathrm{single}}(d_{\mathrm{straw}} - r; w_{\mathrm{th.}})}{\sqrt{2}}, \\
\sigma_{\mathrm{single}}(r; w_{\mathrm{th.}}) &= \left(\frac{\mathrm{d}f_{\mathrm{XT}}(r)}{\mathrm{d}r}\right)^{-1} \sigma_t(r; w_{\mathrm{th.}}), \\
\sigma_t(r; w_{\mathrm{th.}}) &= \delta t_{\mathrm{int.}}(r) \oplus \delta t_{\mathrm{const.}} \oplus \delta t_{\mathrm{ROESTI}}\left(\Delta t_{\mathrm{sync.}}(r)\right) \oplus \delta t_{\mathrm{wf}}(r; w_{\mathrm{th.}}), \\
\delta t_{\mathrm{wf}}(r; w_{\mathrm{th.}}) &= \frac{C_{\mathrm{noise}}}{\sqrt{w_{\mathrm{th.}}}} \oplus C_{\mathrm{gain}}\sqrt{w_{\mathrm{th.}}} \oplus C_{\mathrm{2nd}}\delta t_{\mathrm{2nd}}(r),
\end{aligned} \tag{5.30}$$

where $f_{\mathrm{XT}}(r)$, $\delta t_{\mathrm{int.}}(r)$, and $\delta t_{\mathrm{2nd}}(r)$ represent input parameters, and C_{noise}, C_{gain}, and C_{2nd} represent free-fitting parameters. While they depend on the combination of the gas mixture and applied HV,

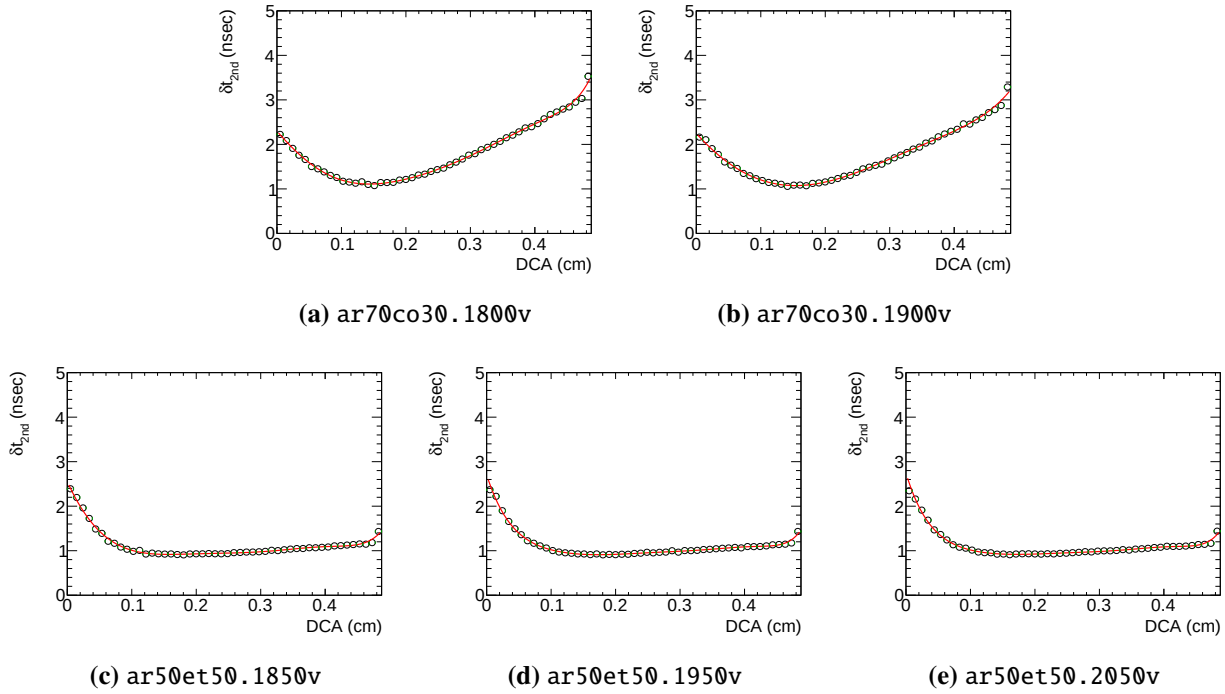

(a) `ar70co30.1800v` **(b)** `ar70co30.1900v`

(c) `ar50et50.1850v` **(d)** `ar50et50.1950v` **(e)** `ar50et50.2050v`

Figure 5.41: Fluctuation of the time difference between the first- and second-arrival drifted electrons, as simulated by Garfield++. The data are fitted using ninth-order polynomial functions.

i.e., dataset, $\delta t_{\mathrm{ROESTI}}$ and $\delta t_{\mathrm{const.}}$ are independent input and fitted parameters, respectively. Therefore, fitting using this model needs to be applied to all spatial-resolution curves simultaneously. In addition, we prepared spatial-resolution curves reconstructed with thresholds of $w_{\mathrm{th.}} = 0.5,\ 1.0,\ 1.5,\ ...,\ 3.0$ mV to determine parameters associated with $w_{\mathrm{th.}}$.

5.4.2.2 Fit and Interpretation

Figure 5.42 shows some of the fitted results that correspond to cases using $w_{\mathrm{th.}} = 1.0,\ 2.0$, and 3.0 mV. The fitted curves deviate slightly from the data points with high $w_{\mathrm{th.}}$; it appears that the model becomes inapplicable for such higher $w_{\mathrm{th.}}$. However, the model explains all data well overall because of the fit quality of $\chi^2/\mathrm{ndf} = 1025/685$; however, we need to scrutinize the fitted parameters. Their values are displayed in Figure 5.42(f). The open and full markers are for `ar70co30` and `ar50et50`, respectively. In both gas mixtures, they keep decreasing with the applied HV. This trend is reasonable because their magnitudes are directly related to the low gas gain. The results are better for Ar:C_2H_6 on average.

$\delta t_{\mathrm{const.}}$ is 1.50 nsec, and as discussed above, it includes the T_0 time resolution given as 0.48 nsec for MIP (minimum ionizing particle) electrons in Section 5.3.2. There is also a covariance term between T_0 and the synchronizing signal in the DRS4 chip that recorded the BDC-PMT signals, $t^{\mathrm{PMT}}_{\mathrm{sync.}}$, because the former generates the latter itself. This is referred to as $\mathrm{Cov}\left(t^{\mathrm{PMT}}_{\mathrm{sync.}}, T_0\right) = 0.085$ nsec^2. By removing the external contributions, $\delta t_{\mathrm{const.}}$ slightly changes to

$$\delta t_{\mathrm{const.}} \rightarrow \sqrt{(\delta t_{\mathrm{const.}})^2 - \left\{\left(\sigma^0_t\right)^2 - 2\mathrm{Cov}\left(t^{\mathrm{PMT}}_{\mathrm{sync.}}, T_0\right)\right\}} = 1.48 \text{ nsec.} \tag{5.31}$$

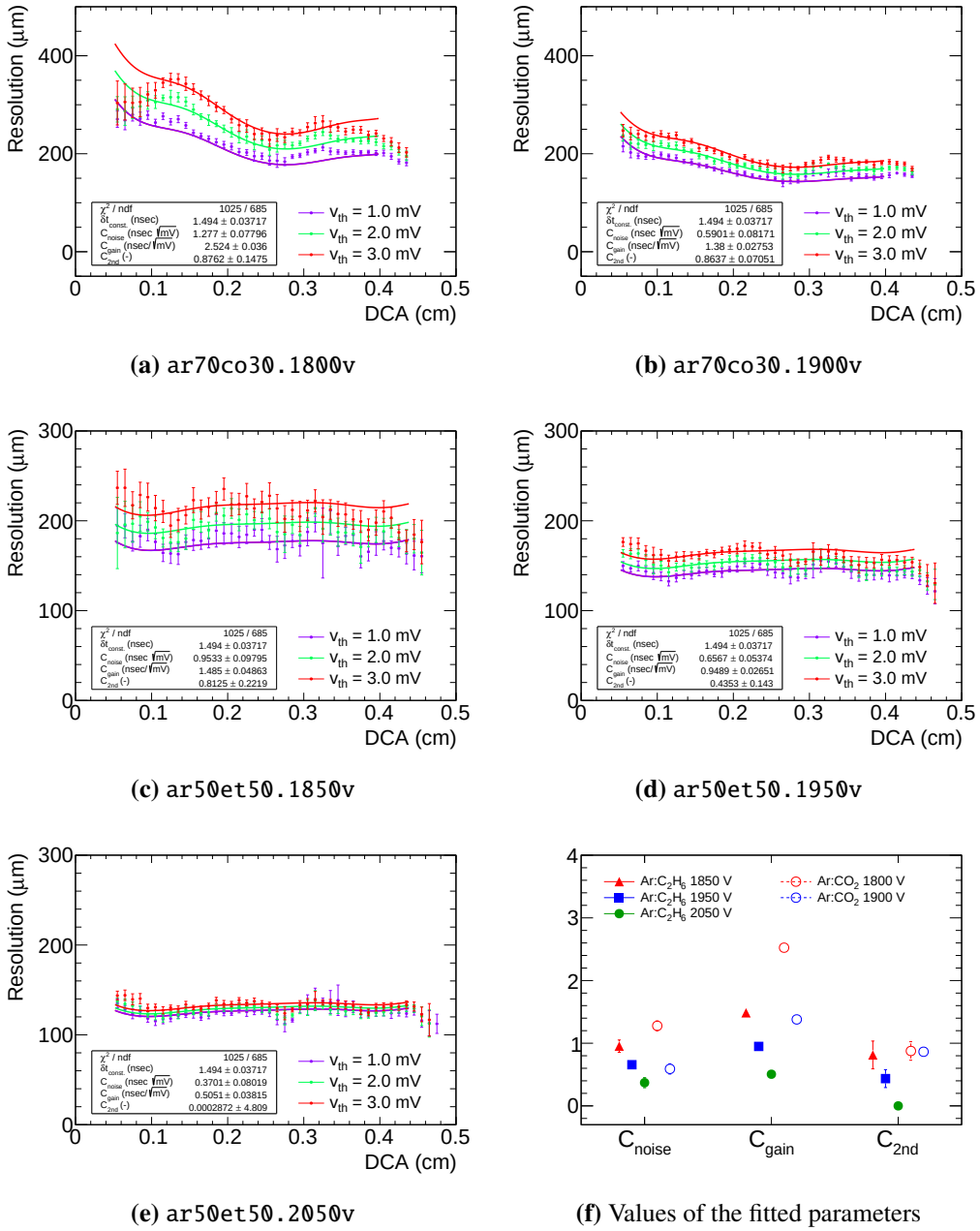

(a) `ar70co30.1800v` **(b)** `ar70co30.1900v`

(c) `ar50et50.1850v` **(d)** `ar50et50.1950v`

(e) `ar50et50.2050v` **(f)** Values of the fitted parameters

Figure 5.42: Fit of the spatial-resolution model to the data reconstructed by various thresholds. The model is fitted to all curves simultaneously. (a–e) The figures show only cases with thresholds of 1.0, 2.0, and 3.0 mV; however, the fit also includes cases with 1.5 and 2.5 mV. The legends display the values of the fitting parameters for each dataset, while only $\delta t_{\text{const.}}$ is common. (f) All fitted parameters according to the dataset are shown and become smaller as the HV increases for both gas mixtures.

Finally, all decomposed spatial-resolution curves are shown in Figure 5.43 for the case of $w_{\text{th.}} =$ 1 mV. The bold blue lines indicate σ_{single}. $\delta t_{\text{const.}}$ contributes the most; however, δt_{ROESTI} is negligible. At low HV, the terms of δt_{wf} become more critical than $\delta t_{\text{int.}}$ and $\delta t_{\text{const.}}$. Therefore, the `ar50et50.2050v` shows the best performance, and it meets the necessary requirement.

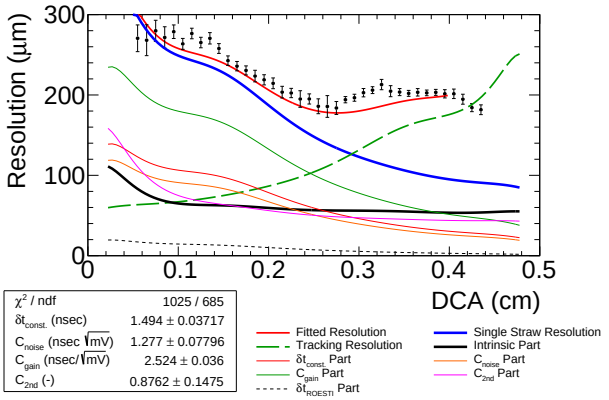

(a) `ar70co30.1800v`

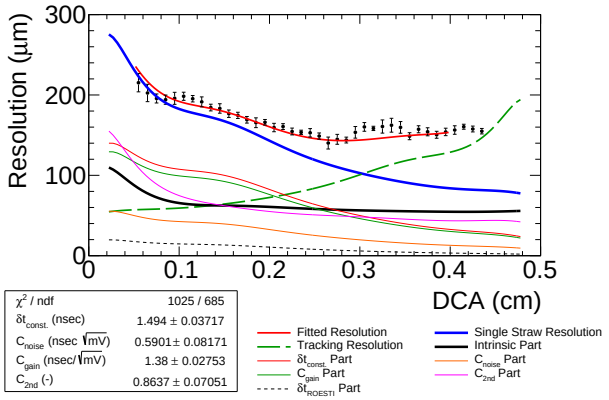

(b) `ar70co30.1900v`

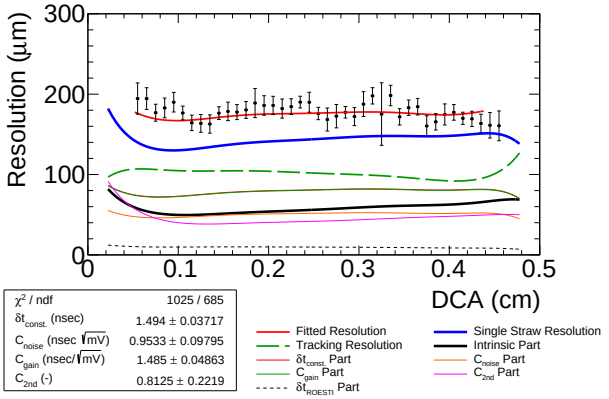

(c) `ar50et50.1850v`

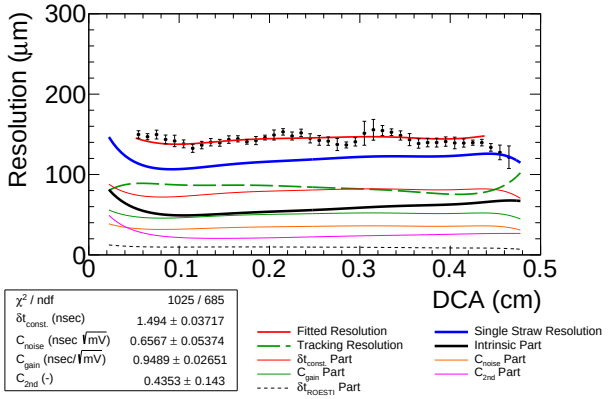

(d) `ar50et50.1950v`

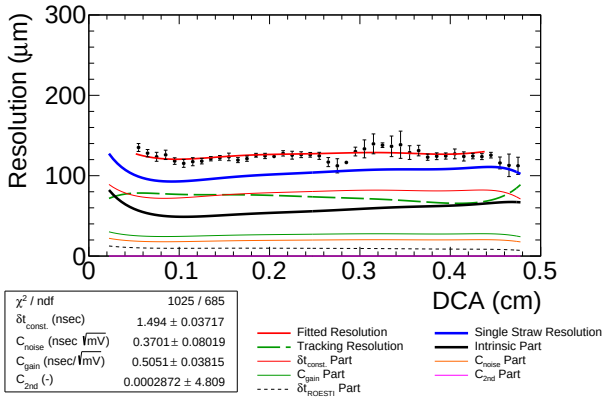

(e) `ar50et50.2050v`

Figure 5.43: Decomposition of the observed spatial resolutions by the fitting model in the case using a threshold of 1 mV. Besides the intrinsic term, $\delta t_{\text{const.}}$ is the most significant in any case. The Ar:C_2H_6 (50:50) gas mixture shows the best performance over the fitted region.

5.5 Performance of the ECAL

5.5.1 Energy Resolution

Figure 5.44 displays $\sigma_E^{\text{tot.}}/E_{\text{peak}}$ and $\sigma_E^{\text{sym.}}/E_{\text{peak}}$ as a function of the beam momentum for each hit region obtained by spectrum fitting. The error bars represent the statistical and systematic uncertainties. The former indicates the fitting error; the latter is evaluated by two different components. The first component is the variation in the fit result obtained by varying the bin width of the fitted spectra as 0.25, 0.50, ..., 2.00 MeV and the lower limit of the fit range as 30%, 40%, ..., 80% of the beam momentum. The second factor is the variation obtained by fluctuating all channel energy calibration factors $c_{\text{ch.}}$ by 5% and the noise-cut factor f_{noise} by 0.5 from the default values fixed in Section 5.3.4.6. As expected, the results are worse in the order of the `center`, `border`, and `corner` hit regions, and the `mix` hit region shows an interim performance. However, the observed $\sigma_E^{\text{sym.}}$ still has several contributions that include the momentum resolution of the electron beam.

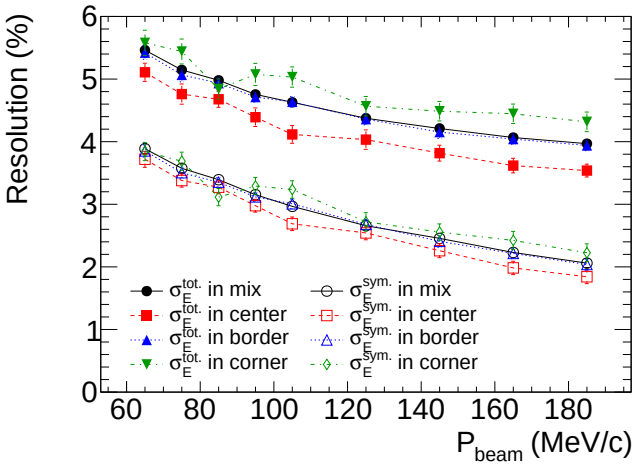

Figure 5.44: Total and symmetric terms in the observed energy resolutions as functions of the beam momentum in different hit regions. On average, these terms worsen in the order of the `center`, `border`, and `corner` hit regions, and those in the `mix` hit region are in the middle.

The observed $\sigma_E^{\text{sym.}}/E_{\text{peak}}$ is fitted with the following expression that is well-known in calorimetry.

$$f_{\sigma_E^{\text{sym.}}}\left(P_{\text{beam}}; a, b, c, d\left(P_{\text{beam}}\right)\right) \equiv \frac{\sigma_E^{\text{sym.}}}{E_{\text{peak}}} = \frac{a}{\sqrt{P_{\text{beam}}}} \oplus b \oplus \frac{c}{P_{\text{beam}}} \oplus d\left(P_{\text{beam}}\right), \tag{5.32}$$

where P_{beam} represents the beam momentum[6]; the first three terms have fitting parameters a, b, and c; and the last term denotes the beam momentum spread. The stochastic term with a reflects the statistical fluctuation of the number of detected scintillation photons N_{photon}. Since N_{photon} is proportional to P_{beam} through the total energy deposit, its Poisson fluctuation is proportional to $\sqrt{P_{\text{beam}}}$. The constant term with b represents uncertainties of any contributions proportional to the energy deposit. For example, the incompleteness of the energy calibration among the crystals deserves it. The noise

[6] In our case, P_{beam} approximates the beam energy well because of the small electron mass.

term with c appears regardless of the energy deposit; therefore, it literally includes non-beam-related effects such as noise. Finally, the beam-momentum-spread term corresponds to Figure 5.2(b), which has to be removed from $\sigma_E^{\text{sym.}}$ to extract the pure resolution of the ECAL. We expresse it as

$$d\left(P_{\text{beam}}\right) = \frac{d_1}{\left(P_{\text{beam}}\right)^{d_2}} + d_3, \tag{5.33}$$

where d_1, d_2, and d_3 denote fitting parameters.

We suppose that the stochastic, noise, and beam-spread terms are independent of the hit region; however, only the constant term is dependent. This is because of the idea that the degree of the energy-deposit sharing among the crystals increases in the order of the `center`, `border`, and `corner` hit regions, and the energy-calibration incompleteness becomes significant. Therefore, all observed $\sigma_E^{\text{sym.}}$ in the four hit regions are fitted by (5.32) simultaneously, and Figure 5.2(b) is inclusively fitted by (5.33).

Figure 5.45 shows the fit result and the extracted pure resolution. The full and open black points represent the observed $\sigma_E^{\text{tot.}}$ and $\sigma_E^{\text{sym.}}$, respectively, and they are the same as those in Figure 5.44. The solid red lines represent fitted functions, and the broken blue lines represent $\sigma_E^{\text{sym.}}$ without the beam-momentum-spread term. The star green points are $\sigma_E^{\text{tot.}}$ retrieved from them, and hence, they indicate the pure energy resolution.

Figure 5.45(f) plots all fitted constant terms as a function of the distance between the center positions of the crystal and the hit region where the horizontal uncertainty is the RMS of the distance from the crystal center to the points over the region. They likely have a linear trend as fitted by $b = p_0 |x|$, where x denotes the distance that agrees with the assumption.

Figure 5.46 compiles with the extracted pure $\sigma_E^{\text{tot.}}$ and $\sigma_E^{\text{sym.}}$. Since they are evaluated with a rich dataset from the simulation, their statistical uncertainty is negligibly small. We evaluated two contributions as systematic uncertainty. The first is a fluctuation caused by $c_{\text{ch.}}$ and f_{noise}, which is similar to the observed $\sigma_E^{\text{sym.}}$ and $\sigma_E^{\text{tot.}}$. The second is the variation caused by the uncertainty of the beam-momentum resolution. As mentioned in Section 5.1.1, the provided beam-momentum resolution is evaluated based on the beamline design before the vacuum pipe can extend [80], and hence, the true value may have been smaller. We also assumed that it is less than 90%, and we scaled it to 90%, 92%, ..., and 100% to investigate the extent to which it would affect the extracted resolution. We found that both uncertainties are almost the same. Finally, the ECAL energy resolution satisfies the requirement of 5% at 105 MeV/c, which is numerically 3.91 ± 0.07% for the `mix` hit region.

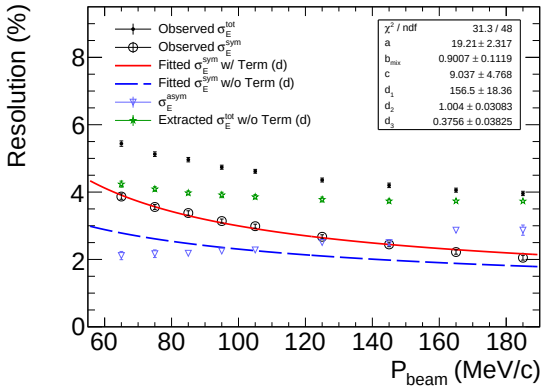

(a) `mix` hit region

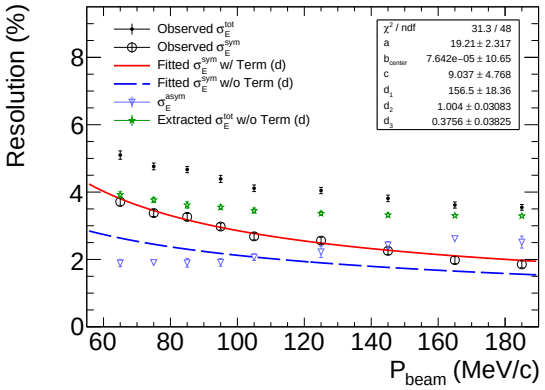

(b) `center` hit region

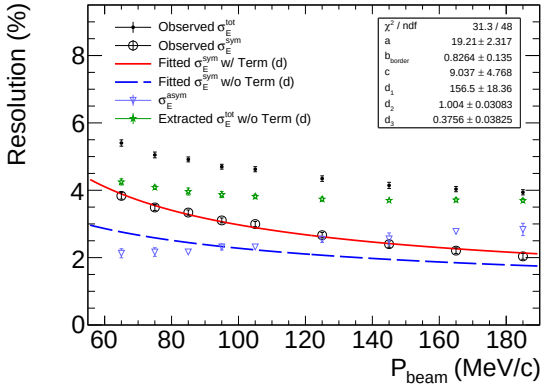

(c) `border` hit region

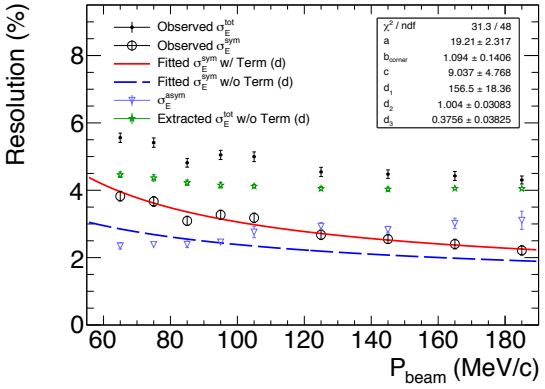

(d) `corner` hit region

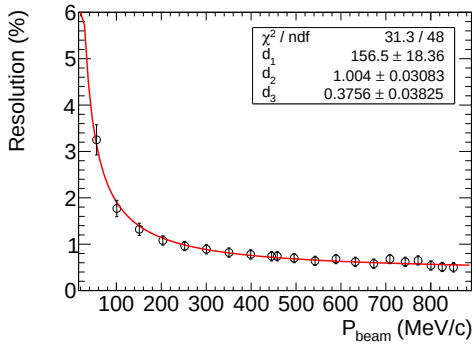

(e) Beam-momentum resolution

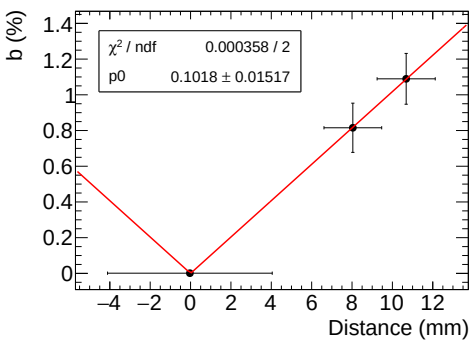

(f) Fitted constant terms

Figure 5.45: Simultaneous fitting for the symmetric part of the observed energy resolutions of all hit regions, including the beam-momentum resolution. (a-d) Full and open black points represent the observed $\sigma_E^{\text{tot.}}/E_{\text{peak}}$ and $\sigma_E^{\text{sym.}}/E_{\text{peak}}$, respectively; the red lines represent those fitted to the latter. The blue lines represent $\sigma_E^{\text{sym.}}$ calculated from the fit result without the beam-momentum-spread term, and the green points indicate the resulting pure energy resolution. (e) The beam-momentum resolution is fitted together, and the fit result is subtracted from the symmetric part. (f) The constant term depends on the distance from the crystal center to each hit-region center. Data are fitted by $b = p_0\,|x|$, where x denotes the distance.

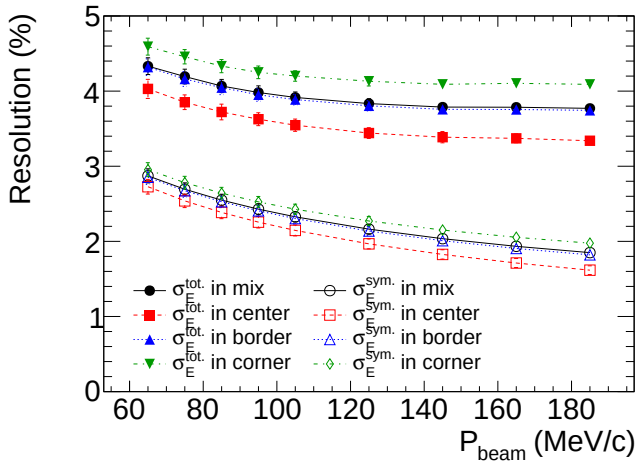

Figure 5.46: Total and symmetric terms in the extracted energy resolutions as functions of the beam momentum in different hit regions. All total energy resolutions at 105 MeV/c satisfy the requirement of 5%.

5.5.2 Time Resolution

The ECAL time resolution is evaluated from the residual of the ECAL timing from the time origin, as

$$\begin{aligned}\Delta T &= T_{\mathrm{ECAL}} - T_0' \\ &= \frac{\sum_i^{N_{\mathrm{clst.}}} e^i \left(t^i_{\mathrm{th.}} - t^i_{\mathrm{sync.}}\right)}{E_{\mathrm{tot.}}} - \left(T_0 - t^{\mathrm{PMT}}_{\mathrm{sync.}}\right),\end{aligned} \tag{5.34}$$

where (5.16) is substituted, and $E_{\mathrm{tot.}} = \sum_i^{N_{\mathrm{clst.}}} e^i$. $t^{\mathrm{PMT}}_{\mathrm{sync.}}$ represents the timing from the synchronizing signal that comes to the DRS4 chip for the PMT channels, which is necessary to synchronize among all DRS4 chips to which the PMT and ECAL channels belong. The standard deviation of a Gaussian function fitted to the ΔT distribution yields the time resolution of ΔT.

Figure 5.47 depicts it as a function of the beam momentum for each hit region. The statistic uncertainty is the fitting error, and the systematic one is evaluated in the same manner for the observed energy resolution. The resolution shows a subtle difference among the hit regions; however, it deteriorates in the order opposite to the energy-resolution case because it is more advantageous to the average time among multiple crystals. Further, the energy-calibration incompleteness has no effect on σ_t^{ECAL}.

The observed resolution still contains the T_0 time resolution, which should be removed to obtain the pure ECAL time resolution σ_t^{ECAL}. However, the synchronization among multiple DRS4 chips makes the evaluation complicated. (5.34) is further expanded as

$$\Delta T = \frac{\sum_i^{N_{\mathrm{clst.}}} e^i t^i_{\mathrm{th.}}}{E_{\mathrm{tot.}}} - \frac{\sum_i^{N_{\mathrm{chip}}} E^c_{\mathrm{chip}} t^c_{\mathrm{sync.}}}{E_{\mathrm{tot.}}} - T_0 + t^{\mathrm{PMT}}_{\mathrm{sync.}}, \tag{5.35}$$

where $t^c_{\mathrm{sync.}}$ represents the synchronization timing of Chip c, E^c_{chip} denotes the total energy over the channels belonging to it, and N_{chip} represents the number of chips. Then, its fluctuation is given as

$$\begin{aligned}(\sigma_{\Delta T})^2 = \frac{1}{(E_{\mathrm{tot.}})^2}\left[\sum_i^{N_{\mathrm{clst.}}} \left\{e^i\, \sigma_t^{\mathrm{cry.}}(e^i)\right\}^2 + (\sigma_t^{\mathrm{sync.}})^2 \sum_c^{N_{\mathrm{chip}}} (E^c_{\mathrm{chip}})^2\right] \\ + \left(\sigma_t^0\right)^2 + \left(\sigma_t^{\mathrm{sync.}}\right)^2 - 2\,\mathrm{Cov}\left(T_0,\, t^{\mathrm{PMT}}_{\mathrm{sync.}}\right),\end{aligned} \tag{5.36}$$

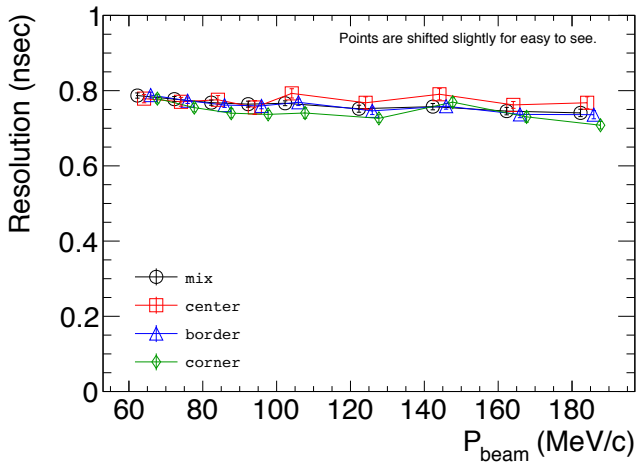

Figure 5.47: Observed ECAL time resolution for each hit region as a function of the beam momentum. The points are shifted to view them easily. There are slight differences among the hit regions.

where $\sigma_t^{\text{cry.}}$ denotes the time resolution of a single crystal as a function of its energy deposit e^i, and $\sigma_t^{\text{sync.}}$ represents the time jitter in the synchronization. We assume that there are no individual differences in $\sigma_t^{\text{cry.}}$ and $\sigma_t^{\text{sync.}}$. The first term corresponds to σ_t^{ECAL} to extract. Since the PMT signals contribute to both T_0 and $t_{\text{sync.}}^{\text{PMT}}$, they must be correlated to form the covariance term $\text{Cov}\left(T_0, t_{\text{sync.}}^{\text{PMT}}\right)$. (5.36) indicates σ_t^{ECAL} can be understood with $\sigma_t^{\text{cry.}}$.

$\sigma_t^{\text{cry.}}$ is evaluated by fitting a Gaussian function to the time difference between two crystals and by dividing its standard deviation by $\sqrt{2}$. To investigate the energy dependence, every crystal pair is required to have similar energy deposits. There are three types of relationships in pairs in terms of the DRS4 chip, and they are as illustrated in Figure 5.48.

Same chip Every pair belongs to the same DRS4 chip.

Same board Every pair is separated into the two DRS4 chips on the same EROS board.

Other Every pair is separated into different EROS boards.

Although $t_{\text{sync.}}^c$ is canceled in the first case, $\sigma_t^{\text{sync.}}$ contaminates the $\sigma_t^{\text{cry.}}$ of the other cases. During data collection, one of the pairs was fixed to a specific channel. Then, sufficient statistics were gained only for the three channels where there was a higher frequency of incident beam electrons. For instance, Figure 5.49 shows the $\sigma_t^{\text{cry.}}$ of the richest channel as a function of the energy deposit per crystal. The curve in *the same chip* case obviously differs from the others because of $\sigma_t^{\text{sync.}}$, while the other cases have similar values. This implies that only the difference in the DRS4 chip influences the results. The curves are fitted with

$$\sigma_t^{\text{cry.}}(e) = \frac{a}{e - E_{\text{th.}}} \oplus b, \tag{5.37}$$

where a, b, and $E_{\text{th.}}$ represent the fitting parameters. Averaging the fitted values in *the same chip* case among the three channels yields $a = 3.77$ nsec MeV, $b = 0.16$ nsec, and $E_{\text{th.}} = 4.31$ MeV. Moreover, from the gap in the other cases, $\sigma_t^{\text{sync.}}$ is estimated as 0.57 ± 0.06 nsec, where the uncertainty is the standard deviation.

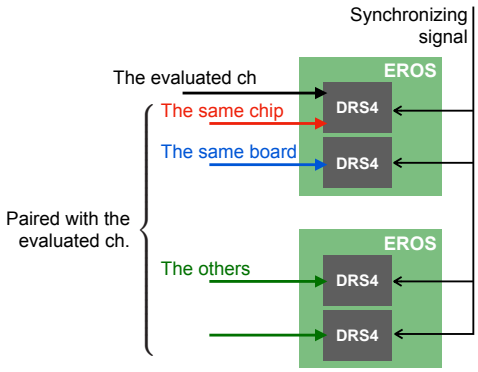

Figure 5.48: Relationships between the crystal pairs for evaluating the single-crystal time resolution. With respect to the evaluated channel, the paired channel belongs to either the same DRS4 chip, same EROS board, or other board. In the last two cases, synchronization is necessary.

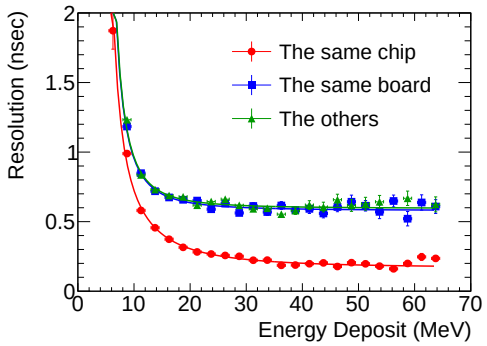

Figure 5.49: Single crystal time resolution as a function of the energy deposit. It is evaluated separately for the three cases illustrated in Figure 5.48. Unlike the other cases, only *the same chip* case does not contain the synchronization time jitter. The curves are fitted by (5.37).

Next, Cov $\left(T_0,\, t_{\text{sync.}}^{\text{PMT}}\right)$ is determined with the simulation. Event-by-event, the timings of the ECAL and PMT channels are fluctuated using (5.37) and (5.4) depending on energy deposits in them. For several values of $\sigma_t^{\text{sync.}}$, the best values of Cov $\left(T_0,\, t_{\text{sync.}}^{\text{PMT}}\right)$ is calculated so that the resulting (5.36) fits the observed $\sigma_{\Delta T}$ (Figure 5.47). Figure 5.50 shows the result, which is fitted with a quadratic polynomial function $\sum_{n=0}^{2} p_{\text{n}} x^n$. From the fit result and $\sigma_t^{\text{sync.}}$ gained above, Cov $\left(T_0,\, t_{\text{sync.}}^{\text{PMT}}\right)$ is evaluated as 0.085 ± 0.061 nsec^2.

Thus, the pure time resolution is obtained after all terms related to T_0 are removed (Figure 5.51). Although they have large uncertainties caused by the significant uncertainty of Cov $\left(T_0,\, t_{\text{sync.}}^{\text{PMT}}\right)$, the results satisfy the requirement of 1 nsec at 105 MeV, which is numerically 0.54 ± 0.12 nsec for the `mix` hit region.

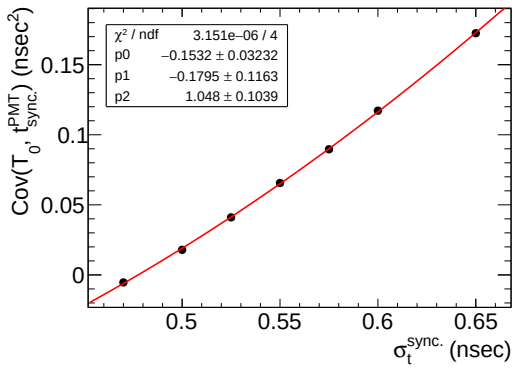

Figure 5.50: Covariance term in the observed ECAL time resolution as a function of the synchronization time jitter, as estimated via simulation. A quadratic polynomial function is fitted to the points, and its fitted parameters are displayed in the legend.

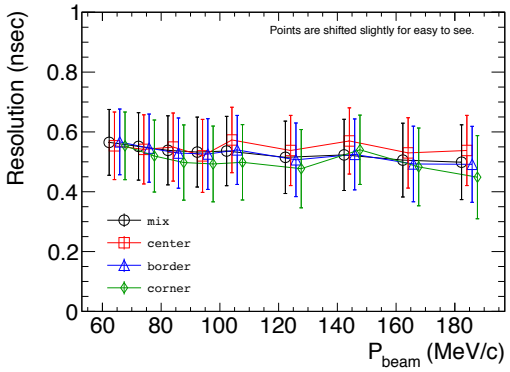

Figure 5.51: Pure ECAL time resolution for each hit region as a function of beam momentum. The points are shifted to make it easier to see. The uncertainty is dominated by that of the covariance term.

5.5.3 Position Resolution

The position resolution is evaluated from the distribution of $\Delta\boldsymbol{R} = \boldsymbol{R}_{\mathrm{ECAL}} - \boldsymbol{R}_{\mathrm{trk.}}$, where $\boldsymbol{R}_{\mathrm{ECAL}} = (X_{\mathrm{ECAL}}, Y_{\mathrm{ECAL}})$ denotes the reconstructed cluster position, and $\boldsymbol{R}_{\mathrm{trk.}}$ represents the incident position on the ECAL surface where the track is reconstructed from the straw tracker and BDC hits points. For example, Figure 5.52 shows this in the case of the `mix` hit region in `mscan.105`. The distribution is fitted by a two-dimensional Gaussian function, and the fitted standard deviation $\sigma_{\Delta\boldsymbol{R}}$ is regarded as the observed position resolution. Again, systematic uncertainty is estimated in the same manner for the other resolutions from the variations caused by the bin width, fit range, energy calibration, and noise-cut factors. $\sigma_{\Delta\boldsymbol{R}}$ contains several contributions including the pure resolution $\sigma_{\boldsymbol{R}}^{\mathrm{ECAL}}$, which is given as

$$\sigma_{\Delta\boldsymbol{R}} = \sigma_{\boldsymbol{R}}^{\mathrm{ECAL}} \oplus \sigma_{\boldsymbol{R}}^{\mathrm{trk.}} \oplus \sigma_{\boldsymbol{R}}^{\mathrm{MS}} \oplus \sigma_{\boldsymbol{R}}^{\mathrm{align}}, \tag{5.38}$$

where $\sigma_{\boldsymbol{R}}^{\mathrm{trk.}}$, $\sigma_{\boldsymbol{R}}^{\mathrm{MS}}$, and $\sigma_{\boldsymbol{R}}^{\mathrm{align}}$ are the contributions from the tracking resolution, multiple scattering, and the misalignment of the apparatus.

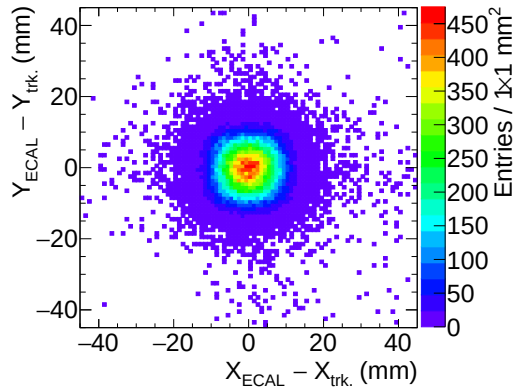

Figure 5.52: Residual distribution of the incident positions on the ECAL surface reconstructed by the clustering and tracking for the `mix` hit region in `mscan.105`. The distribution is fitted by a two-dimensional Gaussian function to evaluate the position resolution.

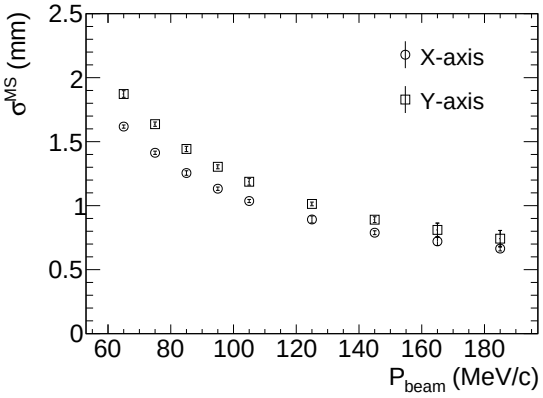

Figure 5.53: Contribution of multiple scattering to the observed ECAL position resolution as a function of the beam momentum. The values of the Y-axis are greater than those of the X-axis because of the different path lengths of the beam electron.

$\sigma_{\boldsymbol{R}}^{\mathrm{trk.}}$ comes from the track fitting to the straw tracker and BDC hits with finite position resolutions. It was evaluated directly from the data by propagating the variance-covariance matrix obtained from the track fitting to the ECAL surface as $\sigma_{\boldsymbol{R}}^{\mathrm{trk.}} = (460, 590)\ \mu$m. Since the Y-axis straw tubes were positioned ahead of the X-axis ones, they had a longer extrapolation length, and thus, the $\sigma_{\boldsymbol{R}}^{\mathrm{trk.}}$ has a greater contribution on the Y-axis.

$\sigma_{\boldsymbol{R}}^{\mathrm{MS}}$ is estimated with the simulation where $\sigma_{\boldsymbol{R}}^{\mathrm{ECAL}}$, $\sigma_{\boldsymbol{R}}^{\mathrm{trk.}}$, and $\sigma_{\boldsymbol{R}}^{\mathrm{align}}$ can become zero or negligible. Figure 5.53 shows the result as a function of the beam momentum. Although statistical uncertainty is negligible, the systematic uncertainty is estimated by varying the fit range. The effect is also more significant on the Y-axis than on the X-axis because of the difference in the path length.

$\sigma_{\boldsymbol{R}}^{\mathrm{align}}$ arises from positional gaps of the apparatus from the design value. The positions of the straw tubes and BDC fibers in the simulation are intentionally shifted within presumable uncertainties to

assess it, and the results after the same analysis scheme are investigated. According to the manufacturer, the mechanical assurance of the straw-tube alignment is about 60 μm. The misalignment of the BDC fibers was estimated as roughly 100 μm on average by comparing the positions reconstructed by each of the straw tracker and BDC hits. The result is $\sigma_{R}^{\mathrm{align}} = (110,\ 130)\ \mu$m, which is smaller than the former two components even if the misalignment doubles.

Figure 5.54 displays both the $\sigma_{\Delta R}$ and the extracted $\sigma_{R}^{\mathrm{ECAL}}$ as a function of the beam momentum. It meets the requirement of 10 mm at 105 MeV/c and is numerically $X_{\mathrm{ECAL}} \oplus Y_{\mathrm{ECAL}} = 7.65 \pm 0.07$ mm for the `mix` hit region.

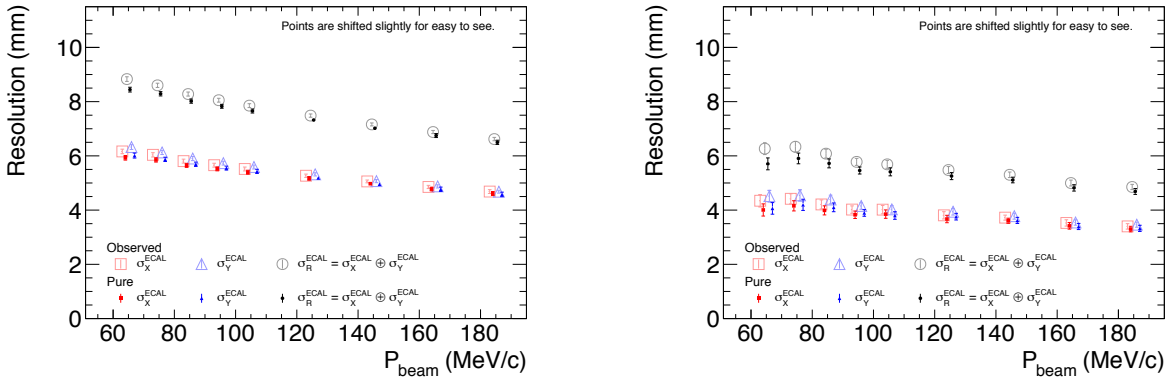

(a) `mix` hit region

(b) `center` hit region

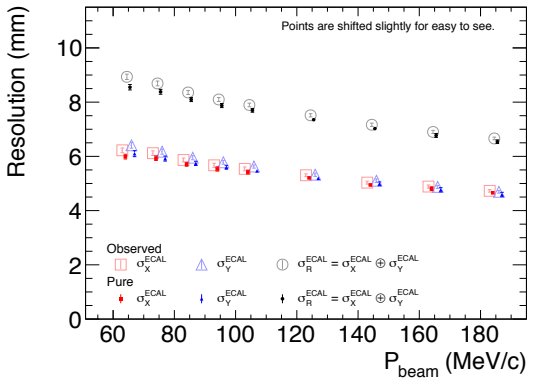

(c) `border` hit region

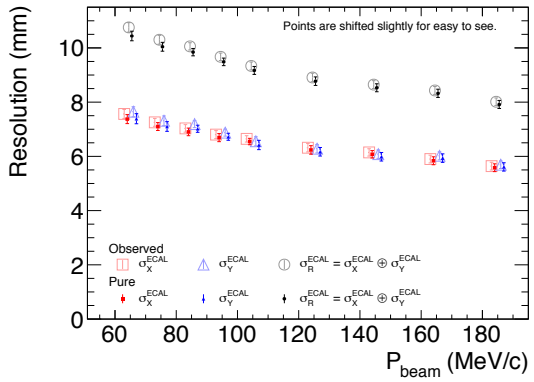

(d) `corner` hit region

Figure 5.54: Observed and pure ECAL position resolutions as a function of the beam momentum for each hit region. The points are shifted to make it easier to see. The open (full) points represent the observed (extracted pure) resolutions.

6

Simulation of The COMET Phase-II

This chapter describes the simulation setup for the Phase-II study. First, the simulation tool discussed in Section 5.3.4.1 is customized such that it can achieve a realistic ECAL response observed in the prototype experiments. Second, because the Phase-II straw tube has a diameter of 5 mm, which is two times smaller than that of the Phase-I straw tube, its performance has to be extrapolated from the obtained Phase-I straw tube performance, and therefore, Garfield++ is utilized again. Third, the COMET collaboration has been developing ICEDUST, which is the official software framework that contains the software for `Geant4`-based full simulation and realistic detector response and digitization process simulations. The customized StrECAL response is implemented into to the latter.

6.1 Realization of the StrECAL Performance

6.1.1 ECAL Waveform Simulation

First, the ECAL waveform is reproduced because it influences all resolutions via the waveform analysis. The waveform simulation splits into two parts: baseline noise and signal pulse induced by energy deposits.

6.1.1.1 Noise Waveform

First, the noise waveform per single channel (*single-channel shape*) is reproduced. However, it is insufficient because channels belonging to the same preamplifier board are correlated. Such a global effect across multiple channels is also considered.

The actual process that a noise waveform occurs would be too complicated and computationally costly. Instead, a simple model was adopted to approximate the *single-channel shape*; the sequence of white noise is filtered by using an LPF (low-pass filter) and HPF (high-pass filter). When the white-noise width is σ_w^{noise}, and the time constants of both filters are τ_{LPF} and τ_{HPF}, a noise waveform

is given by

$$
\begin{aligned}
w^{(1)}_{\text{noise}}[n] &= G_{\text{rand.}}(\sigma^{\text{noise}}_{w}) \\
w^{(2)}_{\text{noise}}[n] &= \begin{cases} w^{(1)}_{\text{noise}}[n] & (n = 1) \\ \alpha_{\text{LPF}}\, w^{(2)}_{\text{noise}}[n-1] + (1-\alpha_{\text{LPF}})\, w^{(1)}_{\text{noise}}[n] & (n > 1) \end{cases} \\
w_{\text{noise}}[n] &= \begin{cases} w^{(2)}_{\text{noise}}[n] & (n = 1) \\ \alpha_{\text{HPF}}\, w_{\text{noise}}[n-1] + \alpha_{\text{HPF}} \left(w^{(2)}_{\text{noise}}[n] - w^{(2)}_{\text{noise}}[n-1] \right) & (n > 1) \end{cases}
\end{aligned}
\tag{6.1}
$$

$$
\alpha_{\text{HPF}} = \frac{\tau_{\text{HPF}}}{\tau_{\text{HPF}} + \Delta t_{\text{step}}}, \qquad \alpha_{\text{LPF}} = \frac{\tau_{\text{LPF}}}{\tau_{\text{LPF}} + \Delta t_{\text{step}}},
$$

where n is incremented from 1 to 1024, which is the waveform length recorded by DRS4. Further, $G_{\text{rand.}}(x)$ is the random generator with the Gaussian probability density function with a width of x. $\Delta t_{\text{step}} = 1$ nsec is the time width between $n-1$ and n steps.

$\sigma^{\text{noise}}_{w}$, τ_{LPF}, and τ_{HPF} were tuned so that the Fourier power spectrum of the resulting w_{noise} becomes close to the data. Thus, $\tau_{\text{LPF}} = 18.5$ nsec and $\tau_{\text{HPF}} = 6.5$ nsec were selected, and then, $\sigma^{\text{noise}}_{w}$ was adjusted to 9.02 mV. Figure 6.1 compares a typical noise waveform generated by (6.1) with tuned parameters for an example noise waveform from the data, in addition with the averaged Fourier power spectra of both. There remains a small difference in the spectra; however, the waveform shapes look sufficiently similar.

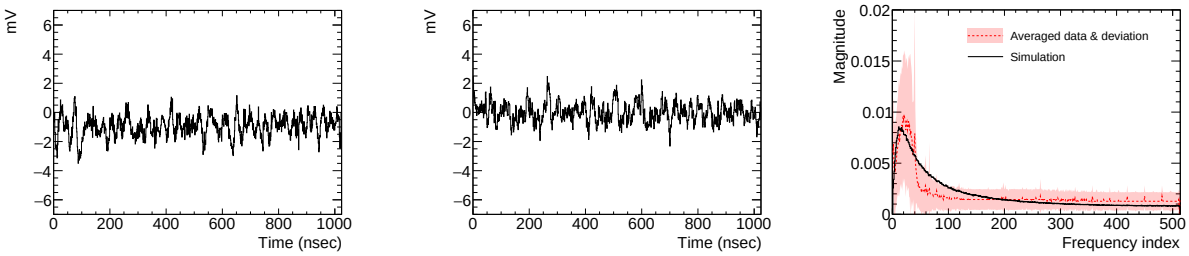

(a) Data **(b)** Simulation **(c)** Fourier power spectra

Figure 6.1: Comparison of noise waveforms of the data and simulation. (a) The data noise shape is well reproduced by (b) the simulation. (c) The averaged Fourier power spectra of both cases are compared. The dashed red line is the average of the data over all channels, and the red shade represents its standard deviation. The solid black line is the average of the simulated noise waveforms.

Next, to verify the correlation among channels, the noise waveforms from the data are accumulated over multiple channels: 8 channels from the same DRS4 chip, 16 channels from the same preamplifier and EROS board, and similarly, 32 and 64 channels. Figure 6.2 shows their projected distributions and their width as a function of the number of accumulated channels fitted with

$$
p_0\ (N_{\text{acc.}})^{p_1}\,, \tag{6.2}
$$

where $N_{\text{acc.}}$ denotes the number of channels used for the accumulation. p_0 and p_1 represent the width of the *single-channel shape* and the dependence on $N_{\text{acc.}}$. p_1 must be 1 if all noise waveforms

are completely independent; however, the fit results shows $p_1 = 0.64$. We assumed that channels belonging to the same preamplifier had both coherent and incoherent components, which are mixed as

$$w_{\text{noise}}^{\text{single}}[n] = f_{\text{coh.}}\, w_{\text{noise}}^{\text{coherent}}[n] + \sqrt{1-(f_{\text{coh.}})^2}\, w_{\text{noise}}^{\text{incoherent}}[n], \tag{6.3}$$

where $f_{\text{coh.}}$ is a mixising parameter, and both $w_{\text{noise}}^{\text{coherent}}$ and $w_{\text{noise}}^{\text{incoherent}}$ are different w_{noise}. $w_{\text{noise}}^{\text{incoherent}}$ is prepared for the individual channels separately, while the same $w_{\text{noise}}^{\text{coherent}}$ is shared by each of the 16 channels per preamplifier board. Further, $f_{\text{coh.}}$ was tuned to 0.49 so that the noise width evaluated from (6.3) reproduces the fitted trend in Figure 6.2(b) until $N_{\text{acc.}} = 1024$. Figure 6.3 shows that the simulated noise width is wholly consistent with the data.

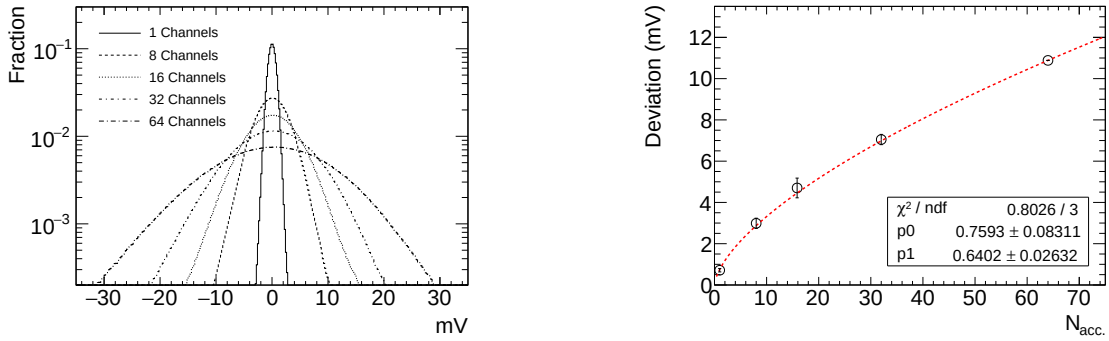

(a) Projected distributions

(b) Trend of the deviations

Figure 6.2: Accumulation of the noise waveforms of the data. (a) The horizontal axis is the waveform amplitude. The legend shows the number of accumulated channels $N_{\text{acc.}}$. (b) The width of each distribution depends on $N_{\text{acc.}}$ and is fitted by (6.2).

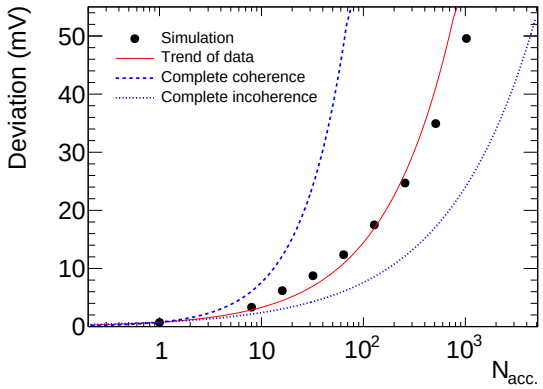

Figure 6.3: Comparison of the noise width between the data and the simulation. The horizontal axis is the number of accumulated channels. The simulation with the tuned mixing parameter between the coherent and incoherent components show a good agreement with the trend line of the data, which is the same as Figure 6.2(b). For reference, the dashed blue lines indicate the trends in both complete coherent and incoherent cases.

6.1.1.2 Signal Waveforms

The simulation generates true energy deposits and timings in the ECAL. We averaged the waveforms that had a significant signal pulse and created a signal waveform template as shown in Figure 6.4(a). After a noise waveform is formed, this template pulse is appended to it at the given timing in proportion to the energy. However, the energy and timing from the simulation are shaken beforehand such that we discuss how to reproduce the observed ECAL resolutions. Figure 6.4(b) is a typical waveform created with this procedure. The simulated waveforms are processed by the same reconstruction algorithms that are used for the data.

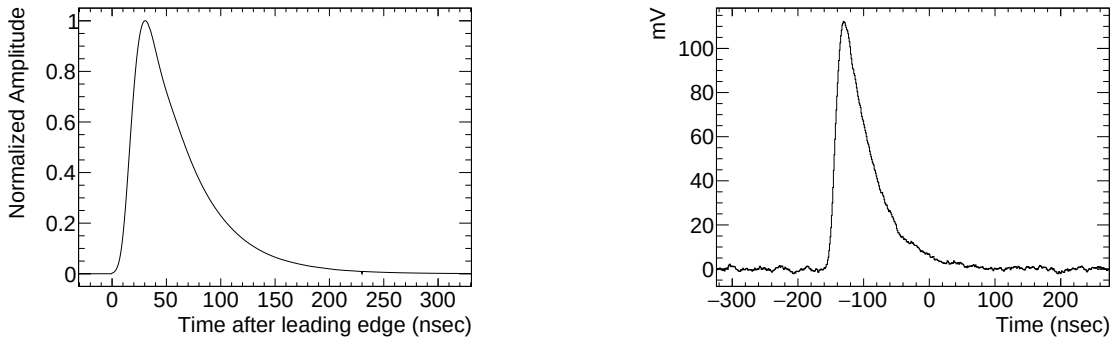

(a) Waveform template

(b) Simulated waveform

Figure 6.4: Formation of the ECAL signal waveform in the simulation. (a) The signal waveform template is created by averaging experimental data. (b) A signal pulse created with the template is added to a simulated noise waveform.

6.1.2 The ECAL Resolutions

6.1.2.1 Energy Resolution

The goal is to reproduce energy resolution curves in Figure 5.46 via the simulation. To this end, the energy resolution of a single crystal is assumed to be

$$\frac{\sigma_E^{\text{MC-cry.}}(e_{\text{MC}},\, r_{\text{MC}})}{e_{\text{MC}}} = \frac{a}{\sqrt{e_{\text{MC}}}} \oplus (b_0 + b_1\, r_{\text{MC}})\,, \tag{6.4}$$

where e_{MC} denotes the energy deposit from the simulation, and r_{MC} represents the distance between the energy-deposited position and the crystal center. The stochastic term with a depends on e_{MC} as in conventional; however, the so-called constant term with b has a linear dependence on r_{MC} for the hit-region dependence. We assumed $b_0 = 0$ because of Figure 5.45(f). A noise-related term is not included because it is expected to appear from the waveform baseline noise.

By scanning the resulting energy resolution, the parameters $a = 15.0\%\ \sqrt{\text{MeV}}$ and $b_1 = 0.23\%/\text{mm}$ were found to best reproduce the experimental results. These results are illustrated in Figure 6.5. The simulated resolutions are consistent with the experimental data within their uncertainties over all hit regions.

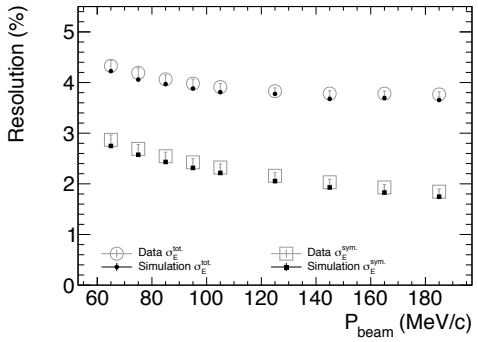

(a) `mix` hit region

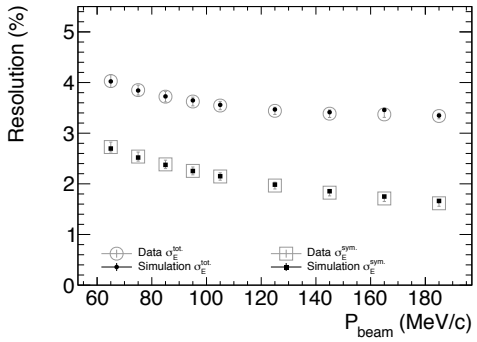

(b) `center` hit region

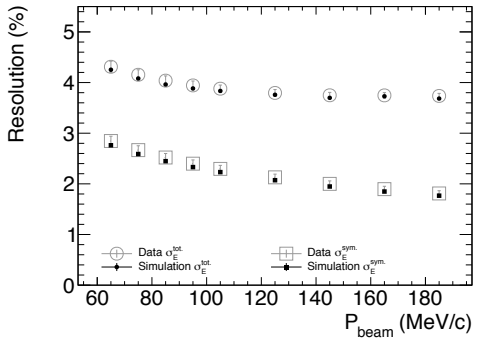

(c) `border` hit region

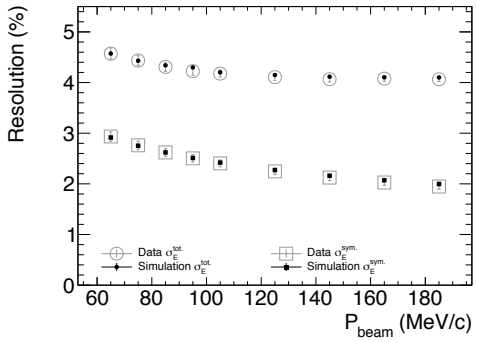

(d) `corner` hit region

Figure 6.5: Comparison of the energy resolution between the data and simulation for each hit region. The open points are the same as those in Figure 5.46, and the full points indicate the results from the simulation with the best-tuned parameters. Both the total (round markers) and symmetric (rectangular markers) parts are well reproduced.

6.1.2.2 Time Resolution

A single-crystal time resolution is tuned based on the analogy of the energy resolution. Although we obtained the single-crystal time resolution from data in Section 5.5.2, its expression (5.37) has a nonzero energy threshold and it includes the waveform-analysis effect, which are not adequate for simulation. Instead, parameters a and b were adjusted for the model,

$$\sigma_t^{\text{MC-cry.}}(e_{\text{MC}}) = \frac{a}{e_{\text{MC}}} \oplus b. \tag{6.5}$$

No term explicitly depends on the energy-deposited position because such a strong dependence was not observed.

The tuning result indicates that $a = 3.6$ nsec MeV and $b = 0.1$ nsec. Figure 6.7 compares the resulting time resolution with the data for each hit region. Yet again, it is consistent with the experimental data.

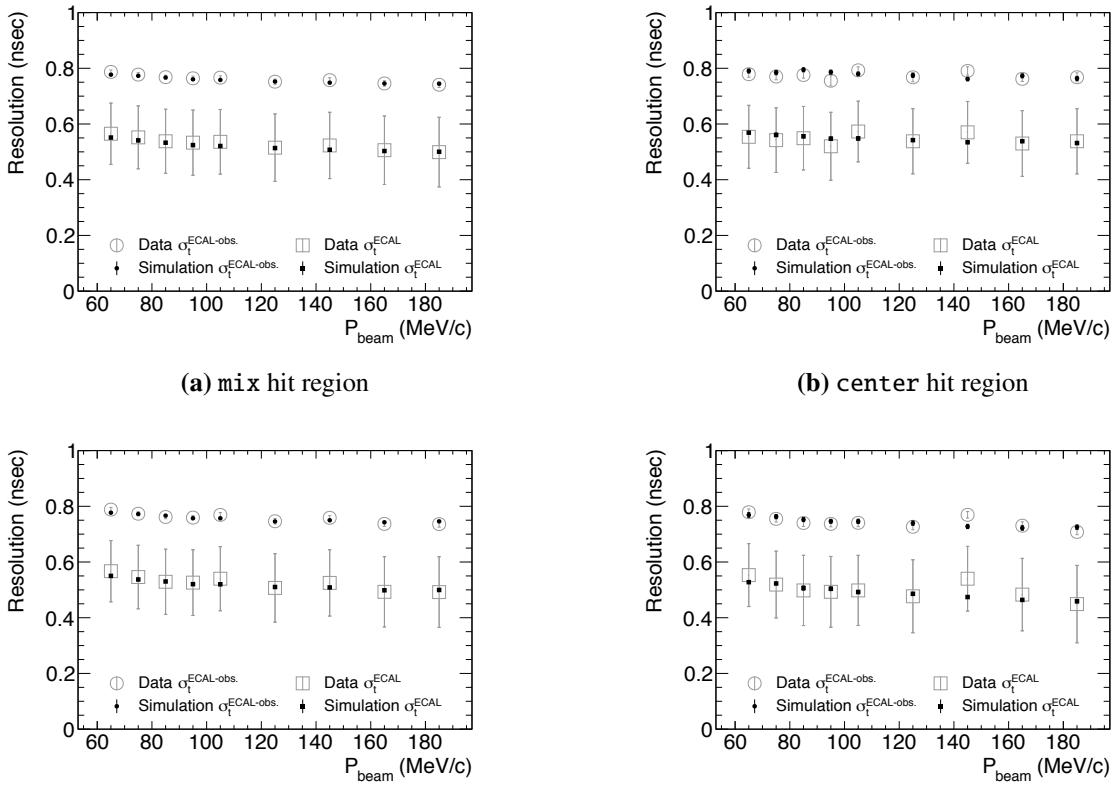

(a) `mix` hit region

(b) `center` hit region

(c) `border` hit region

(d) `corner` hit region

Figure 6.6: Comparison of the time resolution between the data and simulation for each hit region. The open points are the same as those shown in Figures 5.47 and 5.51; the full points indicate the results from the simulation with the best-tuned parameters. Both the observed (round markers) and pure (rectangular markers) parts are well reproduced.

6.1.2.3 Position Resolution

No direct fluctuation is applied to the simulation for the position resolution. However, it appears that the position resolution is almost determined by the ECAL geometry. Figure 6.6 compares the position resolutions on both axes between the data and the simulation after the application of (6.4) and (6.5). They are in agreement, and only the `corner` hit-region result slightly deviates from the target at low momenta; however, it is not significant.

6.1.3 Resolution of the Phase-II Straw Tube

We do not simulate the waveform generation for the straw tracker response because the waveform formation of gaseous detectors is complicated[1]. Therefore, we focused only on the spatial resolution via

[1] In the ECAL case, the scintillation photons appear instantly after the energy deposits within less than 1 nsec, and hence, the charge current flowing into the electronics has the same time structure. Therefore, the waveform template can be regarded as an impulse response. The deposited energies in the straw tube go through multiple steps with a time scale longer than that of the electronics. It is more difficult to obtain an appropriate impulse response, and it is lacking at present.

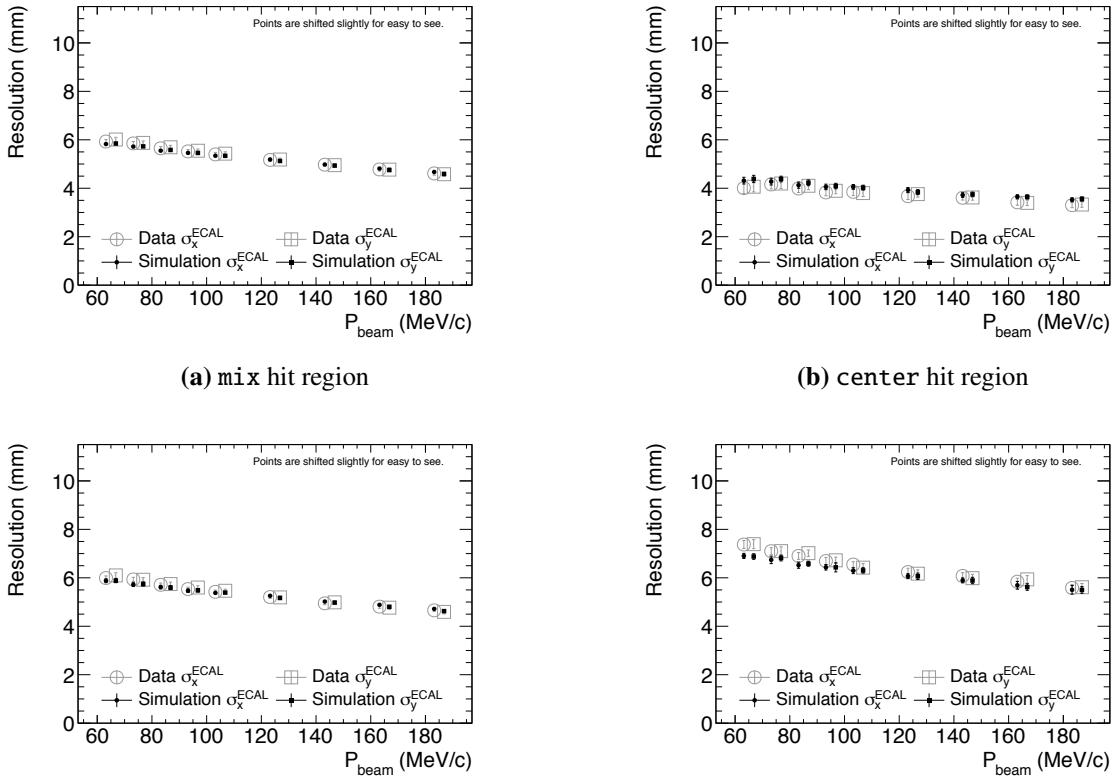

(a) `mix` hit region

(b) `center` hit region

(c) `border` hit region

(d) `corner` hit region

Figure 6.7: Comparison of the position resolution between the data and simulation for each hit region. The open points are the same as those shown in Figure 5.54, and the full points indicate the results from the simulation. The round (rectangular) points are the pure resolution on the X-axis (Y-axis).

the fluctuation in the drift time. The time resolution was estimated by considering the measurement aspects in (5.24). The hit timing t_{hit} is shifted by the drift time given by an X-T curve as $t_{\mathrm{hit}} + f_{\mathrm{XT}}(r)$ with a finite fluctuation of σ_t, where r denotes the DCA from the particle track to the wire.

Although σ_t obtained from the experiment is for the Phase-I straw tube whose diameter is 10 mm, it has to be extrapolated for the Phase-II straw tube with a diameter of 5 mm. Based on the discussion in Section 5.4.2.1, the terms related to the measurement—$\delta t_{\mathrm{const.}}$, $\delta t_{\mathrm{ROESTI}}$, and δt_{wf}—are assumed to be the same in the Phase-II case. However, the $\Delta t_{\mathrm{sync.}}$ dependence of $\delta t_{\mathrm{ROESTI}}$ is not included because the latest version of ROESTI does not have it. The remaining task is the reevaluation of the intrinsic term $\delta t_{\mathrm{int.}}$ for the Phase-II straw tube with Garfield++ and the X-T curve. We concluded to use Ar:C_2H_6 (50:50) and 2050 V for the gas mixture and applied HV in Phase-I. Its electric field in the Phase-I straw tube is equivalent to that arising from 1820 V in the Phase-II straw tube. We can use a higher voltage in the future; however, we conservatively adopt 1820 V in this study.

In addition, the magnetic field effect needs to be considered. The drifting behavior can vary based on the angle of the particle trajectory to the magnetic field direction. For investigating $\delta t_{\mathrm{int.}}$ for all possible cases, two angles θ and ϕ are defined against the magnetic field, as indicated in Figure 6.8. In addition, there is a charged-particle track and a magnetic field along the X-axis with a strength of B. The angles range from 0° to 90°, and the other values are converted into it via symmetry.

We ran 105 MeV/c electrons with random DCAs in the Garfield++ simulation to evaluate $\delta t_{\text{int.}}$ for several values of B, θ, and ϕ. Figure 6.9 shows some results and the corresponding spatial resolutions. $\delta t_{\text{int.}}$ does not differ considerably with B and θ; however, ϕ enhances the difference. The spatial resolutions finally result in similar values of around 100 μm because of the significant $\delta t_{\text{const.}}$.

Cases of muon and pion were also investigated. Since their $\beta = p/E$ varies around 100 MeV/c, the resolution for the momenta of 50, 75, and 100 MeV/c was also checked. They showed large differences in $\delta t_{\text{int.}}$; however, the consequent spatial resolution does not differ.

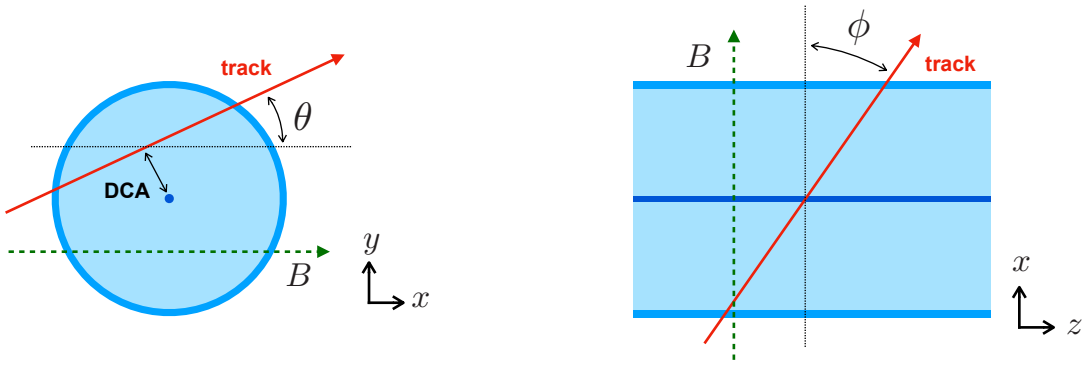

(a) Definition of θ **(b)** Definition of ϕ

Figure 6.8: Definition of the angles against the magnetic field in the straw tube for the Garfield++ simulation. The straw tube wire is aligned with the Z-axis, and the magnetic field is oriented towards the X-axis. When a charged particle passes through the straw tube, (a) θ and (b) ϕ are the angles between its trajectory and the magnetic field direction on the XY- and ZX-planes, respectively.

6.2 The COMET Software Framework: ICEDUST

We have been developing the COMET official software framework ICEDUST. The tools for producing simulation data for this study include the `Geant4`-based full simulator (`SimG4`), event merger (`SimHitMerger`), and detector response simulator (`SimDetectorResponse`). First, `SimG4` simulates all particle flights, decays, and interactions in the full COMET geometry: from the proton-beam injection to the energy deposits into the detectors. We refer to a set of simulated objects that originate from a POT (proton on target) as a POT event, and the `SimG4` repeats the simulation POT by POT. However, from a practical point of view, a large number of POT events constitute a single beam bunch. `SimHitMerger` combines such bunched POT events into "merged" events based on realistic beam time structure. Finally, `SimDetectorResponse` processes the merged events to simulate realistic detector responses from the `SimG4` hits.

6.3 SimG4: Geant4-based Simulation Software

`SimG4` is the most fundamental simulation software based on `Geant4` for all COMET simulation studies.

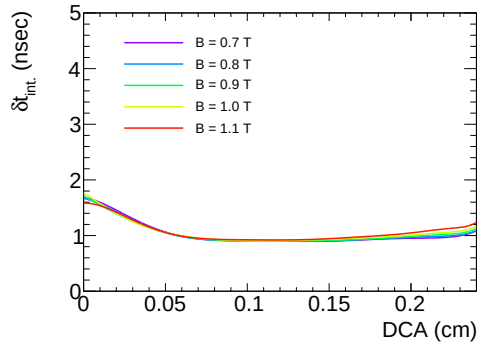

(a) Intrinsic time fluctuation for magnetic fields

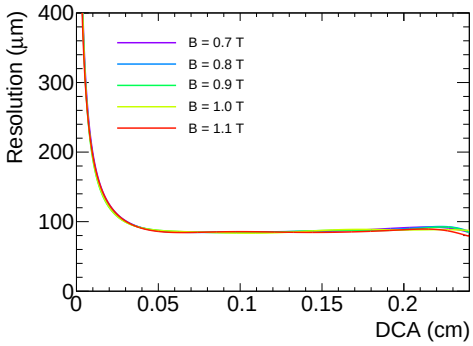

(b) Spatial resolution for magnetic field

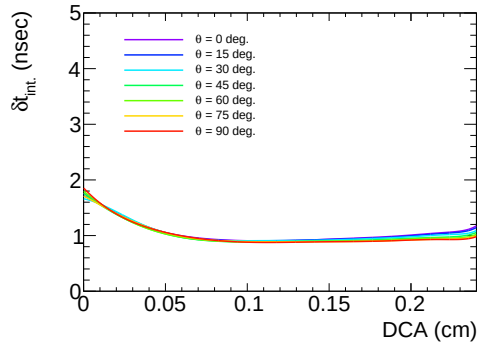

(c) Intrinsic time fluctuation for θ

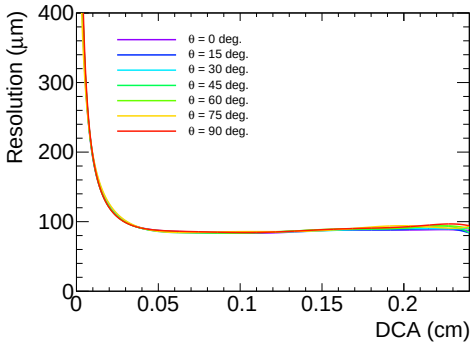

(d) Spatial resolution for θ

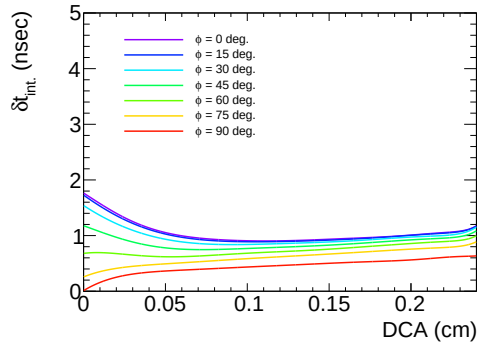

(e) Intrinsic time fluctuation for ϕ

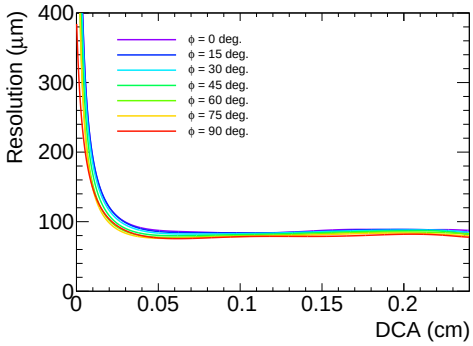

(f) Spatial resolution for ϕ

Figure 6.9: Intrinsic time fluctuation and spatial resolution estimated by the Garfield++ simulation for the Phase-II straw tube to which 1820 V is applied. (a, b) The magnetic field strength B; (c, d) θ; and (e, f) ϕ are changed from the default setup in which $B = 1.0$ T and $\theta = \phi = 0°$. Only ϕ contributes the most significant difference in the intrinsic time fluctuation, while the resulting spatial resolution does not differ from about 100 μm.

6.3.1 Geometry and Magnetic Field

Figure 6.10 shows the entire Phase-II geometry in `SimG4`. The small figure at the bottom left includes the experimental facility as well. The central figure shows the beamline, which starts from the point where the beam protons are injected. The size and position of the pion production target have been optimized by the collaborators to maximize the number of muons stopped at the target disks (radius

and length of these disks = 4 mm and 25 cm, respectively). Collimators installed in the muon transport solenoid with the optimized magnetic field create low-momentum muons that are easy to stop at the muon stopping target. The aluminum muon-stopping-target disks with a radius of 10 cm and a length of 0.2 mm are lined up with 17 pieces every 5 cm, and they are followed by the tungsten beam blocker with a radius of 20 cm and a length of 4 cm. There are 13 γ collimators around the wall of the muon stopping target section, which are equally spaced from the beam blocker to the electron spectrometer. They shield the electron spectrometer from the secondary γ-rays and the electron–positron pairs from the beam blocker. The DIO blocker at the bottom of the spectrometer stops the downwardly shifted low-momentum particles. In the detector solenoid, the straw tracker has five stations that are 110 cm apart from each other; the ECAL is located as close to the final straw station as possible. Finally, the cosmic-ray veto surrounds the detector solenoid.

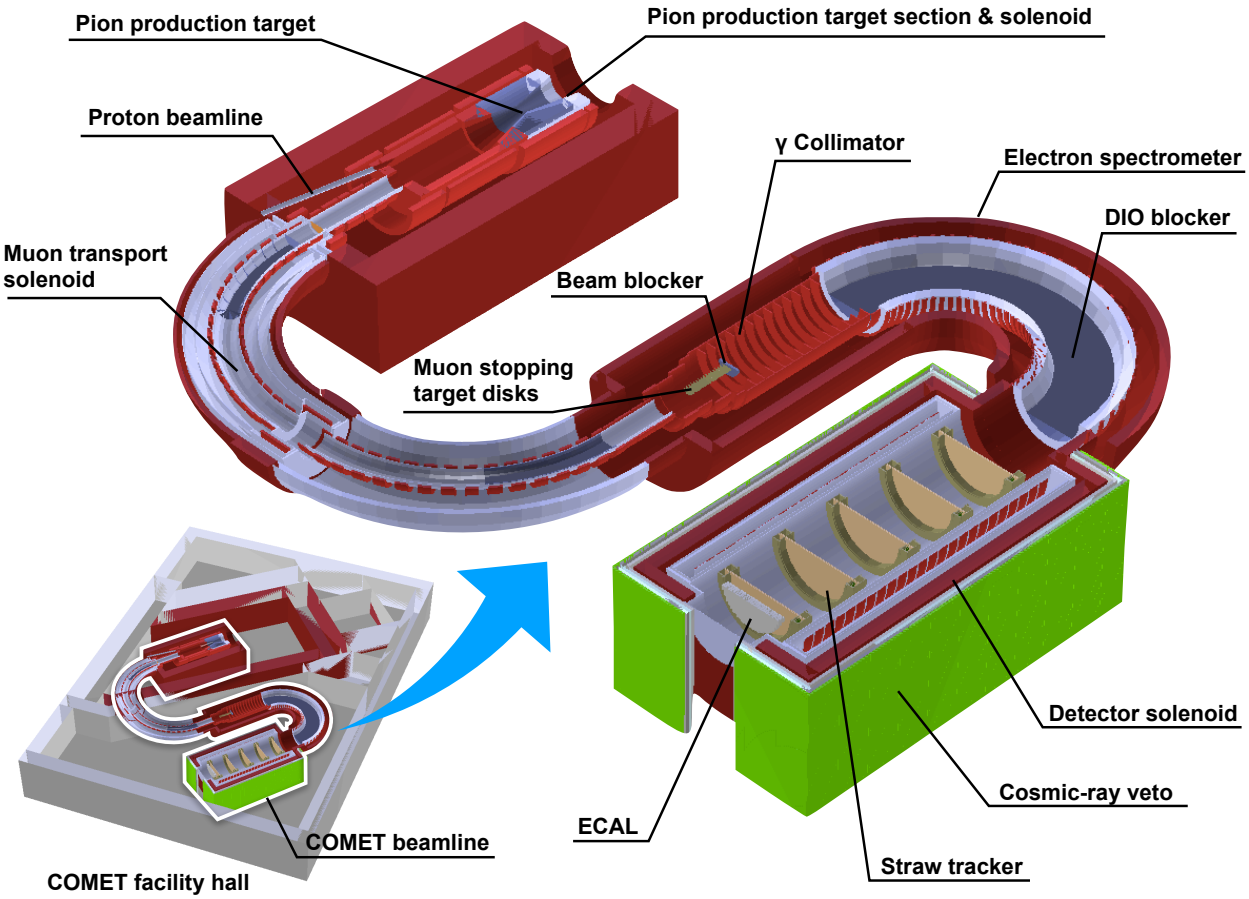

Figure 6.10: Geometry of COMET experimental hall constructed in `SimG4`. The geometry contains all walls around the beamline as shown at the bottom left. See the text for details of every component.

The magnetic field is introduced into `SimG4`. A part of the field was supplied by the solenoid manufacturer, and the other parts were calculated by the collaborators. Figure 6.11 displays the full magnetic field and its several crucial components. The first figure indicates the magnitude of the entire field used for the simulation on the ZX-plane. The strength is up to 5 T around the pion production target, and it decreases by 2 T until the muon transport solenoid to capture and transport the pions

produced backwardly. Further, it decreases by 1 T around the muon stopping targets to enlarge the trajectory radius of the electrons emitted from them. This helps the electrons to go beyond the beam blocker efficiently and prevents them from losing their energy in the targets. The field decreases down to 1 T at the spectrometer entrance and is maintained at this value until the end. There are correcting dipole magnet fields in both bent solenoids, and their fields are shown in Figure 6.11(b). However, the dipole field in the electron spectrometer has never been calculated entirely. Although a uniform but unrealistic dipole field was used in the previous study [6], it was replaced in this study with the dipole field of the muon transport solenoid by modifying its dimensions so that it fits the geometry. Yet, it is incomplete, and it should be corrected by future works. The strength of the dipole fields was optimized by the collaborator to transport particles properly; the typical vertical strength is 0.056 and 0.042 T in the first and second halves of the muon transport solenoid, respectively, and it is −0.195 T in the electron spectrometer. Figure 6.11(c) displays the field map in the detector solenoid. The nearly uniform field of 1 T forms ideal helix trajectories and helps the reconstruction; however, a small deviation around the end distorts the trajectory.

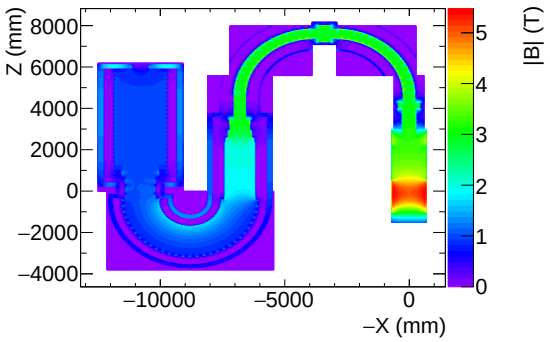

(a) Magnitude

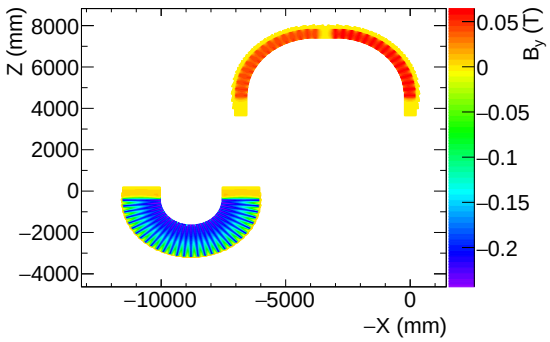

(b) B_y of the dipole magnet field

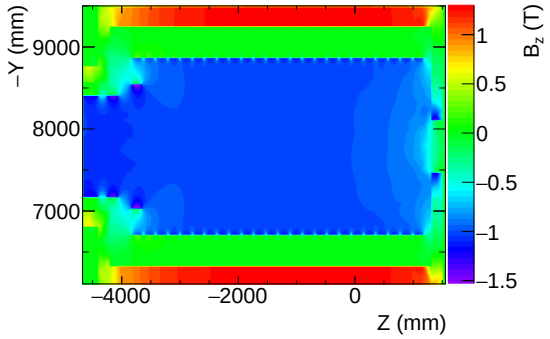

(c) B_z in the detector solenoid

Figure 6.11: Magnetic fields in `SimG4`. (a) Magnitude of the whole field in the full geometry. (b) Vertical component of the dipole fields applied in both bent solenoids. (c) Component along the beam axis in the detector solenoid. See the text for details.

6.3.2 Simulation of POT Events

The simulation per POT event starts with an 8 GeV proton. The proton-beam profile was prepared by a collaborator; its horizontal and vertical sizes are 1.46 and 1.36 mm, respectively. `SimG4` has the "`RooTracker`" mechanism to accelerate the simulation. It separates the simulation into several regions along the beamline. When a particle leaves a region, its tracking stops; however, all its information is saved into a `RooTracker` file. The simulation for the next region starts from such `RooTracker` data. Changing the seed value for the random generator in `SimG4` can introduce multiple different simulation results from even a single `RooTracker` file. By repeating this reseeding in each region, we prepared 4.1×10^{10} POT events in the last detector-solenoid region.

6.3.3 Simulation of Signal Events

The signal event needs to contain a 105 MeV signal electron of μ-e conversion in a muon stopping target disk and the associated hits in StrECAL. Such events are not produced in the POT-event simulation. First, we sampled both the position and timing of the muons that stopped in the disks in the simulated POT events, and we saved them as `RooTracker` data. Then, the number of stopping muons per POT was evaluated as 3.8×10^{-3}, which denotes the muon stopping efficiency. Figure 6.12 shows the stopping position distributions, and every disk has a nonuniform distribution. Next, the signal-event simulation starts from this `RooTracker` data. 17.5% of all simulated events can reach the ECAL, and it corresponds to geometrical acceptance. Finally, only those signal events are mixed with the POT events in the next section.

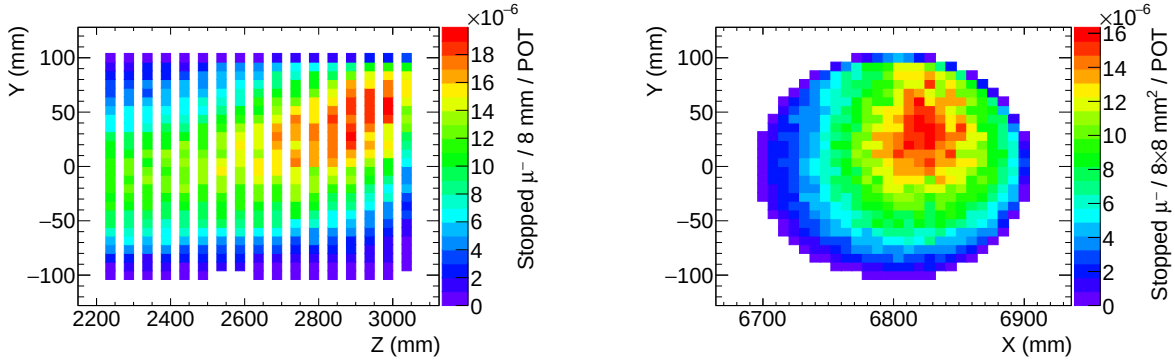

(a) Projection on the ZY-plane

(b) Projection on the XY-plane

Figure 6.12: Muon stopping position distribution. In the coordinates, the Z-axis is along the beamline, and the X- and Y-axes represent the horizontal and vertical directions perpendicular to it. The color of each bin indicates the muon stopping rate per POT. (a) The distribution projected on the ZY-plane shows different concentrations depending on the position Z. (b) All distributions over all 17 disks are projected on the XY-plane.

6.4 SimHitMerger: Event Merger

`SimHitMerger` congregates many POT events and creates merged events with the bunched-beam time structure. The number of protons in a single bunch is calculated as follows.

Since the proton energy and power are planned to be 8 GeV and 56 kW in the Phase-II experiment, the number per second is

$$\frac{56 \times 10^3 \text{ W}}{8 \times 10^9 \text{ eV} \times 1.6 \times 10^{-19} \text{ C}} = 4.375 \times 10^{13} \text{ sec}^{-1} .$$

The COMET beam operation fills only four out of the nine buckets of the J-PARC main ring whose bunch-to-bunch distance is 585 nsec. Then, the designed bunch distance of 1170 nsec is realized in most of the bunches; however, it is precisely $585 \times 9/4 = 1316.25$ nsec on average. It is assumed that the Phase-I beam operation is available in Phase-II; a single beam spill lasts 2.48 sec, from which the protons are extracted for 0.5 sec into the COMET beamline. This implies that the number of bunches per second is

$$\frac{0.5 \text{ sec}}{2.48 \text{ sec}} \times \frac{1}{1316.25 \text{ nsec}} = 1.53 \times 10^5 \text{ sec}^{-1} .$$

Therefore, the number of POTs per single bunch is calculated as $4.375 \times 10^{13} / 1.53 \times 10^5 = 2.86 \times 10^8$.

A merged event has to contain more than one bunches because long-lived particles mix with particles from the succeeding bunches. We accumulate 20 bunches per merged event. Figure 6.13 demonstrates how they accumulate by 20 bunch injections. The horizontal time axis starts from the first bunch injection, and the vertical axis counts the number of particles entering the ECAL per 10 nsec, which indicates the hit rate. In reality, there is a 1755 nsec bunch interval; however, conservatively, we ignore its effect and line up all bunches in the same span of 1170 nsec. The colored lines associate with electrons, muons, gammas, and neutrons. The neutrons dominate the hit rate, while their energy deposit into the ECAL via neutron capture is less than a few tens MeV. After the 15th bunch, the accumulation is almost saturated. In the following, only the data between the 19th and 20th injections will be used by placing the timing window there. Moreover, a single signal electron track from the signal events is merged into the timing window for each merged event.

Finally, the following point should be noted even though it is a technical issue. Because even a single merged event requires $20 \times 2.86 \times 10^8$ POT events, `SimG4` has to take a considerably long time to produce many POT events sufficiently for more than thousands of merged events. Therefore, we reused the same POT events for different merge events by changing their merging timing. It can still realize different phases of BG tracks for the signal electron. With this technique, we created 7.5×10^4 merged events.

6.5 SimDetectorResponse: Detector Response Simulator

`SimDetectorResponse` provides realistic fluctuations to the hit information from `SimG4`, and it generates digitized data that indicate what we will obtain from the experiment. It contains all procedures that were described in the beginning of this chapter to simulate the StrECAL detector response. For instance, Figure 6.14 is a typical ECAL waveform digitized by `SimDetectorResponse`, where the signal electron-induced pulse is around 22100 nsec with several pile-up BG pulses.

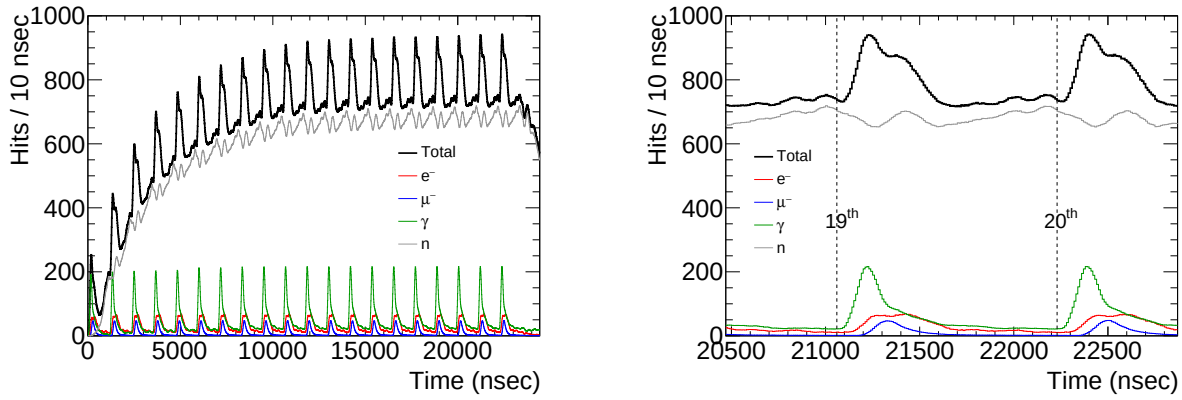

(a) All bunches

(b) Focused on between 19th and 20th bunches

Figure 6.13: ECAL hit rate by 20 bunch injections as a function of time. The horizontal and vertical axes are the time after the first bunch injection and the number of ECAL hits per 10 nsec. The colored lines associate with four cardinal particles, electrons, muons, gamma rays, and neutrons, and the bold line indicates the total amount. The hits accumulate because they cannot diminish fully within the bunch separation of 1170 nsec.

`SimDetectorResponse` is also designed to simulate a realistic triggering procedure; however, it was not used because it would also be a massive study item. In this study, we assumed that `SimDetectorResponse` could trigger properly when every signal electron hit the ECAL. However, it is too naïve an assumption that the trigger system can capture all signal electrons, no matter when they come and no matter how many BG hits contaminate the ECAL. Therefore, we will estimate the trigger effect on the acceptance.

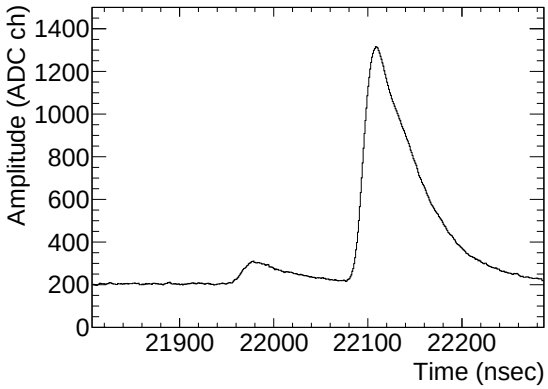

Figure 6.14: Typical ECAL waveform of a merged event. The most significant peak at 22100 nsec is associated with a signal electron, and the others are pile-up BGs.

6.6 Signal Acceptance of the Triggering

The trigger criteria are determined using the simulation data created by `SimG4`. The criteria comprise the timing window and an energy threshold. First, we check their acceptance of the signal electron that reaches the ECAL. Second, we evaluate the trigger rate generated by the beam particles. Finally, we draw a conclusion by considering both the signal acceptance and the trigger rate.

The timing window needs to be as wide as possible to look for more signal electrons. However, the faster the timing window, the more exposed ECAL is to the beam BGs. This results in a high trigger rate compared to what the electronics can handle, and a considerable number of pile-up hits in the ECAL cannot be separated easily. In the previous study [6], the timing window between 600 and 1200 nsec was suggested. This study also follows the same timing window but checks its feasibility in terms of the trigger rate.

6.6.1 Signal Acceptance

Figure 6.15 shows the probability distributions of the timing and total energy deposit when the signal electrons reach the ECAL. They were created from the signal events reported in Section 6.3.3. Some of the signal electrons are too early to enter the timing window. In addition, Some may lose their energy significantly by interacting with materials or deposit only low energy by escaping from the ECAL. Therefore, the trigger system needs to have a high energy threshold to suppress the trigger rate, which causes it to not capture them. These aspects consequently limit signal acceptance.

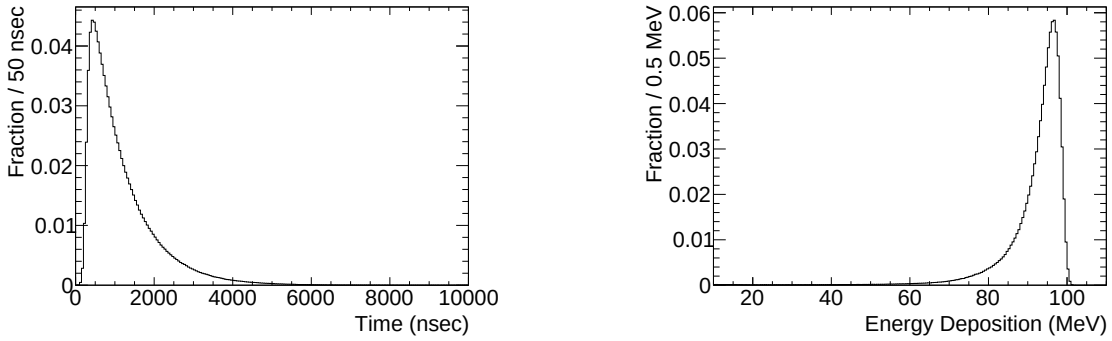

(a) Timing

(b) Energy deposit

Figure 6.15: Distributions of (a) the hit timing and (b) total energy deposit of signal electrons reaching the ECAL. They are sampled from the signal events simulated by `SimG4`.

Figure 6.16 shows the signal acceptances as functions of the timing-window start and energy threshold. The calculation of the timing-window acceptance involves all entries in the periodic range from $600n$–$1200n$ nsec (n = 1, 2, ...) if taking 600 nsec as the timing-window start. A variation of the timing-window start changes its acceptance linearly. However, because most of the signal electrons deposit sufficiently high energy, the energy-threshold acceptance is relatively stable along the energy threshold below 70 MeV.

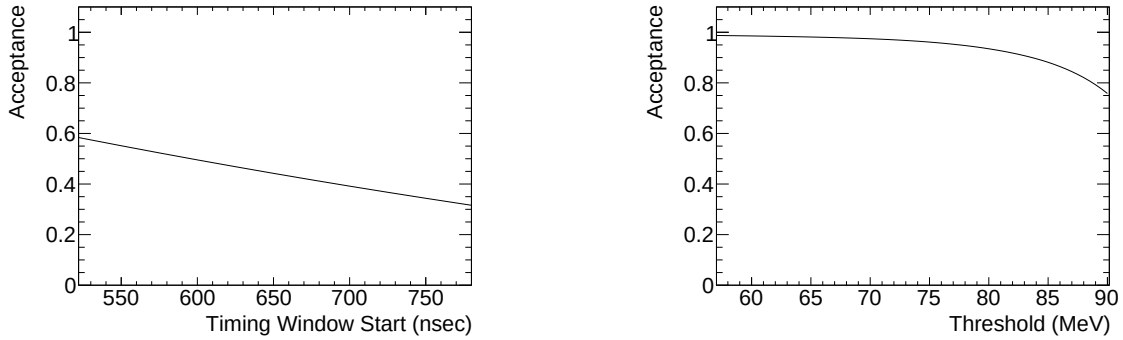

(a) Timing-window start

(b) Energy threshold

Figure 6.16: Signal acceptance caused by the ECAL triggering as a function of (a) the timing-window start and (b) energy threshold. The end of the timing window is fixed at 1200 nsec.

6.6.2 Trigger Rate and Pile-Up

Figure 6.17(a) shows the distribution of the energy deposit and hit timing for the individual beam particles between the 19th and 20th bunch injections. The values denote the particle hit rate per bunch. The timings on the left-side ends on the X-axis and the dashed line represents each bunch injection timing. The concentration after each bunch injection will be masked with the timing window. The trigger rate is calculated by integrating part of the distribution and dividing it by the number of bunches per second. Figure 6.17(b) shows it as a function of the timing-window start and energy threshold. Although the COMET Phase-I trigger electronics requires the trigger rate to be a few tens of kilohertz at most, we expect that it will be upgraded to handle up to 100 kHz in Phase-II. When using 600 nsec for the timing-window start, we need to use at least an energy threshold above 70 MeV.

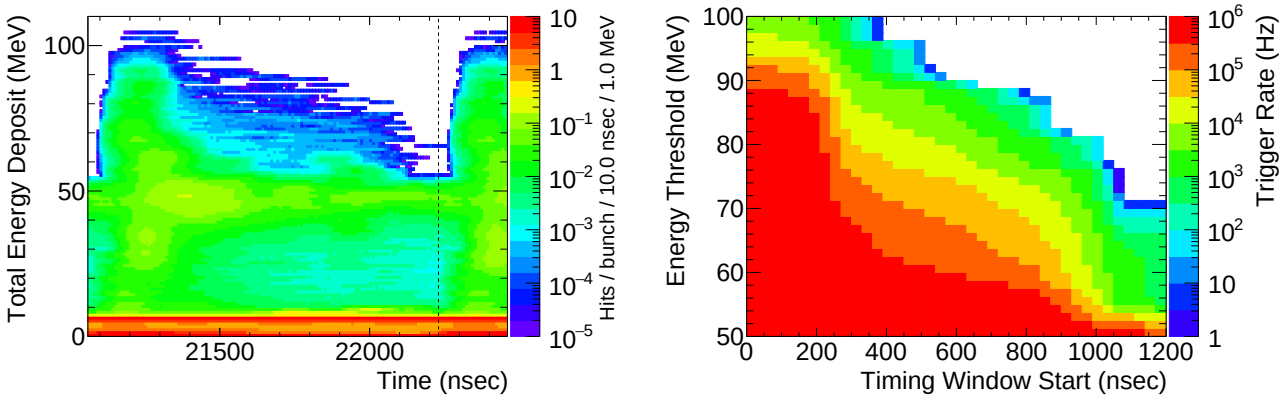

(a) The number of hits per bunch as a function of the total energy deposit and the timing

(b) Trigger rate as a function of the timing-window start and energy threshold

Figure 6.17: Trigger rate estimated from the energy deposit and timing by the individual beam particles. (a) The color of each bin indicates the number of particle hits per bunch. The timings at the left-side end on X-axis and the dashed line represents the 19th and 20th bunch injections. (b) The color of each bin indicates the trigger rate as a function of the timing-window start and energy threshold.

In addition to the trigger rate, the pile-up rate in the ECAL needs to be kept low. We defined the following "cluster separation" estimator to evaluate the amount and severity of the pile-up hits.

$$(\Delta_{\text{clst.}})^2 = \frac{|\boldsymbol{r}_\text{A} - \boldsymbol{r}_\text{B}|^2}{(\delta x_\text{A})^2 + (\delta y_\text{A})^2 + (\delta x_\text{B})^2 + (\delta y_\text{B})^2}. \tag{6.6}$$

Figure 6.18 illustrates the definition of the variables. When two independent particles hit the ECAL in a close distance and timing, their energy clusters A and B may cause a pile up, where $\boldsymbol{r}_i$, δx_i, and δy_i ($i = A$ or B) denote their center positions and two-dimensional sizes under standard deviation, respectively. (6.6) indicates the distance normalized by their size, and it should be as large as possible.

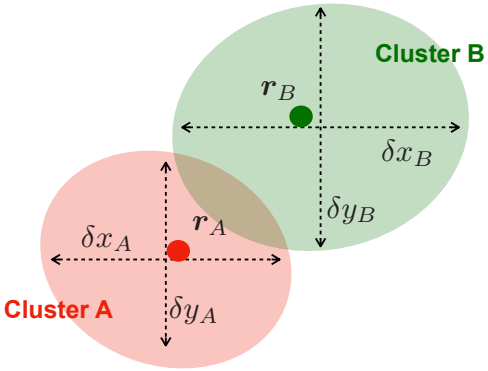

Figure 6.18: Definition of the cluster separation estimator. There are two piled-up energy clusters A and B. The markers indicate each position $\boldsymbol{r}$ and the arrows indicate each standard deviation as its size for each axis δx and δy. The cluster separation is defined as the distance between them normalized by their sizes.

Figure 6.19(a) shows the distribution of the cluster separation and timing of all cluster pairs whose timings are closer than 10 nsec. There are many clusters after the bunch injection that have low separation. In such a scenario, the waveforms may be so heavily piled-up that they can hardly be separated easily. Figure 6.19(b) shows the integration of Figure 6.19(a) as a function of the timing-window start for several upper limits on $\Delta_{\text{clst.}}$. All curves drop to less than 10% at 600 nsec and become relatively stable compared to those before 400 nsec. We concluded to use the timing window from 600–1200 nsec with the energy threshold of 70 MeV for the trigger. Then, the signal acceptance caused by the triggering was estimated at 0.482 = 0.495 (timing window) ×0.975 (energy threshold) from Figure 6.16.

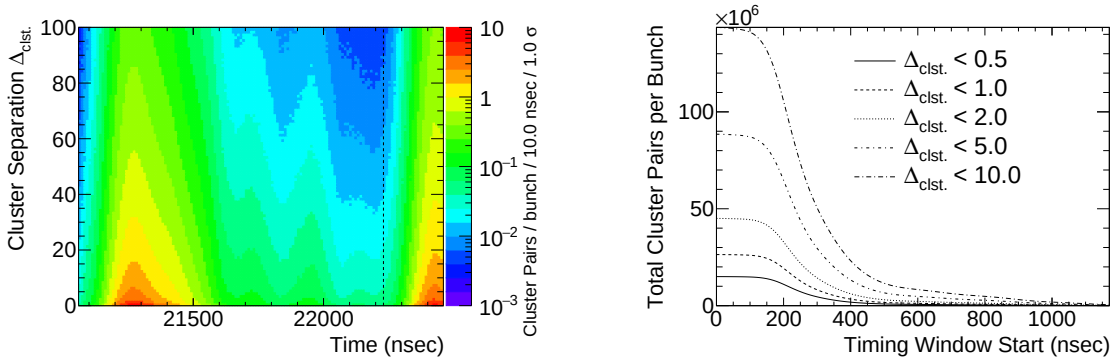

(a) Cluster separation estimator vs timing

(b) Total cluster pairs

Figure 6.19: Estimation of cluster pile up. (a) The cluster separation estimator has greater values after each bunch injection. The color of each bin indicates the number of pile up cluster pairs per bunch. The timings at the left-side end on the X-axis and the dashed line represent the 19th and 20th bunch injections. (b) The lines indicate the total number of cluster pairs cluster pairs as a function of the timing-window start by integrating (a) with upper limits on the cluster separation of 0.5, 1.0, 2.0, 5.0, and 10.0.

7

Reconstruction

This chapter discusses the schemes to reconstruct the tracks of the signal electron for the StrECAL hits and the performance. The schemes are divided into `ReconECAL` and `ReconStrawTrk` packages in ICEDUST. The goal of `ReconECAL` is to determine and reconstruct signal-like energy clusters and supply their timings to `ReconStrawTrk`. `ReconStrawTrk` uses each reconstructed cluster as the seed information to find candidate hits that appear to build a track and fit a track to them to reconstruct its momentum.

Both reconstruction packages utilize MVA (multivariate analysis) techniques. First, we explain their fundamental idea followed by the details of the reconstruction algorithms. In the end, we apply several quality cuts to further eliminate the reconstructed objects induced by BG hits.

7.1 Multivariate Analysis and Machine Learning

Recently, many experiments have been adopting machine learning techniques to perform MVA in their data analysis. There are two types of requirements for using machine learning: "classification" and "regression." In the former, the output is a single Boolean value that separates an input event into signal-like or background-like event. The latter provides a continuum value appropriate for each set of input variables. In other words, it is equivalent to fitting an arbitrary function to multidimensional data points.

There are several architectures associated with machine learning. These architectures are "trained" with their own mathematical algorithms to optimize their output[1]. For the reconstruction in this study, we attempted designing an ANN (artificial neural network) with MLP (multilayer perceptron), BDT (boosted decision tree), and GBDT (gradient boosting decision tree), which is a derivative of BDT. ANN originated from a mathematical model of the human brain, wherein cells called neurons are connected in a complex manner and they transfer electrical signals to each other to create ideas. MLP is the most common implementation of ANNs and comprises multiple layers with multiple neurons or cells. BDT and GBDT are types of algorithms that exploit many binary decision trees.The

[1] In this content, we discuss only "supervised learning," wherein the dataset of inputs and corresponding outputs are prepared in advance. The explanation about "unsupervised learning" is beyond the scope of this thesis; the reader can refer to textbooks for the same.

fundamental ideas of both architectures are briefly discussed in Appendix B. Furthermore, because we used the `TMVA` [89] toolkit that provides a universal interface for multiple machine-learning algorithms for training and evaluating them, it is recommended to read its users guide.

There are several parameters to design the MLP and BDT, and we optimized some of them to maximize each performance. For MLP, every cell has a function to activate itself with the inputs from the previous layer; we compared two shapes for it: the sigmoid and hyperbolic tangent (tanh) functions. We name MLPs using each of them `MLPsig` and `MLPtan`. Although the numbers of hidden layers and cells in each layer are arbitrary parameters, only two hidden layers with $n_{\mathrm{var}} + 5$ and n_{var} cells were used in this study, where n_{var} denotes the number of input variables. For BDT and GBDT, some combinations of the depth of every decision tree and number of trees were optimized. Below, they are denoted as `BDT` and `BDTG.DepthXX.NTreesYYYY`, where `XX` and `YYYY` are the former and latter values, respectively.

We prepared 2.5×10^4 merged events to train the MVA schemes. They differ from those prepared for the analysis, and they are divided evenly into training and testing event samples. When training the schemes with the first half, the `TMVA` tests their performance with the other.

7.2 ReconECAL: Reconstruction for the ECAL

`ReconECAL` is divided into five parts. First, it performs waveform fitting to separate piled-up hits and extract each charge information. Second, it roughly collects the extracted hits that have occurred and are from the same origin. The next two parts combine some of these extracted hits to reconstruct energy clusters and examine if they are associated with the signal electron by utilizing the MVA classification technique. We compared several MVA methods with different options and optimized several parameters for them to maximize performance. Finally, the "shower" object is reconstructed from every cluster. The shower reconstruction finds the incident angle of the hit particle[2] and corrects the energy leakage from the ECAL by using the MVA regression technique.

7.2.1 Waveform Fitting

In the COMET situation, even a single waveform can contain multiple peaks because of the piled-up hits, and we cannot use a simple waveform analysis such as that used in Section 5.3.1. Waveform fitting aims to separate the waveforms and extract each signal strength separately. To model the function to fit the waveforms, we averaged many waveforms without pile-up and created a waveform template[3]. The pile-up separation is accomplished by fitting multiple templates simultaneously to all peaks in a waveform. However, unless all peak positions are determined well before the fitting, the fitting with the minimum chi-square method tends to fall into an incorrect local minimum. Therefore, we developed a simple peak search algorithm.

[2] In other words, the direction the electromagnetic shower grows in the ECAL.

[3] In principle, this template results in the same output as that of the waveforms generate with `SimDetectorResponse` in Section 6.1.1.2.

The peak search and waveform fitting proceed as follows, and Figure 7.1 demonstrates it with a typical example of the waveform that has piled-up hits.

1. The highest peak is detected, and its position and wave height are obtained.
2. The template is fitted locally with them as the initial parameters to the waveform.
3. The second maximum peak is located by subtracting the fitted template from the waveform.
4. By combining the second peak's parameters with the first peak, the original waveform is fitted again, wherein the first peak position is fixed.
5. The procedure above is repeated until the maximum height becomes less than the noise threshold $3\sigma_{\text{noise}}$, where $\sigma_{\text{noise}} = 0.7$ mV is the standard deviation of the baseline noise.
6. Multiple templates are fitted simultaneously to all identified peaks by loosely limiting the fit parameters around each peak; the peak positions are then eventually determined.

Figure 7.2 shows two more examples via the same procedure.

The fit results yield the decomposed peak heights that are converted into energy using calibration coefficients. In this study, we used a single constant for them, and it is the reciprocal of the conversion factor between the fluctuated energy deposits and the waveform amplitudes used in `SimDetectorResponse`.

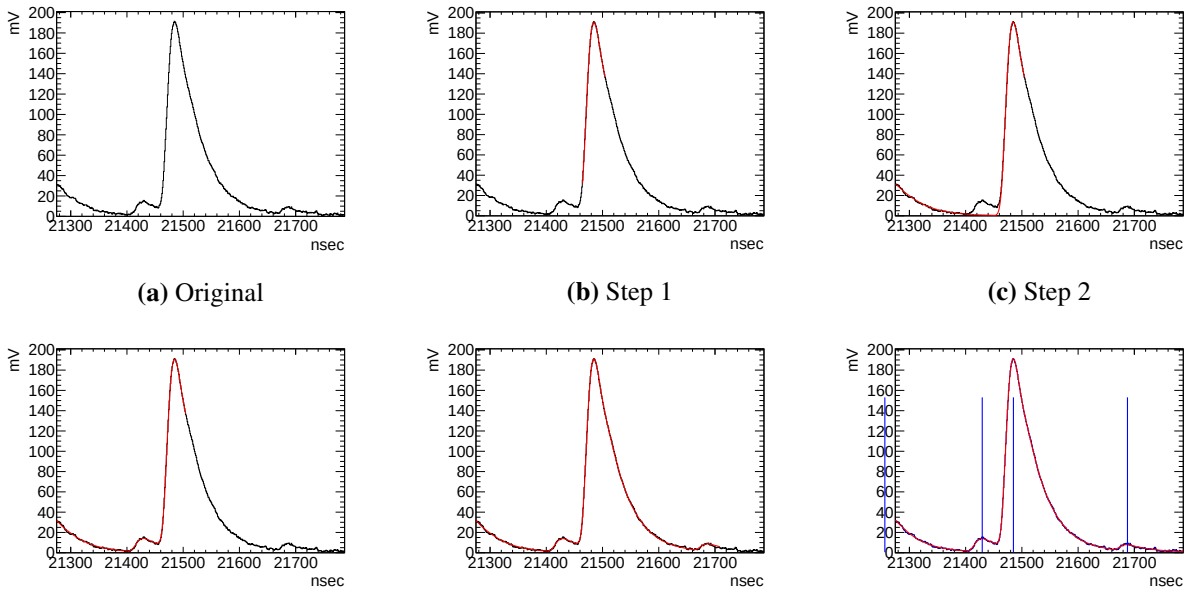

(a) Original **(b)** Step 1 **(c)** Step 2

(d) Step 3 **(e)** Step 4 **(f)** Overall Fitting

Figure 7.1: Procedure of the peak search for a piled-up waveform. From (a) the waveform, (b-e) individual peaks with heights exceeding the noise threshold are fitted (red lines) in the order of their wave height. Finally, (f) the entire waveform is fitted with all determined peaks, and the positions are indicated by the blue lines.

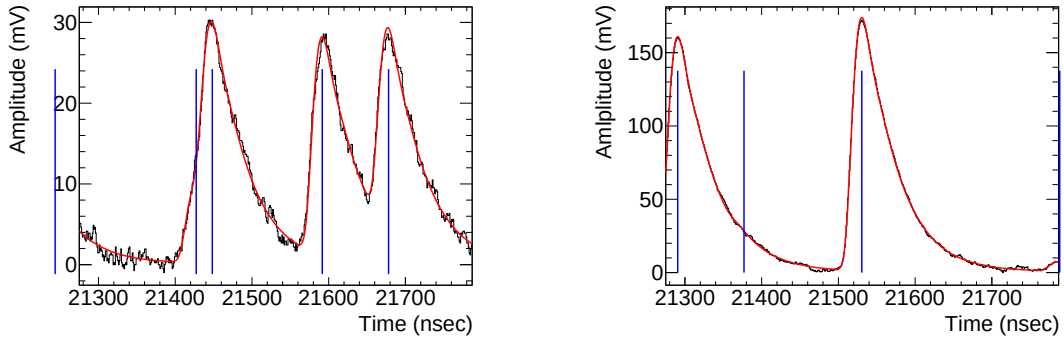

(a) Sample 1 **(b)** Sample 2

Figure 7.2: Examples of waveform fitting. The waveforms (black line) are fitted by the waveform template (red line). The blue lines indicate the positions found by the peak search. Signals in (a) and (b) are relatively weak and strong compared to the baseline-noise amplitude.

7.2.2 Timing-Based Peak Merging

Owing to many BG hits, the number of fitted peaks is considerably high to pass them directly to the clustering step. Therefore, `ReconECAL` performs the first hit selection based on the timings when the peaks arise. The electron showers that we target in this study grow and yield energy deposits instantly in the ECAL. We do not have to consider the relationship of the temporally separated peaks.

The hits with similar peak timings are combined into a hit selection with the procedure illustrated by Figure 7.3. First, the fitted peak information is added into histograms. Figure 7.3(a) shows the multiplicity of the peaks obtained from an event. Then, the black histogram in Figure 7.3(b) shows the total energy in each bin. Second, for every bin, the entries belonging to it and its neighboring four (±2) bins are collected. This range considers the timing fluctuation of the waveform fitting, and it is sufficient to hold all plausible peaks. Finally, if a bin has a total energy of more than 35 MeV, one dataset is built from its entries. In the red histogram of Figure 7.3(b), the peaks belonging to every nonempty bin constitute a hit selection.

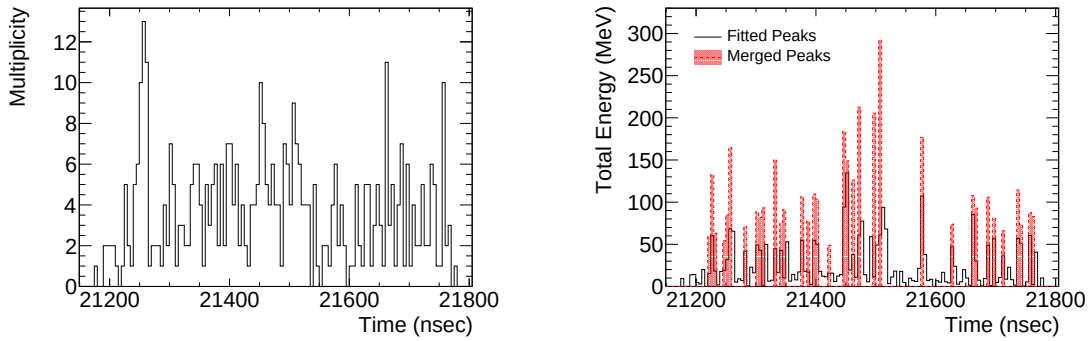

(a) Multiplicity **(b)** Total Energy

Figure 7.3: Timing-based peak merging. The horizontal axis of both histograms denote the fitted peak timing, separated every 5 nsec. (a) There are numerous peaks that are distributed throughout. (b) The black histogram shows the total energy deposit in each bin, and the red one is the result of the peak merging.

7.2.3 Cluster Reconstruction

There are three steps related to clustering: seed finding, pre-clustering, and clustering. The first step creates a seed list from the input hit selection, and every hit in the list is required to achieve an energy higher than 15 MeV. The next step identifies one or more seeds that are likely induced by the signal electron and combines them into a precluster. The last collects hits around every precluster to construct a cluster. The MVA classification schemes were applied to the preclustering and clustering steps to utilize the limited information obtained from the hits maximally.

7.2.3.1 Preclustering

Preclustering repeats combining a pair of seeds. It starts by picking up the first two seeds from the list, which is sorted in the order of high energy. The position, timing, and energy of the seed with the higher (lower) energy are denoted by $\boldsymbol{r}_{\mathrm{high(low)}}$, $t_{\mathrm{high(low)}}$, and $E_{\mathrm{high(low)}}$, respectively. As input variables to the MVA classifier for the seed pairs, four variables are defined, and they are listed in Table 7.1. If its response is higher than a certain threshold, the pair is combined into a precluster. Next, the pair of the first and third elements is tested. If the response also passes, the third one also joins the same precluster; otherwise, it remains in the seed list. After all pairs with the first element are examined, the created precluster goes to the next clustering step. When seeds remain in the seed list, the same procedure is applied to them to create new preclusters.

Table 7.1: Input variables for the seed-pair classifier. $\boldsymbol{r}_{\mathrm{high(low)}}$, $t_{\mathrm{high(low)}}$, and $E_{\mathrm{high(low)}}$ are the crystal position, timing, and energy of the tested seed with the higher (lower) energy ($E_{\mathrm{high}} > E_{\mathrm{low}}$).

No.	Name	Definition	Unit	Description
1	`pos.diff`	$\left\lvert \boldsymbol{r}_{\mathrm{low}} - \boldsymbol{r}_{\mathrm{high}} \right\rvert$	mm	Distance of both seed crystals
2	`time.diff`	$\left\lvert t_{\mathrm{low}} - t_{\mathrm{high}} \right\rvert$	nsec	Time distance of both seeds
3	`energy`	E_{high}	MeV	The higher energy
4	`e.ratio`	$E_{\mathrm{low}}/E_{\mathrm{high}}$		Ratio of both seed energies

7.2.3.2 Training and Optimizing the MVA Classifier

The classifier for the seed pairs was trained with several seed samples. Samples are sorted into signals and BG datasets, based on whether they originate from the signal electrons or other BG particles. The classifier has to then respond positively only to the signal samples. Both datasets are further divided into half for training and testing every MVA method. Figure 7.4 shows the probability distributions and correlation coefficients of the input variables for each dataset, wherein the variable number is defined by Table 7.1. `pos.diff` and `time.diff` have discrepancies between the signal and BG samples.

The attempted MVA methods are `MLPsig` and `MLPtan`, and the BDT and GBDT methods with 100, 200, 500, and 1000 trees with a depth of 2 and 4[4]. For example, Figure 7.5 shows the response distribution of `MLPtan`, `BDT.Depth04.NTrees1000`, `BDTG.Depth04.NTrees0200`, and `BDTG.Depth04.`

[4]To enumerate all methods clearly, `BDT.Depth02.NTrees0100`, `BDT.Depth02.NTrees0200`, `BDT.Depth02.NTrees0500`, `BDT.Depth02.NTrees1000`, `BDT.Depth04.NTrees0100`, `BDT.Depth04.NTrees0200`, `BDT.Depth04.NTrees0500`, `BDT.Depth04.NTrees1000`, and `BDTG.`

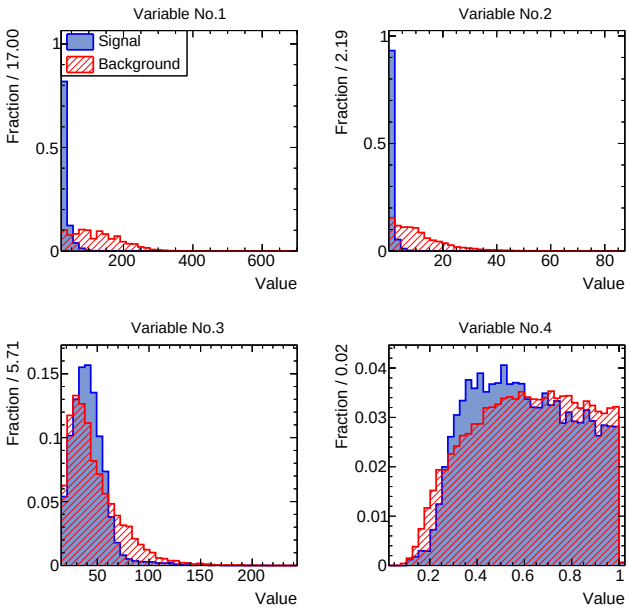

(a) Distributions

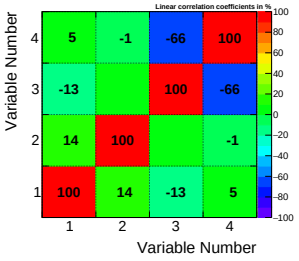

(b) Correlation coefficient (Signal)

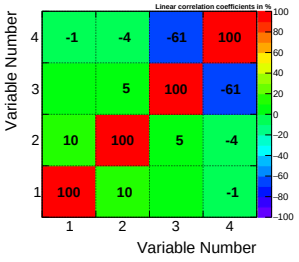

(c) Correlation coefficient (BG)

Figure 7.4: Distributions and correlation coefficients of the input variables for the seed-pair classifier. (a) The blue (red) histograms belong to signal (BG) samples. See Table 7.1 for the index number and unit of each variable. (b, c) The value and color in each bin represent the correlation coefficient between each two input variables in percentage.

`NTrees1000`. The blue and red histograms belong to the signal and BG seed samples, respectively. For each sample, the red marked one comes from the training samples, and the filled one comes from the testing samples. A mismatch between both such as that in the left side of the `BDTG.Depth04.NTrees1000` case, is interpreted to be caused by overtraining, and hence, we avoid using it. A high (low) response value implies that the event has originated presumably from the signal electrons (of other BGs), and both the signal and BG samples are on each appropriate side but are somewhat mixed.

If a signal (BG) sample is classified into the signal (BG) group properly, it is called a true positive (negative); otherwise, it is a false negative (positive). The signal-selection and BG-rejection efficiencies are defined as

$$\begin{aligned} \epsilon_{\mathrm{S}} &= \frac{N_{\mathrm{TP}}}{N_{\mathrm{TP}} + N_{\mathrm{FN}}}, \\ \epsilon_{\mathrm{B}} &= \frac{N_{\mathrm{TN}}}{N_{\mathrm{TN}} + N_{\mathrm{FP}}}, \end{aligned} \tag{7.1}$$

where N_{TP}, N_{FN}, N_{TN}, and N_{FP} denote the numbers of true positive, false negative, true negative, and false positive samples, and thus, $N_{\mathrm{TP}} + N_{\mathrm{FN}}$ and $N_{\mathrm{TN}} + N_{\mathrm{FP}}$ are equal to the total numbers of signal and BG samples, respectively. A low cut-off threshold realizes a high ϵ_{S} and low ϵ_{B}, vice versa. A scatter plot of ϵ_{S} and ϵ_{B} with the cut-off threshold as an auxiliary variable is called the ROC (receiver operating characteristic) curve. Figure 7.6 shows the ROC curves for all trained MVA methods, where horizontal and vertical axes represent ϵ_{S} and ϵ_{B}, respectively. The legend lists all methods in order of better performance; however, differences among them are not significant. `BDTG.Depth04.NTrees0500` appears to be the best. However, it also appears overtrained like `BDTG.Depth04.NTrees1000` in Figure 7.5(c). Finally, `BDTG.Depth04.NTrees0200` is adopted.

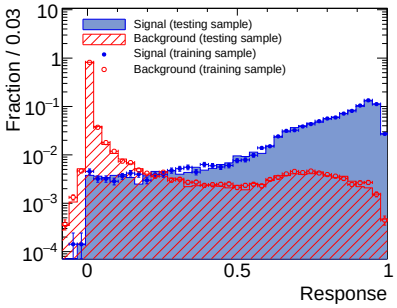

(a) `MLPtan`

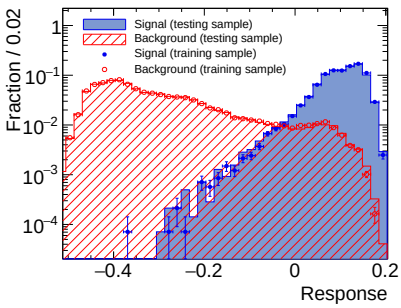

(b) `BDT.Depth04.NTrees1000`

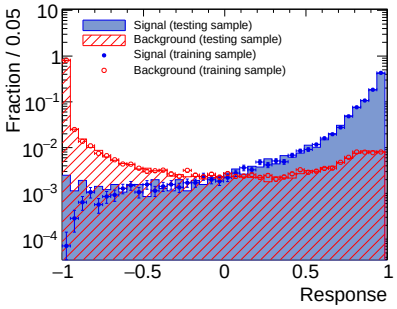

(c) `BDTG.Depth04.NTrees1000`

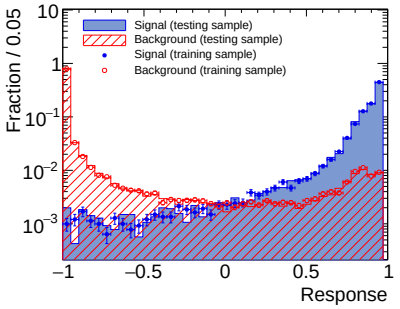

(d) `BDTG.Depth04.NTrees0200`

Figure 7.5: Probability distributions of the response value from several methods for the seed-pair classifier. See the text for the definition of the methods and their options. Horizontal axes are the responses; a higher value indicates that the tested event is more likely induced by the signal. The blue (red) histograms represent them for the signal (BG) samples, and the red marked (filled) histograms represent them for the training and testing samples.

Figure 7.7 shows the degree of importance of the input variables for the `BDTG.Depth04.NTrees0400` method. The importance values are normalized by the total. `pos.diff` is the most frequently used variable, followed by `time.diff`.

The cut-off threshold was optimized as follows. First, the following signal significance is defined as

$$\mu_S = \frac{N_{TP}}{\sqrt{N_{TP} + N_{FP}}}. \tag{7.2}$$

Next, three variables R_S, R_B, and $\bar{\mu}_S$ are calculated, where R_S and R_B denote the event fraction with ϵ_S and ϵ_B by more than 99%, respectively, and $\bar{\mu}_S$ is the average of the higher 95% of μ_S. Figure 7.8 shows them as a function of the threshold and their multiplication as a FOM (figure of merit). Finally, -0.7 was calculated as the threshold to maximize the FOM.

7.2.3.3 Clustering

The clustering step utilizes the MVA classification to assemble the remaining nonseed hits and the preclusters reconstructed above. For each precluster, every pair with a hit is examined by the MVA classifier, and all passed hits are combined with the precluster to build a cluster. Table 7.2 lists the nine input variables for the precluster-hit-pair classifier, where $\boldsymbol{r}_{hit} = (x_{hit}, y_{hit})$, t_{hit}, and E_{hit} are the crystal position, timing, and energy associated with the paired hit. When the paired precluster comprises

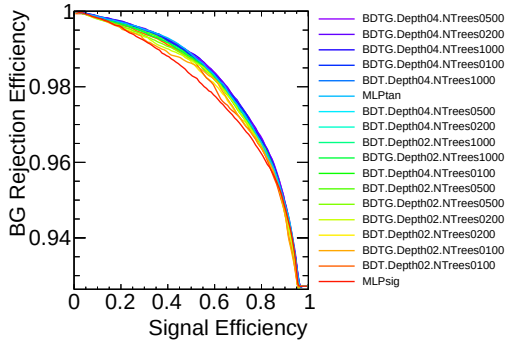

Figure 7.6: ROC curves of the seed-pair classifier. See the text for the definition of the methods and their options. The horizontal and vertical axes represent the signal selection and BG-rejection efficiencies, respectively. In the legend, the methods are sorted and colored in the order of better performance.

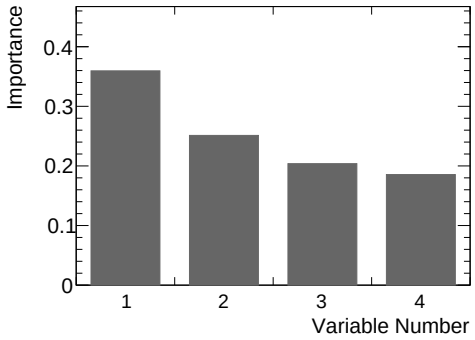

Figure 7.7: Importance of the input variables to the seed-pair classifier with the `BDTG.Depth04.NTrees0200` method. See Table 7.1 for the variable index number on the horizontal axis. The first variable (`pos.diff`) shows the highest importance.

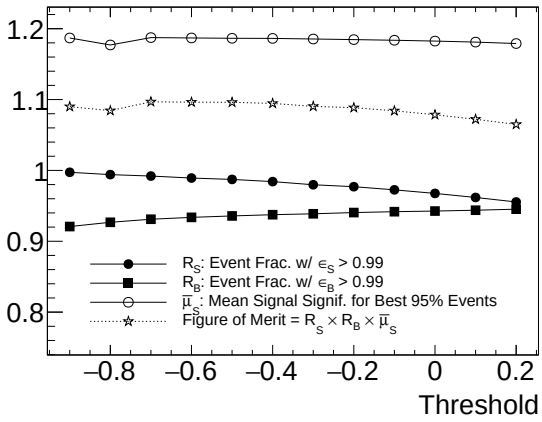

Figure 7.8: Optimization of the cut-off threshold for the seed-pair classifier with `BDTG.Depth04.NTrees0200`. The full markers indicate the event fractions with the signal-selection and BG-rejection efficiencies greater than 99%, respectively. The open round shows the average of the higher 95% of the signal significance. The FOM, the multiplication of the three curves, is maximized at −0.7.

N_{seed} seeds, $E_{\text{pre.}}$, $\bar{\boldsymbol{r}}_{\text{pre.}} = (\bar{x}_{\text{pre.}}, \bar{y}_{\text{pre.}})$, $\text{Cov}(x_{\text{seed}}, y_{\text{seed}})$, $\text{Var}(x_{\text{seed}})$, and $\bar{t}_{\text{pre.}}$ are calculated as

$$
\begin{aligned}
E_{\text{pre.}} &= \sum_{i}^{N_{\text{seed}}} E^i_{\text{seed}}, \quad (\bar{\boldsymbol{r}}_{\text{pre.}}, \bar{t}_{\text{pre.}}) = \frac{\sum_i^{N_{\text{seed}}} E^i_{\text{seed}} (\boldsymbol{r}^i_{\text{seed}}, t^i_{\text{seed}})}{E_{\text{pre.}}}, \\
\text{Cov}(x_{\text{seed}}, y_{\text{seed}}) &= \frac{\sum_i^{N_{\text{seed}}} E^i_{\text{seed}} (x^i_{\text{seed}} - \bar{x}_{\text{pre.}})(y^i_{\text{seed}} - \bar{y}_{\text{pre.}})}{E_{\text{pre.}}}, \quad \text{Var}(x_{\text{seed}}) = \text{Cov}(x_{\text{seed}}, x_{\text{seed}}),
\end{aligned}
\tag{7.3}
$$

where $\boldsymbol{r}^i_{\text{seed}} = (x^i_{\text{seed}}, y^i_{\text{seed}})$ and t^i_{seed} represent the crystal position and timing of the i-th seed in the precluster.

The same training and evaluation procedures as in the precluster step were applied to this step too. However, the depth of BDT and GBDT changed to 6 and 8 because of the increased number of input variables. Thus, `BDTG.Depth08.NTrees0200` was adopted. The last column of Table 7.2 shows the

rank of the variable importance assigned to the variable. The cut-off threshold was optimized to 0.8.

Table 7.2: Input variables for the precluster-hit-pair classifier. See the text for the detail of the variable definition. The last column shows the rank of the variable importance given by the `BDTG.Depth08.NTrees0200` method that showed the most optimum performance.

No.	Name	Definition	Unit	Description	Rank
1	`pos.diff.x`	$x_{\mathrm{hit}} - \overline{x}_{\mathrm{pre.}}$	mm	Horizontal distance between the precluster and the hit	3
2	`pos.diff.y`	$y_{\mathrm{hit}} - \overline{y}_{\mathrm{pre.}}$	mm	Vertical distance between the precluster and the hit	4
3	`time.diff`	$\left\lvert t_{\mathrm{hit}} - \overline{t}_{\mathrm{pre.}} \right\rvert$	nsec	Time distance between the precluster and the hit	2
4	`nseeds`	N_{seed}		The number of seeds in the precluster	9
5	`energy`	$E_{\mathrm{pre.}}$	MeV	Precluster energy	1
6	`e.ratio`	$E_{\mathrm{hit}}/E_{\mathrm{pre.}}$		Energy ratio of the hit to the precluster	5
7	`var.x`	$\mathrm{Var}(x_{\mathrm{seed}})$	mm^2	Horizontal positional variance of the seeds in the precluster	7
8	`var.y`	$\mathrm{Var}(y_{\mathrm{seed}})$	mm^2	Vertical positional variance of the seeds in the precluster	8
9	`cov`	$\mathrm{Cov}(x_{\mathrm{seed}}, y_{\mathrm{seed}})$	mm^2	Positional covariance of the seeds in the precluster	6

7.2.3.4 Cluster Classification

One more classification step is added to evaluate the reconstructed cluster. Table 7.3 lists the input variables. Most of these variables are also calculated by replacing the seed-associated terms in (7.3) with the hits in the cluster, whose crystal position, timing, and energy are $\boldsymbol{r}_{\mathrm{hit}} = (x_{\mathrm{hit}}, y_{\mathrm{hit}})$, t_{hit}, and E_{hit}, respectively. In addition, $\max(E_{\mathrm{hit}})$ and $\mathrm{med}(\mathrm{E_{hit}})$ are the maximum and median energies of the hits in the examined cluster. The `BDTG.Depth08.NTrees0200` method was found to work most optimally with a cut-off threshold of -0.9. The last column of the table shows the rank of the variable importance.

Table 7.3: Input variables for the cluster classifier. See the text for the detail of the variable definition. The last column shows the rank of the variable importance assigned by the `BDTG.Depth08.NTrees0200` method that showed the best performance.

No.	Name	Definition	Unit	Description	Rank
1	`nhits`	N_{hit}		The number of hits in the cluster	5
2	`energy`	$E_{\mathrm{clst.}}$	MeV	Cluster energy	1
3	`var.x`	$\mathrm{Var}(x_{\mathrm{hit}})$	mm^2	Horizontal positional variance of the hits in the cluster	9
4	`var.y`	$\mathrm{Var}(y_{\mathrm{hit}})$	mm^2	Vertical positional variance of the hits in the cluster	7
5	`cov`	$\mathrm{Cov}(x_{\mathrm{hit}}, y_{\mathrm{hit}})$	mm^2	Positional covariance of the hits in the cluster	8
6	`rms`	$\sqrt{\mathrm{Var}(\lvert\boldsymbol{r}_{\mathrm{hit}}\rvert)}$	mm	Positional RMS of the hits in the cluster	6
7	`e.max`	$\max(E_{\mathrm{hit}})/E_{\mathrm{clst}}$		Fraction of the maximum energy in the hits in the cluster	4
8	`e.mean`	$(N_{\mathrm{hit}})^{-1}$ $(= E_{\mathrm{clst.}}/N_{\mathrm{hit}}/E_{\mathrm{clst}})$		Fraction of the mean energy over the hits in the cluster	2
9	`e.med`	$\mathrm{med}(E_{\mathrm{hit}})/E_{\mathrm{clst}}$		Fraction of the Median single hit energy in the cluster	3

7.2.4 Shower Reconstruction

The reconstructed cluster is not sufficient as seed information for `ReconStrawTrk`. The energy-weighted cluster position $(\overline{x}_{\mathrm{clst.}}, \overline{y}_{\mathrm{clst.}})$ deviates from the true incident position $(x_{\mathrm{inc.}}, y_{\mathrm{inc.}})$ because of a finite incident angle. Figure 7.9 shows their typical residual distribution related to the signal electrons that have an obvious bias from zero. The shower reconstruction process aims at modifying this

deviation. Consequently, it infers $\theta_{\text{inc.}}$ and $\phi_{\text{inc.}}$, which are the zenith and polar angles of the incident track against the ECAL surface, respectively.

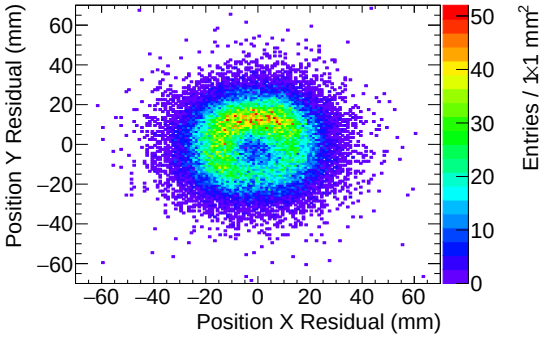

Figure 7.9: Position residual distribution of the reconstructed clusters and the incident tracks for signal electrons. The cluster position has a bias because of a finite incident angle.

Furthermore, the incident energy $E_{\text{inc.}}$ is a target variable because the ECAL cannot capture the entire shower energy in principle, and the pile-up hits obstruct the reconstruction. However, because only the 105 MeV signal electrons are focused in this study, it is natural that the reconstruction results in a similar value of around 105 MeV. Based on this study as the first step, future studies can develop an even better algorithm to handle a broader range of $E_{\text{inc.}}$ for more applications such as the beam measurement program before Phase-I.

The MVA regression technique was exploited to obtain these values. Table 7.4 lists all input and target variables. We use some variables for the cluster classifier and the absolute cluster position, $\overline{\boldsymbol{r}}_{\text{clst.}} = (\overline{x}_{\text{clst.}}, \overline{y}_{\text{clst.}})$, which is also input. E^n_{hit} is the n-th highest energy in the cluster, and $(\boldsymbol{r}_{\text{hit}})_{E^n_{\text{hit}}}$ is the relative position from $\overline{\boldsymbol{r}}_{\text{clst.}}$ of that hit.

We trained `MLPtan`, `MLPsig`, and GBDT[5] with 20, 50, 100, 200, and 500 trees at depths of 4, 6, and 8. The rank of the variable importance for each target is shown in Table 7.4. Their performance was evaluated by the residual of the regressed values from the true target value. For example, Figure 7.10 shows it for `shift.x` with `MLPsig`. There is still a weak correlation; however, the residuals concentrate on zero. Figure 7.11 compares the width of the residual distributions among all methods. The circle and rectangular markers represent the standard deviations of all and the 90% better samples of the distributions; the open and full markers belong to the training and testing samples, respectively. The method with a large discrepancy between the training and testing samples should be avoided. In conclusion, the `MLPsig` was adopted, and the resulting residual of the reconstructed shower positions will be presented in the next section.

[5]We attempted several variations of the BDT methods but failed to finish them because of the limit of the computing resource. They consumed it more than the GBDT methods did, and they also did not achieve a significantly better performance.

Table 7.4: Input and target variables for the MVA regression of the shower reconstruction. The variables enumerated by numbers are input variables, and the others with alphabets are the target variables to be regressed. See the text for details on the variable definition. The last five columns show the ranks of the correlation of the input variable with each target variable labeled with the corresponding alphabet, as given by `TMVA`.

No.	Name	Definition	Unit	Description	Rank for target No.				
					a	b	c	d	e
1	`nhits`	N_{hit}		The number of hits in the cluster	12	17	11	10	2
2	`pos.x`	$\overline{x}_{\mathrm{clst.}}$	mm	Cluster position X	6	2	6	1	11
3	`pos.y`	$\overline{y}_{\mathrm{clst.}}$	mm	Cluster position Y	2	14	1	7	6
4	`energy`	$E_{\mathrm{clst.}}$	MeV	Total cluster energy	4	11	4	14	1
5	`var.x`	$\mathrm{Var}(x_{\mathrm{hit}})$	mm^2	Horizontal-spatial variance of the cluster	6	9	12	13	4
6	`var.y`	$\mathrm{Var}(y_{\mathrm{hit}})$	mm^2	Vertical-spatial variance of the cluster	14	5	10	15	5
7	`cov`	$\mathrm{Cov}(x_{\mathrm{hit}}, y_{\mathrm{hit}})$	mm^2	Spatial covariance of the cluster	7	4	16	3	13
8	`rms`	$\sqrt{\mathrm{Var}(\lvert\boldsymbol{r}_{\mathrm{hit}}\rvert)}$	mm	Spatial RMS of the cluster	8	6	9	16	3
9	`e.1`	$E^1_{\mathrm{hit}}/E_{\mathrm{clst.}}$		Fraction of the first highest energy in the hits	11	16	8	11	7
10	`e.2`	$E^2_{\mathrm{hit}}/E_{\mathrm{clst.}}$		Fraction of the second highest energy in the hits	10	15	7	12	8
11	`e.3`	$E^3_{\mathrm{hit}}/E_{\mathrm{clst.}}$		Fraction of the third highest energy in the hits	15	10	2	8	9
12	`pos.1.x`	$(x_{\mathrm{hit}})_{E^1_{\mathrm{hit}}} - \overline{x}_{\mathrm{clst.}}$	mm	Relative crystal position X of the hit with E^1_{hit}	1	12	5	6	10
13	`pos.1.y`	$(y_{\mathrm{hit}})_{E^1_{\mathrm{hit}}} - \overline{y}_{\mathrm{clst.}}$	mm	Relative crystal position Y of the hit with E^1_{hit}	9	1	3	2	14
14	`pos.2.x`	$(x_{\mathrm{hit}})_{E^2_{\mathrm{hit}}} - \overline{x}_{\mathrm{clst.}}$	mm	Relative crystal position X of the hit with E^2_{hit}	13	7	13	9	12
15	`pos.2.y`	$(y_{\mathrm{hit}})_{E^2_{\mathrm{hit}}} - \overline{y}_{\mathrm{clst.}}$	mm	Relative crystal position Y of the hit with E^2_{hit}	16	8	17	5	17
16	`pos.3.x`	$(x_{\mathrm{hit}})_{E^3_{\mathrm{hit}}} - \overline{x}_{\mathrm{clst.}}$	mm	Relative crystal position X of the hit with E^3_{hit}	3	13	14	17	15
17	`pos.3.y`	$(y_{\mathrm{hit}})_{E^3_{\mathrm{hit}}} - \overline{y}_{\mathrm{clst.}}$	mm	Relative crystal position Y of the hit with E^3_{hit}	17	3	15	4	16
Targets									
a	`shift.x`	$\overline{x}_{\mathrm{clst.}} - x_{\mathrm{inc.}}$	mm	Shift of position X from the incident position					
b	`shift.y`	$\overline{y}_{\mathrm{clst.}} - y_{\mathrm{inc.}}$	mm	Shift of position Y from the incident position					
c	`costh`	$\cos\theta_{\mathrm{inc.}}$		Incident zenith angle in cosine					
d	`phi`	$\phi_{\mathrm{inc.}}$		Incident polar angle					
e	`e.leak`	$E_{\mathrm{inc.}}/E_{\mathrm{clst.}}$		Ratio of incident energy to cluster energy					

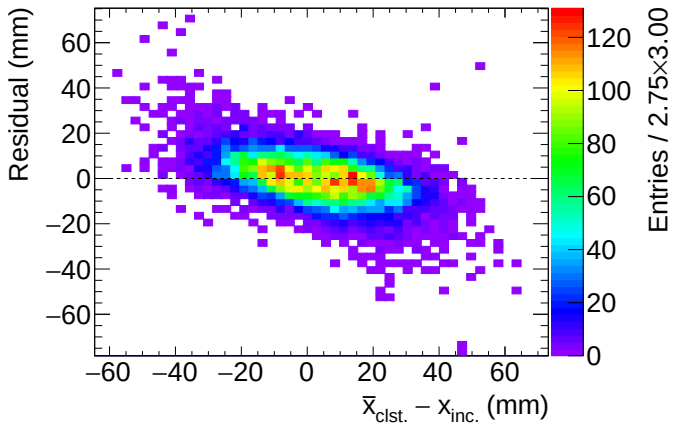

Figure 7.10: Residual of the `shift.x` values regressed by `MLPsig` for the shower reconstruction. The horizontal and vertical axes indicate the true and residual values, respectively. Most entries concentrate on zero.

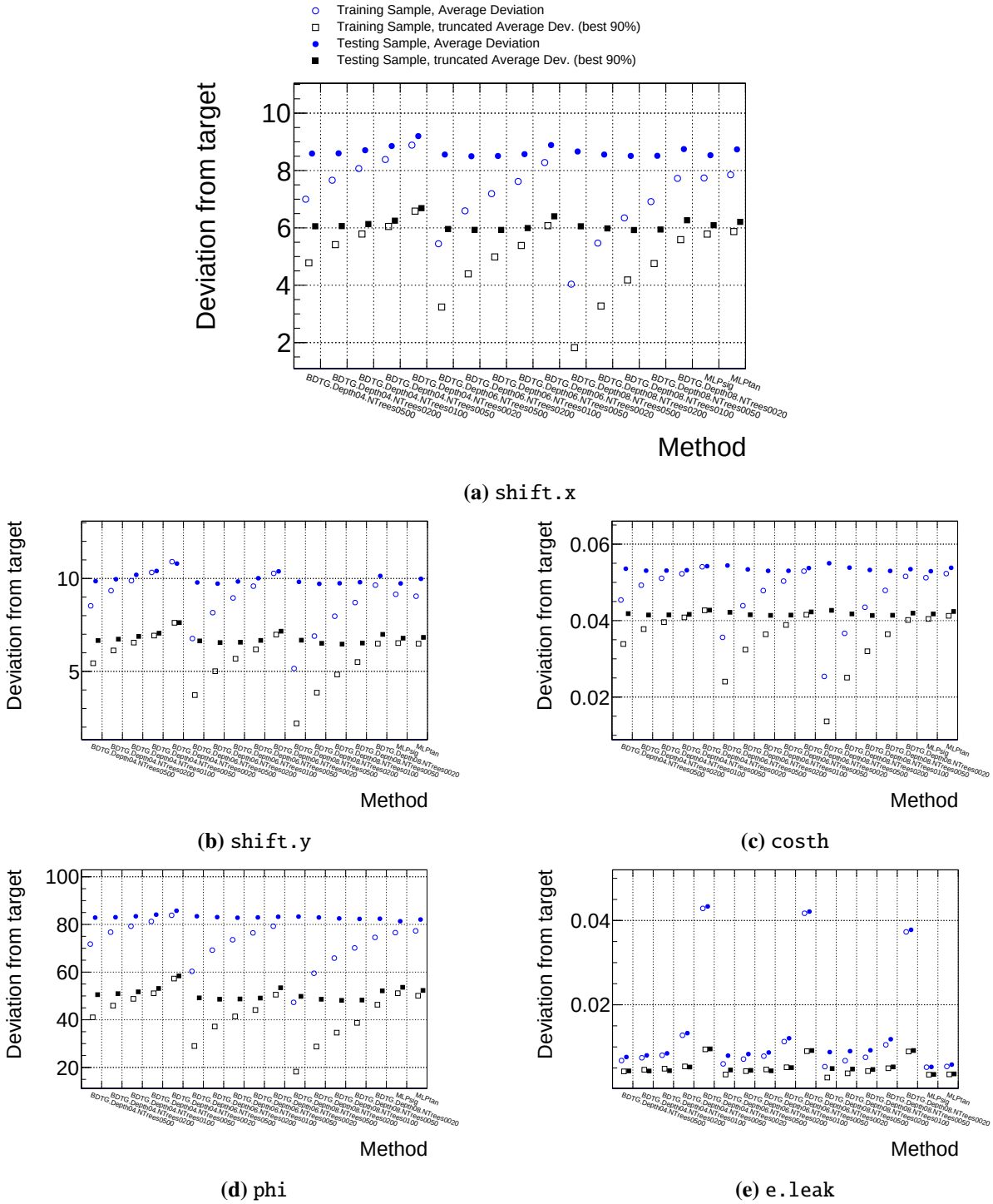

(a) `shift.x`

(b) `shift.y`

(c) `costh`

(d) `phi`

(e) `e.leak`

Figure 7.11: Comparison of the MVA regression methods trained for the five targets of shower reconstruction. The horizontal axis denotes every method, and the vertical axis shows the standard deviation of its residual. The open (full) markers indicate it was calculated from the training (testing) samples. All samples are used for round markers, but only the 90% better events are truncated for the rectangular ones.

7.2.5 Demonstration with Signal-Pure Data

The prepared data contains about 50,000 events, each of which has only a signal electron with an energy of about 105 MeV but no other BG particles; it certainly yields a total energy deposit of $E_{\text{dep.}} > 70$ MeV. More than 99.9% of the events succeed in reconstructing a single cluster when processed by `ReconECAL`, and 96.3% survive cluster classification, followed by shower reconstruction. Figure 7.12 shows the results. The first three figures relate to the energy reconstruction; the first and second figures show the reconstructed cluster energy and the residual of the shower energy from the true incident energy. The former is fitted in the same manner as stated in Section 5.3.4.5; the energy resolution defined by its HWHM is estimated at about 3%. Given the residual distribution with a standard deviation of 0.4 MeV, the performance of the leak-energy correction is demonstrated well. The signal-energy coverage is defined as the fraction of the signal-induced energy in the cluster; further, it is more than 0.8 for most reconstructed clusters. The corrected shower positions gather at zero. Fitted by a two-dimensional Gaussian, which shows a position resolution of $6.6 \oplus 6.6 = 9.3$ mm. The timing residual has a resolution of 0.5 nsec. The zenith angle θ has a sharp peak with a standard deviation of 6°; however, the polar angle ϕ spreads broader.

7.2.6 Reconstruction Efficiency and Performance

Figure 7.13 shows the reconstruction results for the realistic data that contain all BG particles and the timing windows from 600 to 1200 nsec. The blue-shaded histograms represent all events; however, the entries of the red-filled histogram belong to events that pass the criteria for calculating the reconstruction efficiency. Such events need to have a signal-energy coverage of more than 0.8. Further, it is required that the residuals from the signal electron track of the timing, position, and incident zenith angle are within 5σ, where σ is 0.5 nsec, 9.3 mm, and 7° based on the result for the signal pure data. Table 7.5 lists changes in the reconstruction efficiency by each condition. The reconstruction efficiency is 94.1% and 92.4% for the signal pure and realistic data, respectively.

In addition, Figure 7.14 shows its dependence on the timing when the signal electron hits the ECAL; however, there is no significant dependence.

Table 7.5: Reconstruction efficiency of `ReconECAL` for the signal pure and realistic data. The top condition assures one or more clusters, and showers are reconstructed. The other criteria are applied to the data from the top sequentially, and the absolute efficiency and relative change from the previous condition are presented.

	Signal pure		Realistic	
Condition	Efficiency	Relative	Efficiency	Relative
(Pass the cluster classification)	96.3%		96.6%	
Signal-energy coverage	94.7%	98.3%	92.9%	96.2%
Timing residual	94.5%	99.8%	92.8%	99.9%
Position residual	94.1%	99.6%	92.4%	99.6%
Zenith angle residual	94.1%	100%	92.4%	100%

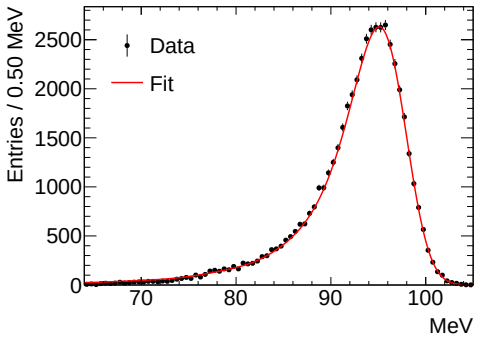

(a) Reconstructed energy distribution

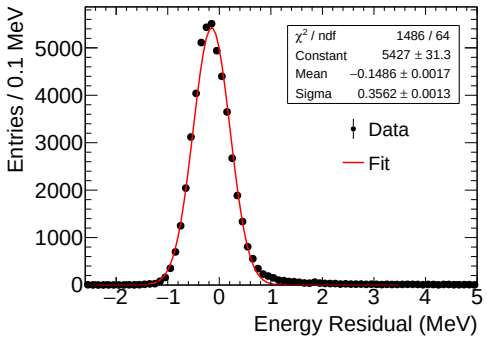

(b) Corrected energy residual

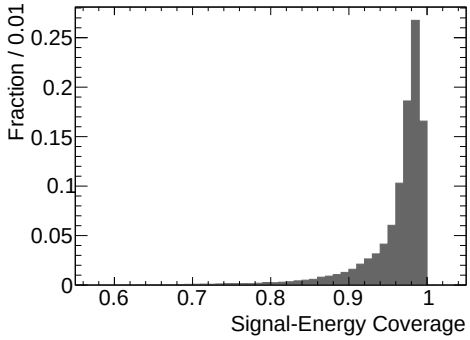

(c) Signal-energy coverage

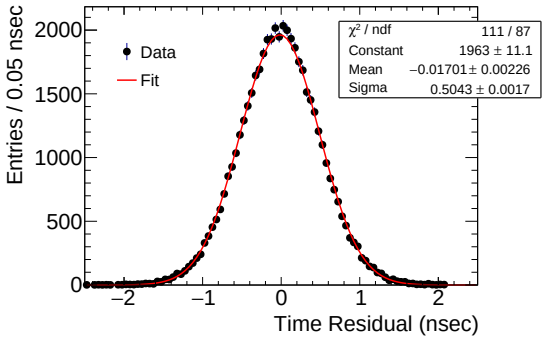

(d) Timing residual

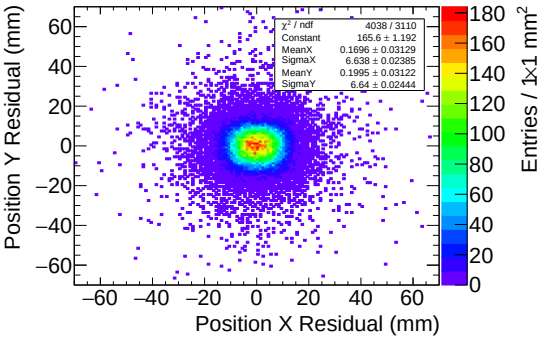

(e) Position residual

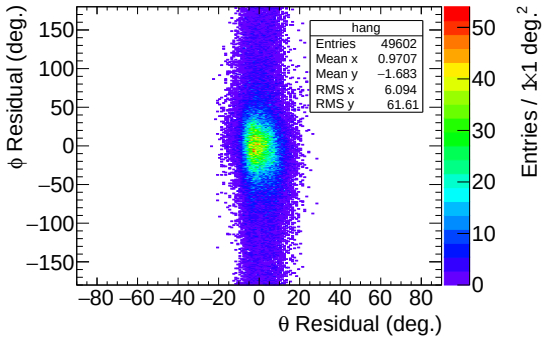

(f) Angular residual

Figure 7.12: Performance of `ReconECAL` for the signal pure data. (a) Reconstructed energy distribution is fitted in the same manner as that in Section 5.3.4.5, and it has an energy resolution of about 3%. (b) The residual of the reconstructed incident energy is fitted by a Gaussian function with $\sigma = 0.4$ MeV. (c) The signal-energy coverage indicates the fraction of the signal-induced energy in the reconstructed cluster. (d) Residual of the reconstructed timing is fitted by a Gaussian function with $\sigma = 0.5$ nsec. (e) The residual of the reconstructed shower position from the incident position concentrates on zero and has a resolution of $6.6 \oplus 6.6 = 9.3$ mm. (f) The zenith angle θ distributes by 6° in the standard deviation; however, the polar angle ϕ has a broad peak.

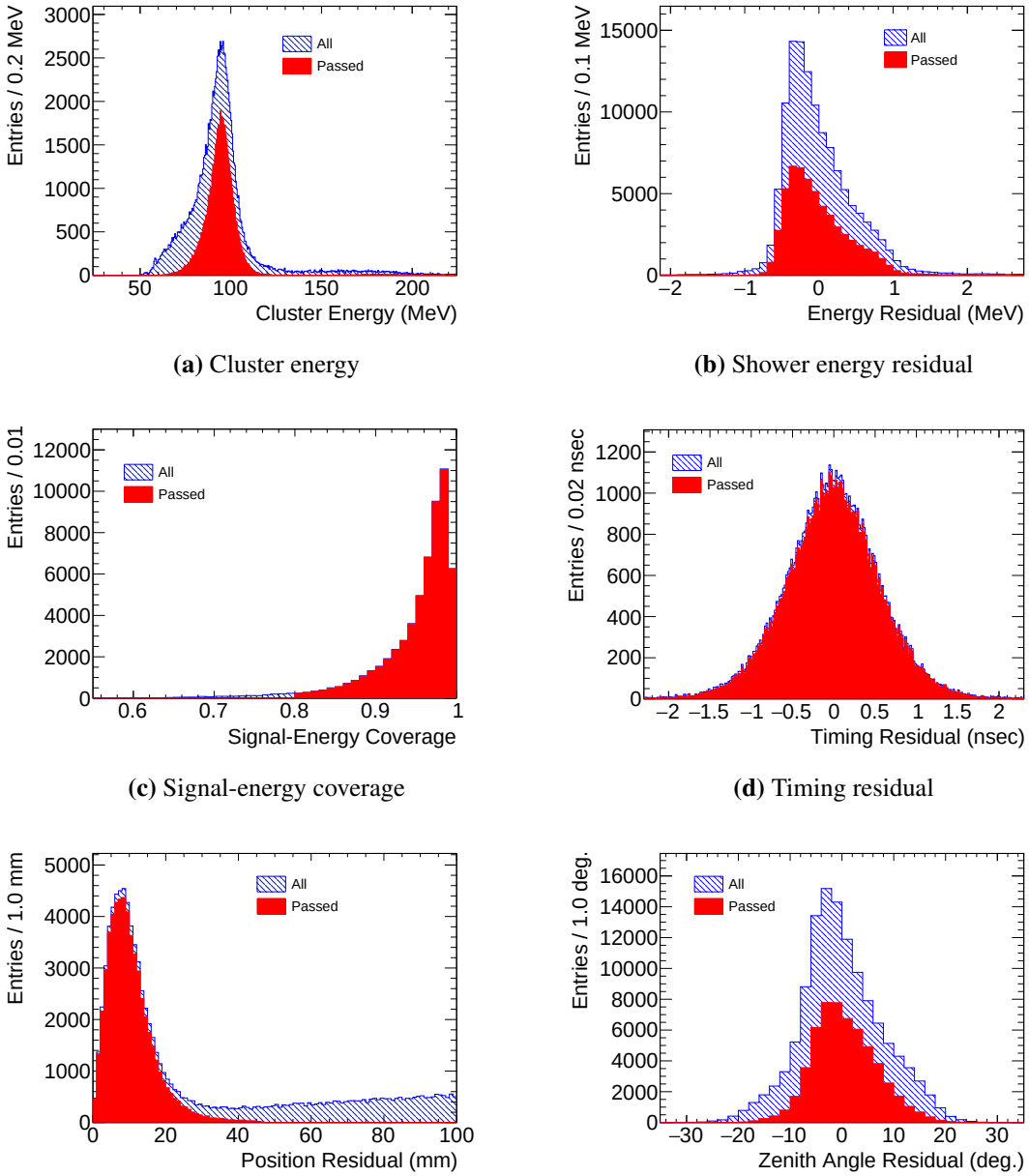

(a) Cluster energy

(b) Shower energy residual

(c) Signal-energy coverage

(d) Timing residual

(e) Position residual

(f) Zenith angle residual

Figure 7.13: `ReconECAL` performance for realistic data. The blue-shaded histograms belong to all reconstructed clusters and showers, and the entries in the red-filled histograms pass the criteria of the reconstruction efficiency. (a) Reconstructed cluster energy distribution. (b) Residual of the reconstructed shower energy from the incident energy. (c) Signal energy coverage. (d) Residual of the reconstructed timing. (e) Residual of the reconstructed shower position from the incident position. (f) Residual of the reconstructed incident zenith angle θ.

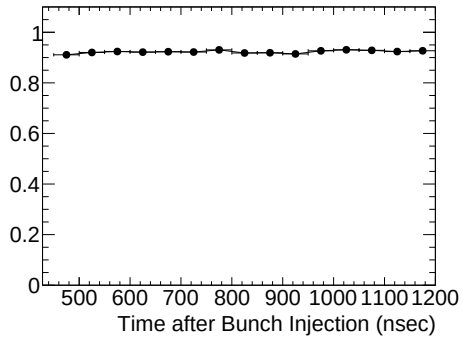

Figure 7.14: Reconstruction efficiency of `ReconECAL` as a function of the timing when the signal electron hits the ECAL. The timing is subtracted by the bunch injection timing, and it does not have a strong dependence.

7.3 ReconStrawTrk: Reconstruction for the Straw Tracker

`ReconStrawTrk` aims to identify the straw tracker hits associated with a signal track that connects to one of the reconstructed showers. This is divided into three parts: hit preselection, track finding, and track fitting. Hit preselection collects the signal-induced hits and rejects the others; track finding part combines passed hits from all straw stations to make candidate tracks and examines them with the MVA classification technique; and finally, the hits of every candidate track are fitted by a trajectory with Kalman filtering to reconstruct its momentum.

7.3.1 Hit Preselection

The hit preselection cleans up the hit list with multiple MVA classifiers. It also aims to infer the DCA of every hit. For that, the TOF calibration process is performed to obtain t_{TOF}, which is the TOF from the hit straw tube to the ECAL. Then, the DCA is calculated from the drift time, which is the time difference of the hit from it. Although t_{TOF} cannot be completely reconstructed before track fitting, it is approximated from the pitch angle of the track against the beam direction θ_{pitch} as

$$t_{\mathrm{TOF}} = \frac{L_{\mathrm{ECAL}}}{c\ \cos\theta_{\mathrm{pitch}}}, \tag{7.4}$$

where L_{ECAL} represents the distance on the beam axis between the straw tube and the ECAL surface, and c denotes the speed of light. θ_{pitch} is obtained with the MVA regression technique.

Figure 7.15 shows the flow chart. The procedure is applied to each straw station separately. The blue elements are hit lists with different hit combinations, and the classification from (A) to (E) clean up each of them. First, a timing cut and classification (A) are applied to every "single hit." Second, the classification (B) and (C) process the combinations of every two passed hits in the same straw layer (hit "pairs"), and the classification (D) and (E) process the combinations of every two passed hit pairs in the same straw station (hit "quartets"). Third, the regression (B) and (D) are used for the TOF calibration to create the "calibrated" hit lists. Gaining the calibrated hit quartets (the left side) over the calibrated hit pairs (the right side) is a priority because the hit quartet is more useful for regressing θ_{pitch}. Further, once the preselected hit quartets are obtained, the noncalibrated hit pairs belonging to

them are removed from the pair list at the "clean up" step. Then, the remaining hit pairs go through the classification (C) via the TOF calibration.

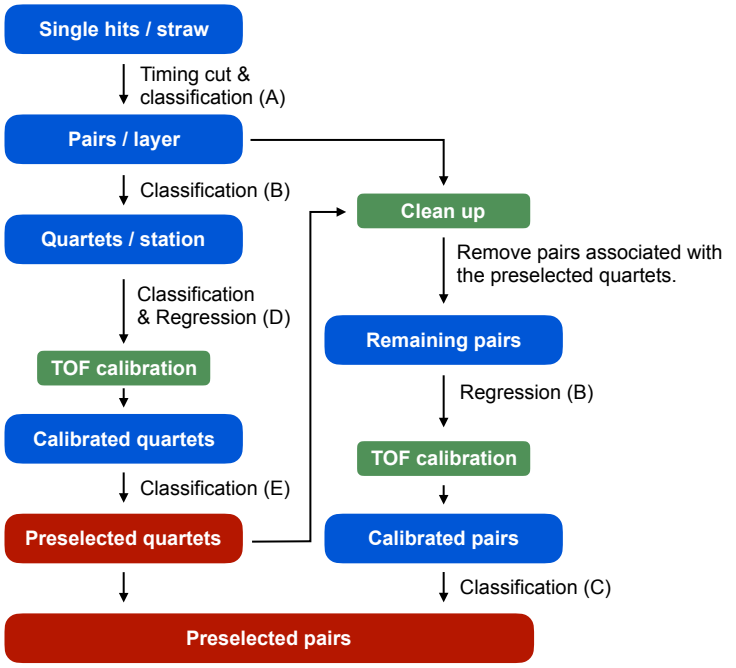

Figure 7.15: Flowchart of the hit preselection. The blue elements are hit lists with different hit combinations: single hit, two hits (pair), and two pairs (quartets). The five MVA classification schemes find signal-induced hits, and the two MVA regression schemes (B) and (D) infer the pitch angle of the trajectory for the TOF calibration. At the "clean up" stage, the hit pairs contained by the preselected quartets are removed from the pair list, and the remaining hit pairs are reprocessed by classification (C).

7.3.1.1 Timing Cut of the Single Hits

Before the application of classification (A), several single hits are cut by their timing t_{hit}. Figure 7.16 shows the typical distributions of $|t_{\text{hit}}|$ of the single hits in the first and last straw layers[6]. The blue-shaded and red-dashed distributions are associated with the signal and other BGs, respectively. Owing to difference in the distance to the ECAL and the resulting t_{TOF}, the characteristics of the signal distribution differs. A simple cut was set at $|t_{\text{hit}}| = 60$ nsec, and it could remove more than 80% of the BG hits. Yet, the ratio of the signal hits to the BG hits is 3%, which is considerably low. Therefore, the MVA classification is required.

7.3.1.2 MVA Classification and Regression

Table 7.6 lists all input variables for each classification and regression (A) to (E). In particular, the four variables in Table 7.6a belong to the seed ECAL shower and are always used by all of them. Figure 7.17(a) illustrates the variable definition of the single hit based on a given seed ECAL shower. In addition to the seed information, the hit has two positions (u_{hit} and v_{hit}) and t_{hit}, which are defined

[6]The last straw station is the closest to the ECAL.

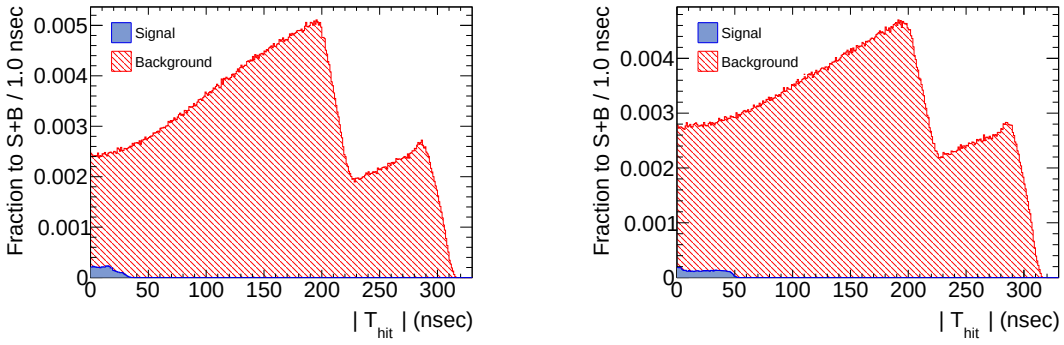

(a) The first straw layer (the farthest from the ECAL) **(b)** The last straw layer (the closest to the ECAL)

Figure 7.16: Time difference of single hits in the first and last straw layers from the seed timing. The blue-shaded and red-dashed distributions represent the signal and other BGs, respectively. The entries are normalized by the total of both, and the signal fraction is only 0.5%. The hit timings include the TOF between the layer and the ECAL that differs depending on the distance.

relative to the seed. u_{hit} is its wire position along the orientation of the straw layer, and v_{hit} is its longitudinal position along the wire.

Reconstructing v_{hit} requires a signal readout at both ends of the straw tube. Although the straw tracker does not have this capability in Phase-I, Phase-II still has the potential to realize it. The Mu2e collaboration that handles the straw tube tracker demonstrated a longitudinal position resolution of 4.3 cm [90]. The resolution is roughly determined by $\sigma_L = c/\sigma_t$, where σ_t is the time resolution of the readout electronics, which needs to be $\sim$ 100 psec. Since ROESTI has $\sigma_t < 100$ psec, the COMET straw tracker can also be used to achieve a similar σ_L; hence, we assume a Gaussian-shape uncertainty of 5 cm into v_{hit}.

The hit pair is a combination of every two single hits in the same straw layer, and the hit quartet is a combination of every two hit pairs in the X- and Y-directed straw layers in the same straw station. Their variables comprise parameters in their single hits.

Figure 7.17(b) illustrates the variables of the TOF-calibrated hit pair. Once the DCAs of the paired single hits are calculated, up to four tangents can be drawn with respect to the consequent drift circles. Each tangent has the middle position u_{pair}, and the distances on the U- and Z-axes, i.e., Δu_{pair} and Δz_{pair}, respectively. The calibrated hit quartet comprises these calibrated hit pairs.

The MVA methods trained for each of the classification and regression steps were compared in the same manner as in Section 7.2. Thus, considering the balance between performance and computational cost, we adopted `BDTG.Depth06.NTrees0500` for classification (A), `BDTG.Depth08.NTrees0200` and `MLPtan` for classification and regression (B), `BDTG.Depth06.NTrees0200` for classification (C), `BDTG.Depth06.NTrees0200` and `BDTG.Depth10.NTrees0100` for classification and regression (D), and `BDTG.Depth08.NTrees0500` for classification (E). The cut-off thresholds for the classifiers will be optimized in Section 7.3.5.

Table 7.6: Input variables for the classification and regression (A) to (E) in the hit preselection. (a) These four variables from the seed ECAL shower are shared by (b-f). See the text and Figure 7.17 for details.

(a) Common for (A) to (E)

Definition	Description
x_{seed}	Position X of the seed ECAL shower
y_{seed}	Position Y of the seed ECAL shower
ϕ_{seed}	Direction ϕ of the seed ECAL shower
$\cos\theta_{\text{seed}}$	Direction θ of the seed ECAL shower

(b) Classification (A) for the single hit

Definition	Description
u_{hit}	Hit position U
v_{hit}	Hit position V
t_{hit}	Hit timing

(c) Classification and regression (B) for hit pair containing two single hits: "hit1" and "hit2"

Definition	Description
$(u_{\text{hit1}} + u_{\text{hit2}})/2$	Averaged position U
$u_{\text{hit2}} - u_{\text{hit1}}$	Difference in the positions U
$(v_{\text{hit1}} + v_{\text{hit2}})/2$	Averaged position V
$v_{\text{hit2}} - v_{\text{hit1}}$	Difference in the positions V
$(t_{\text{hit1}} + t_{\text{hit2}})/2$	Averaged timing
$t_{\text{hit2}} - t_{\text{hit1}}$	Difference in the timings

(d) Classification (C) for the calibrated hit pair containing two single hits: "hit1" and "hit2"

Definition	Description
u_{pair}	Position U of the calibrated pair
$\Delta u_{\text{pair}}/\Delta z_{\text{pair}}$	Slope of the calibrated pair
$(v_{\text{hit1}} + v_{\text{hit2}})/2$	Position V of the calibrated pair
$(t_{\text{hit1}} + t_{\text{hit2}})/2$	Pair timing

(e) Classification and regression (D) for the hit quartet containing four single hits: "hit1" to "hit4"

Definition	Description
$(u_{\text{hit1}} + u_{\text{hit2}})/2$	Averaged position U of the X-pair
$u_{\text{hit2}} - u_{\text{hit1}}$	Difference in the positions U of the X-pair
$(u_{\text{hit3}} + u_{\text{hit4}})/2$	Averaged position U of the Y-pair
$u_{\text{hit4}} - u_{\text{hit3}}$	Difference in the positions U of the Y-pair
$(u_{\text{hit1}} + u_{\text{hit2}})/2 - (v_{\text{hit3}} + v_{\text{hit4}})/2$	Difference in the pair positions on the X-axis
$(u_{\text{hit3}} + u_{\text{hit4}})/2 - (v_{\text{hit1}} + v_{\text{hit2}})/2$	Difference in the pair positions on the Y-axis
$(t_{\text{hit1}} + t_{\text{hit2}} + t_{\text{hit3}} + t_{\text{hit4}})/4$	Averaged timing
$(t_{\text{hit3}} + t_{\text{hit4}})/2 - (t_{\text{hit1}} + t_{\text{hit2}})/2$	Difference in timings

(f) Classification (E) for the calibrated hit quartet containing two calibrated hit pairs: "pair1" and "pair2." They further consist of four single hits—"hit1" to "hit4"—and $t_{\text{TOF},i}$ is the regressed TOF for each.

Definition	Description
u_{pair1}	Position U of the calibrated X-pair
$\Delta u_{\text{pair1}}/\Delta z_{\text{pair1}}$	Slope of the calibrated X-pair
u_{pair2}	Position U of the calibrated Y-pair
$\Delta u_{\text{pair2}}/\Delta z_{\text{pair2}}$	Slope of the calibrated Y-pair
$(t_{\text{hit1}} + t_{\text{hit2}} + t_{\text{hit3}} + t_{\text{hit4}})/4$	Averaged timing
$\sum_i^4 t_{\text{TOF},i}/4$	Average of the regressed TOFs

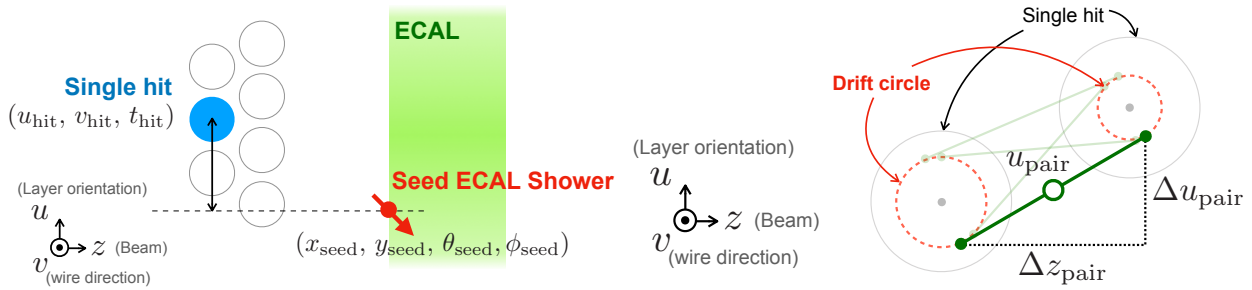

(a) Single hit **(b)** TOF-calibrated hit-pair

Figure 7.17: Variable definition of (a) the single hit and (b) the TOF-calibrated hit pair. The Z- and V-axes are along the beam axis and wire direction, respectively. The U-axis is defined as the alignment orientation of the straw tubes. (a) The seed object (an ECAL shower) has the incident position and angles on the ECAL surface. The single hit variables are defined relative to the position and timing of the seed. (b) The red-dashed lines represent the drift circles for every single hit, and the four green lines are the tangents. Every tangent has the middle position $u_{\rm pair}$, and the distances on the U- and Z-axes, i.e., $\Delta u_{\rm pair}$ and $\Delta z_{\rm pair}$, respectively.

7.3.2 Track Finding

Track finding involves constructing "tracklets" from the preselected calibrated hit pairs and combining them to construct candidate tracks, which then enter the track fitting stage. The tracklet is a minimal set forming a helix that links two hit pairs. All tracklets between two hit pairs are examined with the MVA classification technique. Tracklets with similar parameters are considered to be caused by the same trajectory. To find those, a histogramming method is employed.

7.3.2.1 Tracklet

The tracklet has four track parameters for each axis; they are given as

$$\begin{aligned} x(z) &= x_0 + R\cos(\alpha(z)) \\ y(z) &= y_0 + R\sin(\alpha(z)) \\ \alpha(z) &= \frac{\tan\theta}{R}z + \phi_0, \end{aligned} \tag{7.5}$$

where (x_0, y_0), R, θ, and ϕ_0 denote the center, radius, pitch angle, and phase of the helix, respectively.

Figure 7.18 illustrates the connection of tracklets between two hit pairs in different straw stations. In the case of the XZ-plane, the hit pairs at z_1 and z_2 have four parameters: $(x_1, x'_1, x_2, and x'_2)$, where $x_i\,(i = 1, 2)$ are the positions X of each hit pair, and $x'_i = {\rm d}x_i/{\rm d}z$ is the direction or the slope of the tangent for the drift circles. One can draw several tracklets to connect them smoothly. The same is valid for the YZ-plane.

The following nonlinear simultaneous equations should be solved to derive (x_0, R, θ, ϕ_0) from

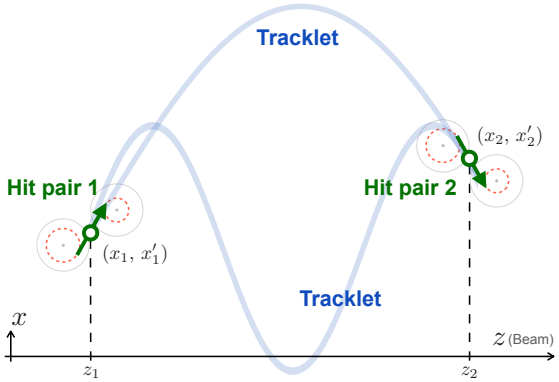

Figure 7.18: Tracklet connecting two TOF-calibrated hit pairs in different straw stations. The straw stations are located at z_1 and z_2, where the Z-axis is the beam direction, and the hit pairs are oriented on the X-axis. Their position and direction parameters are $(x_1,\ x_1',\ x_2,\ and x_2')$, where $x' = \mathrm{d}x/\mathrm{d}z$. There are many tracklets connecting the hit pairs. The same discussion is valid for the YZ plane.

$(x_1,\ x_1',\ x_2,\ x_2')$

$$\begin{aligned} x_1 &= x_0 + R\cos\alpha_1, \\ x_1' &= -\tan\theta\sin\alpha_1, \\ x_2 &= x_0 + R\cos\alpha_2, \\ x_2' &= -\tan\theta\sin\alpha_2, \end{aligned} \tag{7.6}$$

where $\alpha_i = \alpha(z_i)$. Mathematically, they have infinite solutions that satisfy

$$\frac{\left(\frac{\Delta x}{\Delta z}\right)^2}{\left(x_1' + x_2'\right)^2} = \left(\frac{\tan\frac{\Delta\alpha}{2}}{\Delta\alpha}\right)^2, \tag{7.7}$$

$$\Delta\alpha = \alpha_2 - \alpha_1, \quad \Delta x = x_2 - x_1, \quad \Delta z = z_2 - z_1.$$

However, $\Delta\alpha$ is limited within the valid range to ensure that the corresponding trajectory travels in the detector solenoid with a momentum of ~ 100 MeV/c. For each $\Delta\alpha$, $\tan\theta$ is given by

$$\tan^2\theta = \frac{(x_1')^2 + (x_2')^2 - 2x_1'x_2'\cos\Delta\alpha}{\sin^2\Delta\alpha}, \tag{7.8}$$

where $\tan\theta > 0$ ($\sin\theta$ and $\cos\theta > 0$) is assumed, and then, $\cos\alpha_1$ is

$$\cos\alpha_1 = \frac{-x_2' + x_1'\cos\Delta\alpha}{\sin\Delta\alpha\ \tan\theta}. \tag{7.9}$$

Finally, one obtains

$$\begin{aligned} R &= \frac{\tan\theta\,\Delta z}{\Delta\alpha} \\ x_0 &= x_1 - R\cos\alpha_1 \\ \phi_0 &= \cos^{-1}(\cos\alpha_1) - \frac{\tan\theta}{R}z_1. \end{aligned} \tag{7.10}$$

7.3.2.2 Classification of the Tracklets

All constructed tracklets are classified with the MVA technique. Table 7.7 lists the input variables. The first four variables belong to the seed ECAL shower, and the next four belong to the two hit

pairs; the last four are the tracklet parameters. `BDTG.Depth08.NTrees0200` was adopted in the same training and evaluation procedure as in the hit preselection. Together with the classifiers of the hit preselection, the cut-off threshold will be optimized in Section 7.3.5.

Table 7.7: Input variables for the tracklet classifier. The first four variables belong to the seed ECAL shower, and the next four belong to two hit pairs oriented on either the X- or Y-axis: "pair1" and "pair2." See the text and Figure 7.18 for details.

Definition	Description
x_{seed}	Position X of the seed ECAL shower
y_{seed}	Pposition Y of the seed ECAL shower
ϕ_{seed}	Direction ϕ of the seed ECAL shower
$\cos\theta_{\text{seed}}$	Direction θ of the seed ECAL shower
x_1 or y_1	Position of the pair 1
x'_1 or y'_1	Slope of the pair 1
x_2 or y_2	Position of the pair 2
x'_2 or y'_2	Slope of the pair 2
$\cos\theta$	Pitch angle of the tracklet
R	Radius of the tracklet
x_0 or y_0	Helical center of the tracklet
ϕ_0	Phase of the tracklet's curve

Figure 7.19 shows an example of the tracklet construction and classification for an event. For each of the XZ- and YZ-planes, colored lines are tracklets that have passed the classification. A few expected tracklets are not present; however, most constructed tracklets follow the trajectory of the signal electron painted by the light gray line. Although there are still some wrong hit pairs and tracklets, the next histogramming method collects only the appropriate tracklets.

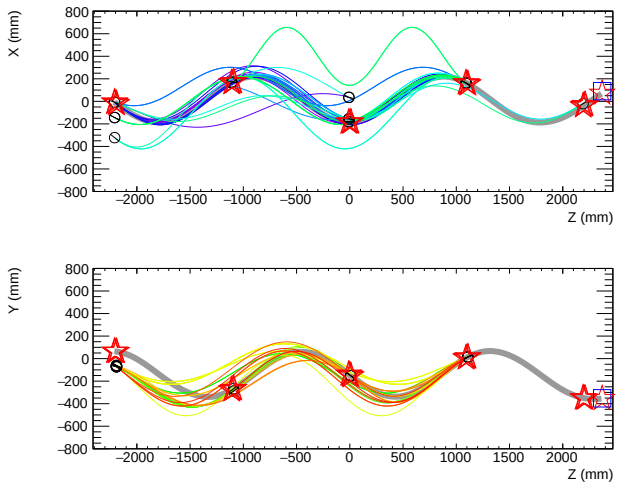

Figure 7.19: Tracklets and preselected hit pairs belonging to them for each plane of an event. The light gray lines and red star markers represent the signal electron track and true positions of the hits belonging to it, respectively. The colored lines represent the tracklets that have passed the MVA classification. The black circle markers and lines inside them represent the position and direction of each hit pair, and the blue square markers indicate the seed position.

7.3.2.3 Histogramming Method

Tracklets with similar track parameters are found by filling the parameters of all tracklets into a histogram that has three dimensions of $(\sin\theta,\ \phi_0,\ 1/p)$, where $p = 0.3BR/\sin\theta$ (MeV/c/T/mm) is a rough estimation of the momentum that forms a helical trajectory in a solenoid magnetic field of B. Uncertainties of the tracklet parameters are considered for filling them. Figure 7.20 illustrates that in the case of two variables for the sake of simplicity. The circle markers correspond to the parameters of each tracklet, and the round region surrounding each represents its uncertainty. When multiple tracklets overlap at a certain region, they are further checked to see if they have similar x_0 and y_0 within σ_{XY}, which is a control parameter to be optimized. If the found tracklets hold more than five layers, the hits that belong to them constitute a track candidate.

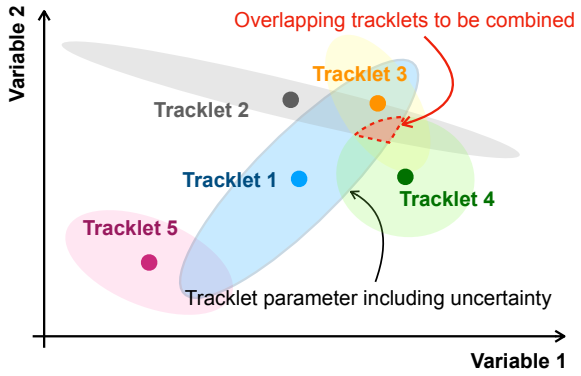

Figure 7.20: Histogramming method to find tracklets with similar track parameters. For the sake of simplicity, this is for the case of two variables. The same color marker and ellipse correspond to the parameters of each tracklet and their uncertainty region, respectively. When several tracklets overlap at a certain point, they are grouped to form a candidate track.

All correlated uncertainties are considered to draw the uncertainty regions. The following Σ represents the variance and covariance matrix among the four tracklet parameters.

$$\Sigma = \begin{pmatrix} (\sigma_{x_0})^2 & \mathrm{Cov}(x_0, \sin\theta) & \mathrm{Cov}(x_0, \phi_0) & \mathrm{Cov}(x_0, 1/p) \\ \mathrm{Cov}(\sin\theta, x_0) & (\sigma_{\sin\theta})^2 & \mathrm{Cov}(\sin\theta, \phi_0) & \mathrm{Cov}(\sin\theta, 1/p) \\ \mathrm{Cov}(\phi_0, x_0) & \mathrm{Cov}(\phi_0, \sin\theta) & (\sigma_{\phi_0})^2 & \mathrm{Cov}(\phi_0, 1/p) \\ \mathrm{Cov}(1/p, x_0) & \mathrm{Cov}(1/p, \sin\theta) & \mathrm{Cov}(1/p, \phi_0) & (\sigma_{1/p})^2 \end{pmatrix}, \tag{7.11}$$

where σ_p denotes the error of p, and $\mathrm{Cov}(p_1, p_2)$ represents the covariance between the parameters p_1 and p_2. Σ contains $(x_1,\ x_1',\ x_2,\ x_2')$ of the hit pairs, and they further depend on $(d_{11},\ d_{12},\ d_{21},\ d_{22})$ where d_{ij} represents the DCA of the j-th single hit of the i-th hit pair. They also have errors caused by

the straw tube spatial resolution (σ_{11}, σ_{12}, σ_{21}, σ_{22}). Therefore, their variance and covariance matrix

$$D = \sum_{j=1}^{2} \begin{pmatrix} \left(\frac{\partial x_1}{\partial d_{1j}}\right)^2 (\sigma_{1j})^2 & \left(\frac{\partial x_1}{\partial d_{1j}}\right)\left(\frac{\partial x_1'}{\partial d_{1j}}\right)(\sigma_{1j})^2 & 0 & 0 \\ \left(\frac{\partial x_1}{\partial d_{1j}}\right)\left(\frac{\partial x_1'}{\partial d_{1j}}\right)(\sigma_{1j})^2 & \left(\frac{\partial x_1'}{\partial d_{1j}}\right)^2 (\sigma_{1j})^2 & 0 & 0 \\ 0 & 0 & \left(\frac{\partial x_2}{\partial d_{2j}}\right)^2 (\sigma_{2j})^2 & \left(\frac{\partial x_2}{\partial d_{2j}}\right)\left(\frac{\partial x_2'}{\partial d_{2j}}\right)(\sigma_{2j})^2 \\ 0 & 0 & \left(\frac{\partial x_2}{\partial d_{2j}}\right)\left(\frac{\partial x_2'}{\partial d_{2j}}\right)(\sigma_{2j})^2 & \left(\frac{\partial x_2'}{\partial d_{2j}}\right)^2 (\sigma_{2j})^2 \end{pmatrix}, \tag{7.12}$$

is propagated to Σ as $\Sigma = JDJ^T$, where J denotes the Jacobian[7]

$$J = \begin{pmatrix} \frac{\partial x_0}{\partial x_1} & \frac{\partial x_0}{\partial x_1'} & \frac{\partial x_0}{\partial x_2} & \frac{\partial x_0}{\partial x_2'} \\ \frac{\partial(\sin\theta)}{\partial x_1} & \frac{\partial(\sin\theta)}{\partial x_1'} & \frac{\partial(\sin\theta)}{\partial x_2} & \frac{\partial(\sin\theta)}{\partial x_2'} \\ \frac{\partial \phi_0}{\partial x_1} & \frac{\partial \phi_0}{\partial x_1'} & \frac{\partial \phi_0}{\partial x_2} & \frac{\partial \phi_0}{\partial x_2'} \\ \frac{\partial(1/p)}{\partial x_1} & \frac{\partial(1/p)}{\partial x_1'} & \frac{\partial(1/p)}{\partial x_2} & \frac{\partial(1/p)}{\partial x_2'} \end{pmatrix}. \tag{7.13}$$

Further, C_{hist} is defined as a parameter to scale Σ globally and the consequent uncertainty regions in the histogram. When it is set to be larger (smaller), more tracklets overlap easily (hardly). This is why it will also be optimized in Section 7.3.5 with σ_{XY}.

Figure 7.21 demonstrates the method with an event. For the sake of visibility, every two dimensions of the original histogram are projected onto the individual histograms. The color indicates the number of layers that belong to the tracklets overlapping at each bin. Those tracklets have already passed the criterion for (x_0, y_0). In this case, five candidate tracks are constructed, and their averaged track parameters are shown by the black markers. Some of them are close to the signal track parameters at the star markers.

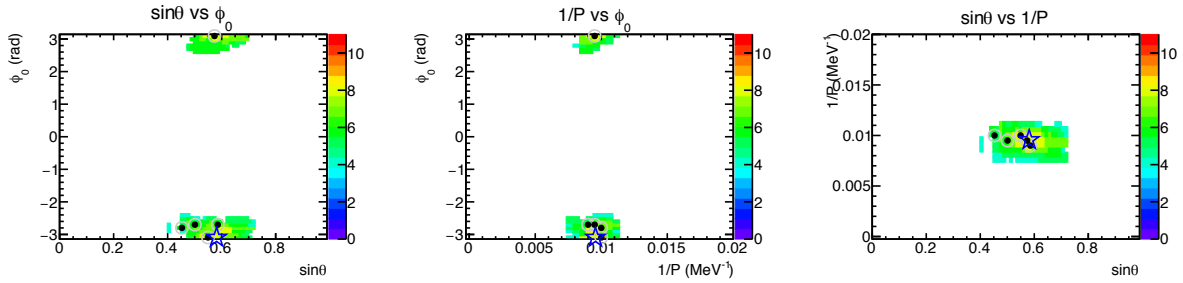

Figure 7.21: Track finding with the histogramming method for an event. The histograms show the projection of every two dimensions of ($\sin\theta$, ϕ_0, $1/p$). The star markers denote the parameters of the signal track. The color of each bin indicates the number of layers belonging to the overlapping tracklets, wherein each x_0 and y_0 is also consistent. The tracklets at each black marker constitute a track candidate.

[7] In practice, it is more accessible to compute J via its inverse matrix J^{-1}, which is derived from (7.5).

7.3.3 Track Fitting

In track fitting, a trajectory is fitted to all drift circles in every track candidate and the seed ECAL shower position. To this end, ICEDUST adopted `Genfit`, which is a generic framework for any track-fitting work in particle experiments that use complex detector systems [91]. Its theoretical detail is left to other textbooks; however, its concept with respect to our specific purpose is explained below.

The fitting uses the Kalman filter that handles not only the hit information but also any effects that change the trajectory such as the material effect that reduces the particle energy and scatters it. `Genfit` attempts to obtain the true "state" or the actual trajectory shape from the "measurements" that are either DCAs or the seed position in our case. It starts from an initial state of the track at the first measurement and predicts the state at the next measurement from the current state by considering all effects that are expected to have been caused between the two measurements, and it repeats that until the last measurement. This process is iterated until the resulting final state becomes stable. `Genfit` can also resolve the left–right ambiguity of the drift circle by testing two different measurements on both sides of every hit.

The track-fitting procedure is divided into "pre-fitting" and "full-fitting." The pre-fitting uses a simplified geometry for reducing the computational cost. Every straw station is replaced with a plane in which all materials are averaged. The resulting pre-fitted tracks are less accurate than the full-fitting with the full geometry; however, they are used for TOF recalibration. The pre-fitted track yields a more precise t_{TOF} at each hit compared to (7.4). Finally, the full-fitting applied after every hit in the pre-fitted track is modified.

Figure 7.22 is a typical full-fitted track compared with the signal electron track. The initial state shown by the green line has been calculated from the tracklets of the candidate track. The fitted track of the blue line is close to the signal track of the red line. The black lines indicate the straw tubes that contain hits in the fitted track.

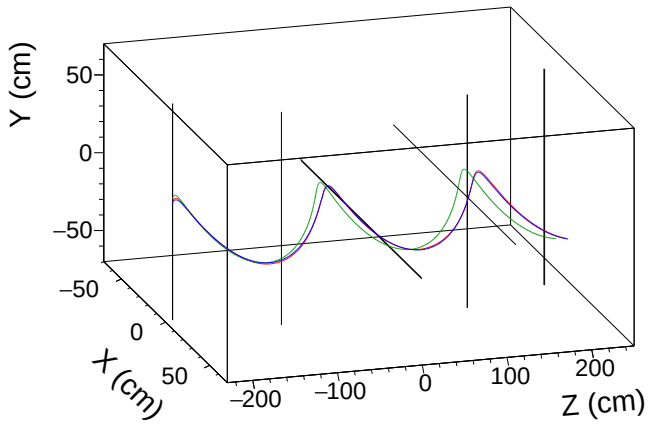

Figure 7.22: Example of full fitting to the hits of a track candidate. The green trajectory represents the initial track state given by the track finding stage. The signal electron track is drawn by a red trajectory. The blue trajectory and black lines indicate a fitted track and straw tubes associated with it.

7.3.4 Reconstruction Efficiency

The reconstruction efficiency of `ReconStrawTrk` is determined as follows. The criteria are set based on `ReconStrawTrk` because it aims to find and reconstruct only the signal track. The fitted track is expected to pass through the straw tubes that the signal track has hit. The difference between the fitted and signal tracks is calculated over the fitted hits to evaluate the fitted track quantitatively as

$$\overline{\delta p_i} = \frac{1}{N_{\text{hits}}} \sum_{j}^{N_{\text{hits}}} \left(p_{ij}^{\text{fit}} - p_{ij}^{\text{sig.}} \right), \tag{7.14}$$

where N_{hits} is the number of hits in the fitted track; p_i represents each of the track parameters of (x, y z, θ, ϕ), where θ and ϕ are the zenith and polar angles of the direction to the beam axis; p_{ij}^{fit} is p_i of the fitted track at the location of the j-th hit, and $p_{\text{ij}}^{\text{sig.}}$ is the point along the signal track closest to the j-th hit.

The $\overline{\delta p_i}$ is required to be within $3\sigma_i$, where σ_i is defined differently for the positions and directions. σ_i for the positions is $5/\sqrt{12}$ mm, which is the standard deviation of a uniform probability distribution over the straw-tube diameter. The σ_i of the directions was evaluated from the data. Figure 7.23 shows the distributions of $\overline{\delta\theta}$ and $\overline{\delta\phi}$ when the track finding can construct a candidate track with all signal-induced hits in every event. Their RMS were set as $\sigma_\theta = 4.9 \times 10^{-3}$ rad and $\sigma_\phi = 5.1 \times 10^{-3}$ rad.

Before discussing the `ReconStrawTrk` performance with this reconstruction efficiency, several parameters to control `ReconStrawTrk` are optimized.

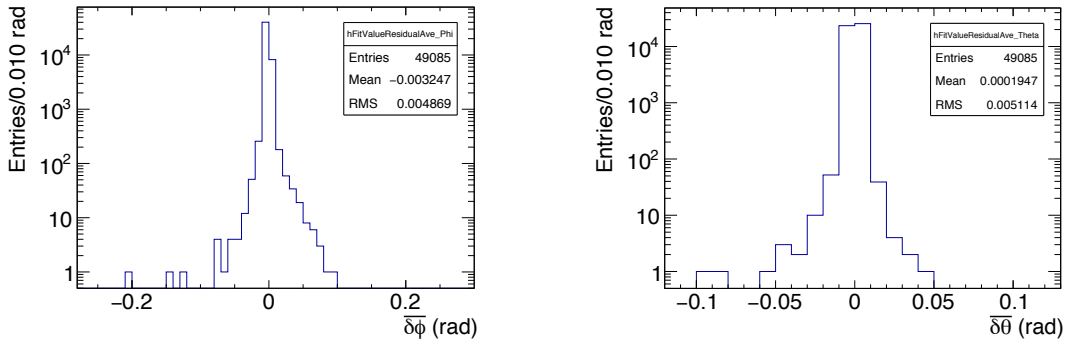

(a) $\overline{\delta\theta}$ **(b)** $\overline{\delta\phi}$

Figure 7.23: Distributions of the averaged residual of the direction parameters between the fitted and signal tracks. They are the results when all signal-induced hits are used in the track fitting in every event. Their RMSs were used to define the criteria of the reconstruction efficiency for `ReconStrawTrk`.

7.3.5 Optimization

There are four types of control parameters that need to be optimized experimentally. The first two are the thresholds for the classifiers in the hit preselection and track finding. The other two are for the histogramming method.

σ_{XY} denotes the acceptable width for the consistency of x_0 and y_0 of the tracklets. C_{hist} denotes the scale factor of the uncertainty regions in the histogram.

Every cut-off threshold for the classifiers T_i was determined to satisfy

$$R_S(T_i) = R_c, \tag{7.15}$$

where R_c denotes a constant parameter, and R_S represents the fraction of the events with $\epsilon_{\mathrm{S}} > 99\%$ when using T_i. The reconstruction efficiency was scanned with R_c for the classifiers in the hit preselection and the track finding, separately. Figures 7.24(a) and 7.24(b) show the results. In the hit preselection, all thresholds were optimized with a single R_c, and the reconstruction efficiency was maximized at $R_c = 0.97$ and 0.98; hence, $R_c = 0.975$ was taken. In the case of the tracklet classifier, $R_c = 0.6$ was found to maximize and stabilize the efficiency.

Similarly, Figures 7.24(c) and 7.24(d) show the scan results for σ_{XY} and C_{hist}. In conclusion, $\sigma_{\mathrm{XY}} = 2$ cm and $C_{\mathrm{hist}} = 1.85$ were adopted.

7.3.6 Performance

Table 7.8 lists the change in the reconstruction efficiency caused by the criteria defined in Section 7.3.4. The first two are set as reference to evaluate the performance of the track finding and fitting stages. In total, one or more fitted tracks remain in 92.3% of the events. The last two decrease it relatively by about 10%. The reconstruction efficiency is estimated at 83.6%.

Figure 7.25 shows the momentum residual of the fitted track that passed the criteria from the signal track. Both momenta are evaluated at the first hit position of the fitted track. Further, it is fitted by the triple Gaussian function whose average standard deviation is 190 keV/c, which satisfies the requirement for the momentum resolution.

Figure 7.26 shows the dependence of the efficiency on the seed timing and pitch angle of the signal track. It deteriorates as the timing moves to the bunch injection and the pitch angle increases. It is reasonable because a trajectory with a relatively high longitudinal momentum does not interact with the solenoid magnetic field.

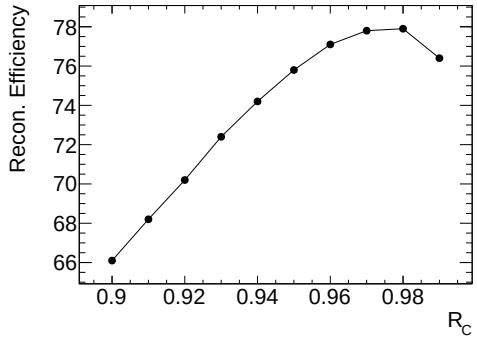

(a) The classifiers of the hit preselection

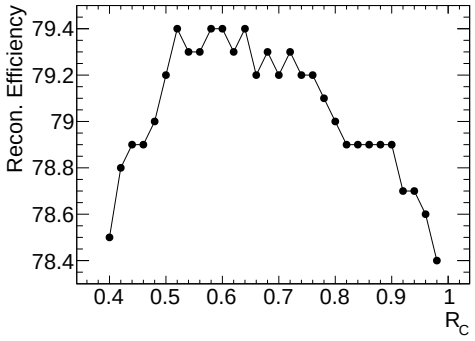

(b) The classifier of the track finding

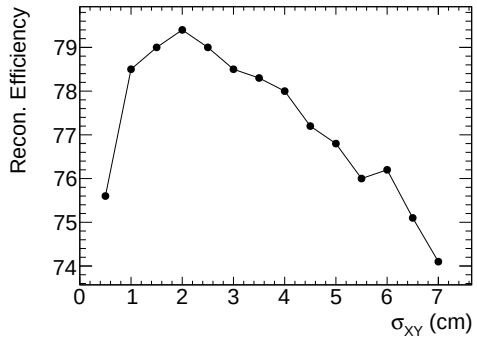

(c) The acceptable width for the tracklet helical center

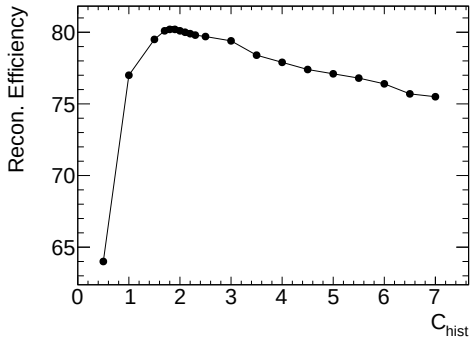

(d) The scale factor of the uncertainty regions

Figure 7.24: Optimization of (a, b) the classifier cut-off thresholds and (c, d) the control parameters for the histogramming method. The vertical axes represent the reconstruction efficiency. (a, b) The horizontal axes are R_c form (7.15). The efficiency is maximized at (a) $R_c = 0.975$ and (b) $R_c = 0.6$. (c, d) The horizontal axes are the acceptable width for helical centers of the tracklets and the scale factor of the uncertainty regions in the histogram. The reconstruction efficiency is maximized at $\sigma_{\mathrm{XY}} = 2$ cm and $C_{\mathrm{hist}} = 1.85$.

Table 7.8: Reconstruction efficiency of `ReconStrawTrk`. In every event, the data has a signal electron in the timing window from 600–1200 nsec after bunch injection. The last column shows the relative change from the previous condition.

Condition	Efficiency	Relative
At least one track was found.	92.3%	
At least one track was successfully fitted.	92.3%	100.0%
Position criteria: $3\sigma_i > \overline{\delta p_i}$ ($i = x, y, z$)	84.4%	91.4%
Direction criteria: $3\sigma_i > \overline{\delta p_i}$ ($i = \theta, \phi$)	83.6%	99.1%

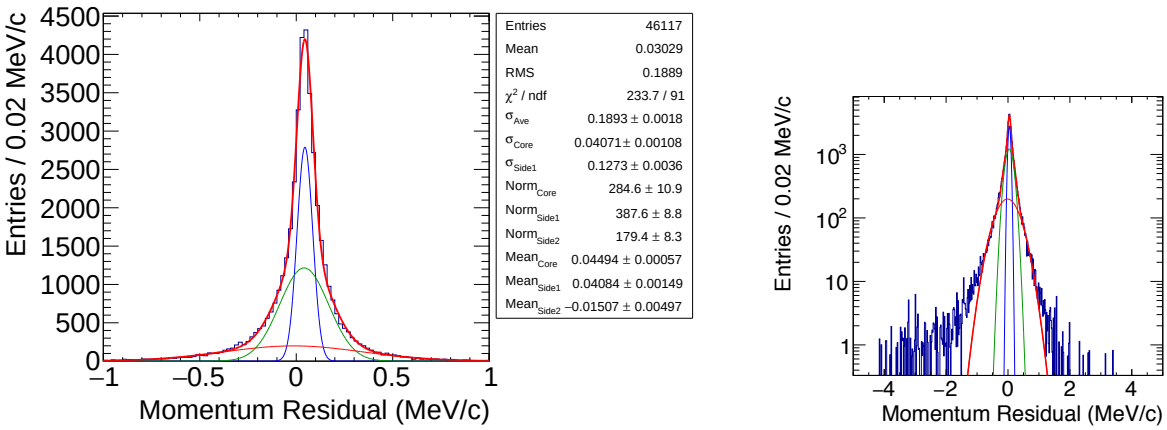

(a) In linear scale

(b) In logarithmic scale

Figure 7.25: Momentum residual of the fitted track from the signal track. The momenta are evaluated at the first hit position of the fitted track. The peak is fitted by triple Gaussian functions. In the legend, σ_{ave} denotes the average of their standard deviations. σ_{core} and σ_{side1} belong to the sharper of the two Gaussian functions.

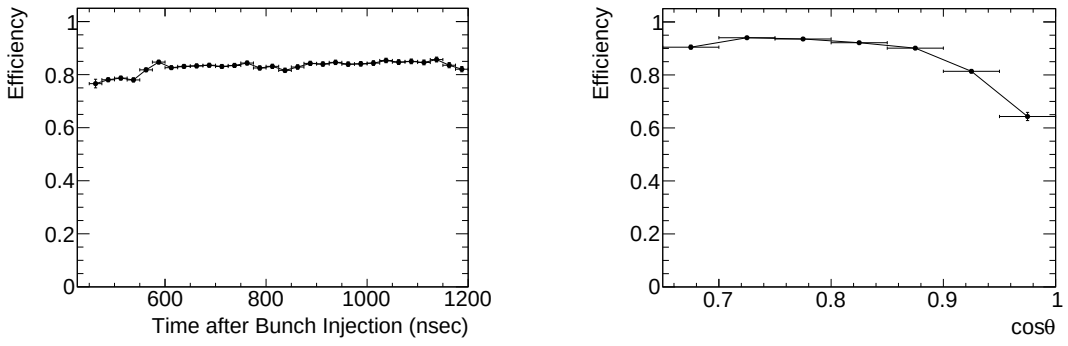

(a) The seed timing

(b) The pitch angle

Figure 7.26: Reconstruction efficiency of `ReconStrawTrk` as a function of (a) the seed timing and (b) pitch angle of the signal track. It deteriorates as the seed comes close to the bunch injection timing when the pitch angle increases.

7.4 Purity and Quality Cut

Data after the reconstruction have pairs of reconstructed shower and track in the StrECAL. Since some may be BG, their contamination decreases data purity. Purity is defined as the ratio of the pairs associated with the signal tracks to tracks. `ReconECAL` achieved a high reconstruction efficiency, whereas the purity still stayed at only 36.7%. Because of several selection algorithms in `ReconStrawTrk`, it increased further to 73.5%. To enhance it even further, the following quality cuts are applied to the pairs.

- Number of hits in the fitted track: $N_{\text{hits}} \geq 12$
- Quality of the track fitting given by `Genfit`: p-value > 0.002
- Ratio of the reconstructed energy to momentum: $0.985 < E/p < 1.015$

Figure 7.27 shows their distributions for all pairs and pairs associated with the signal tracks. The criteria for them were optimized to extract the latter so that the product of the purity and cut efficiency was maximized.

Table 7.9 presents the breakdown of the purity and reconstruction or cut efficiency through the reconstructions and quality cuts. After the reconstruction, instead of an efficiency drop of about 6%, the purity was successfully improved to 97.6% by more than 30%.

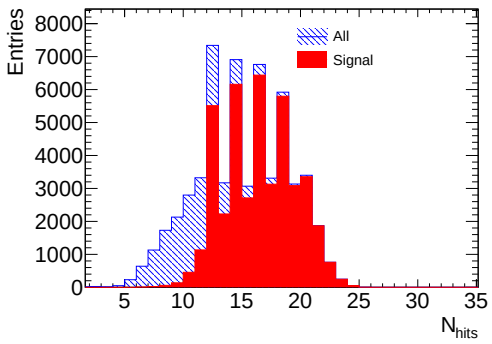

(a) N_{hits}: the number of hits in the fitted track:

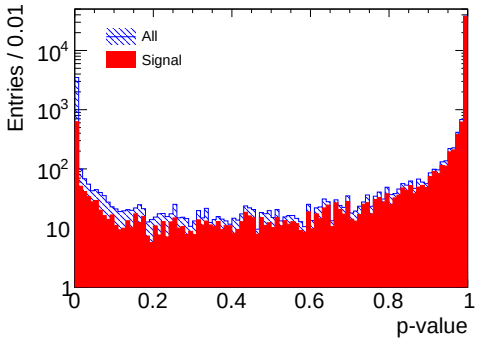

(b) p-value: the quality of the track fitting

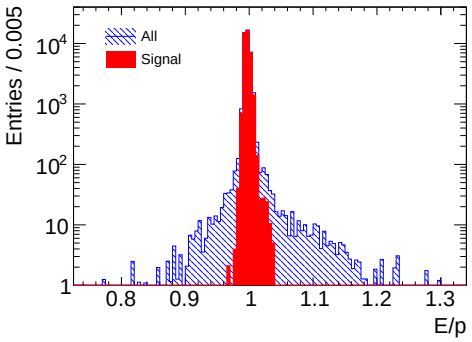

(c) E/p: the ratio of the reconstructed energy to momentum

Figure 7.27: Distributions of the quality-cut variables. The blue dashed histograms belong to all reconstructed objects, and red solid ones belong to those associated with signal tracks.

Table 7.9: Variation of the purity and reconstruction or cut efficiency during the two reconstruction steps and three quality cuts. The last column indicates the relative change from the previous item.

Reconstruction or Cut	Purity	Efficiency	Relative
`ReconECAL`	36.7%	92.4%	
`ReconStrawTrk`	73.5%	77.2%	83.6%
$N_{\text{hits}} \geq 12$	89.4%	73.8%	95.6%
p-value > 0.001	95.9%	72.7%	98.5%
$0.985 < E/p < 1.015$	97.6%	72.5%	99.7%

8

Signal Sensitivity

We use the following SES (single event sensitivity) as a sensitivity estimator,

$$\mathrm{SES} = \frac{1}{N_\mu \, \mathcal{B}_{\mathrm{capture}} \, A_{\mu\text{-}e}}, \tag{8.1}$$

where N_μ denotes the number of muons stopped in the target, $\mathcal{B}_{\mathrm{capture}}$ represents the branching ratio for muon capture in aluminum, and $A_{\mu\text{-}e}$ represents the total acceptance to the signal electron from μ-e conversion. The SES implies a statistical accuracy of the experimental result when one signal electron is observed, and it is roughly equivalent to the branching ratio of μ-e conversion.

Here, we followed the SES definition reported in the previous study [6]. However, in the COMET Phase-I TDR (technical design report), it includes another parameter f_{gnd} into the dominator [4]. It is approximately equivalent to the fraction of "coherent" capture events that leave the nuclei unexcited. Although it is expressed as $f_{\mathrm{gnd}} = 0.9$ in the TDR, it can vary based on the model of μ-e conversion [92]. We consider that this SES calculation is for coherent conversion events; however, we avoid such a model-dependent parameter in this study. In the future, such model-dependent parameters will need to be considered to fit the experimental result to theoretical predictions.

The net acceptance $A_{\mu\text{-}e}$ is estimated for the experimental configuration and the reconstruction and analysis schemes developed for this study. Not only the mean value but also the systematic uncertainty of the SES is assessed. Finally, the SES in the case of using different timing windows is reviewed in addition with the systematic uncertainty.

8.1 Signal Acceptance

The net acceptance $A_{\mu\text{-}e}$ contains five items: geometrical acceptance, trigger and DAQ acceptance, reconstruction efficiency, quality cut efficiency, and momentum cut acceptance. We have already discussed the first four (See the comments in Table 8.1). Below, before reviewing all acceptance values, we discuss the momentum cut acceptance.

8.1.1 Momentum Cut

The momentum cut is applied to the reconstructed momentum. The dashed blue line in Figure 8.1(a) shows the momentum distribution of the signal electrons at the first straw station at the truth level.

We smear the first straw station with the momentum resolution obtained (Figure 7.25) to achieve a realistic reconstruction effect; this is shown by the red line. We obtain the momentum cut acceptance by integrating it in a momentum cut window divided by the total entries. Further, we follow the default momentum cut suggested by the previous study [6] for comparison, which ranges from 104.2–105.5 MeV/c.

Figure 8.1(b) shows the acceptance as a function of the lower limit of the window, with the fixed upper limit of 105.5 MeV/c. The acceptance at 104.2 MeV/c is indicated by the dotted line; it is 0.624.

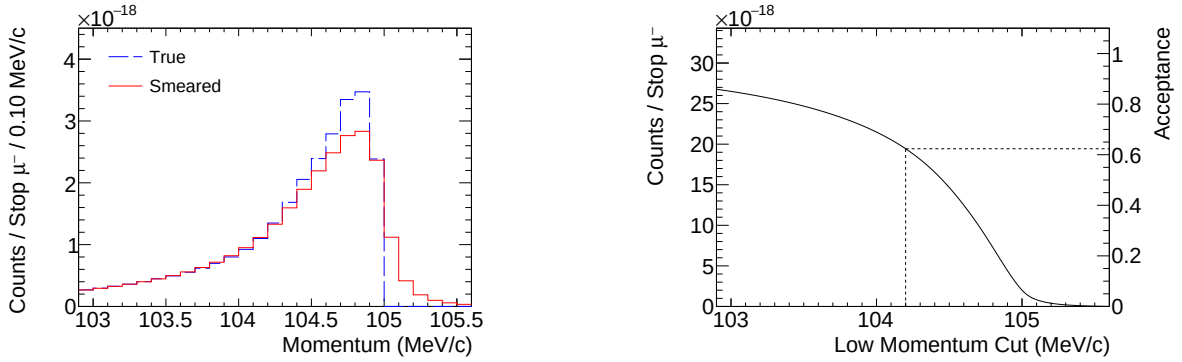

(a) Momentum distributions

(b) Momentum cut acceptance

Figure 8.1: Momentum distribution of signal electrons and momentum cut acceptance. (a) The red line indicates the true momentum at the first straw station. The vertical axis is normalized to the number of stopped muons in the stopping targets. The blue dashed line indicates the same distribution that is smeared by the momentum resolution of `ReconStrawTrk` (Figure 7.25). (b) The vertical axis at the left side represents the integration of (a) as a function of the lower limit of the range, wherein the upper limit is fixed at 105.5 MeV/c. The momentum cut acceptance corresponds to the vertical axis at the right side. The dashed line indicates the value at the default lower limit of 104.2 MeV/c, i.e., 0.624.

8.1.2 Total Acceptance

Table 8.1 provides a summary of the evaluated acceptance values. The acceptances of the geometrical and the trigger and DAQ aspects were estimated at the truth level. For the latter, we added a DAQ efficiency of 0.9 from a conservative point of view. The values of (3)–(5) are especially related to the theme of this study, and they result in 0.453 in total. Thus, we obtained a net acceptance of 3.44%.

The acceptances evaluated by the previous study [6] were also displayed for comparison. The previous study estimated the geometrical acceptance at the first straw station, which was likely an overestimation because signal electrons have to reach the ECAL to generate DAQ triggers.

This study estimates a smaller value at the ECAL, while a number similar to the previous one is obtained at the straw station. The trigger and DAQ acceptance decreased because of the energy threshold acceptance that was introduced. The time window acceptance varied a little because of the geometrical change. As seen in Figure 6.16(a), the timing window acceptance is sensitive to a small change in the timing structure of the signal electron. The previous study did not estimate the

reconstruction and quality cut efficiencies, and instead, they referred to the COMET CDR (conceptual design report) [2] in 2009 which was based on more primitive simulation and analysis schemes.

The deterioration of the momentum cut acceptance is attributed to two reasons: (1) The move of the muon stopping target to the upstream side. The longer path to the detector imposes more energy loss on the signal electrons; however, even a slight difference can cause a large variation, as shown in Figure 8.1(b). (2) The shape of the momentum resolution. The previous study assumed a Gaussian function with a standard deviation of 200 keV/c. The realistic vlue obtained in this study is formed by triple Gaussians that have a long tail which escapes the momentum cut window.

Table 8.1: Summary of acceptances. The unnumbered items are a breakdown of each numbered (bold) item. The values in the last column are obtained from the previous study for (1, 2, 5) and the COMET CDR for (3, 4) [2, 6]. They partly do not use the same definitions as in this study. See the text for details.

Acceptance	Value	Comments	In [2, 6]
(1) Geometrical acceptance	**0.18**	Section 6.3.3	**0.22**
(2) Trigger and DAQ acceptance	**0.43**	Section 6.6	**0.48**
Timing window acceptance	0.49	$600 < t < 1200$ nsec	0.53
Energy threshold acceptance	0.97	$E > 70$ MeV	N/A
DAQ efficiency	0.90		0.90
(3) Reconstruction efficiency	**0.77**	Chapter 7	**0.88**
ECAL reconstruction	0.92	Section 7.2.6	
Straw tracker reconstruction	0.84	Section 7.3.6	
(4) Quality cut efficiency	**0.94**	Section 7.4	**0.89**
The number of hits in the track	0.96	$N_{\text{hits}} \geq 12$	
p-value of the track fitting	0.98	p-value > 0.001	
E/p	1.00	$0.985 < E/p < 1.015$	
(5) Momentum cut acceptance	**0.62**	104.2 MeV/c < p < 105.5 MeV/c	**0.70**
Total of (3)–(5)	*0.45*		*0.55*
Total acceptance	**0.034**		**0.057**

8.2 Single Event Sensitivity

The SES is calculated as

$$\text{SES} = \frac{1}{(I_p/e)\, t_{\text{run}}\, R_{\mu/p}\, \mathcal{B}_{\text{capture}}\, A_{\mu\text{-}e}} = 1.4 \times 10^{-17}. \tag{8.2}$$

N_μ in (8.1) is expanded as $(I_p/e)\, t_{\text{run}}\, R_{\mu/p}$, where I_p denotes the beam current, and $e = 1.6 \times 10^{-19}$ C represents the elementary charge. t_{run} denotes the run time, and $R_{\mu/p}$ represents the muon stopping rate per POT. Table 8.2 summarizes all parameters and their values.

The previous study estimated it as 2.6×10^{-17} for $t_{\text{run}} = 1.57 \times 10^7$ sec [6], which is scaled to 2.0×10^{-17} for the same t_{run} as in this study. The obtained SES is better because of the improvement of $R_{\mu/p}$, which was 1.61×10^{-3} in the previous geometry.

Table 8.2: Parameters in the SES calculation (8.2). $R_{\mu/p}$ and $A_{\mu\text{-}e}$ are given in Sections 6.3.3 and 8.1.2, respectively.

Parameter	Value	Comments
I_p	$7\ \mu$A	8 GeV proton beam current in the Phase-II beam power of 56 kW
t_{run}	2×10^7 sec	One-year live time of the data taking
$R_{\mu/p}$	3.8×10^{-3}	Muon stopping rate per POT
$\mathcal{B}_{\text{capture}}$	0.61	Branching ratio for muon capture in Aluminum
$A_{\mu\text{-}e}$	0.034	Total signal acceptance

8.2.1 SES with Different Timing Windows

We also investigated SES with different timing windows whose start timings moved by ±50 nsec from the default value of 600 nsec. This change affects only signal acceptance, and Table 8.3 summarizes its transition and the resulting SES, in addition to their systematic uncertainty. The geometric and energy threshold acceptances do not change.

The timing window acceptance varied most by Figure 6.16(a). Although the same DAQ efficiency is assumed in all scenarios, it may decrease as more piled-up hits exponentially increase as discussed in Section 6.6.2. Similarly, the BG contamination would deteriorate the reconstruction and quality cut efficiencies, while they were found to be successfully stable.

Table 8.3: Variation of the acceptances and SESs with timing window starts of 550, 600, and 650 nsec, and their systematic uncertainty. The unnumbered items are a breakdown of each numbered (bold) item. The systematic uncertainty of the geometrical acceptance includes that of the muon stopping rate per POT, $R_{\mu/p}$ in (8.2). The total uncertainties are the quadratic sum of all values.

Timing window start (nsec)	550		600		650	
	Mean	Syst. (%)	Mean	Syst. (%)	Mean	Syst. (%)
(1) Geometrical acceptance	**0.18**	**10**	**0.18**	**10**	**0.18**	**10**
(2) Trigger and DAQ acceptance	**0.48**	**5.4**	**0.43**	**5.8**	**0.39**	**6.1**
Timing window acceptance	0.55	5.2	0.49	5.6	0.44	5.9
Energy threshold acceptance	0.97	1.5	0.97	1.5	0.97	1.5
DAQ efficiency	0.90		0.90		0.90	
(3) Reconstruction efficiency	**0.77**	**1.1**	**0.77**	**1.1**	**0.77**	**1.1**
ECAL reconstruction	0.92	1.1	0.92	1.1	0.92	1.1
Straw tracker reconstruction	0.83	0.3	0.84	0.3	0.84	0.3
(4) Quality cut efficiency	**0.94**	**0.3**	**0.94**	**0.4**	**0.94**	**0.4**
The number of hits in the track	0.96	0.2	0.96	0.3	0.96	0.3
p-value of the track fitting	0.98	0.2	0.98	0.2	0.98	0.2
E/p	1.00	0.1	1.00	0.1	1.00	0.1
(5) Momentum cut acceptance	**0.62**	**0.1**	**0.62**	**0.1**	**0.63**	**0.1**
Total of (3)–(5)	*0.45*	*1.2*	*0.45*	*1.2*	*0.45*	*1.2*
Total acceptance	**0.038**	**11.4**	**0.034**	**11.6**	**0.031**	**11.8**
Single event sensitivity	1.3×10^{-17}		1.4×10^{-17}		1.6×10^{-17}	

8.2.2 Systematic Uncertainties

The systematic uncertainty in Table 8.3 was evaluated as follows. The estimation of the geometrical acceptance with simulation mostly depends on the physics model, and in particular, one that describes

the hadronic processes in the pion production from the 8-GeV protons. In the COMET TDR, several physics models are investigated, and they show a standard deviation of 8% around the default model of `SimG4` in the number of produced pions and muons. Further, there are other concerns such as the simulation of the pion and muon tracking, uncertainty in the magnetic field measurement, and a geometrical gap from the design. Since these aspects also influence $R_{\mu/p}$, a 10% uncertainty was set conservatively. For the DAQ efficiency, we avoid adding more assumptions without any reasonable explanation.

The uncertainty of the timing window acceptance arises from the time jitter of the trigger electronics cause by its clock width of 25 nsec (40 MHz). Owing to the linear dependence on the timing window start in Figure 6.16(a), it results in an uncertainty of about 5%. The threshold for the total energy deposit is 70 MeV; however, it will effectively fluctuate because some piled-up hits cannot be separated in the trigger electronics. We again assume a conservative fluctuation of 10%, but fortunately, its effect on the acceptance is weak (Figure 6.16(b)) and it adds only 1.5% to its uncertainty.

Finally, we investigated the uncertainty of the last three acceptances by varying the control parameters of `ReconECAL` and `ReconStrawTrk` from the optimum values. Since the parameters could correlate in a complicated manner, all them were varied simultaneously in a Gaussian distribution with a standard deviation of 0.05 for the cut-off threshold of the MVA classifiers, 0.1 cm for σ_{XY}, and 0.1 for C_{hist}. Thus, the ECAL reconstruction efficiency had the largest uncertainty of 1.1%, whereas the others were so stable that the resulting uncertainties were less than 0.5%.

In conclusion, the uncertainties arising from the developed reconstruction and analysis schemes achieved a total systematic uncertainty of 1.2%, which is sufficiently small compared to the others.

9

Summary

The SM has been confirmed to be consistent with nature, and lepton-flavor conservation is a fundamental requirement in that frame. However, we already know neutrino oscillation exists because of finite neutrino masses, which also stimulates searches for CLFV. Although the probability that CLFV processes occur is assumed to considerably low even with nonzero neutrino mass, some theories that support physics BSM suggest higher rates. Currently, modern experimental technology is about to reach these rates. Muon-to-electron conversion (μ-e conversion)—the decay of the muon captured in an atom to only a single electron—has been long researched since the discovery of the muon. Together with $\mu \to e\gamma$ and $\mu \to eee$, it is a cardinal CLFV muon decay mode to investigate and validate the BSM models.

The COMET experiment is attempting to search for μ-e conversion in aluminum by utilizing the high-intensity proton beam of the J-PARC in Japan. The experiment will be performed in two stages (Phase-I and -II) with excellent sensitivities of 10^{-15} and 10^{-17} that improve the current upper limit of $\mathrm{BR}\,(\mu\mathrm{Au} \to e\mathrm{Au}) = 7 \times 10^{-13}$, as set by the SINDRUM-II experiment, by a factor of 10000. The dedicated muon beamline exploits various techniques to generate and carry the required low-momentum muons, introduce the signal electrons of 104.97 MeV to the detector, and simultaneously eliminate the other particles that result in BGs. The particle detector system in Phase-II, i.e., StrECAL, comprises a straw tube tracker and the ECAL, which measure the momentum and energy, respectively. It also works in the beam measurement program before the Phase-I experiment to study the beam components first experimentally.

The straw tracker comprises straw tubes with a diameter and thickness of 9.75 mm and 20 μm in Phase-I, and 5 mm and 12 μm in Phase-II. The straw tube is required to have a spatial resolution less than 200 μm and work in a vacuum with a pressure of 100 Pa to achieve a momentum resolution of less than 200 keV/c at 105 MeV/c. The ECAL works as the trigger detector, and it is required to have energy, time, and position resolutions of 5%, 1 nsec, and 1 cm for the 105 MeV electrons. To this end, we formed the ECAL from the LYSO scintillator crystals, which have high density, high light yield, and short decay constant compared to conventional inorganic crystals. The scintillation photons from LYSO are read by APD, and an LED is embedded in the crystal module for gain calibration. Furthermore, its feedthrough made of PCB allows us to gather many wirings and the dedicated preamplifier boards in a small area, thereby minimizing contact noises. We developed the waveform-digitizing electronics with a high sampling rate for StrECAL, ROESTI and EROS to secure the pile-up separa-

tion ability. The development of the StrECAL slow control modules is also ongoing. All electronic parts in the StrECAL system are carefully chosen by considering and testing their radiation tolerance with neutrons and gamma rays.

Based on the latest StrECAL design, we constructed a full-scale StrECAL prototype and evaluated its performance with electron beams from 65 to 185 MeV/c at ELPH in 2017. Both detectors were installed in a single vacuum chamber from which the air could be exhausted down to about 1 Pa; still, the detectors worked correctly. For the straw tracker, we compared two candidates of the gas mixture: Ar:C_2H_6 (50:50) and Ar:CO_2 (70:30). The analysis results showed that at 105 MeV/c, the straw tube had a 100 % hit-detection efficiency with a driving HV of more than 1800 V in both gas mixtures. For the spatial resolution at 1950 V, Ar:C_2H_6 has a relatively stable resolution less than 200 μm and an even better one at 2050 V although Ar:CO_2 looks partly difficult to meet the requirement. From the ECAL, an energy resolution of $3.91 \pm 0.07\%$, a time resolution of 0.54 ± 0.12 nsec, and a position resolution of 7.65 ± 0.07 mm were obtained at 105 MeV/c. In conclusion, we confirmed that all obtained StrECAL performances accomplished the requirement.

The COMET collaboration has been developing the official simulation and analysis software framework named ICEDUST. By using the `Geant4`-based simulator and event-merging tool, we produced 7.5×10^4 events, each of which comprise 20 bunches in the Phase-II beam configuration.

To evaluate the Phase-II sensitivity by considering the evaluated StrECAL performance in the simulation, the detector-response simulator was customized to reproduce the performance. For the spatial resolution of the straw tube, the observed performance for the Phase-I straw tube was extrapolated to the Phase-II straw tube with a different diameter. The ECAL resolutions were reproduced by modeling the resolutions per crystal. The waveform shapes were also modeled including the baseline noise, and the resolution curves—obtained with the same analysis procedure used for the experimental data—showed good agreement with the observation.

We newly developed the reconstruction software for the StrECAL hits by utilizing the MVA techniques. A momentum resolution of 190 keV/c was obtained for the 105 MeV signal electrons, which met the requirement. The reconstruction efficiency was evaluated at 77.2% in total. Since the purity was still 73.5%, which is low, three quality cuts were optimized. Thus, although the reconstruction efficiency deteriorated to 72.5%, the purity improved to 97.6%.

The total acceptance was estimated at 0.034, with the default timing window from 600 to 1200 nsec. This corresponds to an SES of 1.4×10^{-17}. Therefore, the target sensitivity of Phase-II is still achievable after considering the detector aspects. The total systematic uncertainty was evaluated at 11.6%. Finally, the performance of the reconstruction and analysis parts, which is the theme of this study, was found to be very stable for different timing windows; their systematic uncertainty was only 1.2%.

Appendix A

Noise in the Straw-Tracker Waveforms

Owing to its simple structure, the straw tube is sensitive to electric noises. We observed two types of noise during the experiment; however, we could not remove them. The first type is coherent noise that lies at all straw tubes. The second is crosstalk that arises from strong signals at the adjacent channels.

A.1 Coherent Noise

Coherent noise comes externally and has the same shape for each event in all straw waveforms. Figure A.1 shows its elimination with a sample waveform. The blue waveform is the initially recorded data that contains a signal pulse and coherent noise. Since some of the other channels have coherent noise but no signal pulse, the red template waveform is created by averaging them. Removing it from the original waveform yields the noise-reduced green waveform.

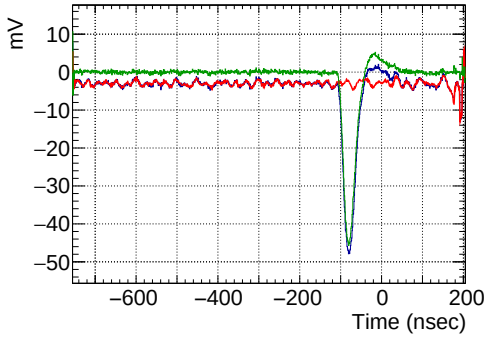

Figure A.1: Coherent-noise reduction. The red waveform signifies the shape of a coherent noise that is also involved in the original blue waveform. The subtraction of the template from the original waveform yields the noise-reduced green waveform.

A.2 Crosstalk

Figure A.2 illustrates how the crosstalk occurs. An electron track passes through three straw tubes: Channels 7, 8, and 9 from the upstream layer. Since it is closer to the sense wires of Channels 7 and

8, the drift times must be shorter than that of Channel 9, and hence, the signal pulses appear faster than that of Channel 9. The following three items are typical crosstalk approaches.

Type 1 One-way crosstalk with an empty channel.

Type 2 Mutual crosstalk with another signal channel; the pulse timings in both are different.

Type 3 Mutual crosstalk with another signal channel, and both pulses appear simultaneously.

Via those routes, there are three interference cases, as shown in the figure.

Case (a) Channel 9 has a crosstalk pulse via Type 2 ahead of its signal pulse.

Case (b) Channel 8 receives crosstalk pulses from Channel 9 via Type 2 and Channel 7 via Type 3.

Case (c) Channel 10 has no pulse initially, but a crosstalk pulse arises there via Type 1.

Case (a) is fatal because the leading-edge of the signal pulse is distorted by the crosstalk, and therefore, it leads to a wrong reconstruction of the drift time. Cases (b) and (c) do not matter; however, the latter plays an essential role in resolving this problem.

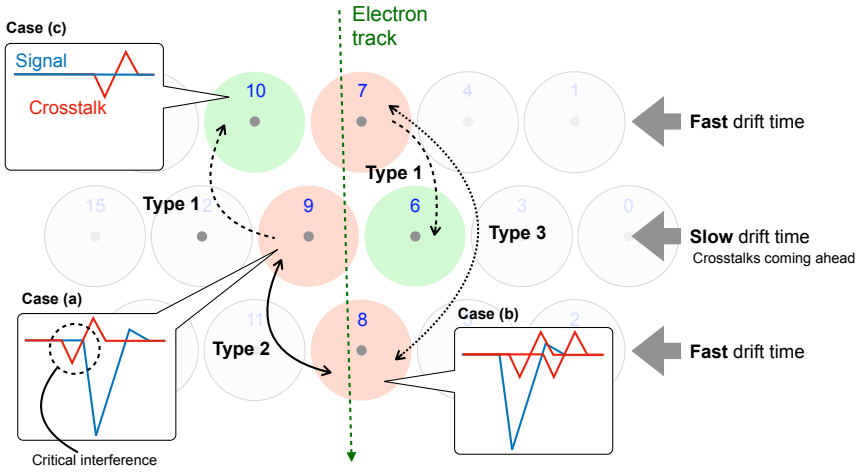

Figure A.2: Typical situation of the crosstalk among straw tubes. When an electron passes through three straw tubes, the induced pulses are very intense to interfere in the neighboring channels. Three types of crosstalk to neighbor channels yields different interference shapes in the resulting waveforms.

Crosstalk templates were created to predict the most likely crosstalk shapes event by event to minimize the crosstalk complexity involved in signal pulses. All Case (c) waveforms collected from all datasets were fitted by

$$\begin{aligned} f(t) &= p_{\text{amp.}} T(t) e^{-\frac{1}{2}(T(t)^2-1)} \\ T(t) &= \frac{t - p_{\text{time}}}{p_{\text{width}}} - 1. \end{aligned} \tag{A.1}$$

The parameters p_{amp}, p_{time}, and p_{width} correlate with two form factors of the source signal pulse: Amplitude height and leading time. Figure A.3 shows a fit result with a typical crosstalk pulse of Case (c), and it illustrates the relationship between the parameters and form factors. p_{time} represents the

time distance from the original pulse's peaking time and is essentially a positive value. Figure A.4 are correlation plots between each parameter and a form factor, each of which is fitted with a polynomial function. Because of the significant data fluctuation around the fitted curves, values given by the curves are used as the initial parameters to fit (A.1) on individual crosstalk pulses; this is shown in Figure A.5. The original green waveform has a small crosstalk pulse at its leading edge that arises from the neighbor channels. The shape of the broken black line is calculated from the fitted curve. The broken red line is the fit result, and it is subtracted to obtain the crosstalk-reduced blue waveform.

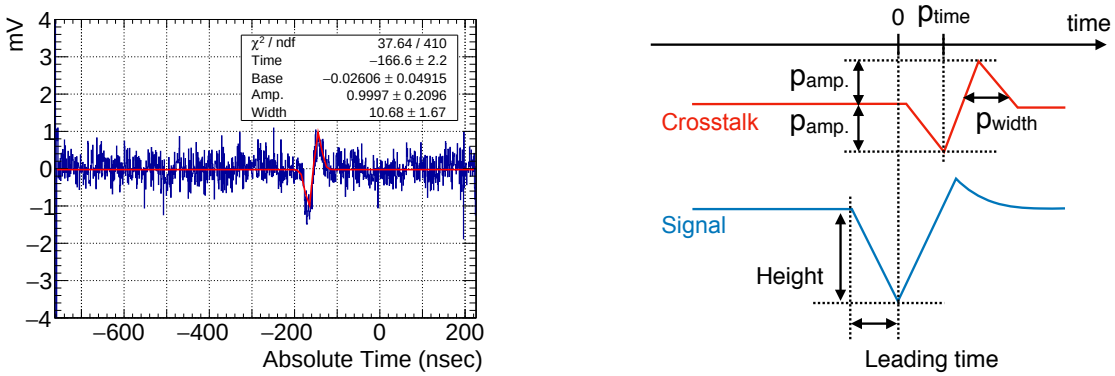

(a) Fitting **(b)** Defition of the parameters

Figure A.3: Pure crosstalk pulse fitted by the crosstalk function. (a) The symmetric shape of the function (A.1) well reproduces the shape of the crosstalk pulse. (b) Two form-factor variables of the signal pulse that yield the crosstalk and influence the shape and timing of the crosstalk pulse.

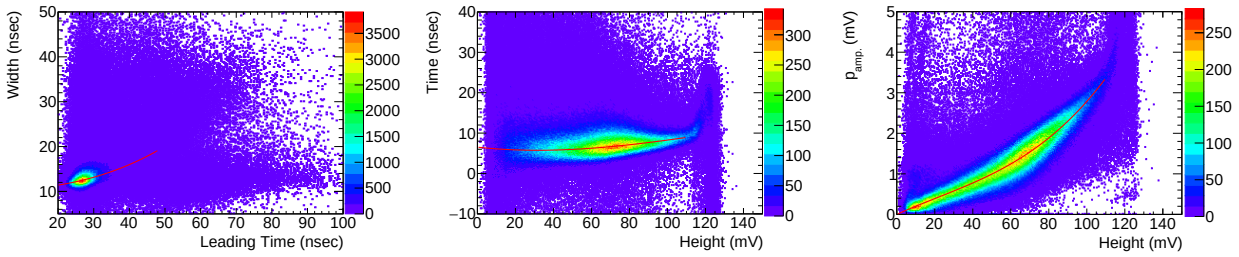

(a) p_{width} vs. leading time **(b)** p_{time} vs. height **(c)** $p_{\text{amp.}}$ vs. height

Figure A.4: Correlations between the fitted parameters and form factors. The parameters roughly depend on the form factors of the signal pulses inducing the crosstalk in neighbor channels. The trends are fitted by polynomial functions.

This crosstalk introduces a strong bias into the drift time reconstruction. Figure A.6 compares the drift-time distributions reconstructed from `ar50et50.2050v` before and after crosstalk reduction. The spikes in the distribution indicate that the bias is suppressed significantly. However, it is not complete, and it results in a kink in the spatial resolution curve, as mentioned in Section 5.4.2.

Because of the crosstalk, the straw tube, electronics, wire, and circuit between both were suspected, while only the last item remains for the following reasons. First, we confirmed only the

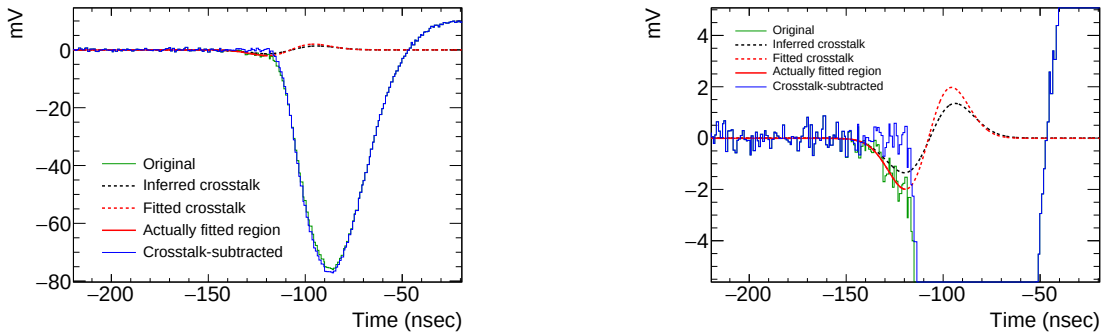

(a) Whole view **(b)** Zoomed view

Figure A.5: Demonstration of crosstalk reduction. The original green waveform is contaminated with a crosstalk pulse fitted by the crosstalk function (A.1). The parameters of the black-line function are calculated from the form factors of the signal pulse inducing this crosstalk, and they are used as the initial parameters for the crosstalk fitting. The red line is the fit result, and it is subtracted to obtain the blue line.

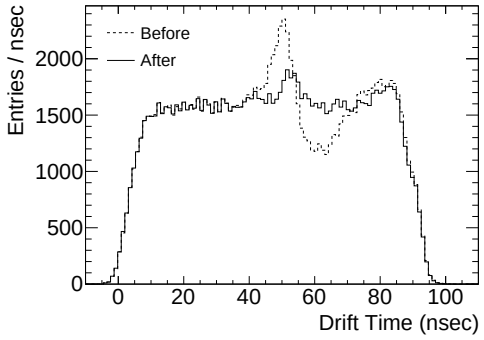

Figure A.6: Comparison of the drift-time distributions before and after crosstalk reduction. The crosstalk introduces the spike; however, the crosstalk reduction successfully moderates it.

interference among the straw tubes with consecutive channel numbers, the geometrical distance was not affected. Second, another type of crosstalk was confirmed in ROESTI. However, it spreads over all 16 channels and is considerably small; in addition, its shape was also different from that shown in Figure A.3(a). Finally, the channels with the crosstalk are adjacent on the filtering circuit in the prototype, and therefore, the crosstalk appears to occur there.

Appendix B

Multivariate Analysis and Machine Learning

B.1 Artificial Neural Network with Multilayer Perceptron

Figure B.1 adopted from [89] illustrates MLP. It comprises n_{layer} layers of artificial neurons[1] represented by circles, where n_{layer} is more than two in MLP; the first and last layers are referred to as the input and output layers, and all others are called hidden layers. The input layer holds n_{var} input variables x_i ($i = 1, 2, ..., n_{\text{var}}$), and the output layer yields the output variable y_{ANN} that is a (neural net) estimator[2] The i-th neuron at the j-th layer owns a state parameter y_i^j, and it contacts all neurons in the previous and following layers. Every layer except the output layer has a special neuron labeled "bias," which provides a constant value. The connection between the neurons with y_i^j and y_k^{j+1} has a weight parameter, w_{ik}^j. Therefore, y_i^j is calculated by

$$y_i^j = f_{\text{act.}}\left(w_{0i}^{j-1} + \sum_k w_{ki}^{j-1}\, y_k^{j-1}\right), \tag{B.1}$$

where w_{0i}^{j-1} represents the contribution from the bias neuron. $f_{\text{act.}}(x)$ denotes the neuron activation function, and it can be an arbitrary form. However, we attempted the following two conventional types.

$$f_{\text{act.}}(x) = \begin{cases} \dfrac{1}{1+e^{-kx}} & \text{Sigmoid} \\ \dfrac{e^x - e^{-x}}{e^x + e^{-x}} & \text{Tanh} \end{cases}. \tag{B.2}$$

Although the input and output layers in the figure have a linear form and the hidden layer has a Tanh form, we used the same one for all layers. The MLP training now depends on the optimization problem of the weights.

The backpropagation algorithm, the original idea for which was reported in [93], is used for the training. This algorithm modifies the weights from the last layer so that y_{ANN} becomes close to the values in the training sample. An error function E is defined to be minimized with the weights as

$$E\left(\mathbf{x}_1,\, \mathbf{x}_2,\, ...,\, \mathbf{x}_{n_{\text{var}}},\, \hat{\mathbf{y}}|\mathbf{w}\right) = \sum_{a=1}^{N} E_a\left(\mathbf{x}_a|\mathbf{w}\right) = \sum_{a=1}^{N} \frac{1}{2}\left(y_{\text{ANN,a}} - \hat{y}_a\right)^2, \tag{B.3}$$

[1] This no longer imitates the real neuron in the human brain.

[2] There can be multiple estimators.

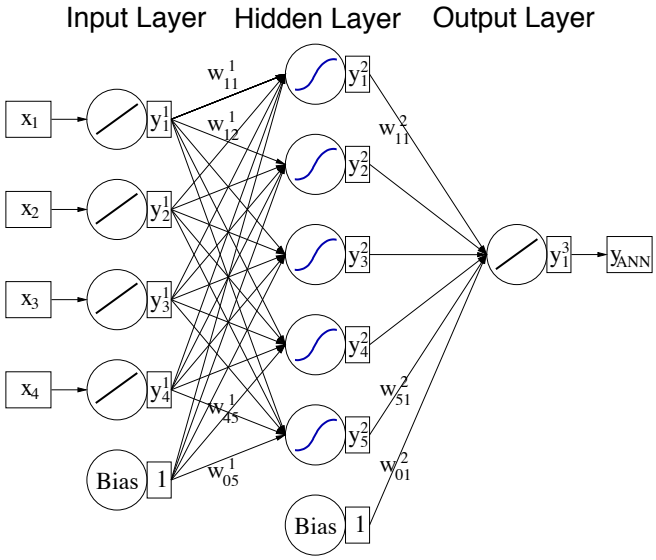

Figure B.1: Schematics of multilayer perceptron with a hidden layer; image adopted from [89]. x_i (i = 1, 2, ...) and y_{ANN} represent the input variables and an output variable, respectively. y_i^j denotes the hidden variables at each j-th layer, where the first and third layers are the input and output layers, and the other is the hidden layer. Every pair of neurons (circle) between a given layer and the following layer is connected with its own weight w_{ik}^j.

where a denotes the index of the N training samples, $\mathbf{w}$ represents the ensemble of the weights, and $\mathbf{x}_i$ and $\mathbf{y}$ represent N samples of the i-th input variable and $\hat{y}$. $\hat{y}_a$ and $y_{\mathrm{ANN,a}}$ represent the target value for the estimator and output of the MLP, respectively. Further, $\mathbf{x}_a = (x_1, x_2, ..., x_{n_{\mathrm{var}}}, \hat{y})_a$ represents the dataset from the a-th event. Since y_{ANN} contains all of $\mathbf{w}$ through $f_{\mathrm{act.}}$, the weight reflects all former weights, and each w_{ik}^j is modified from the last layer with a negative derivative of E as

$$w_{ik}^j \to w_{ik}^j - \eta \sum_{a=1}^{N} \frac{\partial E_a}{\partial w_{ik}^j}, \tag{B.4}$$

where η represents the learning rate and we set it at 0.02. By iterating the modification, $\mathbf{w}$ converges to the best values as the error function does not decrease considerably.

B.2 Boosted Decision Trees

The decision tree comprises a sequence of nodes as shown in Figure B.2, where xi, xj, and xk are input variables. There are two types of nodes: One has binary branches connected to other nodes and a criterion with a variable that guides the decision procedure to one of them. The other node is in the classification case, and it is labeled either as “S” or “B” and it implies that the event reaching there seems to be induced by signal or BG sources. This node can be a real number in the regression type[3]. The maximum depth of the example is three; however, it can be more instead of an increase in the calculation cost. The nodes on the left side stop at a shallower depth by “pruning” because there is no more criterion to enhance the performance.

[3]In the regression cases, it is more appropriate to call the tree “regression tree.”

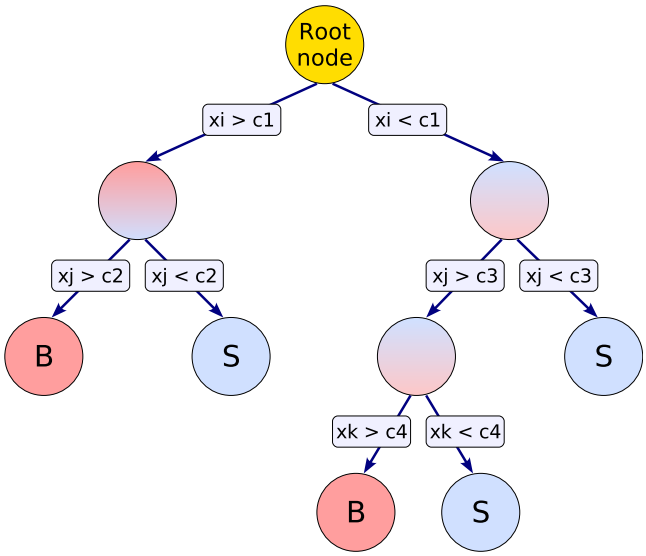

Figure B.2: Schematics of decision trees with a depth of three; image adopted from [89]. This is an example of the classification of events that have input variables xi, xj, and xk; the procedure lasts from the top (root) node to a node indicating "S" (signal) or "B" (background). Every node has binary selections that appear as branches with a criterion for an input variable. Each branch links with another node at the one-stage deep level.

The criteria of the nodes is determined as follows. First, all N training samples are gathered in the root node. Second, the first variable and threshold are determined to minimize the so-called Gini index, which is defined as $p(1-p)$, where p denotes the ratio of the number of signal-labeled events to N. A new node is assigned to each of the two sample sets split by the found criterion; the same algorithm is applied to it. Finally, it repeats until the number of samples in each node becomes less than a threshold for which we used 5% of N.

A single shallow decision tree is fast; however, it is not robust for many applications. Ensemble learning is one method to improve this; in this method, the final decision is made via a majority vote by a large number of trees, wherein a single tree is called a weak learner. Although each performance is low, the variation of the result from the target[4] can be reduced by averaging them as

$$H(x) = \sum_{i=1}^{n_h} w_i \, h_i(x) \qquad \left(1 = \sum_{i=1}^{n_h} w_i\right), \tag{B.5}$$

where x represents the input variables, n_h represents the number of weak learners, and $h_i(x)$ and $H(x)$ denote the outputs of each weak learner and the ensembled learner, respectively. They range from -1 (background-like) to $+1$ (signal-like) in the `TMVA` implementation. Since $H(x)$ becomes a real value, it can be converted into an integer in the binary classification problems; for example, by sign $(H(x))$. w_i represents the weight for each h_i, and for MLP, its determination is key to the learning. The easiest approach is to set $w_i = \frac{1}{n_h}$, which is called bagging (bootstrap aggregation). In this case, n_h sets of n ($n < N$) training data are sampled with a replacement from the original N data; hence, every h_i is generated from each set in parallel, and it results in a different shape. However, if every weak learner

[4] More precisely, this is discussed in terms of bias and variance. See textbooks in detail.

has a principal bias in the learning, the result will still deviate from the goal. Therefore, a boosting algorithm was developed.

Boosting algorithms consider weak learners sequentially based on the performance of the former weak learner and adjust each weight to assign more importance to the better ones. There are many practical algorithms, and they are still being developed. Here, the most basic one called AdaBoost (adaptive boosting) [94] that is used for binary classification problems is introduced. As the prerequisite, x_j and y_j ($j = 1, 2, ..., N$) are the multiple input and single output variables of the j-th event in the training data samples. w_i^j is its weight in the i-th weak learner, $h_i(x_j)$, and w_i^1 is set at $\frac{1}{N}$ as the initial state. Both y_i and $h_i(x_j)$ have either -1 or $+1$. The algorithm loops for $i = 1, 2, ..., n_h$. First, it finds a weak learner h_i that minimizes the error

$$\epsilon_i = \sum_{j=1}^{N} w_i^j \left[h_i(x_j) \neq y_j \right], \tag{B.6}$$

where the sum is only for event j satisfying the condition in the bracket. When $\epsilon_i > 0.5$, the loop aborts because the following calculation becomes nonfuntional. Second, it calculates a confidence value, which is defined as $\alpha_i = \frac{1}{2} \ln \frac{1-\epsilon_i}{\epsilon_i}$. Third, it updates the weight for the next weak learner h_{i+1} by $w_{i+1}^j = w_i^j \exp\left(-\alpha_i\, h_i(x_j)\, y_j\right) / Z_i$ where Z_i is the renormalization factor for all w_{i+1}^j. The power of the exponential becomes positive so that $w_{i+1}^j > w_i^j$ when $h_i(x_j) \neq y_j$; therefore, that event j is accorded more importance in the next learning for h_{i+1}, which boosts the learning. Finally, (B.5) provides the final decision.

In addition to AdaBoost, GBDT is also famous. Although its detail is also left to textbooks such as [95], it is based on a loss function whose actual form is different in each algorithm instead of ϵ_i.

Bibliography

[1] **Super-Kamiokande Collaboration**, Y. Fukuda *et al.*, Evidence for oscillation of atmospheric neutrinos, Phys. Rev. Lett. **81**, 1562 (1998).

[2] **The COMET Collaboration**, Y. Cui *et al.*, Conceptual Design Report for Experimental Search for Lepton Flavor Violating μ^--e^- Conversion at Sensitivity of 10^{-16} with a Slow-Extracted Bunched Proton Beam (COMET), KEK Report 2009-10 (2009).

[3] **COMET Collaboration**, D. Bryman *et al.*, COMET Proposal, (2007).

[4] T. C. Collaboration *et al.*, COMET Phase-I technical design report, Progress of Theoretical and Experimental Physics **2020** (2020), https://academic.oup.com/ptep/article-pdf/2020/3/033C01/32903980/ptz125.pdf, 033C01.

[5] W. Bertl *et al.*, A search for μ-e conversion in muonic gold, Eur. Phys. J. C **47**, 337 (2006).

[6] B. E. Krikler, *Sensitivity and background estimates for phase-II of the COMET experiment*, PhD thesis, Imperial College London, 2017.

[7] E. P. Hincks and B. Pontecorvo, Search for gamma-radiation in the 2.2-microsecond meson decay process, Phys. Rev. **73**, 257 (1948).

[8] Y. Nishina, M. Takeuchi, and T. Ichimiya, On the nature of cosmic-ray particles, Phys. Rev. **52**, 1198 (1937).

[9] S. H. Neddermeyer and C. D. Anderson, Note on the nature of cosmic-ray particles, Phys. Rev. **51**, 884 (1937).

[10] J. C. Street and E. C. Stevenson, New evidence for the existence of a particle of mass intermediate between the proton and electron, Phys. Rev. **52**, 1003 (1937).

[11] R. Davis, D. S. Harmer, and K. C. Hoffman, Search for neutrinos from the sun, Phys. Rev. Lett. **20**, 1205 (1968).

[12] B. Pontecorvo, Mesonium and antimesonium, Zhur. Eksptl'. i Teoret. Fiz. **33** (1957).

[13] B. Pontecorvo, Mesonium and antimesonium, Journal of Experimental and Theoretical Physics **6**, 429 (1957).

[14] M. Gell-Mann and A. Pais, Behavior of neutral particles under charge conjugation, Phys. Rev. **97**, 1387 (1955).

[15] Z. Maki, M. Nakagawa, and S. Sakata, Remarks on the Unified Model of Elementary Particles, Progress of Theoretical Physics **28**, 870 (1962), https://academic.oup.com/ptp/article-pdf/28/5/870/5258750/28-5-870.pdf.

[16] B. Pontecorvo, Neutrino Experiments and the Problem of Conservation of Leptonic Charge, Zhur. Eksptl'. i Teoret. Fiz. **53**, 1717 (1967).

[17] H. H. Chen, Direct approach to resolve the solar-neutrino problem, Phys. Rev. Lett. **55**, 1534 (1985).

[18] **SNO Collaboration**, Q. R. Ahmad *et al.*, Measurement of the rate of $\nu_e + d \rightarrow p + p + e^-$ interactions produced by ^8b solar neutrinos at the sudbury neutrino observatory, Phys. Rev. Lett. **87**, 071301 (2001).

[19] **K2K Collaboration**, M. H. Ahn *et al.*, Measurement of neutrino oscillation by the k2k experiment, Phys. Rev. D **74**, 072003 (2006).

[20] A. M. Baldini *et al.*, The design of the meg ii experiment, The European Physical Journal C **78**, 380 (2018).

[21] M. Aoki and D. Collaboration, An experimental search for muon-electron conversion in nuclear field at sensitivity of 10 − 14 with a pulsed proton beam, AIP Conference Proceedings **1441**, 599 (2012), https://aip.scitation.org/doi/pdf/10.1063/1.3700628.

[22] L. Bartoszek *et al.*, Mu2e technical design report, 2015, 1501.05241.

[23] R. Bernstein and P. S. Cooper, Charged lepton flavor violation: An experimenter's guide, Physics Reports **532**, 27 (2013), Charged Lepton Flavor Violation: An Experimenter's Guide.

[24] A. M. Baldini *et al.*, Search for the lepton flavour violating decay $$\mu ˆ+ \rightarrow \mathrm {e}ˆ+ \gamma $$ μ +→e+ γ with the full dataset of the meg experiment, The European Physical Journal C **76**, 434 (2016).

[25] S. T. Petcov, The processes mu –¿ e gamma, mu –¿ e e anti-e, neutrino' –¿ neutrino gamma in the weinberg-salam model with neutrino mixing, Sov. J. Nucl. Phys. **25**, 641 (1977).

[26] S. Bilenky, S. Petcov, and B. Pontecorvo, Lepton mixing, μ → e + γ decay and neutrino oscillations, Physics Letters B **67**, 309 (1977).

[27] W. Marciano and A. Sanda, Exotic decays of the muon and heavy leptons in gauge theories, Physics Letters B **67**, 303 (1977).

[28] B. W. Lee, S. Pakvasa, R. E. Shrock, and H. Sugawara, Muon and electron number nonconservation in a $v - a$ gauge model, Phys. Rev. Lett. **38**, 937 (1977).

[29] S. L. Glashow, J. Iliopoulos, and L. Maiani, Weak interactions with lepton-hadron symmetry, Phys. Rev. D **2**, 1285 (1970).

[30] A. de Gouvêa, (charged) lepton flavor violation, Nuclear Physics B - Proceedings Supplements **188**, 303 (2009), Proceedings of the Neutrino Oscillation Workshop.

[31] U. Bellgardt *et al.*, Search for the decay $\mu + \rightarrow$ e+e+e $-$, Nuclear Physics B **299**, 1 (1988).

[32] Papa, Angela, Towards a new generation of charged lepton flavour violation searches at the paul scherrer institut: The meg upgrade and the mu3e experiment, EPJ Web Conf. **234**, 01011 (2020).

[33] D. Measday, The nuclear physics of muon capture, Physics Reports **354**, 243 (2001).

[34] H. Chiang, E. Oset, T. Kosmas, A. Faessler, and J. Vergados, Coherent and incoherent (μ $-$, e $-$) conversion in nuclei, Nuclear Physics A **559**, 526 (1993).

[35] N. Teshima, Status of the DeeMe Experiment, an Experimental Search for μ-e Conversion at J-PARC MLF, PoS **NuFact2019**, 082 (2020).

[36] **Mu2e**, S. Miscetti, Status of the Mu2e experiment at Fermilab, EPJ Web Conf. **234**, 01010 (2020).

[37] S. P. MARTIN, A supersymmetry primer, Advanced Series on Directions in High Energy Physics , 1 (1998).

[38] A. H. Chamseddine, R. Arnowitt, and P. Nath, Locally supersymmetric grand unification, Phys. Rev. Lett. **49**, 970 (1982).

[39] R. Barbieri, S. Ferrara, and C. Savoy, Gauge models with spontaneously broken local supersymmetry, Physics Letters B **119**, 343 (1982).

[40] L. Hall, J. Lykken, and S. Weinberg, Supergravity as the messenger of supersymmetry breaking, Phys. Rev. D **27**, 2359 (1983).

[41] H. Nilles, Supersymmetry, supergravity and particle physics, Physics Reports **110**, 1 (1984).

[42] L. Hall, V. Kostelecky, and S. Raby, New flavor violations in supergravity models, Nuclear Physics B **267**, 415 (1986).

[43] S. Dimopoulos and H. Georgi, Softly broken supersymmetry and su(5), Nuclear Physics B **193**, 150 (1981).

[44] N. Sakai, Naturalnes in supersymmetric guts, Zeitschrift für Physik C Particles and Fields **11**, 153 (1981).

[45] U. Amaldi, W. de Boer, and H. Fürstenau, Comparison of grand unified theories with electroweak and strong coupling constants measured at lep, Physics Letters B **260**, 447 (1991).

[46] J. Ellis, S. Kelley, and D. Nanopoulos, Probing the desert using gauge coupling unification, Physics Letters B **260**, 131 (1991).

[47] P. Langacker and M. Luo, Implications of precision electroweak experiments for m_t, ρ_0, $sin^2\theta_W$, and grand unification, Phys. Rev. D **44**, 817 (1991).

[48] R. Barbieri and L. Hall, Signals for supersymmetric unification, Physics Letters B **338**, 212 (1994).

[49] R. Barbieri, L. Hall, and A. Strumia, Violations of lepton flavour and cp in supersymmetric unified theories, Nuclear Physics B **445**, 219 (1995).

[50] J. Hisano, T. Moroi, K. Tobe, and M. Yamaguchi, Exact event rates of lepton flavor violating processes in supersymmetric su(5) model, Physics Letters B **391**, 341 (1997).

[51] M. Gell-Mann, P. Ramond, and R. Slansky, Complex Spinors and Unified Theories, Conf. Proc. C **790927**, 315 (1979), 1306.4669.

[52] T. Yanagida, Horizontal Symmetry and Masses of Neutrinos, Progress of Theoretical Physics **64**, 1103 (1980), https://academic.oup.com/ptp/article-pdf/64/3/1103/5394376/64-3-1103.pdf.

[53] F. Borzumati and A. Masiero, Large muon- and electron-number nonconservation in supergravity theories, Phys. Rev. Lett. **57**, 961 (1986).

[54] A. Masiero, S. Profumo, S. K. Vempati, and C. E. Yaguna, Lepton flavor violation, neutralino dark matter and the reach of the LHC, Journal of High Energy Physics **2004**, 046 (2004).

[55] T. P. Cheng and L.-F. Li, $\mu \to e\gamma$ in theories with dirac and majorana neutrino-mass terms, Phys. Rev. Lett. **45**, 1908 (1980).

[56] C. Han, K. ichi Hikasa, L. Wu, J. M. Yang, and Y. Zhang, Status of cmssm in light of current lhc run-2 and lux data, Physics Letters B **769**, 470 (2017).

[57] A. J. R. Figueiredo and A. M. Teixeira, Slepton mass splittings and clfv in the susy seesaw in the light of recent experimental results, Journal of High Energy Physics **2014**, 15 (2014).

[58] G. Ghosh, Analytical Soft SUSY Spectrum in Supersymmetric Models in Light of $S_4 \times Z_n$ flavor symmetric SUSY SO(10) theory, (2019), 1908.11160.

[59] P. Langacker, The physics of heavy $Z^{'}$ gauge bosons, Rev. Mod. Phys. **81**, 1199 (2009).

[60] B. Murakami, Impact of lepton-flavor violating $Z^{'}$ bosons on muon $g-2$ and other muon observables, Phys. Rev. D **65**, 055003 (2002).

[61] R. Harnik, J. Kopp, and J. Zupan, Flavor violating higgs decays, Journal of High Energy Physics **2013**, 26 (2013).

[62] **ATLAS Collaboration**, M. Aaboud *et al.*, Search for lepton-flavor violation in different-flavor, high-mass final states in pp collisions at $\sqrt{s} = 13$ TeV with the atlas detector, Phys. Rev. D **98**, 092008 (2018).

[63] A. M. Sirunyan *et al.*, Search for lepton-flavor violating decays of heavy resonances and quantum black holes to e μ final states in proton-proton collisions at $$ \sqrt{s}=13 $$tev, Journal of High Energy Physics **2018**, 73 (2018).

[64] G. Aad *et al.*, Search for the Higgs boson decays $H \to ee$ and $H \to e\mu$ in pp collisions at $\sqrt{s} = 13$ TeV with the ATLAS detector, Physics Letters B **801**, 135148 (2020).

[65] V. Khachatryan *et al.*, Search for lepton flavour violating decays of the Higgs boson to $e\tau$ and $e\mu$ in proton–proton collisions at $\sqrt{s}$ =8 TeV, Physics Letters B **763**, 472 (2016).

[66] V. Cirigliano, R. Kitano, Y. Okada, and P. Tuzon, Model discriminating power of $\mu \to e$ conversion in nuclei, Phys. Rev. D **80**, 013002 (2009).

[67] A. Czarnecki, X. Garcia i Tormo, and W. J. Marciano, Muon decay in orbit: Spectrum of high-energy electrons, Phys. Rev. D **84**, 013006 (2011).

[68] S. Agostinelli *et al.*, Geant4 - a simulation toolkit, Nuclear Instruments and Methods in Physics Research Section A: Accelerators, Spectrometers, Detectors and Associated Equipment **506**, 250 (2003).

[69] A. Vasilescu and G. Lindstroem, Displacement damage in silicon, on-line compilation, `https://rd50.web.cern.ch/NIEL`.

[70] S. Ritt and P. A. Amaudruz, New components of the MIDAS data acquisition system, in *1999 IEEE Conference on Real-Time Computer Applications in Nuclear Particle and Plasma Physics. 11th IEEE NPSS Real Time Conference. Conference Record (Cat. No.99EX295)*, pp. 116–118, 1999.

[71] S. Movchan, Straw tracker prototype for the precise measurement of the very rare decay $K^+ \to \pi^+\nu\nu^-$ (NA62 experiment at SPS CERN), Nuclear Instruments and Methods in Physics Research Section A: Accelerators, Spectrometers, Detectors and Associated Equipment **604**, 307 (2009), PSD8.

[72] H. Nishiguchi *et al.*, Development of an extremely thin-wall straw tracker operational in vacuum – the comet straw tracker system, Nuclear Instruments and Methods in Physics Research Section A: Accelerators, Spectrometers, Detectors and Associated Equipment **845**, 269 (2017), Proceedings of the Vienna Conference on Instrumentation 2016.

[73] Guanghua Xu and E. V. Hungerford, Static forces on the anode wires in a straw chamber, IEEE Transactions on Nuclear Science **53**, 549 (2006).

[74] K. Ueno *et al.*, Design and performance evaluation of front-end electronics for comet straw tracker, Nuclear Instruments and Methods in Physics Research Section A: Accelerators, Spectrometers, Detectors and Associated Equipment **936**, 297 (2019), Frontier Detectors for Frontier Physics: 14th Pisa Meeting on Advanced Detectors.

[75] S. Shimazaki *et al.*, Front-end electronics of the belle ii drift chamber, Nuclear Instruments and Methods in Physics Research Section A: Accelerators, Spectrometers, Detectors and Associated Equipment **735**, 193 (2014).

[76] T. Uchida, Hardware-based TCP processor for Gigabit Ethernet, in *2007 IEEE Nuclear Science Symposium Conference Record*, volume 1, pp. 309–315, 2007.

[77] E. Hamada *et al.*, Gigabit ethernet daisy-chain on fpga for comet read-out electronics, 2020, 2011.12529.

[78] K. Oishi, Development of electromagnetic calorimeter using GSO and LYSO crystals for the J-PARC muon-to-electron conversion search experiment, in *2014 IEEE Nuclear Science Symposium and Medical Imaging Conference (NSS/MIC)*, pp. 1–6, 2014.

[79] T. University, Research Center for Electron Photon Science, `https://www.lns.tohoku.ac.jp/en`.

[80] T. Ishikawa *et al.*, A detailed test of a BSO calorimeter with 100–800MeV positrons, Nuclear Instruments and Methods in Physics Research Section A: Accelerators, Spectrometers, Detectors and Associated Equipment **694**, 348 (2012).

[81] R. Brun *et al.*, GEANT: Detector description and simulation tool, (1993), Long Writeup W5013.

[82] I. Nakamura *et al.*, A 64ch readout module for PPD/MPPC/SiPM using EASIROC ASIC, Nuclear Instruments and Methods in Physics Research Section A: Accelerators, Spectrometers, Detectors and Associated Equipment **787**, 376 (2015), New Developments in Photodetection NDIP14.

[83] S. Callier, C. D. Taille, G. Martin-Chassard, and L. Raux, EASIROC, an Easy & Versatile Read-Out Device for SiPM, Physics Procedia **37**, 1569 (2012), Proceedings of the 2nd International Conference on Technology and Instrumentation in Particle Physics (TIPP 2011).

[84] Raspberry Pi Foundation, Raspberry Pi 3 Model B, `https://www.raspberrypi.org/products/raspberry-pi-3-model-b`.

[85] Schindler H., Veenhof R., Garfield++ – simulation of tracking detectors, `http://garfieldpp.web.cern.ch/garfieldpp`.

[86] C. Geuzaine and J.-F. Remacle, Gmsh: A 3-D finite element mesh generator with built-in pre- and post-processing facilities, International Journal for Numerical Methods in Engineering **79**, 1309 (2009), https://onlinelibrary.wiley.com/doi/pdf/10.1002/nme.2579.

[87] IT Center for Science (CSC), Elmer - a general-purpose FEM solver, `http://www.csc.fi/elmer`.

[88] S. Biagi, A multiterm Boltzmann analysis of drift velocity, diffusion, gain and magnetic-field effects in argon-methane-water-vapour mixtures, Nuclear Instruments and Methods in Physics Research Section A: Accelerators, Spectrometers, Detectors and Associated Equipment **283**, 716 (1989).

[89] A. Hocker *et al.*, CERN Report No. physics/0703039, 2007 (unpublished), TMVA-v4 Users Guide: 135 pages, 19 figures, numerous code examples and references.

[90] S. Giovannella, The detectors of the mu2e experiment, Journal of Instrumentation **15**, C06022 (2020).

[91] C. Höppner, S. Neubert, B. Ketzer, and S. Paul, A novel generic framework for track fitting in complex detector systems, Nuclear Instruments and Methods in Physics Research Section A: Accelerators, Spectrometers, Detectors and Associated Equipment **620**, 518 (2010).

[92] T. Siiskonen, J. Suhonen, and T. S. Kosmas, New limits for lepton-flavor violation from the $\mu^- \to e^-$ conversion in ^{27}Al, Phys. Rev. C **60**, 062501 (1999).

[93] D. E. Rumelhart, G. E. Hinton, and R. J. Williams, Learning representations by back-propagating errors, Nature **323**, 533 (1986).

[94] Y. Freund and R. E. Schapire, A decision-theoretic generalization of on-line learning and an application to boosting, Journal of Computer and System Sciences **55**, 119 (1997).

[95] A. Natekin and A. Knoll, Gradient boosting machines, a tutorial, Frontiers in Neurorobotics **7**, 21 (2013).

Acronyms

ADC	analog-to-digital converter
ANN	artificial neural network
APD	avalanche photodiode
ASD	Amplifier-Shaper-Discriminator
ASIC	application specific integrated circuit
BDC	beam-defining counter
BDT	boosted decision tree
BG	background
BSM	beyond the standard model
CDC	cylindrical drift chamber
CDR	conceptual design report
CERN	European Organization for Nuclear Research
CL	confidence level
CLFV	charged lepton flavor violation
CMSSM	constrained MSSM
COTTRI	COMET trigger
CRV	cosmic-ray veto
CsI	caesium iodide
CTH	cylindrical trigger hodoscope
DAQ	data acquisition
DCA	distance of closest approach
DIO	decay in orbit
DRS4	domino-ring sampler ver.4
EASIROC	extended analogue silicon PM integrated read-out chip
ECAL	electromagnetic calorimeter
ELPH	Research Center for Electron Photon Science
EROS	ECAL read-out system

ESR enhanced specular reflector

FNAL Fermi National Accelerator Laboratory
FOM figure of merit
FPGA field programmable gate array
FWHM full width at half maximum

GBDT gradient boosting decision tree
GIM Glashow–Iliopoulos–Maiani
GSO Gadolinium oxyorthosilicate
GUT grand unified theory

HPF high-pass filter
HV high voltage
HWHM half width at half maximum

J-PARC Japan Proton Accelerator Research Complex
JINR Joint Institute for Nuclear Research

KEK High Energy Accelerator Research Organization

LED light emitting diode
LEP Large Electron–Positron Collider
LFV lepton flavor violation
LHC Large Hadron Collider
LPF low-pass filter
LV low voltage
LYSO lutetium-yttrium oxyorthosilicate

MIDAS Maximum Integrated Data Acquisition System
MIP minimum ionizing particle
MLF Materials and Life Science Experimental Facility
MLP multilayer perceptron
MPPC multipixel photon counter
MPV most-probable value
MR Main Ring
MSSM minimal supersymmetric standard model
mSUGRA minimal supergravity
MVA multivariate analysis

ND neutral density
NIM nuclear instrumentation module
NLFV neutral lepton flavor violation
NP Hall Nuclear and Particle Physics Experimental Hall

OpenIt Open Source Consortium of Instrumentation

PCB printed circuit board
PD photodiode
PET polyethylene terephthalate
PID particle identification
PMNS Pontecorvo–Maki–Nakagawa–Sakata
PMT photomultiplier tube
POT proton on target
PSI Paul Scherrer Institut
PTFE polytetrafluoroethylene
PWO Lead Tungstate

RCS Rapid-Cycling Synchrotron
RF radio frequency
RMS root mean square
ROC receiver operating characteristic
ROESTI read-out electronics for straw tracker instrument

S/N signal-to-noise
SES single event sensitivity
SFP small form-factor pluggable
SiPM silicon photon multiplier
SLC Stanford Linear Collider
SM standard model
SNO Sudbury Neutrino Observatory
SUSY supersymmetry

TCP/IP transmission control protocol/internet protocol
TDR technical design report
TOF time of flight

UDP user datagram protocol